Optimization of Internal Hydraulics and of System Design for PUMPS AS TURBINES with Field Implementation and Evaluation

Zur Erlangung des akademischen Grades eines

DOKTOR-INGENIEURS

der Fakultät für
Bauingenieur-, Geo- und Umweltwissenschaften
der Universität Fridericiana zu Karlsruhe (TH)

genehmigte

DISSERTATION

von
Punit Singh

aus Neu Delhi, Indien

Tag der mündlichen Prüfung: 03.06.2005

Hauptreferent: Prof. Dr.-Ing. Dr. h.c. mult. F.Nestmann
Korreferent: Prof. Dr.-Ing. M. Gabi

Karlsruhe 2005

Foreword

The research on 'pumps as turbines' at this critical phase of developing decentralized small hydro systems is appropriate for many reasons. The conventional turbine technologies like pelton and cross flow turbines that have been implemented in the micro hydro sector have to be custom-made and are therefore more expensive. They also need expert design and precise manufacturing skills for a good performance. This often becomes a bottleneck especially for smaller projects below 20 KWs of installed capacity.

An alternative approach of using well-known 'pump as turbine' technology can be contemplated and popularized. Pumps are readily available all over the world in every shape and size, mainly due to the ever-increasing demand for pumping application. Also the maintenance and operational issues in pumps are relatively much simpler.

The most critical step in a 'pump as turbine' technology is the selection of the most appropriate machine for a given application and the accurate prediction of the turbine mode performance characteristics. The dissertation has focused on detailed experimental investigations for both radial and mixed flow 'pumps as turbines', with an objective of developing 'selection and performance' charts for the turbine mode operation that can be readily used. The two major issues impeding the 'pump as turbine' technology are the poor part-load performance and the dangerous runaway problem, which have been appropriately addressed within the dissertation.

A considerable portion of the dissertation has been devoted for understanding the internal flow hydraulics in given 'pump as turbine'. A comprehensive programme to optimize the internal hydraulics through simple geometrical modification on the impeller and the casing has been presented.

The landmark aspect of dissertation comprises of the design, implementation and evaluation of a micro hydro project using 'pumps as turbines' for a tea garden in Darjeeling, India. The part-load problem in this system has been effectively solved using an innovative idea of synchronizing 3 'pumps as turbines' on a single shaft, which has proved to be very successful.

This 'pump as turbine' technology has been simultaneously drafted into the institute's pioneering project within the caves of Java, Indonesia. An underground micro hydro power plant with multiple 'pumps as turbines' is envisaged to operate pumps that will supply drinking water up to a height of 200 m for a population of nearly 20,000 people.

The future application of 'pump as turbine' needs to be carried out in a carefully planned manner. Given a prospective scenario of the decentralized micro hydro market expanding to higher levels, conventional turbines can eventually replace the 'pump as turbine' technology. However, till then 'pumps as turbines' are here to stay and have a bright future of providing decentralized, reliable electricity and energy to isolated communities around the world.

To conclude, this dissertation is one the best examples of carrying out a doctoral research programme that began with fundamental hydraulic principles and led its way towards a successful implementation in the field. In the due course it also helped in collecting many invaluable experiences, which would be essential for the future strategic planning.

The candidate, who is well trained both at the Indian and German universities, has shown that even at young age of 28 years he can fulfill the requirements of high quality scientific work and also deliver practical results with a high level of accuracy.

Having said this, I want to wish him and his work the best of the journeys ahead.

16.06.2005, Karlsruhe   Franz Nestmann

Kurzfassung

Die Dissertation beschäftigt sich mit zwei Optimierungsaspekten bei 'Pumpen als Turbinen'.

Zuerst wird die Optimierung der 'Internen Hydraulik' diskutiert und durchgeführt. Gegründet auf einer ausführlichen theoretischen Analyse mit einer 'flow zone'-Annäherung werden 4 Hauptzonen festgelegt. Durch systematische Variation der Laufrad- und Gehäusegeometrien in diesen Hauptzonen werden die Änderungen der Leistung und des Wirkungsgrades an 8 'Pumpen als Turbinen' experimentell untersucht. Diese 8 untersuchten Pumpen sind typisch als 'radial' bis 'mixed flow' einzuordnen und überdecken den spezifischen Drehzahlbereich zwischen 20 U/min und 95 U/min.

Zur Bewertung der internen Optimierung in Bezug auf die Verteilung der hydraulischen Verluste in den verschiedenen Hauptzonen wird eine 'Percentage Analysis'-Methode entwickelt. Als Ergebnis der internen Optimierung zeigt sich, dass die Abrundung des Laufradeinlasses und die Anbringung von Gehäuseringen die Leistung der 'Pumpen als Turbinen' verbessert haben. Die Auswirkung der Vergrößerung des Saugmundes und der Entfernung der Saugmundrippe sind jedoch nicht einheitlich und hängen von weiteren Geometriedetails ab.

Eine weitere, die 'Combined Suction Head Number'-Analyse genannte Methode wird zur Erfassung des Kavitationsphänomens in 'Pumpen als Turbinen' eingeführt und zeigt erfolgreich, dass das Kavitationsverhalten einer 'Pumpe als Turbine' mit einer einzigen dimensionslosen Kurve dargestellt werden kann.

Der zweite Optimierungsaspekt der Dissertation bezieht sich auf das 'Systemdesign' von 'Pumpe als Turbine'-Anlagen und fokussiert auf die Anwendung der Technologie. Eine theoretische Studie, die auf experimentellen Voruntersuchungen basiert, bereitet die Auswahl der besten 'Pumpe als Turbine' für gegebene Randbedingungen vor. Diese Vorauswahl und die entwickelten Leistungsdiagramme für 'Pumpen als Turbinen' ermöglichen die Synthese der kompletten Leistungskennlinie einer Pumpe im Turbinenbetrieb.

Darüber hinaus werden weitere wichtige Themen für den Betrieb von 'Pumpe als Turbine' Anlagen, wie das Teillastverhalten und das Durchgehen der Maschine, diskutiert und verschiedene mögliche Lösungen vorgeschlagen.

Ein hydroökonomisches Kriterium zur Gegenüberstellung aller Kleinwasserturbinen wird eingeführt. Die Anwendung dieses Kriteriums zeigt, dass einzelne und kombinierte 'Pumpe als Turbine'-Einheiten als Kleinwasserturbine in hohem Grade vorteilhaft sind.

Die Dissertation schließt ab mit einem konkreten 'Systemdesign' einer kombinierten 'Pumpe als Turbine'-Anlage (3 Einheiten) für eine Teeplantage in Darjeeling, Nordostindien. Die Synchronisierung der Maschinen wird so gestaltet, dass unter unterschiedlichen Lastbedingungen eine optimale Energieausbeute erreicht wird. Eine ausführliche Auswertung des Probebetriebs dokumentiert, sowohl für den Einzel- als auch für den kombinierten Betrieb, den Erfolg des ausgearbeiteten Konzeptes.

Abstract

The dissertation deals with two major types of optimization procedures on 'pumps as turbines'. The first procedure is concerning the optimization of '<u>Internal Hydraulics</u>', which is essentially done through an experimental study. Based on a detailed theoretical analysis using a flow zone approach, 4 major optimization stages are identified that combine modifications on the impeller and casing geometry, and experimentally investigated on 8 'pumps as turbines'. The 8 pumps that were selected for the study are of radial flow and mixed flow designs covering a pump specific speed range from 20 rpm to 95 rpm.

An interesting methodology called the 'percentage analysis' is developed to study physical significance of the internal optimization techniques with respect to hydraulic loss distribution in the various flow zones. The results of internal optimization have been very educative and have shown that some techniques like inlet impeller rounding and inlet casing rings have improved the performance of the 'pumps as turbines', while other techniques like suction eye enlargement and casing eye rib removal have had mixed influences on the performance.

An alternative methodology to study the cavitation phenomenon in 'pumps as turbines' called the 'combined suction head number' is introduced. The application of this analysis has successfully demonstrated that cavitation behaviour of a 'pump as turbine' can be represented with a single dimensionless curve.

The second optimization procedure of the dissertation refers to the '<u>System Design</u>' of 'pump as turbine' systems primarily objected towards the application of technology. A theoretical study based strongly on experimental findings is developed to enable the selection of the best 'pump as turbine' for given boundary conditions. The selection and performance charts for both radial flow and mixed flow machines are also developed, which assists the synthesis the complete turbine mode performance characteristics of the selected pump.

The other important subjects concerning the optimization of the '<u>System Design</u>' are the poor part-load performance and runaway problems associated with 'pump as turbine' systems, which are presented and various solutions for the same are discussed.

A hydro-economic criterion is introduced for comparing all micro hydro turbines. The application of this hydro-economic criterion shows that both single and multiple 'pump as turbine' units are highly favourable as turbine options for micro hydro.

The dissertation concludes with elaborative system design for a <u>Field Implementation</u> of 'pump as turbine' system for a tea garden in Darjeeling, northeast India. A multiple 'pump as turbine' system (3 units) in synchronization is envisaged to operate under different part-load conditions. A detailed <u>Field Evaluation</u> is carried out on the units both in isolated and synchronized modes, which reveals a great success of this concept.

Table of Contents

Personal Introduction to the Dissertation

A technical subject of 'pump as turbine', which is the focal point of the dissertation should begin by addressing the issues that justify the cause. The issues that have been raised here are definitely more controversial, though it may seem that a simplistic picture is presented. Coming from the desk of an engineer of mediocre philosophical competence, this essay gives a brief overview the authors mind, motivation and reasons for choosing this line.

Building big things has been man's fascination for many centuries. In fulfilling this urge he developed technologies that met the requirements of big things and centralization was the only way found. All industries were all moving towards centralization under the umbrella of capitalism. During this time when man was busy setting up network for this establishment, there were thinkers who proposed a different approach.

To get a clearer picture of the issues it is important to introduce two individuals of the 20th century of different cultures, backgrounds and worlds whose philosophies are very closely associated with the central philosophical theme of the dissertation. There were delicate differences in the social, political and contextual order prevailing during the times of the two personalities chosen here. This essay is no means of final word, but only a view, which needs to be nurtured and pruned to take any concrete shape.

J. C. Kumarappa [32] one of the non-western thinkers and an accountant by profession came to the forefront during the Indian freedom struggle against the British Empire. He was closely associated with Mahatma Gandhi and evolved a new order of economy famously called as Gandhian economy. Kumarappa, one of India's best known economists of his era, was a firm idealist and in his book Economy of Permanence [32] spoke of human values associated with economy. He strived hard for decentralization by establishing village industries, which according to Gandhi and him was the only way India would and should develop. Kumarappa's approach combined not only with an unchallenged theory but also with unmatched praxis. Though his work could not evolve, he set up one of the earliest and by far the best methods of a successful and sustaining decentralized system, be it industry, banking, market or the most crucial in the context of this dissertation, Energy.

The other personality in this essay is a German born, British economist called E.F. Schumacher, who coined a revolutionary phrase '<u>small is beautiful</u>' in his book [43], after traveling through the villages of the Indian subcontinent in the 1960s. He was not only inspired by the vast and mostly hidden potential of the rural resources but also acknowledged Kumarappa's effort in developing the rural India.

Though Schumacher and Kumarappa shared a lot of likes, there was fundamental difference, i.e. of their cultures. While Kumarappa was from a home grown eastern culture, Schumacher was westerner became the messiah of those in the west who were looking for

alternate ways countering centralization. However Kumarappa's ideals were, unfortunately found and recognized by only a very small percentage of the Indian population.

Schumacher's 'small is beautiful' gave birth to a new terminology called Appropriate or Intermediate Technology. This technology according to him would be essentially decentralized, using local resources and serving the specific needs of a local population. He firmly believed that developing and optimizing such technologies would solve the major problems of the rural areas of the sub-continent and advised the politicians and law makers to make favourable polices to meet this end.

In short Kumarappa's philosophy and campaign for decentralization and Schumacher's small and appropriate technologies are very closely knitted together and forms the backbone for the motivation in the technical theme of 'pump as turbine'.

The 'pump as turbine' technology forms a component of small hydro systems that is essentially aimed for decentralized and standalone application. Though PAT can be a part of a big and centralized schemes like energy recovery in chemical industry, water supply network or pump storage systems, the prime destination foreseen from the philosophical perspective of this dissertation is in the field of isolated power generation for electricity, water pumping or other applications.

There is a gross myth that small technologies are simple and easy to develop and implement. This is incorrect and even from the technological perspective Schumacher agreed that it took special skill to come up with something very simple. In the larger picture, one of the problems with the technology today is that it is grossly out of proportion with the human scale of things. To regain a sense of proportion is definitely a mighty task. Therefore Schumacher's phrase needs to be re-configured as 'small is beautiful but not simple'.

It is possible to draw lines between the 'pump as turbine' technology and the above philosophy. The size of the technology being discussed here is definitely small but the challenges that take to make this small technology working needs to be understood. The lack of proper understanding of hydraulics in 'pumps as turbines' is one of the foremost challenges and coupled with unreliability of the theoretical predictions have made detailed experimental research absolutely inevitable. The other challenges are in the context of developing optimization procedures for making accurate models for selecting the best 'pump as turbine' (from a wide range of designs) for given boundary conditions and subsequently developing compact system designs for field projects with highest efficiency. Therefore though the 'pump as turbine' technology classifies well under the category of 'small is beautiful' it is not as straightforward and simple, as one would expect it to be.

The other challenges that are impeding 'pump as turbine' technology are more to do with the controversial subject of decentralized and appropriate technologies not taking off on a big scale. These technologies in general gave the engineers, economists, policy makers, and social workers a great difficulty in understanding the philosophical concept behind it. A few of them pursued towards the idea, while a majority of them rejected it. Humping of this bandwagon till the early 1970s and after the events of the oil crisis, decentralized energy

was given a fresh impetus mainly in the developed countries through various renewable energy technologies. Appropriate technologies through renewable energy sources have provided isolated examples of success, but have failed to carry on its journey on the big road.

The development of small technologies comes with many questions. Top of all is the fact that the support systems for such technologies have not clearly understood the final destination. In a totally centralized environment, it is a challenge to bring in the concept of small and decentralized technologies, let alone its success. Sometimes one gets a feeling that the words like small, decentralized, appropriate and sustainable are becoming scientific and political jargons only to satisfy personal egos. The idea of subsidizing appropriate technologies however did not succeed in accelerating their growth. With more and more people finding it difficult to survive on developing and implementing decentralized systems, a big vacuum is being created. This can be termed as a dangerous situation for the survival of making small things sustainable.

It is not only the centralized forces that are preventing small things from growing, but also the saddening contradictions that small technologies themselves face. For example electricity from a centralized grid can be used by a customer with a maximum effort of pushing a button and later paying the electricity bill. But electricity from decentralized sources would involve a much more effort in terms of maintenance, service and in case of community-based projects, an extra effort is required in coordination due to the existing complex socio-economic equations and many more uncounted challenges. It is not uncommon that rural customers prefer to wait for years for a central grid electricity to reach their homes. Therefore small technologies have no easy journey.

It is clearly seen that decentralized or small systems are difficult and sometimes complicated, not only from the technological perspective but also from the implementation, logistic and social angles. Though the reasons for the failure of decentralized systems are sometimes controversial, one of the foremost causes is that these technologies are considered to be easy and simple which do not need competence of schooled engineers, scientists or policy makers. One of the easily confused things is equating small to simple, which can more often result in a backfire.

Those who believe in small technologies should not leave the nurturing of Kumarrapa and Schumacher's ideas for chance to fulfill. But look for all possible ways and even consider the use the centralized network to see its logical end. The second and current generation after the likes of Kumarappas and Schumachers, is certainly embodied with skill and energy. But these skills and energies however, need to be collimated and synergized towards a new philosophy of building 'small things in a big way instead of big things'. This would need all the technologies of modern day world, all positive experiences of the centralized systems, intelligent planning (business and management), all honest and sincere ways of winning the hearts of the needy people who are waiting at the end of the tunnel with desperate expectation.

Decentralized technologies can become a reality if and only if we can multiply the examples of successful, well-proven small technologies. PUMP AS TURBINE is only one of the many directions of fulfilling this new modified philosophy of doing '<u>small things in a big way rather than big things</u>'.

The sensibility of using the idea of 'pump as turbine' comes from the fact that there are standard small pumps available in all sizes, thanks to the huge market for pumps. On the other hand it is very difficult to get small turbines off the shelf. Turbines have to be designed and manufactured, which is a longer and expensive route. Some smaller pumps may not be available off the shelf and have to be manufactured on order, but this still simpler and economical because of no design costs involved. But when size crosses a particular limit, PATs become less economical compared to an expensive well-designed turbine to suit varied flow conditions and also considering the total cycle of manufacture, operation and performance.

Therefore the 'pump as turbine' cannot succeed when made big because of complicated performance requirements. However when made small these disadvantages can be negotiated well enough, while the cost and availability issues on the other hand turn it into an advantage. Hence 'pump as turbine' will work only when made small, but necessarily in multiple folds for it to have any future not only in the technological and economical context but also in the social context. The path for achieving this goal is not simple and one may have to contemplate a path of a carefully defined <u>revolution</u>. A revolution that combines thoughts, skills, labour, commitment and most importantly concern. This philosophy is the central motivating theme of the dissertation.

Acknowledgements

I would like to begin with a sincere thanks to the Almighty for listening to my prayers and providing me the strength to complete the dissertation.

This research project would not have taken shape, but for the direction and rock-solid support from Prof. Franz Nestmann. Apart from his charisma and engineering competence, he shared a tremendous amount of philosophical inclination to the practical value of 'pumps as turbines' and took a lot of pride in my work. This gave me a paternal comfort and nurtured the eventful journey. He arranged a scholarship for me from the Institute (Institute for Water Resources Management, Hydraulics and Rural Engineering) funds and gave a free hand in my research. He also traveled with me to my home country, India, many a times and showed immense solidarity in my endeavours, goals, and vision. It was he who coaxed me to physically participate in the field implementation project in Darjeeling, which eventually became the turning point of the dissertation. I would like to pay my heart filled tribute to him and also hope that this partnership continues forever.

I would like to express my gratitude to Prof. Martin Gabi for agreeing to review the dissertation. The staff members of his institute (Institute of Fluid Machinery) have been extremely co-operative and helpful. I would specially acknowledge the efforts of Dr. Saban Caglar, who played a pivotal role in guiding me during abrasive stages of the project.

I would also like to acknowledge the support extended by the pump manufacturer, Kirloskar Brothers Limited, Pune. In particular, I would like to thank Mr. Sanjay Kirloskar, Mr. R.K. Srivastava and Mr. A. Raghunath for all the strategic and logistic support for the research collaboration. They were also instrumental in arranging the supply the 4 pumps for testing in the Theodor Rehbock Laboratory. I also appreciate the efforts of Dr. J.T. Kshirsagar who was involved in some measurements on the test-rig and actively participated in numerical studies. The support from other staff members like Mr. Sanjeev Chabbra and Mr.S.N. Shukla is also worth mentioning.

The support from the other industrial partner, KSB AG, Frankenthal, is also highly commendable. Dr. Sven Baumgarten and Mr. Wolfgang Guder were of great help in arranging a pump for the experimental research. I also thank Mr. Thomas Reinheimer, a former KSB employee and a friend for initiating this collaboration.

I would also want to acknowledge the collaboration with our academic partner, the Nottingham Trent University under which numerical simulation of an experimentally tested 'pump as turbine' was carried out by Dr. Arthur Williams and his student Mr. Arnaldo Rodrigues.

The process of experimentation would have not been possible without the wholehearted participation and co-operation of various departments of our Institute, in particular the workshop, instrumentation and computer sections. I would like to express my deep appreciation and gratitude to Mr. Werner Helm, Mr. Hermann Weiher, Mr. Manfred Lösche

and Mr. Hans Schleisiek. I would also like to take the names of other colleagues Mr. Günther Kühn, Mr. Michael Ritzmann, Mr. Jürgen Ulrich, Mr. Michael Ziegler, Mr. Hans Held, Mr. Marcus Plate and Mr. Dieter Bierwirth, who were not only my closest friends but also showered me with brotherly affection. They have been Samaritans during the most difficult phases of my journey and their unconditional love has overwhelmed me.

I would also like to acknowledge the contributions of our librarian Mrs. Ruth Petters Raskob, who not only arranged for literature material but also showed care and compassion during my stay in Karlsruhe. I also want to mention the help and favours rendered by our secretary, Mrs. Gisela Krause. I am also grateful to the support provided by the department heads, co-researchers, students and other staff members of our Institute who were directly or indirectly involved with my research.

I also want to thank Mr. Ramasubramanian of Sahyadri Energy Systems, Bangalore and Mr. Sanjay Bansal of Ambootia Tea Estate, Darjeeling for accepting our design and permitting us to implement the idea of a multiple PAT system. I would also like to acknowledge the sincere efforts and co-operation extended by Mr. C.S. Ramaswamy and Mr. Adishesh during the execution of the Ambootia micro hydro project.

From a personal perspective, I cannot prevent myself from acknowledging those individuals who have been closely associated to my heart. Mr. Deepak Malghan, a close friend, philosopher and guide has been both a great admirer and critic of my work. An electrical engineer turned ecological-economist, Deepak, has been a tremendous influence on my thinking. He is one person with whom I plan to walk a long journey of self-realization.

It also gives me pleasure in recognizing the support and love received from my landlady Mrs. Schmidt and my neighbour Mrs. Lessl, who showered me with motherly affection. I want to give a special mention to my close friend Mr. Anshul Patni, who brought brightness to my otherwise lackluster social life in Karlsruhe.

Towards the end I would want to say few words about my family. I have grown up seeing my father, Mr. Jasmail Singh, striving hard to help the society. This has inspired me in shaping my goals. I pay obeisance for his constant concern in seeing the completion of my thesis. My mother, Mrs. Sudershan, has been praying for me not only from India, but also visited Karlsruhe and gave me much needed support for 8 long weeks during the final stages of the dissertation. I thank her wholesomely. I am also grateful to my sister, Mrs. Rinku, who stayed with me in Karlsruhe for over a year and put up all the hardships arising from my busy research schedules with a sweet smile. I also appreciate the wishes and prayers from my brother-in-law, Mr. Ramnath Shanbhag. I want to express my gratitude to Mrs. Karin Nestmann, whom I consider a family member, for her understanding, care and concern. My final thanksgivings is reserved for my aging grandmother, whose sincere prayers and blessings have carried me so far.

I, finally pray that the Almighty fulfills the aspirations of all the people (also whom I have not mentioned here) who have been a part of this journey and those who will be a part of future journeys.

Nomenclature

Full Scripts

2	Reference plane at front shroud profile of impeller eye
A	Cross-sectional area, m^2
b	Width, m
B	Casing width, mm
C	Capacity of a bearing, N
C	Torsional stiffness, Nm
D	Reference impeller diameter, m
e	Exit measurement or reference plane
F	Load on Bearing, N
g	Acceleration due to gravity, 9.81 m^2/s
gH	Head, m^2/s^2
h	Vertical weir height, cm
H	Head, m
i	Inlet measurement or reference plane
J	mass moment of Inertia, Kgm^2
k	Coefficient of yaw sphere
K	Coefficient for head or head loss as a function of $v^2/2g$
K	Simplified friction coefficient for head loss as a function of Q^2, s^2/m^5
L	Length, mm
N	Rotational Speed in <u>rpm</u> for specific speed (N_q - SI mode)
N	Rotational Speed in <u>rps</u> for ϕ, ψ, $\mathbf{p}$, ϕ_c, ψ_c and N_{ss}
N_{cr}	Critical speed when N_{ss} = 0.63, rpm
N_q	Discharge based specific speed (SI), rpm
N_{qp}	Discharge based pump mode specific speed (SI), rpm
N_{qt}	Discharge based turbine mode specific speed (SI), rpm
N_{ss}	Suction Specific Speed

m	Lateral static deflection, mm
p	Pressure, N/m^2
p	Power number, $P/\rho N^3 D^5$, (P in watts, N in 'rps', D in 'm', ρ in Kg/m^3)
ℙ	Pfleiderer's slip factor
P	Power output, KW
Q	Discharge, m^3/s
r	Radius, mm
R	Electrical resistance, ohm
s	Reference plane at casing-suction eye flange
sl	Slip
sr	Shroud thickness, mm
t	Thickness, mm
T	Torque, Nm
u	Peripheral velocity at reference diameter D, m/s
v	Velocity, m/s
V	Voltage, volts
X	Clearance within PAT control volume, mm
z	Vertical elevation, m

Greek Symbols

α	Absolute flow angle, degrees
β	Blade angle, degrees
δ	Radial flow angle, degrees
Δ	Specific diameter number, (defined in Equation (5.4))
ϕ	Discharge number, Q/ND^3 (Q in 'm^3/s', N in 'rps', D in 'm')
ϕ_c	Dimensionless discharge number, (Cordier definition, Equation (5.2))
φ	Shock coefficient
η	Efficiency, %
λ	Friction coefficient

μ	Dynamic viscosity, Ns/m^2
μ	Overall friction factor in leakage discharge (Q_{Le})
θ	Swirl angle, 90 - α
ρ	Mass density of water, 1000 Kg/m^3
σ	Specific speed number, (defined in Equation (5.3))
σ	Stress, N/mm^2
ψ	Head number, gH/N^2D^2 (gH in m^2/s^2, N in 'rps', D in 'm')
ψ_c	Dimensionless head number, (Cordier definition, Equation (5.1))
ω	Angular speed, rad/s
ζ	Swirl loss coefficient
ς	Rehbock's constant in weir discharge formula (Equation (A9.3))

Subscripts

1	Turbine mode Inlet
1.C	Casing width at turbine mode inlet
2	Turbine mode exit / Reference plane at front profile of impeller eye
2	Hole '2' of the yaw sphere probe
2.C	Casing section at turbine mode exit (near plane '2')
2.L	Outer leakage profile of impeller eye
4	Hole '4' of the yaw sphere probe
∞	Infinite blade condition
a	Atmospheric conditions
A	Axial clearance of shroud surface
B	Ballast load
b	Back shroud
c	Cordier definition
cr	Critical condition
C	Critical resonance speed

d	Draft Tube
dyn.	Dynamic condition
e	Exit measurement or reference plane
Eu	Euler
Ex	Exit of leakage cross-section
Elec.	Electric quantity
Expt.	Experiment
f	Front shroud of the impeller
f	Fatigue
G	Generator
Hyd.	Hydraulic condition
i	Inlet measurement or reference plane
In	Inlet to leakage cross-section
L	Hydraulic head loss component
Le	Leakage
m	Meridional component
mf	Mixed flow
mech.	Mechanical condition
p	Pump mode condition
r	Relative velocity component
reqd.	Required condition
R	Radial clearance of the outer impeller diameter
R.F	Radial-Free clearance of the outer impeller diameter
s	Reference plane at casing-suction eye flange
s.e	Axial suction eye region, between planes '2' and 's'
sh	Shock condition
ss	Suction specific speed
su	Suction conditions
t	Turbine mode condition
th	Throat (tongue) section
to	Torsion

u	Peripheral component
ul	Ultimate condition of stress
va	Vapour
w	Weir

Superscripts

| * | Modified blade angle due the finite number of blades and slip |
| ** | Actual discharge through the Impeller |

Abbreviations

AISI   American International Standard Institutions

BEP   Best Efficiency Point

CFD   Computational Fluid Dynamics

CRA   Casing Rib Absent

CRP   Casing Rib Present

CSH   Combined Suction Head

CSHN   Combined Suction Head Number (Equation (2.31) and (2.36))

ICR   Inlet Casing Rings

IEC   International Electromechanical Commission

IR   Inlet Rounded

IWK   Institut für Wasserwirtschaft und Kulturtechnik

NPSH   Net Positive Suction Head, m

NPSHA   Net Positive Suction Head Available, m

NPSHR   Net Positive Suction Head Required, m

PAT   Pump As Turbine

PAT1   Pump As Turbine Unit 1 in the Case Study (Chapter 6)

PAT2   Pump As Turbine Unit 2 in the Case Study (Chapter 6)

PAT3   Pump As Turbine Unit 3 in the Case Study (Chapter 6)

rpm   revolutions per minute

rps   revolutions per second

WF   Weight Factor

UREDA   Uttaranchal Renewable Energy Development Agency

1. Introduction and Problem Outline

This chapter comprises of a brief description of the status and state of art of the 'Pump as Turbine' technology from its historical background, research and various applications. It also deals with the clearly defined objectives of the dissertation. The last section of the chapter is dedicated for outlining the problem in detail.

1.1 Status of Technology

1.1.1 Historical Background

The use of pumps as turbines has been a research topic for over 70 years. Its journey began when Thoma [54]&[26] and his engineers accidentally found that pumps operated very efficiently in turbine mode, when they were trying to evaluate the complete characteristics of pumps. The turbine mode operation became an important research question to many manufacturers pumps were prone to abnormal operating conditions. Knapp [29] later published the complete pump characteristics for few pump designs based on experimental investigation.

In the 1950s and 1960s, the concept of pumped storage power plants was evolved mainly in developed countries to manage the peak power requirements. 'Pumps as Turbines' hence found one of its important applications and this sustained the research to a certain extent. However the capacity of such plants was in the order of 50 MW to 100 MW, and the numbers of them were few.

In the later years chemical industries became another area for the application of PATs. In certain chemical processes it was necessary to dissipate the energy of high-pressure fluids through small pipe lengths. Instead of simply throttling, PATs were installed to recovery some energy. Even in water supply networks identical applications of this technology were found.

1.1.2 Research Activities

Some of the big and medium pump manufacturers became interested in the practical niche the turbine mode operation presented. They began characterizing their pumps in turbine mode as well. As it was found to be expensive to test all pumps, manufacturers along with researchers worked in trying to predict the turbine mode performance of all types of pumps based on pump mode characteristics. Many prediction techniques, at least a dozen of them have been published till date. Few of the early contributors to these techniques were Kittredge [27] and Stepanoff [52]. In the later years many more techniques were developed by a host of researchers namely Gopalakrishnan [15], Sharma [44], Schmiedl [42], Grover

[14], and more recently by Williams [57], Alatorre-Frenk [2] and Cohrs [6]. There are many uncertainties associated with the various prediction methods (as seen in section B1, Appendix B), nevertheless they have served as a starting point in the technological dissemination.

1.1.3   New Area of Application – Micro and Small Hydro

In the recent years, small and micro hydro has become a new application area for pumps as turbines, where they are aimed to replace the expensive turbine units. These are often decentralized energy systems of capacities below 100 KW. Due to the huge market for pumps of all possible sizes it is easily available, cheap and reliable. Also with respect to the maintenance it has many advantages compared to custom-made turbines.

1.1.4   Challenges with PAT Technology

Due to the fixed geometric conditions of the flow within the casing and impeller, pumps as turbines have poor part-load performance. This is one of most challenging problem to handle for a micro hydro system based on PAT.

In addition to this it is often come to notice that the predicted data on the turbine performance do not match with the experimentally obtained values (as seen in section B1.2, Appendix B). Therefore the selection of a good pump becomes a great challenge. A pump operating as a turbine is very sensitive towards changing boundary parameters, namely head and discharge. Hence a wrong pump selection will result is shift of the operating point, delivering the non-desired output and ultimately may even cause the failure of the project.

The requirements for a pump as turbine system is very site specific and it therefore offers only a very small market. This is one of the major bottlenecks in the further development of this technology.

1.1.5   Unattended Problems of PAT

One of the unattended areas of the research on PAT is with respect to the optimization of the turbine mode performance. Optimization in this context is defined as the improvement of the turbine mode performance characteristics (efficiency related) through definite geometric modification on the pump design. Some pumps have design features, which may not suit turbine operation. However, optimization requires a detailed understanding of the hydraulic energy transfer mechanisms, which can be obtained only from a combination established hydraulic fundamentals, elaborate experiments and more recently from numerical techniques. Though optimization techniques cannot bring about a revolutionary change to

the part-load operation of PAT, it can play a decisive and beneficial role in PAT projects that already have a good system design.

The next problem of crucial consequence to this technology is the overall system design where very little resource is available. System design will not only involve characteristics of the pump as turbine unit but also of associated components summarized below.

- Generators for electricity generation,

- Components involved in mechanical, pumping or other application.

- Hydraulic system including penstock and draft tubes.

It is necessary to have a thorough understanding of each of the smaller components and their operation together as an integrated unit. This is very critical for making 'pumps as turbines' successful at the application level.

1.2 Objectives of the Dissertation

1. To make a thorough experimental investigation on the performance of a wide range of radial flow pumps and mixed flow pumps as turbines. In particular to study the following,

    i.   Overall performance.

    ii.   Internal flow conditions at turbine mode exit.

    iii. Cavitation phenomenon based on availability criterion.

2. To understand the hydraulic energy transfer mechanism within a structured control volume of the machine and to identify the critical zones that affect the turbine mode performance.

3. To perform simple geometric modification on the identified critical zones and to determine the change in performance through detailed experimental investigations. In short a thorough optimization study of the internal hydraulics, which involves the understanding of the physical effects of the performed modifications with respect to the loss mechanisms within the various zone of the PAT control volume.

4. To recommend those optimization techniques which are simple, economic and result in maximum benefit with respect to machine's performance.

5. To understand cavitation in PATs and develop a holistic approach to deal with this phenomenon.

6. To develop a scientific, systematic model to help the complete system design of a PAT based micro hydro system inclusive of the following components.

   i. Accurate selection pump for a given conditions.

   ii. Synthesis of operating characteristics.

   iii. Device methods to improve the part-load operating performance of PAT systems.

   iv. Special focus on the runaway problems in both radial and mixed flow PATs.

   v. Appropriate mechanical design for given application.

7. To design and implement a complete micro hydro scheme using PATs based on the model developed with due considerations to the part-load performance. This system should also adopt all the recommended internal optimization techniques on the PAT.

8. To study the hydro-economics of the PAT based system in different configurations and to prove its efficacy as compared to a standard custom made turbine.

1.3 Detailed Problem Outline

1.3.1 Problem 1: Optimization of the Internal Hydraulics in PATs

The hydraulics of a PAT is unconventional since a pump is generally not designed for turbine mode operation. Therefore many regions of the PAT control volume, namely the volute casing and the impeller may or may not have optimum or favourable hydraulics. The chief problem here is to identify the zones that are critical for the energy transfer, which is only possible with a structured and programmed approach using experimentation or numerical technique.

Within the PAT hydraulics the first zone that comes to the consideration is the spiral volute casing, whose design should be reviewed. The second zone classifies as radial clearance region where the flow comes under the influence of the complex effects. Different pumps have different clearance designs, which need to be considered. The differences in design are not only with respect to the extent of the radial length between the turbine mode-casing

inlet width and the outer impeller periphery, but also considering the axial distances of the impeller shrouds.

The next region of the consideration is the primary power transmitting component, the impeller or runner. The impellers of pumps have a characteristic backward curved vane design with varying blade number. Within the impeller there are three different regions that require consideration, namely the inlet impeller zone, the main flow passage between blades and the exit impeller zone. The inlet impeller zone forms the peripheral transition between the stationary and the rotary frame of reference, characterized by blade profiles that are sharp edged. Along with this the shrouds that hold the blades are also sharp edged both in the inner and outer sides. Though the main flow zone within the impeller can be considered, it may be difficult in terms economic optimization since it comes with re-designing issues. The exit impeller zone, which is again a transition zone, has an effect on the overall energy transfer of the PAT that needs to be reviewed.

The eye region of the various pumps needs to be studied for optimization. Many pumps have converging designs (from exit impeller zone towards the casing flange). However some pumps also come with diffusing eye. More importantly the eye region of the pumps are characterized by the presence of physical inbuilt obstructions called ribs. These ribs are used for breaking the pre-rotational flow (swirl) in pumping mode. Their influence on the turbine mode operation and flow hydraulics is another important problem for optimization.

The last region in the PAT hydraulics, external to the main control volume is the draft tube. The draft tube classifies as one of the critical component of conventional reaction turbine system with respect to cavitation phenomenon and maximum head recovery. Therefore it also plays a crucial role on PAT performance and needs due consideration for overall optimization

Therefore summing up the chief regions of the geometric modifications for the problem of internal hydraulics optimizations are,

i.   The inlet region of the turbine mode comprising of the clearance zone and the impeller blade region.

ii.   The exit region of the turbine mode comprising of the eye geometry and the draft tube.

1.3.2   Problem 2: Selection and Synthesis of the Operating Characteristics

One of the major problems and challenges in the PAT technology is the selection of the most optimum pump from the available ones to suit a given turbine application. The application is characterized by input boundary conditions namely the available head and the mean discharge along with output boundary conditions namely minimum load and speed criterion.

With so many manufacturers and non-standard designs the selection PAT becomes even more difficult. To reduce the impacts of a wrong selection it becomes paramount to develop a scientific model or application technique. The horrendous impact of a wrong selection includes shift of the operating point within the characteristics leading to suppressed energy production. The two probable conditions (under speed constraints) that could arise are,

1. Non-usability of the available discharge due to saturation of characteristics at a given head or

2. Non-usability of the net available head at a given discharge.

These impacts render the application system unfit for optimum or guaranteed outputs. And in the long run they make the PAT technology unpopular and ruin the growth of the idea.

The development of the PAT application chart for different pump designs namely radial flow, mixed flow and axial flow designs should not only define the operating PAT conditions at the best efficiency point but focus more on the holistic approach which comprises of synthesis of complete operating characteristics. Earlier PAT research emphasized on predicting only the best efficiency conditions. With the availability of the total PAT characteristics, one can evaluate the operation of PAT at other conditions, which are essentially different from the BEP due to special design requirement. There are also some advantages to operate PATs at off-BEP conditions.

Therefore summarizing the problem, it is desired to develop a 'performance and selection chart' for PATs of different designs based on principles of fundamental hydraulics (namely dimensionless analysis) and experimental investigations.

1.3.3   Problem 3: Optimization of the Overall System Design

The next problem that assumes critical significance in the development of PAT technology is with respect to system design optimization. This level of optimization is different from the internal hydraulic optimization as in problem 1. The prime topic that needs to be handled in this section is the development of intelligent methods of improving the part-load performance of a micro hydro scheme using PAT in an economic way. The part-load operation refers to operation of the system under conditions of reduced flows, which is often a season dependent. It is obviously required to operate the system is a highest possible efficiency even at reduced flows.

A micro hydro plant with single PAT has disadvantages of optimum operation only within a small range discharge where the net head utilization and operating efficiency are the highest. At flows lower than that at BEP, a two-fold problem occurs in a PAT. Due to the problem of the fixed geometry and single speed operation in PAT, firstly the efficiency drops and secondly the net head utilized also falls. Therefore along with the problem of drop in operating efficiency there is also a decrease in the head utilization, which further decreases the net generated output.

One of the probable methods to deal with the problem of part-load operation of a single PAT is to operate a series of smaller PATs in parallel. Sometimes each PAT may have a dedicated load though generator or mechanical load. But it may not be always possible to have isolated loads due to complex demand and excessive work required on the design of a new load distribution system. Therefore it may be required to setup smaller PATs to a single load, which is essentially a complex system design and calls for the synchronization of PAT units. This an interesting and challenging problem which needs detailed analysis comprising of hydraulic design that pertains to the 4 quadrant analysis (special operating conditions) of PATs and mechanical design that comprising of shaft loads, bearing selection, drive design and critical speed analysis.

The problem of optimizing system design should be necessarily focused on the complete engineering and economic evaluation of multiple synchronized PAT systems. The economic criterion of such systems includes both hydro-economics and cost economics. The hydro-economics deals with the maximum head and discharge utilization at maximum operating efficiency, while cost economics pertains to the investment required to have a series of PATs and all its accessories required for the mechanical power transmission.

1.3.4 Problem 4: Field Implementation and Evaluation

The ultimate goal of the research efforts in the dissertation is the problem of a systematic implementation of a fully decentralized project based on good selection procedure, accurate synthesis of operating characteristics, optimum system design to handle part-load problems and finally to incorporate all techniques of internal optimization to improve the PAT efficiency.

This problem would involve appropriate site identification with the prime intention that it would be used and operated by the end users. The other components as in any implementation programme would comprise of mechanical fabrication, detailed civil works, erection and commissioning. However at the end, the problem should involve elaborate and critical examination of the system through field tests. This examination should check for the selection of the PATs, accuracy of the synthesized characteristics, mechanical operation and safety issues. The problem should also review the system from the customer's perspective and also from the technology perspective.

2. Theory of Optimization

This chapter has been built up on the basis of the stated objective No. 2 (section 1.2, Chapter 1) and problem 1 (section 1.3.1, Chapter 1) concerning the understanding the internal hydraulic energy transfer and optimization in a PAT control volume. Nestmann et al[36] and Singh et al[45] showed that a flow zone approach could be very useful in understanding the physical effects of optimization in medium and low specific speed PATs. This chapter begins with the definition of 7 flow zones within the PAT control volume. The behaviour of the system hydraulics variables (acting on the PAT control volume) under the influence of any geometric modification is very useful in understanding the internal flow mechanisms and a procedure for the same is described. A comprehensive qualitative treatment is later given to every flow zone with respect to the energy transfer and corresponding loss mechanisms. Cavitation from the perspective of PATs is given a thorough review and an analytical method for studying this phenomenon in PATs is introduced. Towards the end the conceived programme for experimental optimization for the test PATs is laid out.

2.1 Flow Zones in a Pump as Turbine control volume

The various regions of PAT control volume have already been briefly introduced in Problem 1 (section 1.3.1, Chapter 1). The pump design selected for the flow zone description is common to most of the single stage pumps of N_{qp} (SI) in range of 20 rpm and 80 rpm.
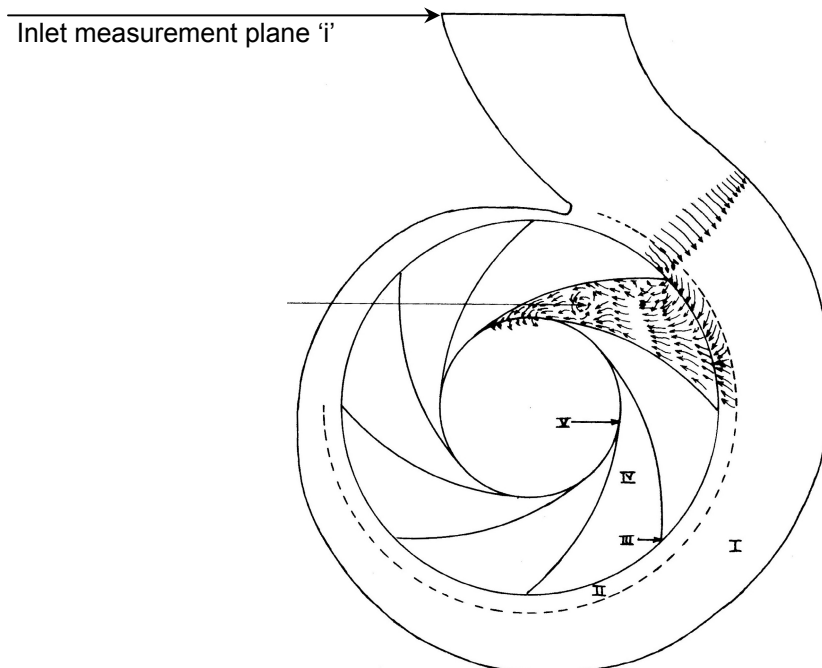

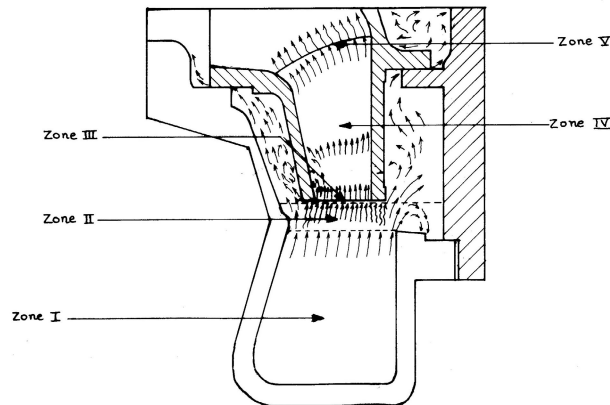Figure 2.1, Flow zones in a PAT control volume – Front view

Figure 2.2, Flow zones in a PAT control volume – Side view

The entire control volume of a PAT system is divided into 7 zones beginning from the inlet plane (casing inlet in turbine mode) and ending at the exit plane corresponding to the draft tube outlet. The basis of the division is on the geometry, which is described henceforth

1) Zone *i*: This zone is defined from the inlet reference plane situated before the beginning of the volute, and stretching itself into the complete circumference of the volute casing as seen in Figure 2.1. At the cross-sectional level the zone ends at the casing mouth where the radial cross-section opens into a free of clearance space of zone *ii* (Figure 2.2) Therefore zone *i* comprises of the enclosed flow from the inlet plane till the tongue cross-section (known as throat) and the semi-enclosed flow throughout the spiral path of the volute ending back at the tongue.

2) Zone *ii*: This zone begins from the casing mouth and extends in a radial direction until the outer impeller interface plane (impeller inlet in turbine mode) as seen in Figure 2.1 and 2.2. The zone *ii* comprises of the following sub-zones,

 i. Zone *ii-a*: The main or central flow sub-zone shown in Figure 2.5.

 ii. Zone *ii-b*: is the sub zone between interface of the zone *ii-A* and the rear casing surface (Figure 2.5).

 iii. Zone *ii-c*: is the sub-zone formed between the interface of zone *ii-A* and the front casing surface, also seen in Figure 2.5.

3) Zone *iii-iv-v*: This zone encompasses the entire impeller control volume from the turbine mode inlet to the exit and comprises of 3 zones. The entire impeller zone is in the rotary frame of reference.

 i. Zone *iii*: is defined at the interface between the stationary frame of zone *ii* and the rotary frame of the impeller, as seen in Figure 2.1 and 2.2. Therefore this interface zone extends by a micro-length into both zone *ii* and impeller zone *iv*.

ii. Zone *iv*: This zone is the main flow zone of the impeller, which contains of the flow within the blade passages (Figure 2.1 and 2.2).

iii. Zone *v*: This zone is defined at the exit impeller interface between the rotary and stationary frame of reference. Similar to zone *iii* it extends by a small distance into the main flow zone *iv* and casing eye zone *vi*.
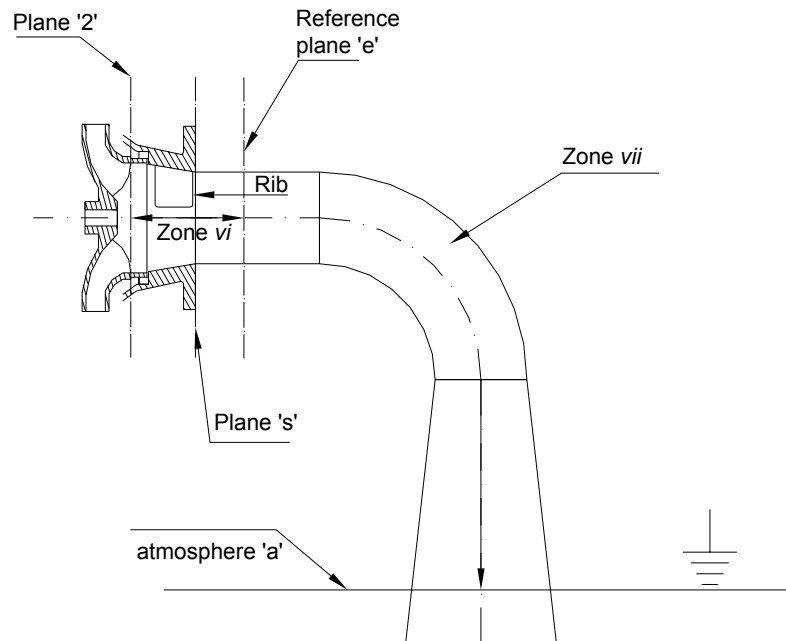
Figure 2.3, Flow zone *vi* and *vii*

4) Zone *vi*: This zone comprises of the entire region beginning from zone *v* and extending until the exit reference plane 'e'. This reference plane is built at the draft tube entrance where the exit pressure measurements are carried out. Therefore zone *vi* comprises of not only the casing eye region but also a small section of the draft tube Figure 2.2 and 2.3.

5) Zone *vii*: This is the flow zone starting from the exit-measuring plane until the draft tube outlet, where it exposes itself to atmospheric conditions. It comprises of straight sections, bends and diffuser sections.

Losses in the Flow Zones

The flow within the PAT control volume is necessarily associated with hydraulic losses. These losses give an idea about the performance of the machine. They are dealt in greater detail in section 2.3. Each flow zone is associated with losses, which are designated in Table

<u>2.1</u>. These losses are the total sum of all the complex loss formations taking placing within each of those zones.

Table <u>2.1</u>, Designation of hydraulic losses in the zones of the PAT control volume

<u>Zone</u>	<u>Total Hydraulic Loss</u>
Zone *i*	$H_{L.i}$
Zone *ii*	$H_{L.ii}$
Zone *iii*	$H_{L.iii}$
Zone *iv*	$H_{L.iv}$
Zone *v*	$H_{L.v}$
Zone *v'*	$H_{L.vi}$

2.2 The System Hydraulic Variables

There are four important variables acting on the 'Pump as Turbine' control volume, which are classified into two categories namely, the input variables and the output variables. The input variables include the total head (gH) acting on the PAT and the discharge (Q) flowing through it, while the output variables include the hydraulic output power (P_{hyd}) delivered to the shaft and the speed (N) of the machine. The variables are described below,

1) Total Head (gH): This parameter is defined between the inlet measurement plane and the exit measurement plane. It is composed of the Bernoulli energy components namely the static pressures, mean velocity heads and the vertical elevations between the respective measurement planes.

2) Discharge (Q): This is the volumetric mass flow rate through the PAT control volume. It is also composed of some leakage flow through the wear rings and the gland packing.

3) Hydraulic shaft power ($P_{hyd.shaft}$): This is the output hydraulic shaft power generated within the impeller control volume resulting from the energy transfer between the fluid and the rotating impeller. The hydraulic output is then transmitted to the shaft.

4) Speed (N): This is the rotational speed of the impeller at which the energy transfer takes place.

[Note: The $P_{hyd.shaft}$ is actually obtained from variable hydraulic torque, $T_{hyd.shaft}$. Any of the two variables can be considered, since they are symbolic to each other]

There are other variables affecting the PAT control system. They are the geometric variables generally represented as the outer diameter of the impeller, D, and the flow variables namely the mass density, ρ, and the dynamic viscosity, μ. Amongst the four main variables, two of them that control the whole system are taken to be the discharge, Q and speed, N. They are referred to as control variables since by changing one of the two variables the whole system can be effectively controlled. Therefore Q and N would be used as crucial reference parameters for the interpretation of the complex hydraulic effects arising due to the geometric modifications in the various optimization stages. The total head, gH and the hydraulic shaft power, $P_{hyd.shaft}$ hence become the dependent variables. Applying the principles of dimensional analysis on the PAT system, and neglecting the effects with respect to viscosity, the following dimensionless groups are evolved and summarized in Table 2.2.

Table 2.2, Dimensionless groups used for interpretation

$Q/(ND^3)$	ϕ	Discharge Number
gH/N^2D^2	ψ	Head Number
$P_{hyd.shaft}/\rho N^3 D^5$	p	Power Number
η_{hyd}	$p/(\phi\psi)$	Hydraulic Efficiency

Subsequently the following functionalities can be established.

$$\psi = f(\phi) \tag{2.1}$$

$$p = f(\phi) \tag{2.2}$$

$$\eta = f(\phi) \tag{2.3}$$

2.2.1 Interdependence of Variables

The interlink between the two dependent variables total head gH and the hydraulic shaft power $P_{hyd.shaft}$ in a PAT scenario needs to be mentioned before studying the behaviour of these variables. The Euler head gH_{Eu}, which is the theoretical energy transfer between a fluid and rotating impeller, is the link between the two variables. The Euler head is obtained from the velocity triangles at the inlet and outlet of the machine (defined in Equation (2.4)) and depends only on the design parameters of the impeller and flow conditions. The gH_{Eu} is also symbolically referred to the net rotational momentum across the PAT impeller.

$$gH_{Eu.\infty} = u_1 \cdot v_{u1} - u_2 \cdot v_{u2} \tag{2.4}$$

The $gH_{Eu.\infty}$ is defined for infinite number of blades and hence should be corrected for the finite number of blades in reality. The corrected head includes slip and is represented as $gH_{Eu.slip}$ (elaborated in Equation 2.15), section 2.3.3)

The total head gH is higher compared to the base value of $gH_{Eu.slip}$ by a value corresponding to the total losses within the entire control volume (zone *i* to *vi*). The total head is therefore represented as,

$$gH = gH_{Eu.slip} + g\left(H_{L.i} + H_{L.ii} + H_{L.iii} + H_{L.iv} + H_{L.v} + H_{L.vi}\right) \qquad (2.5)$$

$$gH = \text{Net rotational momentum} + \text{Hydraulic losses in the PAT control volume}$$

On the other hand the output power $P_{hyd.shaft}$ is also a function of the Euler head $gH_{Eu.slip}$ and the losses within the impeller control volume (zone *iii-iv-v*). Therefore $P_{hyd.shaft}$ is given by,

$$P_{hyd.shaft} = T_{hyd.shaft} \cdot \omega = \rho Q \cdot \left(gH_{Eu.slip} - gH_{L.iii} - gH_{L.iv} - gH_{L.v}\right) \quad (2.6)$$

$$P_{hyd.shaft} = \text{Net rotational momentum} - \text{Hydraulic losses in the impeller control volume}$$

The hydraulic efficiency η_{hyd} is then defined as,

$$\eta_{hyd} = \frac{P_{hyd.shaft}}{\rho Q \cdot (gH)} \qquad (2.7)$$

$$\eta_{hyd} = \frac{gH_{Eu.slip} - g\left(H_{L.iii} + H_{L.iv} + H_{L.v}\right)}{gH_{Eu.slip} + g\left(H_{L.i} + H_{L.ii} + H_{L.iii} + H_{L.iv} + H_{L.v} + H_{L.vi}\right)} \qquad (2.8)$$

$$\eta_{hyd} = \frac{\text{Net rotational momentum} - \text{Hydraulic losses in the impeller control volume}}{\text{Net rotational momentum} + \text{Hydraulic losses in the PAT control volume}}$$

Therefore it can be seen that any change to the Euler head ($gH_{Eu.slip}$) or net rotational momentum causes both the total head, gH and the output power, $P_{hyd.shaft}$ to change. Increase in Euler head increases both total head and output power and vice versa. The hydraulic efficiency is affected accordingly. Based on the above build up, the constitution of the two dependent variables can be summarized below.

gH: Apart from the influence of the Euler head $gH_{Eu.slip}$, any change in the magnitude of hydraulic losses zones *i*, *ii*, *iii*, *iv*, *v* and *vi* causes a change in the magnitude of gH (clearly

seen from Equation (2.5)). A decrease of the hydraulic losses in any of the above zones causes a drop in the total head and vice versa. Therefore the parameter gH is sensitive to the hydraulic changes in any of the zones defined within the entire PAT control volume.

$P_{hyd.shaft}$: In addition to the influences of the Euler head $gH_{Eu.slip}$ the output power is altered by the losses within the impeller control volume only. It is clear from Equation (2.6) that a decrease in the hydraulic losses in zone *iii-iv-v* results in a rise of the output power generated by the PAT and vice versa. Therefore the variable $P_{hyd.shaft}$ is sensitive only to the effects within the impeller control volume and insensitive to the effects taking outside the impeller zone.

Thus apart from the obvious link of the Euler head $gH_{Eu.slip}$, the impeller control volume losses $H_{L.iii}$, $H_{L.iv}$ and $H_{L.v}$ also form a common link between the two dependent variables total head, gH and output hydraulic shaft power, $P_{hyd.shaft}$

2.2.2   Behaviour of Hydraulic Variables

The behaviour of the gH, and the $P_{hyd.shaft}$ with respect to the control variables Q and N is very helpful in explaining the hydraulic effects in the various flow zones within the PAT control volume. There are two important conditions encountered during the interpretation of the characteristics between any two consecutive optimization stages, under constant values of control variables Q and N.

1) Condition 1: Decrease of the gH and no change in $P_{hyd.shaft}$

   This condition defines the decrease of the input power with same output power generated and it results in the increase of hydraulic efficiency, η_{hyd} (Equation (2.7)).

2) Condition 2: Increase of $P_{hyd.shaft}$ and no change in gH

   This condition defines the increase in the output power generated under the identical input power supplied and also results in the increase of hydraulic efficiency, η_{hyd} (Equation 2.7)).

Therefore both the conditions 1 and 2 have identical impacts on the hydraulic efficiency. But internally within the flow zones the condition 1 and 2 relate to different hydraulic effects with respect to the loss distribution. The physical significance of the above conditions is interpreted below assuming no change to the Euler head or net rotational momentum between the two stages. However Euler head changes could also exist and its influence should also be considered during analysis of optimization stages.

Significance of condition 1:

The decrease of gH means a drop in the hydraulic losses of zone *i, ii, iii, iv, v* or *vi*. But the unchanged magnitude of the $P_{hyd.shaft}$ represents no change in the hydraulic loss patterns within the impeller control volume, i.e. *iii-iv-v*, which means that the total losses in zone *i, ii* and *vi* has reduced.

Significance of condition 2:

The increase of output hydraulic power signifies a decrease of hydraulic loss within the impeller control volume *iii-iv-v*. Decrease of losses within the impeller control volume would also mean that the gH should also decrease. But from the condition gH remains unchanged. This can be possible only if the losses in zone *i, ii* and *vi* have increased in such a way as to nullify the decrease of impeller control volume losses.

There are other conditions that could be encountered during two optimization stages,

- Condition 3: Decrease of gH and increase of $P_{hyd.shaft}$
- Condition 4: Decrease of $P_{hyd.shaft}$ and increase of gH
- Condition 5: Increase of both $P_{hyd.shaft}$ and gH
- Condition 6: Decrease of both $P_{hyd.shaft}$ and gH

The physical effects due to conditions 3 to 6 can also be answered through the loss analysis. The test PAT would necessarily come under the influence of any of the conditions (1 to 6). The above methodology paves ways for a better understanding of the effects taking place under different geometric modifications.

2.3 Energy Transfer in the 'Pump as Turbine' Control Volume

Cohrs [7] presented a very comprehensive theory on the energy transfer in a multistage pump as a turbine based on the classical Euler equation and Pleiderer's [38] slip theory. It aimed at synthesizing the complete turbine mode characteristics of a pump. Cohrs [6] presented equations for both the total head gH and the output power $P_{hyd.shaft}$ by treating the two variables independently. For the variable gH, he considered several effects like shock, friction and leakage and for the variable $P_{hyd.shaft}$, effects like disc friction and circulation within impeller passage. He also demonstrated a very accurate similarity between the theoretical and the experimental characteristics.

2.3.1 Flow Zone *i*

As described in section 2.1, the zone *i* comprises of two sub zones, namely the enclosed zone till the radial plane at the tongue and the semi-enclosed zone, beginning from the tongue plane and tracing the entire spiral path of the volute as seen in Figure 2.1, 2.2 and 2.4. The first part of the flow in the enclosed area is identical to a pipe flow situation in a bend with a gradual contraction of area. The loss associated with this section is the traditional frictional loss designated as $H_{Li\text{-}en}$.
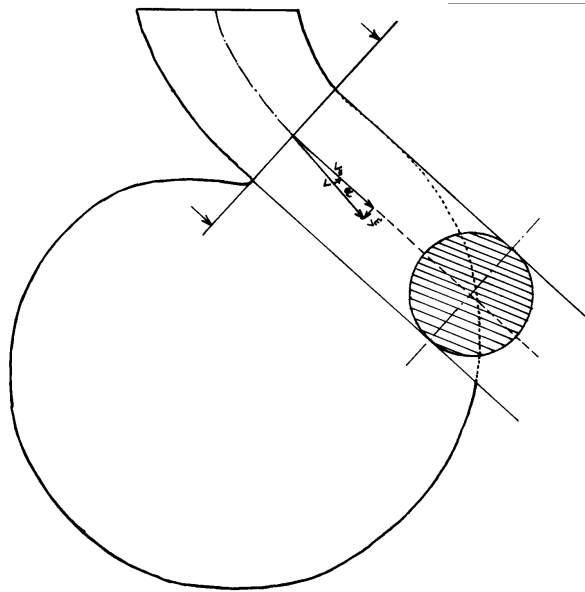
Figure 2.4, Flow zone *i* - tongue section and velocity triangle

At the transition from enclosed flow to the semi-enclosed section, the flow undergoes a distinct transformation. Within the semi-enclosed section, the flow would find an opening of uniform width in the radial direction of zone *ii*. Due to this opening the flow traverses in the radial direction and the flow gets a meridional flow component, v_m. Due to the spiral path of the volute a tangential component, v_u also gets added up to the flow. The flow in the entire semi-enclosed section is forced vortex in nature with an average inclination of α degrees. The increased acceleration of flow within the volute along with difference in the respective areas of the throat section and the opening of semi-enclosed section prompts flow to have a much higher tangential component than meridional component. For a constant condition of flow and speed of the machine, the tangential component v_u remains in a dynamic equilibrium with the meridional component v_m at all regions of the semi-enclosed spiral path of the volute.

The inclination α as seen in Figure 2.4 can be represented by,

$$\tan(\alpha) = \frac{v_m}{v_u} \qquad (2.9)$$

The flow inclination can either be determined by directly from the tangent drawn on the two-dimensional volute profile or by an analytical procedure. Given the normal flow area at the tongue section (often called the throat area) and the discharge Q, the average velocity at tongue section,

$$v_{th} = \frac{Q}{A_{th}}$$
(2.10)

Since the v_m is very small, the tangential velocity v_u can be approximated to the velocity at the tongue section, v_{th}, i.e. $v_u = v_{th}$, and inclination (α) can be determined from Equation (2.9).

The losses in the semi-enclosed section (represented as $H_{Li\text{-semi.en}}$) comprises of the frictional losses across the solid boundaries and other secondary flow effects due to the radial opening. The total loss in the zone i is then given by,

$$H_{Li} = H_{Li\text{-en}} + H_{Li\text{-semi.en}}$$
(2.11)

Given that the velocity triangle (Figure 2.4) is right angled, the energy contained in the fluid at the interface zone i-ii is represented as,

$$\text{Fluid Energy} = \frac{v_u \cdot v_{th \cdot u}}{g} = \left(\frac{v_{th}^2}{g} \right)_{zone\ i-ii}$$
(2.12)

In the PAT system, the inclination (α) of flow would remain unchanged for the entire operating range of the characteristics.

2.3.2   Flow Zone *ii*

The major components of flow zone *ii* have been illustrated in Figure 2.5. This zone is one of the most critical zones as far as energy transfer in a PAT is concerned. The distance between the casing mouth and the impeller periphery often known as radial clearance (see X_R in Figure A4.3, section A4, Appendix A) varies with different pump designs. This distance can be quite considerable in some radial flow pumps. The width of the casing mouth (B_{1C} in Figure A4.3, section A4, Appendix A) is far greater than the inner impeller width (B_1 in Figure A4.1, section A4, Appendix A). Also the total impeller width inclusive of the front and back shrouds is lesser than that of the casing mouth. This results in considerable axial clearances in both directions of the impeller as seen in Figure 2.5 (and 'X_A' in Figure A4.3, section A4, Appendix A). The front axial clearance (sub-zone *ii-c*) leads to the wear ring near the casing eye and the back clearance (sub-zone *ii-b*) leads to gland packing/mechanical seal arrangement. In Figure 2.5 the various sub zones of the zone *ii* are illustrated with the central sub-zone *ii-a* forming interfaces with the sub zone *ii-b* and *ii-c* on either side.

Excluding the leakage, the flow that enters the impeller comes under the influence of the hydraulic conditions of zone *ii-b* and zone *ii-c*. It is also governed by the conditions at the interface zone *iii*.
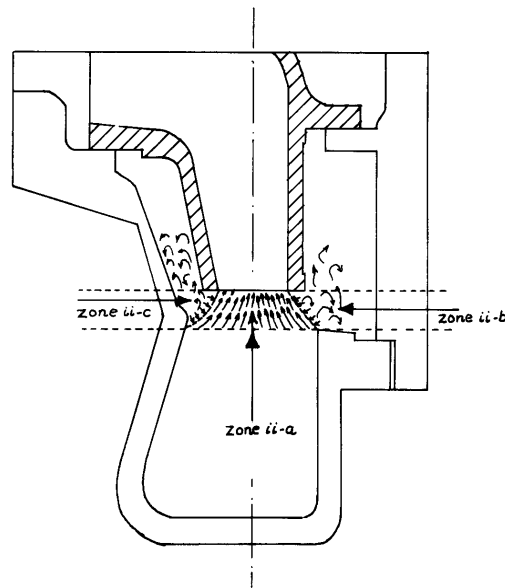

Figure 2.5, Magnified view of Flow zone *ii*

2.3.2.1 Sub zone *ii-b* and *ii-c*

The flow in these zones is essentially decelerating due to the large resistance imposed by the wear rings and gland packing/seal arrangement. Combined with deceleration, there are eddy formations due to the interactions of the rotating impeller with the almost stationary fluid. Added to these there is an interesting interaction of the fluid with the shroud thicknesses (both front, s_{1F} and rear, s_{1R} in Figure A4.1, section A4, Appendix A) in the premises of the interface zone *iii*. The contact of the flowing fluid with the shroud creates local compression and shock waves emanating depending the Mach number. Also there could flow separation due to the sharp edges of the outer surfaces of the shrouds, which adds to this zone's loss. All the above effects are occurring in differentials ratios that results in a very complex turbulent and secondary flow condition. The loss due all these combined effects in sub-zone *ii-b* and *ii-c* is represented as $H_{L.ii\ b-c}$. The disturbances in these sub-zones affect the streamlines at the interface of the central flow zone *ii-a* (as seen in Figure 2.5).

2.3.2.2 Interface with zone *iii*

In addition to the disturbances at the interface of sub-zone *ii-b* and *ii-c*, the streamlines in the central flow zone also come under the influence of two effects at the interface with zone *iii*. The first effect is that discontinuity created due to the sharp edges of the blades and the associated losses are represented as $H_{L\ ii-iii}$.

However the second predominant effect is that of shock created at the blade interface due to fixed direction α_1, of the flow entry at different loading conditions of the PAT. This causes a directional shift of the relative velocity with respect to the already altered blade direction β^*_1 (discussed in section 2.3.3) in the inlet velocity triangle of the PAT, and results in the emergence of a shock velocity v_{sh} of different magnitudes depending upon the loading situation. This shock velocity assumes different directions for part load operation and overload operation respectively.

In addition to the correction on the Euler head (as will be seen in Equation (2.15)), the shock velocity v_{sh} needs to be separately accounted. The losses associated with velocity v_{Sh}, often called 'shock losses' is defined as,

$$H_{L.ii\ sh} = \varphi \frac{v_{sh}^2}{2g} \qquad (2.13)$$

Where φ is called the shock co-efficient. Therefore the total loss in zone *ii* is the sum of all the above loss components.

$$H_{L.ii} = H_{L.ii\ b-c} + H_{L.ii-iii} + H_{L.ii\ sh} \qquad (2.14)$$

It will also be interesting to study the velocity triangle of the fluid before it comes in contact with the blade at interface zone *iii*. The flow area at the inner impeller width is much smaller than that at the casing mouth. Therefore for the same discharge *Q* to flow through a smaller area, there is an increase of the local meridional velocity v_m.

The total energy of the fluid in the zone *ii-iii* interface is reduced compared to that at the casing mouth (zone *i-ii*, given Equation (2.12)) by a value corresponding to $H_{L\ ii}$. Therefore the energy term $(v_u^2/g)_{zone\ ii-iii}$ is smaller than $(v_u^2/g)_{zone\ i-ii,}$ which essentially causes the reduction of the tangential velocity (v_u) in the zone interface *ii-iii* . Representing it on the velocity triangle in <u>Figure 2.6</u>, this transformation can take place only at the expense of the increase of absolute flow angle α_1. Even if there were to be no decrease in v_u in zone *ii-iii* the flow angle α_1 should increase owing to the rise of v_m.
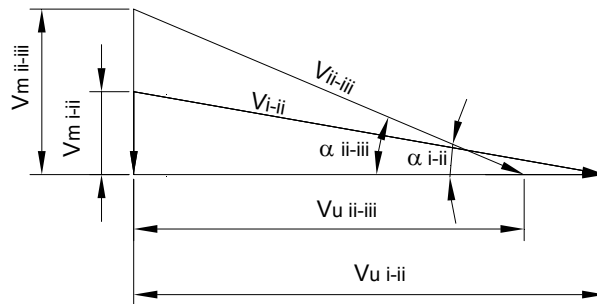

<u>Figure 2.6</u>, Comparison of velocity triangle in the interface zone *i-ii* and zone *ii-iii*

2.3.3   Flow Zone *iii-iv-v*

The classical energy transfer equation defined by Euler applies only to ideal circumstances of infinite number of blades with extremely small thicknesses. In practice, however turbo-machines have finite number of blades and considerable thickness. This resulted in the evolution of the concept of 'slip', essentially due to the pressure difference between finite blade surfaces. The 'slip' is occurring at delivery side of a pump and suction side of a turbine.

Pfleiderer [36] was the first the study 'slip' in pumps. He evolved a derivation of slip factor in pumps, which he denoted by 'p'. However he also presented an equation for slip factor in Francis turbines, which was later used by Cohrs [6] in bringing out the slip factor for a PAT system. There are many contributors to the slip theory as pointed out by Cooper [8] namely Busemann and Wiesner. But Cooper [8] found Pleiderer's method more preferable.

In any case, the due to the ever-presence of slip at the exit of a PAT system, Cohrs [6] proposed that the Euler head given by '$gH_{Eu.\infty}$' (defined in Equation (2.4)) is reduced. The actual Euler head would take the form,

$$gH_{Eu.slip} = \frac{gH_{Eu.\infty}}{(1+sl)} \qquad (2.15)$$

In fact Cohrs [6] went further and argued that the finite number of blades would also cause a change to the relative velocity direction at the turbine mode inlet of a PAT system. The new direction β_1^* will always be smaller than the original blade direction β_1 as seen in Figure 2.7. However, the extent of changes to relative velocity direction is not well understood.
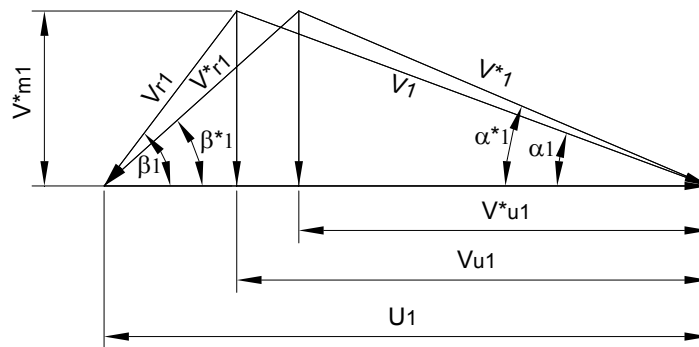
Figure 2.7, Turbine mode inlet velocity triangle with infinite and finite blades (after Cohrs [6])

In section 2.2.1, the losses in the impeller zone were briefly summarized. These losses are further substantiated here.

1. Flow separation loss at zone *iii-iv* ($H_{L.iii-iv.flow-sep}$):

This loss component arises from the sharp blade edges of the backward curved vanes of the PAT inlet and inner surfaces of the shrouds (back and front) at zone *iii*. The losses extend into the flow passage zone *iv* also.

2. Friction at the impeller periphery due to circulation within blade passages ($H_{L.iii\text{-cir}}$):

This loss component was introduced by Cohrs [12] and showed that for all flows less than a Q_{min} defined, a loss component for the power would arise.

3. Frictional losses in zone *iv* ($H_{L\ iv\text{-fric}}$)

The solid boundaries within the flow passages offer resistance to the flow. And especially with high flow velocities, they can be considerable.

4. Other power losses ($H_{L.iv-\text{secon.}}$)

Within the zone of the blade passages there are several loss mechanisms that are complex to visualize. Recirculation and secondary flow losses are some of the prominent flow losses, which are represented as $H_{L.iv\text{-secon.}}$

5. Losses at the interface zone *v*

The losses at the zone *v* interface have been taken care of in definition of Euler head with slip conditions in Equation (2.15). In the presence of slip, exit shock losses similar to that in the inlet region (zone *ii*) may arise at changing load condition. This shock loss does not come under the purview of zone *v*, but influences conditions of zone *vi* only. Nevertheless, there could be other mechanisms causing losses in the interface zone due to conditions upstream or downstream of this zone.

Therefore the total losses in the impeller zone *iii-iv-v* is given by,

$$H_{L.iii\text{-}iv\text{-}v} = H_{L.iii\text{-}iv.\text{flow-sep}} + H_{L.iii\text{-cir}} + H_{L.iv\text{-fric}} + H_{L.iv\ \text{secon.}} \qquad (2.16)$$

As discussed in Equation (2.6), section 2.2.1 the absolute hydraulic shaft power $P_{hyd.shaft}$, delivered by the PAT is dependent only on the loss mechanisms within the impeller control volume (zone *iii-iv-v*) and not on the mechanisms taking place outside (namely the zone *i*, *ii*, *vi* and *vii*). There are mechanical power loss components like disc friction, losses in gland packing, seals and bearings, which have to be considered for the final mechanical shaft power (P).

2.3.4   Flow Zone *vi*

Only the section between planes '2' and 's' of the zone *vi* is considered for hydraulic analysis in detail.

2.3.4.1   The eye section '2-s'

In Figure 2.8 it can be noted that the area is contracting from the impeller eye section at zone *v* (plane '2') towards the casing eye flange (plane 's'), which is a common design feature in most of the pumps. However some manufacturers incorporate zone *vi* which is of enlarging type (as will be seen in for the 79.1 rpm PAT, section 3.2.1).
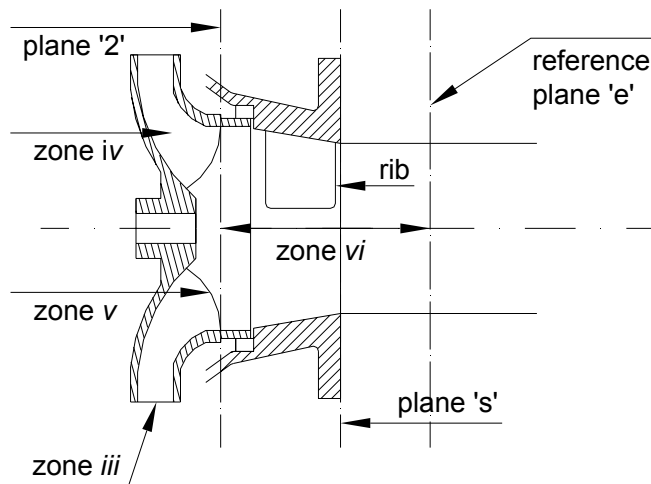
Figure 2.8, Magnified view of the pump eye section

The hydraulic characteristics of flow in zone *vi* can be understood with the help of the Bernoulli equation along with basic swirl analysis. The two sections under consideration are the blade exit (zone *v*) represented with sub-script '2' and the casing eye flange with 's'. The plane '2' is defined just outside rotary zone *v*. Due to the swirling nature of flow the velocity v_2 is defined as,

$$v_2^2 = v_{u2}^2 + v_{m2}^2 \qquad (2.17)$$

and the velocity v_s at section 's' as,

$$v_s^2 = v_{us}^2 + v_{ms}^2 \qquad (2.18)$$

The velocity triangles at these two sections in compared in Figure 2.9. During the traverse through the length between the two sections, the swirl component v_u gradually decreases. Also due the contraction of area at 's' the meridional velocity there, v_{ms} would be greater than that at section '2', v_{m2}. Nothing can be clearly said about the absolute velocity v_s as it depends on the reduction of v_u and the increase of the v_m components. But from the Figure 2.10, the velocity v_s has reduced compared to v_2, but only marginally and the two velocities

have comparable magnitudes. It can also be seen that the flow has slightly straightened with α_s greater than α_2.
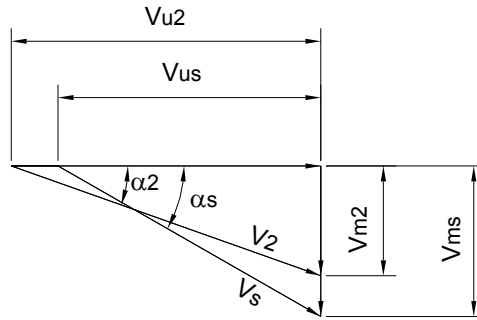
<u>Figure 2.9</u>, Velocity triangles at section '2' and 's'

Applying the Bernoulli's equation between '2' and 's',

$$\frac{p_2}{\rho g} + \frac{v_2^2}{2g} = \frac{p_s}{\rho g} + \frac{v_s^2}{2g} + H_{L\ vi.2\text{-}s}$$

$$H_{L\ vi.2\text{-}s} = \left(\frac{p_2 - p_s}{\rho g}\right) + \left(\frac{v_2^2 - v_s^2}{2g}\right) \qquad (2.19)$$

The term $H_{L\ vi.2\text{-}s}$ represents the net hydraulic losses between the plane '2' and the suction flange plane 's', which will always remain positive. The velocity head term $\left(\frac{v_2^2 - v_s^2}{2g}\right)$ will be only slightly positive as seen from the velocity triangle in <u>Figure 2.9</u>. Therefore to ensure that the loss $H_{L\ vi.2\text{-}s}$ is always positive, the term $\left(\frac{p_2 - p_s}{\rho g}\right)$ should also necessarily be positive.

However, with $\frac{p_2}{\rho g}$ having a negative sign due to suction atmosphere within the whole zone, the pressure $\frac{p_s}{\rho g}$ will naturally have a greater negative magnitude, which is not a favourable condition in PATs. It is seen that there is no significant velocity head gain in section '2-s' and subsequently no pressure recovery (at plane '2') as expected at the exit of all turbines, which is an issue of considerable thought. Therefore the area contraction in zone *vi* is not a favorable design for turbine mode operation.

2.3.4.2   Representation of hydraulic loss $H_{L\ vi}$

The net hydraulic loss $H_{L.vi}$ (between section planes '2' and 'e') can be represented as sum of the swirl loss component and the frictional loss component.

$$H_{L \cdot vi} = \zeta \frac{v_{u2}^2}{2g} + \lambda \frac{v_2^2}{2g} \qquad (2.20)$$

The swirl loss coefficient, ζ and the frictional loss coefficient, λ are based on local flow and geometrical conditions. The coefficient ζ is generally taken between 0.6 and 0.8. However the coefficient λ is based local geometries and flow constraints.

Many pump manufacturers add physical obstructions called ribs in the casing eye region, mainly to break the pre-swirl that is a characteristic of pump mode operation at the entry. Therefore the frictional coefficient λ is increased due to this rib. In turbine mode this rib is bound to add its influence, which is a topic of research.

Similar to the shock losses in the inlet region of the PAT control volume, i.e zone *ii* and zone *iii*, there will also be a shock component in zone *v* and zone *vi* (as discussed in pt. 5, section 2.3.3) This loss component is integrated in the swirl loss coefficient, ζ..

2.3.5   Flow Zone *vii*

As mentioned in section 2.2, the zone *vii* comprises of the complete draft tube configuration. A draft tube is an important component of a PAT system, similar to that of any reaction hydro turbine. In the process of designing an optimum draft tube, it goes without saying that cavitation behaviour of a PAT needs to be given due importance (elaborated in section 2.5). Figure 2.3 illustrates the composition of zone *vii*. Typically it is composed of constant diameter sections, bends and diffuser sections. From the Bernoulli equation defined between the reference measurement plane 'e' and the draft tube exit plane (atmosphere) 'a', the draft tube loss can be represented as,

$$H_{L \cdot vii} = \left(\frac{p_e - p_a}{\rho g} \right) + \left(\frac{v_e^2 - v_a^2}{2g} \right) + z_s \qquad (2.21)$$

The total loss component is composed of frictional losses due to the swirl velocity component and the meridional velocity component.

$$H_{L \cdot vii} = \frac{\lambda_d}{2g} \left(v_{ue}^2 + v_{me}^2 \right) \qquad (2.22)$$

As seen section 2.3.4.1, the swirl component of flow v_{u2} changes in its magnitude and direction depending on the load condition. Changes in v_{u2} also cause identical changes to v_{ue}. At swirl free condition, v_{ue} becomes zero and draft tube loss is represented only by the meridional component, v_{me}. The losses due swirl component, $\frac{\lambda_d}{2g} v_{ue}^2$, increases only on either side of the swirl free operating conditions. This behaviour of swirl component v_{u2} over the complete operating range is unique property of a particular design of the zone *v* (impeller exit) of a PAT system. The absolute static pressure associated with the flow at reference plane 'e', p_e, is critical for studying the cavitation phenomena. It would be important to know

what values p_e would take under different operating conditions, i.e. changing speeds and changing turbine settings (dealt in section 2.5.2.2 and applied in section B2, Appendix B).

2.4 Optimization in Pumps as Turbines

Optimization in the context of 'pumps as turbine' refers to the enhancement of the overall performance as a direct result of modification carried out on the pump's geometry. Therefore the objective of the optimization study would be to reduce the hydraulic losses in the individual flow zones of the PAT control volume. The aim of carrying out the modifications is to avoid major and complicated changes to the design of the pump. These are performed on the different zones depending upon the confidence of reducing local losses.

The overview of the various regions of optimization was briefly discussed in Problem 1 (section 1.3.1, Chapter 1), which recommended the focus of optimization to be on two regions namely the turbine mode inlet and exit regions. The detailed energy transfer mechanisms within every zone of the PAT control volume presented in section 2.3 also provide the basis to evolve an optimization programme by identifying the critical zones and specifying the exact nature of modifications.

- Zone *i* (described in section 2.3.1): More often the design of the spiral volute casing of a pump is optimum for turbine mode operation as well. Therefore within this zone, the scope of modification is very little.

- Zone *ii*: As seen in section 2.3.2, the energy transfer in this zone is very complex under the influence of secondary flow effects and turbulence. Therefore the radial clearance zone has scope for external modification.

- Zone *iii*: (described in section 2.3.3): The impeller inlet interface zone also represents a critical region where optimization can be attempted especially on the sharp edged blade profiles with an expectation to reduce the flow separation loss component at zone *iii-iv* ($H_{L.iii-iv.flow-sep}$):

- Zone *iv*: (described in problem 1, section 1.3.1, Chapter 1 and section 2.3.3): Since the objective of optimization programme is to restrict to simple techniques, the main flow zone of the impeller blade passage does not call for intensive modification or re-design.

- Zone *v*: (described in section 2.3.3): The exit blade interface zone could be considered for optimization essentially to reduce the exit shock losses. But it is still not clear the exit shock characteristics and hence not considered for optimization.

- Zone *vi*: (described in section 2.3.4): This zone classifies as another region where simple modifications can be performed. One level could be to remove all flow obstructions like casing eye rib. The other level of modification could be to gradually enlarge the pump eye as well as the casing eye thus imparting a diffuser effect.

- Zone *vii*: : (described in section 2.3.5): A good design of draft tube is important for the overall performance of the PAT. Its design could be based on conventional draft tubes for maximum energy recovery and minimum losses, off course giving cavitation due consideration (as seen in section 2.5).

Therefore within the PAT control volume defined between planes 'i' and planes *'e'*, the important zones of focus for the optimization programme are,

- Zone *ii*

- Zone *iii* and

- Zone *vi*

2.4.1   Optimization Stage I – Inlet Impeller Rounding

This is the first stage of optimization pertains to the interface zone *iii*. Figure 2.10 and Figure 2.11 illustrate this modification, which involves rounding of the sharp blade edges and the sharp edges of the shrouds (both front and rear). On the blade edge profile, the rounding radius 'R' is taken to be equal to half the blade thickness and care is taken to ensure that the overall diameter D_1 is not altered. Therefore there is a certain trade-off in selecting the rounding radius 'R'. The shrouds are subjected to rounding both at the outer as well as the inner edges of the front and the back shrouds.

This modification could reduce the net flow separation loss component at blade profiles and shroud surfaces essentially reducing the losses in zone *ii* and *iv*. However this modification can also cause rearrangement of inlet velocity triangle and changing the shock loss component (Equation (2.13), section 2.3.2), which is reflected in the losses of zone *ii* (Equation (2.14)). The loss reduction associated with the shock wave, $H_{L.ii\text{-}iii}$ (mach number effects discussed in section 2.3.2.2), coming in contact with smoother geometric profiles and the complex interaction in the clearance zone *ii* (with rounded outer shrouds), $H_{L.ii\ b\text{-}c}$ (discussed in section 2.3.2.1) can also be expected. Therefore in total, this modification can affect both the loss mechanism in impeller zone *iii-iv* and clearance zone *ii*.

Lueneburg [34] reported that such a kind of modification would result in an increase of efficiency by 1 to 2 % at BEP flow and also in the overload flows. Later Williams [57], attempted similar modification on a PAT and found that efficiency would actually decrease considerably and recommended that it should not be attempted. However both Cohrs [6] and Hirschberger [19] have reported of an improvement in efficiency due to impeller rounding.
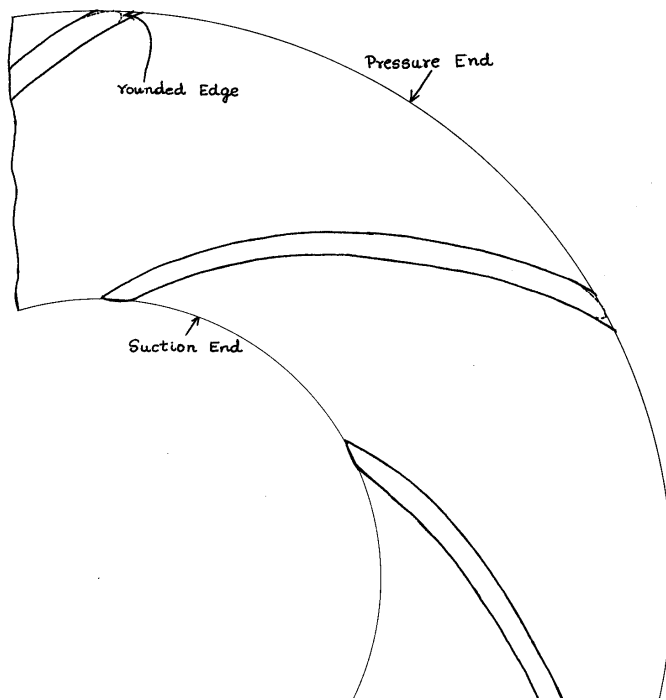
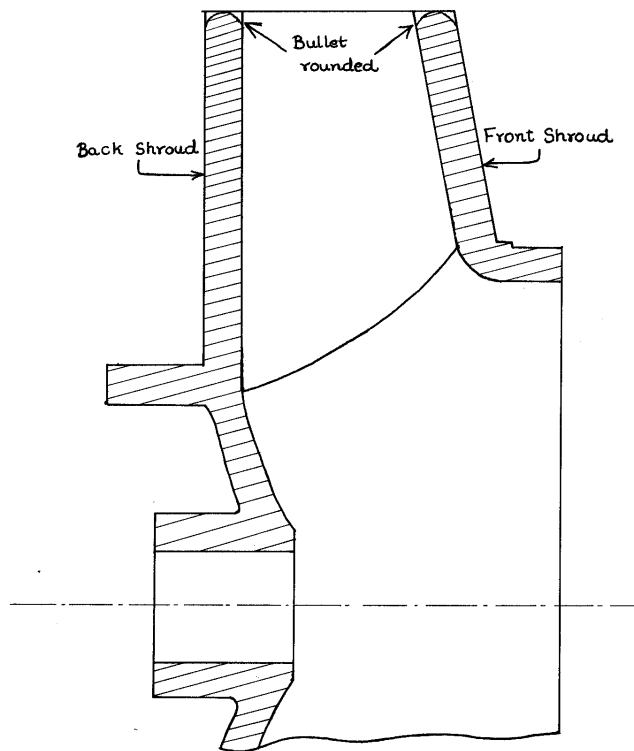Figure 2.10, Rounding of blade profiles at the impeller inlet

Figure 2.11, Rounding of the front and rear shrouds

2.4.2   Optimization Stage II – Inlet Casing Rings

This optimization stage comprises of closing the radial clearances of zone *ii-b* and zone *ii-c* using external stationary rings fixed to the casing mouth. The rings are fixed to the opposite surfaces of the casing mouth in such a way that they protrude inwardly towards the impeller at zone *iii* and have only a marginal clearance with the outer impeller diameter (in the order of 0.5 mm). Different designs of casing rings, namely flat type and wedge type are foreseen.

This modification prevents the scope of the interference of the complex hydraulic in zone *ii-b* and zone *ii-c* with that of the main flow zone of *ii-a*, in effect reducing the loss component $H_{L.ii\ b-c}$ (indicated in section 2.3.2.1). However, being solid boundaries with a certain roughness they also cause frictional losses. The dimensioning of the rings should accommodate a clearance to take care of leakage flow through the wear rings and gland packing/mechanical seal. This type of modification has not been reported in the literature so far.

2.4.3   Optimization Stage III – Suction Eye Enlargement

The optimization stage 3 is carried out on the zone *vi* (casing eye region) of the PAT control volume. It comprises of systematically enlarging the impeller and casing eye as shown in Figure 2.12.

The impeller eye is given a diffuser type enlargement with a cone angle of 10^0 to 12^0. The casing eye has been subjected to a constant enlargement of area. The new diameter of the casing eye is equal to or slightly larger than the outer diffuser diameter of the impeller. This optimization stage therefore does not alter the design of the exit blade profile at the interface zone *v*. There is, however no report on the effects of such a kind of optimization in the literature of PAT.

The enlargement of suction eye would necessarily cause with deceleration of flow and associated pressure recovery as against the behaviour of a converging eye (as explained in section 2.3.4.1) .The reduced resistance created could have a practical significance of sediment flushing.
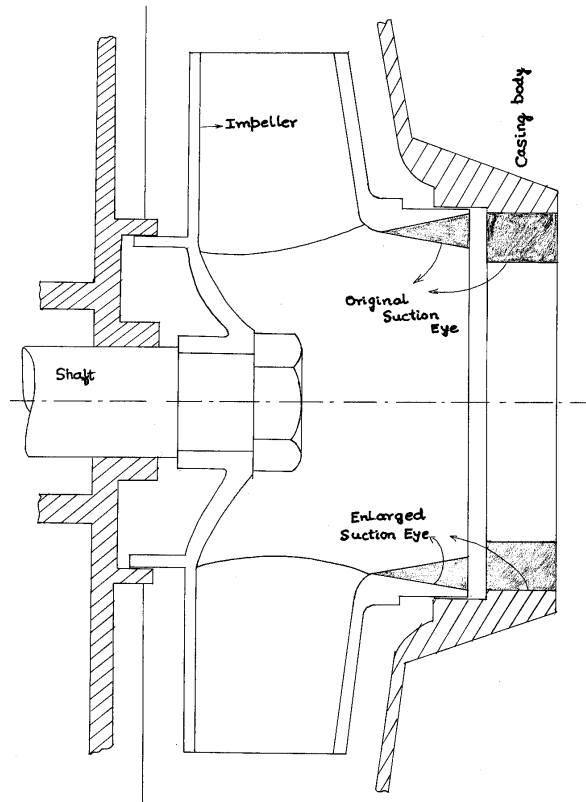
Figure 2.12, Suction-eye enlargement.

2.4.4   Optimization Stage IV – Casing-Eye Rib Removal

This optimization stage is carried out on pumps that are manufactured with in-built obstructions called as a 'rib' as mentioned in section 2.3.4. These rib/s generally run axially along the casing eye length and their prime function is to break any pre-swirl within the fluid flow at the entry of the pump mode operation. Singh et al[46] demonstrated that the casing eye rib has very interesting influence on the characteristics in turbine mode, using both experimental and computational techniques.

The head loss $H_{L.vi}$ (in Equation (2.20)) has both a swirl and frictional loss component. The absence of rib would essentially increase the swirl loss component (ζ) depending on the load condition (section A1, Appendix A) and simultaneously reduce the frictional loss component (λ) of the total loss. It is to be seen which of these two components overweigh each other to either increase or decrease the head loss ($H_{L.vi}$) for a given rib geometry and eye design.

Another effect of the change in the swirl component is on the exit swirl velocity (v_{u2}) and subsequently the net rotational momentum given by Equation (2.4).

2.5 Cavitation in Pumps as Turbines

Understanding of the cavitation phenomena is PAT from a holistic sense is one of the objectives of the dissertation (objective no. 5, section 1.2, Chapter 1). This phenomenon has not been extensively studied in PATs, though some theoretical work mainly based on the available literature of pump and turbine mode cavitations has been carried out. Only few researchers have actually carried out elaborative experimentation to determine the cavitation occurrence in pumps operate as turbines.

There are two criteria in analyzing the cavitation performance in PATs like any other hydraulic turbo-machine. One is based on the requirement criterion (section A2.1, Appendix A) and the other is based on the availability criterion (section A2.2, Appendix A). While the requirement criterion is machine dependent, the availability criterion refers mainly to combination of system conditions consisting of draft tube design, the turbine settings and machine conditions (related to suction blade geometry).

Some of the early researchers on cavitation theory in general turbo-machines were Pfleiderer [38], Arndt [4], and Dixon [10] who provided the fundamental direction to subsequent researchers like Surek [51], Henninger [17], Lobonoff [33] and Alatorre-Frenk [2].

Cavitation in 'pumps as turbines' is a considerably important phenomenon that cannot be ignored. It is clear that requirement based analysis is needed to understand the critical effects of cavitation, that can be either obtained from the standard 3% head-drop criterion (IEC Standards) or bubble/noise formation criterion. It should be pointed out that requirement-based studies need elaborative experimentation with a closed loop test-rig and is by and large expensive. The requirement based and availability based cavitation studies in PATs have been dealt in detail in section A2.1 and A2.2 (Appendix A) respectively which shows that PAT in general is less susceptible to critical cavitation conditions.

One of the methodologies developed in this dissertation is called the CSHN analysis, to understand cavitation given the constraint of an open loop test-rig (characterized with non-variable suction pressure conditions, section 3.1.1, Chapter 3). This methodology is based on the combination of both the availability criterion and the impeller properties like exit geometry, etc. It brings out a non-dimensional cavitation characteristics for tested model PATs for a given system conditions. The CSHN analysis along with another important parameter that characterizes cavitation in turbo-machines, namely the suction specific speed is used to evaluate the cavitation conditions.

2.5.1   Suction Specific Speed

Early scientists like Pfleiderer [38] introduced the concept of suction specific speed. Dixon [10] elaborated that during the process of selecting a turbo-machine with the highest specific speed, the size of the machine is necessarily reduced and correspondingly it's cost and weight. However the machines could not be made extremely small, as the corresponding increase in fluid velocities would lead to the dangerous phenomenon of cavitation.

He authored that in order to accommodate the cavitation phenomenon the performance laws of pumps and turbines of constant geometry should incorporate an additional variable 'NPSH' to the existing system variables defined in section 2.2. Therefore in addition to the independent dimensionless group of Q/ND^3, another independent group is to be incorporated that includes the effects of NPSH, which is called suction specific speed, N_{ss}. Hence the functionalities of a turbo-machine defined in Equations (2.1), (2.2) and (2.3) should be rewritten as,

$$\psi = f(\phi, N_{ss})$$

$$p = f(\phi, N_{ss})$$

$$\eta = f(\phi, N_{ss}) \tag{2.23}$$

The derivation of N_{ss} is similar to that of specific speed (except that NPSH is used instead of the net head, gH in the representation of head number, gH/N^2D^2). Hence, the suction head number ψ_s can be defined as,

$$\psi_s = \frac{g \times (NPSH)}{N^2 D^2} \tag{2.24}$$

With the discharge number $\phi = Q/(ND^3)$ and after eliminating D from ϕ and ψ_s using the operation, $\dfrac{\phi^{1/2}}{\psi_s^{3/4}}$, the resulting term is nothing but suction specific speed.

$$\frac{NQ^{\frac{1}{2}}}{[g(NPSH)]^{\frac{3}{4}}} = N_{ss} \tag{2.25}$$

where N is represented in rev/sec, Q in m^3/s and g(NPSH) in m^2/s^2.

Dixon [10] advocated that the cavitation inception occurs at a constant value of N_{ss} for all pumps and turbines, which was experimentally determined and found to be 0.63. This is therefore limiting value for a condition of cavitation free operation.

$$N_{ss} \leq 0.63 \tag{2.26}$$

Similar to the Q/ND^3, the discharge number, which represents the condition of geometric similarity, Dixon argued that the suction specific speed N_{ss} represents the conditions of

cavitation similarity only and is independent of the machine design parameters. The NPSH defined in Dixon's analysis is based on the availability condition.

Arndt et al[4] also support Dixon's views that N_{ss} is a natural consequence of dynamic similarity in the low-pressure region of the turbo-machine. Arndt [4] proposed a range from 0.36 and 0.72 for N_{ss} for safe conditions with respect to cavitation. He used this range of N_{ss}, to correlate between the more classical Thoma's critical cavitation coefficient σ_{cr} and the machine specific speed, N_q.

Other researchers like Lobonoff [33] who have studied cavitation in pumps only have given a different meaning the term suction specific speed. He said N_{ss} should be defined based on NPSHR instead of NPSHA as advocated by Dixon and Arndt. However, Lobonoff strongly emphasizes for comparing cavitation performance and analytically predicting NPSHR, the use of N_{ss} is more significant compared to cavitation coefficient σ, since N_{ss} relates only to the pump mode inlet/suction conditions and is essentially independent of outer pump geometries and pump specific speed.

Surek [50] has also used suction specific speed in the cavitation analysis of pumps in both pump mode and turbine mode. He used Pfleiderer's theory and defines suction specific speed as a function of NPSHR, which is based originally on pump suction geometry and local velocity triangles. He furthered tried to evaluate N_{ss} for a range of pumps and studied the dependence of specific speed N_q, discharge Q and exit diameter, D_2 on N_{ss}. He found an average range between 0.6 and 0.8 for the N_{ss} in most of the radial flow 'pumps as turbines' and corresponding pumps. He however does not say what is the limiting value of N_{ss} to avoid cavitation.

Surek proposed a sigma, σ -N_q chart for pumps and corresponding 'pumps as turbines' for a wide range of pump specific speeds (SI - 5 rpm to 200 rpm), where he clearly shows that $\sigma_{cr.\,p}$ is much greater than the $\sigma_{cr.\,t}$ for given pump, which is another proof of turbine mode being less susceptible to cavitation.

Therefore summing up the study of suction specific speed, it can be concluded that,

1. N_{ss} could be a useful basis for studying cavitation in PATs.

2. It would be sufficient to calculate N_{ss} based on NPSHA at different load points of the PAT and to check if it is any where close to the Dixon's limit of 0.63 (Equation (2.26)).

3. A curve of N_{ss} versus Q/ND^3 would be good representation of cavitation characteristics through out the machine's operating conditions.

2.5.2   CSHN analysis

This method is developed mainly to counter the limitation of the non-availability of the requirement based cavitation studies on PATs and still trying to make a thorough attempt to

understand their cavitation behaviour. The procedure developed is for model tested PATs whose pressure distribution along the reference plane 'e' is already experimentally determined for a given system boundary conditions namely draft tube design and geodetic turbine setting. However for non-tested machines this methodology can be applied with suitable assumptions. It will be of great significance to be able to predict the reference pressure p_e of given model PAT (whose basic cavitation performance is known) at two different types of operating conditions namely,

i. Different speeds (that cannot be attained during model tests)

ii. Different turbine setting (different draft tube design)

Once the reference pressure p_e is calculated the NPSHA and suction specific speed, N_{ss} can be determined and the extent of cavitation be analyzed.

2.5.2.1   Combined Suction Head Number

In section 2.3.5 the flow zone *vii* was analyzed and the head loss $H_{L.vii}$ was represented by the Bernoulli's equation in Equation (2.21) and by the swirl and meridional velocities in Equation (2.22). Combining Equation (2.21) and (2.22) and eliminating $H_{L.vii}$, the new equation takes the form of,

$$\left(\frac{p_e}{\rho g} + z_s \right) = \left(\frac{v_a^2 - v_e^2}{2g} \right) + \frac{\lambda_d}{2g} \left(v_{ue}^2 + v_{me}^2 \right) \tag{2.27}$$

The left hand side of the equation is composed of static pressure at reference 'e' and suction head elevation, z_s. The static elevation is measured from the pump centerline to the datum at draft tube exit. Together they are termed as combined suction head (CSH). The right hand side contains all types of velocity head terms. Dividing both sides by the square of the peripheral velocity at impeller periphery, u_1^2, or N^2D^2, then Equation (2.27) becomes dimensionless.

$$\frac{\left(\frac{p_e}{\rho g} + z_s \right)}{N^2D^2} = \frac{\left(\frac{v_a^2 - v_e^2}{2g} \right)}{N^2D^2} + \frac{\frac{\lambda_d}{2g} \left(v_{ue}^2 + v_{me}^2 \right)}{N^2D^2} \tag{2.28}$$

The left hand side is coined as the 'Combined Suction Head Number' (CSHN), whose functionality with the parameter 'discharge number, Q/ND^3' is established by considering the various components of the right hand side of Equation (2.28). It is important to note that Q/ND^3 can be simplified as the ratio of meridional velocity to the peripheral velocity at the inlet of the PAT, 'v_{m1}/u_1'

i)   The draft tube loss term

This term $\dfrac{\lambda_d}{2g}\left(\dfrac{v_{ue}^2}{u_1^2} + \dfrac{v_{me}^2}{u_1^2}\right)$ can be studied as follows. v_{me} is direct function of v_{m1}. Also swirl velocity v_{ue} has been described in the section 2.3.5 is a machine dependent parameter and it can be represented as a function of v_{me} and hence also a function of v_{m1}. Therefore both the terms have some kind of functional relationship with ϕ as shown below.

$$k\frac{\lambda_d}{2g}\left(f^1(\phi)^2 + f^2(\phi)^2\right) \tag{2.29}$$

Hence the draft tube head loss number is therefore necessarily a function of Q/ND^3.

ii) The velocity gain term

The term v_e in the velocity gain term can be written as,

$$\frac{v_e^2}{u_1^2} = \frac{v_{ue}^2}{u_1^2} + \frac{v_{me}^2}{u_1^2} \tag{2.30}$$

It is seen that both v_{ue} and v_{me} are functions of v_{m1}. Hence $\dfrac{v_e^2}{u_1^2}$ also becomes a function of

ϕ. Similarly $\dfrac{v_a^2}{u_1^2}$ can also be proved to be function of ϕ. Therefore the velocity-gain term also becomes a function of the independent control parameter ϕ.

Since all the terms of the right hand side of Equation (2.28) hold functionalities with Q/ND^3, the Combined Suction Head Number, CSHN should also have a unique functionality with Q/ND^3 for a given machine and draft tube design.

2.5.2.2 Application of CSHN analysis on a model tested PAT

2.5.2.2.1 Change in operating speed

Given the CSHN characteristics of a PAT for a given draft tube design condition, it is very simple to work backwards and evaluate p_e for any operating speed. For a given loading condition of a PAT, CSHN is known. The static elevation z_s is also fixed. Therefore p_e is given by,

$$\frac{\left(\dfrac{p_e}{\rho g} + z_s\right)}{N^2 D^2} = CSHN \tag{2.31}$$

The NPSHA and N_{ss} are subsequently determined.

2.5.2.2.2   Change in Turbine setting

The change in turbine setting would result in a change of suction elevation, z_s. This would also cause a change in the draft tube design and hence the coefficient λ_d.

For the PAT with original CSHN characteristics and draft tube design, the combined suction head (CSH) is given by Equation (2.32).

$$CSH = \left(\frac{v_a^2 - v_e^2}{2g}\right) + \frac{\lambda_d}{2g}\left(v_e^2\right) \tag{2.32}$$

For a new turbine setting, the combined suction head (CSH_1) would given by,

$$CSH_1 = \left(\frac{v_{a1}^2 - v_e^2}{2g}\right) + \frac{\lambda_{d1}}{2g}\left(v_e^2\right) \tag{2.33}$$

The velocity at the reference plane 'e' is essentially the same. Performing a mathematical operation on Equation (2.33), in which $\dfrac{\lambda_d}{2g}\left(v_e^2\right)$ and $\dfrac{v_a^2}{2g}$ is added and subtracted,

$$CSH_1 = \left(\frac{v_{a1}^2 - v_e^2}{2g}\right) + \frac{\lambda_{d1}}{2g}\left(v_e^2\right) + \frac{\lambda_d}{2g}\left(v_e^2\right) - \frac{\lambda_d}{2g}\left(v_e^2\right) + \frac{v_a^2}{2g} - \frac{v_a^2}{2g}$$

$$CSH_1 = CSH + \frac{v_e^2}{2g}\left(\lambda_{d1} - \lambda_d\right) + \frac{\left(v_{a1}^2 - v_a^2\right)}{2g} \tag{2.34}$$

And converting Equation (2.34) to dimensionless form,

$$CSHN_1 = CSHN + \frac{v_e^2\left(\lambda_{d1} - \lambda_d\right) + \left(v_{a1}^2 - v_a^2\right)}{2g \times \left(N^2 D^2\right)} \tag{2.35}$$

The coefficient λ_{d1} for the new draft tube setting needs to be determined. The draft tube exit velocities v_{a1} and v_a for the new and old settings also need to be approximately calculated. The v_e can then be determined from original PAT characteristics at different load conditions i.e. at different Q/ND^3. CSHN is also known for the original draft tube setting. Therefore $CSHN_1$ can be determined, and subsequently $p_{e1}/2g$ can also be found out. If z_{s1} is greater than z_s, the frictional coefficient λ_{d1} will be greater than λ_d and vice versa.

The problem B2.1 (solved in section B2.2.1, Appendix B) deals with a CSHN application problem on a model tested PAT with new draft tube design (new turbine setting).

2.5.2.3   Application of CSHN on new machines

2.5.2.3.1   Evaluation of CSHN at BEP and Critical Cavitation conditions

In order to apply the CSHN on new PATs, a reorganization of Equation (2.32) needs to be carried out. This equation defines the 'Combined Suction Head', CSH for any general PAT, is reduced to dimensionless form as follows.

$$CSH = \left(\frac{v_a^2 - v_e^2}{2g} \right) + \frac{\lambda_d}{2g} \left(v_e^2 \right) \tag{2.32}$$

$$CSHN = \frac{1}{N^2 D^2} \left[\left(\frac{1}{D_a^4} - \frac{1}{D_e^4} \right) \cdot \frac{8 \cdot Q^2}{\pi^2 \cdot g} + \lambda_d \frac{8 \cdot Q^2}{\pi^2 \cdot g \cdot D_e^4} \right] \tag{2.36}$$

$$CSHN = \frac{Q^2}{N^2 D^2} \left[-\lambda_{VG} + \lambda_d^1 \right] \tag{2.37}$$

$$CSHN = \left[\frac{Q}{ND^3} \right]^2 \left[\lambda_d^1 - \lambda_{VG} \right] \times D^4 \tag{2.38}$$

It can be seen from Equation (2.38) that CSHN for any PAT is a function of discharge number, Q/ND^3, the reference impeller diameter (refer Table 3.1, Chapter 3), and the various constants of the new draft tube. Therefore for a new PAT, whose geometry and draft tube is defined, it would be sufficient to define the discharge number at two important operating conditions to evaluate the cavitation properties. The conditions of importance are,

   i.   The BEP condition

   ii. The minimum CSHN condition

The determination of BEP condition of a new PAT is dealt in section 5.2 of Chapter 5, for both radial and mixed flow PATs. However the determination of minimum CSHN conditions is difficult to be analytically determined. The experimentally determined CSHN profiles (CSHN versus Q/ND^3) for various PATs (presented in section 4.1.2, Chapter 4 and section A6, Appendix A) would be very useful in approximately fixing the discharge number for the minimum CSHN conditions. The problem B2.2 (solved in section B2.2.2, Appendix B) deals with the application of CSHN analysis on new PATs.

2.5.2.3.2   Evaluation of complete CSHN profiles

The method described in section 2.5.2.3.1, however does evaluate the complete CSHN profiles for the complete operating range of new PAT. Approximate CSHN profiles can still be approximately determined. The first process for this approach would be to match the new PAT to a closest model tested machine of similar geometry.

For this it would be necessary for the model PAT to be a geometrically, dynamically similar to the new PAT. Owing to the different draft tube conditions of the two PATs the CSHN profile of the new PAT would be displaced compared to the model PAT (though the shape of the two CSHN profiles may be identical). The situation now becomes essentially similar to that in the previous section 2.5.2.2, where a model PAT's CSHN profiles are evolved for different draft tube designs.

2.5.2.4 Summary

CSHN represents in physical terms a combination of machine (internal) dependent and system (external) dependent parameters. It may just appear to be a reorganization of the terms of the Bernoulli's equation representing the zone *vi* and *vii* of the PAT control volume but with a intention to analyze cavitation without extensive measurements of the requirement based studies.

To summarize the CSHN methodology requires the following essentials.

1. CSHN Versus Q/ND^3 characteristics for a given PAT along with

2. Draft tube design for the above characteristics along with approximate velocity profiles.

It will be interesting to see whether or not the CSHN characteristics for given machine will collapse into one single CSHN curve at different operating speeds and validating the above proposed theory.

3.   Means of Solution and Review of Tested PATs

For the stated problem concerning the optimization of the internal hydraulics in a PAT control volume (section 1.3.1, Chapter 1) and the objective of a holistic understanding of the cavitation phenomena (objective no. 5, section 1.2, Chapter 1), two possible means of solution can be conceived. One is a classical experimental approach that would need a well-calibrated test-rig, while the other means of solution is the use computational tools known as Computational Fluid Dynamics, or CFD.

Experimental considerations have been given prominence during the course of the dissertation as the means of solution for all the identified problems of internal optimization. However, the means of CFD is also used in a limited way. This comprises of the comparisons between the experimental and CFD results on 3 of the 8 tested PATs along with the analysis of the internal optimization stage IV (absence of casing eye ribs, section 2.4.4, Chapter 2) on the 39.7 rpm PAT. The CFD results have been externally sourced from two collaborating bodies namely Kirloskar Brothers Limited (industrial partner) and Nottingham Trent University (academic partner). The details of the means of solution through CFD along with the results are dealt in section B3, Appendix B.

3.1   Experimental Means

3.1.1   Test Rig

The objective of the design of the test rig is to ensure simplicity on one hand and to make measurements as accurate as possible on the other hand. The general layout of the open loop test-rig along with the hydraulic and mechanical components is summarized in section A3.1 of Appendix A, comprising of the feed pump, the complete piping and valves, the mounting bay and the loading generator. Section A3.1 also briefly discusses the operating range of the test-rig with respect to available input energy (head and discharge) and output load capacities.

3.1.2   Measured Variables and Instrumentation

The test rig is equipped for making two broad classes of measurements. One of the classes is related to global variables (or the system hydraulic variables, section 2.2, Chapter 2), namely the net head (H), discharge (Q), torque (T) and speed (N). The other class pertains to the internal variables corresponding to the measurements carried out at the reference

plane 'e' (shown in Figure 2.8, Chapter 2, dividing the zone *vi* and *vii* of the PAT control volume).

The technical specification of the instruments used for measuring the global variables are elaborated in section A3.4 (Appendix A) along with the concept of data processing. Section A3.5 of Appendix A deals with the internal variables using a 5-hole yaw probe.

3.1.3   Methodology of Calculations and Analysis

The overall operating efficiency of the PAT unit is determined from the simple formula provided in Equation (3.1) (which is essentially similar to Equation (2.7), Chapter 2), that combines the global variables listed in section 3.1.2. The efficiency determined from Equation (3.1) combines both the hydraulic efficiency of the PAT and mechanical efficiency of the bearings and seal system, since torque measured is essentially mechanical (section A3.4.3, Appendix A).

$$\eta = \eta_{hyd} \times \eta_{mech} = \frac{2\pi NT/60}{\rho gQH} \qquad (3.1)$$

The dimensionless groups (Table 2.2, Chapter 2) developed based on the control variables Q and N, would be used for the entire study. The functional relationship illustrated in Equation (2.1), (2.2) and (2.3) would be plotted for all the optimization stages of the respective PATs.

The reference diameter (D) used in all these dimensionless groups needs to be clarified for both the radial flow and mixed flow PATs. Table 3.1 summarizes the considerations for this reference diameter.

Table 3.1, Consideration for the reference impeller diameter (D)

PAT type	Reference D	Description
Radial flow PAT	D_1	Turbine mode inlet impeller diameter, in Figure A4.1, section A4.1, Appendix A
Mixed flow PAT	D_{1f}	Turbine mode inlet impeller diameter at front shroud, in Figure A4.4, section A4.2, Appendix A

3.1.3.1   Optimization Study

The physical significance pertaining to the changes in the values of the hydraulic variables between any two consecutive optimization stages has been briefly dealt in section 2.2.2 of Chapter 2, where 6 different conditions were listed.

In order to make a thorough interpretation of the results for any optimization stage, a 'percentage analysis plot' is developed. This plot is in addition to the plot that makes a direct comparison between the dimensionless head number, power number and efficiency characteristics for the two stages. The 'percentage analysis plot' consists of three percentage curves plotted against a common abscissa of discharge number, Q/ND^3, namely,

    i.   Head reduction curve

    ii.   Power improvement curve

   iii.   Efficiency rise curve

The terminology for above percentage curves is based on the assumption that the modified stage (synonymous to the latter stage) is having an overall better performance compared to the non-modified stage (synonymous to the former stage). The internal geometric optimization methods (I to IV – section 2.4 of Chapter 2) could have complex influences on the behaviour of the system hydraulic variables. Hence the above percentage (i.e. head reduction and power improvement) curves could take both positive and negative values in any of the operating regions of the machine's characteristics (stretching from the no-load line to the overload region) depending the influences.

The 'percentage analysis plot' helps in studying the relative influences of the head reduction and the power improvement on the overall performance change (related to efficiency) at every operating point (Q/ND^3). These relative influences are used to qualitatively analyze the loss formations in 6 zones of the PAT control volume (defined in <u>Figure 2.1</u>, <u>2.2</u> of Chapter 2) and net rotational momentum across the impeller (or Euler Head, $gH_{Eu.slip}$, in Equation (2.4) and (2.15), section 2.2.1, Chapter 2). To simplify the procedure of analysis using 'percentage analysis plots' three operating points of the characteristics are chosen, namely,

    i.   The part-load point (chosen by visual judgment within the part-load region),

    ii.   The best efficiency point and

   iii.   The overload point (also selected by visual judgment).

A clear physical interpretation of the head reduction, power improvement and efficiency rise is needed to understand their relative influences under two stages of optimization.

3.1.3.1.1   Head Reduction

The head reduction between modified and non-modified stages can be represented as,

$$\text{Head Reduction} = \frac{gH_{non-modified} - gH_{modified}}{gH_{non-modified}} \tag{3.5}$$

Therefore from Equation (3.5), positive head reduction would mean that the modified stage has a lower head number consumption compared to the non-modified stage and vice versa.

Combining Equation (2.5) (of Chapter 2) with Equation (3.5),

$$\text{Head Reduction} = \frac{\left(gH_{Eu-slip} + gH_{L.i-ii-iii-iv-v-vi}\right)_{non-modified} - \left(gH_{Eu-slip} + gH_{L.i-ii-iii-iv-v-vi}\right)_{modified}}{\left(gH_{Eu-slip} + gH_{L.i-ii-iii-iv-v-vi}\right)_{non-modified}}$$

$$\tag{3.6}$$

For head reductions to be positive, there are two possibilities as seen from Equation (3.6).

i.   There is decrease in net rotational momentum ($gH_{Eu.slip}$) in the modified stage, OR

ii.   There is decrease in the overall hydraulic losses in the PAT control volume ($H_{L.i-ii-iii-iv-v-vi}$) in the modified stage.

3.1.3.1.2   Power Improvement

The power improvement equation between the modified and the non-modified stages is represented as,

$$\text{Power Improvement} = \frac{P_{modified} - P_{non-modified}}{P_{non-modified}} \tag{3.7}$$

From Equation (3.7) positive power improvement implies that the modified stage has an more power generation compared to the non-modified stage and vice versa. Combining Equation (3.7) with Equation (2.6) (of Chapter 2), the power improvement equation can be further simplified to,

$$\text{Power Improvement} = \frac{\left(gH_{Eu-slip} - gH_{L.iii-iv-v}\right)_{modified} - \left(gH_{Eu-slip} - gH_{L.iii-iv-v}\right)_{non-modified}}{\left(gH_{Eu-slip} - H_{L.iii-iv-v}\right)_{non-modified}}$$

$$\tag{3.8}$$

It can be seen from Equation (3.8) that for the power improvement to be positive, any of the following situations should occur.

i. A rise in the net rotational momentum ($gH_{Eu.slip}$) across the impeller control volume in the modified stage, OR

ii. A drop in the hydraulic losses within the in impeller control volume ($H_{L.iii\text{-}iv\text{-}v}$) in the modified stage.

3.1.3.1.3 Efficiency Rise

The efficiency rise can be represented as,

$$\Delta\eta = \eta_{modified} - \eta_{non-modifed}$$

$$\Delta\eta = \frac{1}{\rho Q} \cdot \left(\frac{P_{modified}}{gH_{modified}} - \frac{P_{non-modified}}{gH_{non-modified}} \right) \tag{3.9}$$

Equation (3.9) can be further simplified to,

$$\Delta\eta = \frac{1}{\rho Q} \cdot \frac{P_{non-modified}}{gH_{modified}} \left[\left(\frac{P_{modified} - P_{non-modified}}{P_{non-modified}} \right) + \left(\frac{gH_{non-modified} - gH_{modified}}{gH_{non-modified}} \right) \right] \tag{3.10}$$

$$\Delta\eta = \frac{1}{\rho Q} \cdot \frac{P_{non-modified}}{gH_{modified}} \cdot \left[\text{Power Improvement} + \text{Head Reduction} \right]$$

Though Equation (3.10) looks more complex with interaction of many parameters, it can be generalized that a positive efficiency rise can come from any of the following behaviours.

i. A positive power improvement and a positive head reduction

ii. A relatively greater positive power improvement and smaller negative head reduction

iii. A relatively greater positive head reduction and a smaller negative power improvement

The discussion of the results of any optimization stage will be first carried out on the behaviour power improvement curve to get an approximate picture of the conditions within the impeller with respect to both rotational momentum and hydraulic losses. Subsequently the behaviour of the head reduction will be studied to get information on the hydraulic loss composition in the entire PAT control volume and also the rotational momentum. The

conditions of the rotational momentum predicted by both power improvement and head reduction curves would be compared. Subsequently focus can be shifted on hydraulic loss composition both within and outside the impeller.

The discussion would only point towards direction of changes with respect to rotational momentum and hydraulic losses. However this analysis cannot give absolute values of changes within the rotational momentum and the hydraulic loss components.

3.1.3.2   Internal Performance Study

The internal performance study is carried out mainly in reference to the optimization stage IV (absence of ribs-section 2.4.4, Chapter 2). The study deals only with the presentation and analysis of the swirl (θ) profiles over the cross-sectional plane 'e' at different load points encompassing the entire operating characteristics. The velocity profiles for the meridional (v_m) and swirl (v_θ) components illustrated in section A3.5, Appendix A are left out for the analysis, as they don't reveal much information to evaluate the behaviour of rib at the PAT exit.

The study also compares the isolated swirl profiles between the 'casing rib present' and 'casing rib absent' stage at three major points of the operating characteristics namely, the part-load, BEP and overload points.

3.1.3.3   Cavitation Analysis

The theoretical consideration for the analysis of the cavitation (based on availability criteria) in PAT has been thoroughly presented in section 2.5.1 (suction specific speed) and section 2.5.2 (CSHN analysis) of Chapter 2.

As mentioned the methodology of cavitation analysis comprises of obtaining the CSHN plot for every PAT. Subsequently the magnitudes of the CSHN and the Q/ND^3 are evaluated for both,

   i.   The BEP condition and

   ii.   The minimum CSHN condition.

The suctions specific speed, N_{ss} (as defined in Equation (2.25)) is also determined for the above two conditions and compared with the Dixon's criterion (given by Equation (2.26), discussed in section 2.5.1) to jointly study the measure of cavitation occurrence.

3.1.3.4   Experimental and CFD Correlation

The methodology of comparisons between the experimental and the CFD results (obtained from section B3.2, Appendix B) is similar to the methodology employed in the optimization study in section 3.1.3.1.

3.1.3.4.1   Comparisons of Dimensionless Characteristics

To make the direct comparisons of dimensionless characteristics, the experimental and CFD variables need to be brought to a common basis. There are only two variables for which corrections require to be incorporated, namely the discharge (Q) and output power (P). The net head (H) and the speed (N) do not need any corrections. The proposed corrections would be applied to only to the experimental variables leaving the CFD results from section B3.2, Appendix B, unchanged. Table 3.2 summarizes the influences on the discharge and power variable and the recommended corrections.

Table 3.2, Corrections for discharge (Q) and power (P) in Experimental-CFD correlation

Measured Variable	CFD	Experiment	Correction Eqns.
Net Discharge, Q	The net discharge (Q) is assumed to flow through the impeller passages. (Boundary conditions – section B3.1.4, Appendix B)	The actual discharge (Q*) through the impeller is smaller than the net discharge (Q) due leakage. The measured discharge (Q) needs to be corrected to the actual discharge (Q*).	$Q = Q^{**} + Q_{Le}$ $Q_{Expt} = Q^{**} = \eta_{Le} \cdot Q$ (3.11)
Output power, P	The CFD evaluates only the hydraulic power (as seen in section B3.1.4, Appendix B)	The experiment measures the mechanical shaft power, which includes losses due to disc friction and the bearings/seal system. Therefore output measured power (P) needs to be corrected to the hydraulic output power $P_{Expt.\,Hyd}$.	$P_{Expt\cdot Hyd} = \dfrac{P}{\eta_{mech}}$ (3.12)

Due to the corrections imposed in Table 3.2, the dimensionless numbers used for comparisons needs to be redefined (as shown in Table 3.3).

<u>Table 3.3</u>, Modified dimensionless groups for Experimental-CFD correlation

Number	Experiment	CFD
Discharge Number	$\dfrac{Q^{**}}{ND^3}$	$\dfrac{Q}{ND^3}$
Head Number	$\dfrac{gH_{Expt}}{N^2D^2}$	$\dfrac{gH_{CFD}}{N^2D^2}$
Power Number	$\dfrac{P_{Expt\cdot Hyd}}{\rho N^3D^5}$	$\dfrac{P_{CFD\cdot Hyd}}{\rho N^3D^5}$
Efficiency	$\dfrac{P_{Expt\cdot Hyd}}{\rho \cdot g \cdot Q^{**} \cdot H_{Expt}}$	$\dfrac{P_{CFD\cdot Hyd}}{\rho \cdot g \cdot Q \cdot H_{Expt}}$

It is seen from <u>Table 3.3</u> that the discharge number, power number and efficiency for experimental results need to be recalculated for a holistic comparison with the CFD. It is also seen that the discharge values (Equation (3.11)) used in the experimental dimensionless groups have reduced and the power values (Equation (3.12)) have increased. It is therefore needed to determine the leakage discharge and the net mechanical power loss.

Determination of Leakage Discharge -Q_{Le}

The determination of leakage discharge is a standard hydraulic problem, which can be derived from the Bernoulli's equations and the pressure energy gradient across the leakage area. Both Cohrs [6] and Williams [57] have provided the background for the determination of leakage discharge. The leakage cross-section can be treated as pipe section with a pressure difference on both sides of the cross-section. After solving the Bernoulli's equation between the inlet and exit section along with consideration for entry and exit losses, the leakage discharge can be represented as,

$$Q_L = \mu \cdot A_{Le} \cdot \sqrt{\frac{2\Delta p_{Le}}{\rho}} \qquad (3.13)$$

The overall friction factor, μ, is represented as,

$$\mu = \frac{1}{\sqrt{\xi_{In\cdot Le} + \lambda \dfrac{L_{Le}}{2t_{Le}} + \xi_{Ex\cdot Le}}} \qquad (3.14)$$

where, 'L_{Le}' is the length of the leakage section, 't_{Le}'; the thickness of the section; $\zeta_{In.Le}$ (0.4 to 0.5), the inlet loss factor; $\zeta_{Ex.Le}$ (1.0), the exit loss factor; and λ (0.03 to 0.04), the surface friction factor of the cross-section (calculated depending on Reynolds number). The pressure

difference, Δp_{Le}, is calculated from Equation (3.15), after correcting for the pressure lost in the centrifugal action between the inlet radius of the impeller ($r_1 = D_1/2$ in Figure A4.1, Appendix A) and the eye radius at the leakage section ($r_{2.Le} = D_{2.Le}/2$ also in Figure A4.1)

$$\Delta p_{Le} = p_1 - p_{2.Le} - \omega^2 \rho \left(\frac{r_1^2 - r_{2.Le}^2}{2} \right) \qquad (3.15)$$

Determination of Mechanical Efficiency -η_{mech}

The second important parameter to be determined from Equation (3.12) is the overall mechanical efficiency (η_{mech}). This can be determined by an elaborate evaluating the power losses due disc friction, gland packing, and bearing losses. The other way is through approximation as found in Cooper in [8]. For the 3 PATs that are to be compared (section 4.2, Chapter 4) between experimental and CFD methods, an overall mechanical efficiency of 98.5% is assumed.

3.1.3.4.2 Percentage Analysis Plots

In the 'percentage analysis plots' (similar to that developed in section 3.1.3.1), the experimental results are considered to be synonymous to the former stage and the CFD results to the latter stage.

The terminologies of the 'percentage analysis plot', namely the head reduction, power improvement and the efficiency rise remains unchanged, however the physical interpretations are slightly different. A positive head reduction would mean that the CFD predicts head numbers that are lower than the experimental head numbers at same discharge number, Q/ND^3 and vice versa. Similarly a positive power improvement and efficiency rise implies that the CFD is predicting more power and efficiency compared to the experimental results.

The relative influences of the head reductions and power improvements are examined at the part-load, BEP and overload points respectively. The physical interpretations corresponding to these influences essentially reflect the deviations of the CFD model from the experimental results with respect to the loss mechanisms in the various zones of the PAT control volume and the rotational momentum theory across the impeller.

3.2   Review of the Tested PATs

There have been a total of 8 pumps tested during the PAT research programme. Seven of these pumps are radial flow end-suction type, while one of the pumps is a mixed flow end-suction type. All the pumps that are tested are single stage pumps. The pumps or PATs are represented always with their 'pump mode specific speed' at the prefix (which have been defined in Table B1.1, Appendix B). Table 3.4 illustrates the test PATs by their nomenclature along with optimization stages (section 2.4, Chapter 4) implemented on them.

Table 3.4, Tested PATs and respective Optimization Stages

Sl. No.	Pump or PAT Name	Type	Experimental Optimization Stages
1	24.5 rpm PAT	Radial Flow	Optimization Stage I and III
2	35.3 rpm PAT	Radial Flow	Optimization Stage I and III
3	36.4 rpm PAT	Radial Flow	Optimization Stage I and IV
4	39.7 rpm PAT	Radial Flow	Optimization Stage I, II, and IV
5	45.2 rpm PAT	Radial Flow	Optimization Stage I
6	46.4 rpm PAT	Radial Flow	Optimization Stage I and IV
7	79.1 rpm PAT	Radial Flow	Optimization Stage I, II, and IV
8	94.4 rpm PAT	Mixed Flow	Optimization Stage I

The design of all the 7 radial flow PATs and the single mixed flow PAT are summarized in section A4.1 and section A4.2, Appendix A.

4. Results and Discussion

Two main categories of results are presented and discussed in this chapter. One of the categories pertains to the experimental results, which includes the results on the optimization stages (explained in section 2.4, Chapter 2) and the cavitation results (based on CSHN analysis in section 2.5.2, Chapter 2). The second category of results comprises of the correlation between experimental and CFD methods.

4.1 Experimental Results

4.1.1 Optimization Studies

In this section every optimization stage is separately treated. For each optimization stage, detailed presentation and analysis of the results is carried out on only one of the tested PATs (from the list in Table 3.4, Chapter 3). The analysis is based on the methodology laid out in section 3.1.3.1, Chapter 3 and followed by a discussion for a given PAT. Subsequently an elaborative summary for each optimization stage, which combines the results of all the tested PATs at part-load, BEP and overload regions respectively. The results and analysis of the remaining PATs of given optimization are presented in section A5, Appendix A.

4.1.1.1 Optimization Stage I – Inlet Impeller Rounding

This level of optimization has been carried out on all the test PATs (mentioned in Table 3.4, Chapter 3). The 35.3 rpm PAT is chosen for detailed analysis in this section. The results for the other 7 PATs have been presented and comprehensively discussed in section A5.1, Appendix A for further reference.

4.1.1.1.1 35.3 rpm PAT

The modification on the 35.3 rpm PAT consists of rounding of all the blade profiles as well as that of the shrouds (as mentioned in section 2.4.1, Chapter 2). The effect of inlet rounding on the 35.3 rpm PAT is studied using the dimensionless plot in Figure 4.1. It is clearly seen that the head number line for the inlet rounded PAT has considerably lowered compared to that for the non-modified stage. The reduction of head numbers are pretty constant throughout the range with slightly magnified effects in the part-load and overload region compared to the BEP region. The power number characteristics for the two stages looks more or less identical, however the power numbers for the inlet rounded PAT are higher in the no-load and overload regions. Owing mainly to the reduction of head number, the efficiency of the modified PAT has increased from uniformly over the entire operating range between 1.5% and 2.5%.
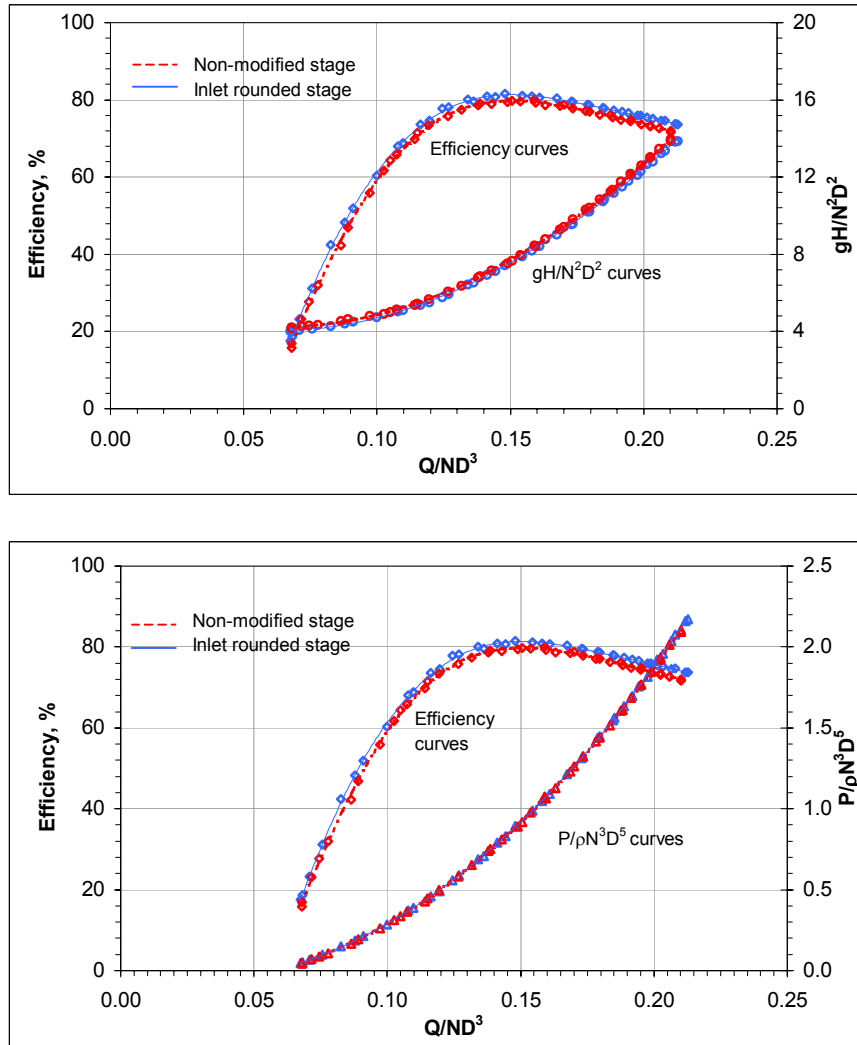
Figure. 4.1, Comparisons of dimensionless characteristics for Optimization Stage I on the 35.3 rpm PAT

Table 4.1 analyses the BEP for both the stages, where it is seen that the head number for the inlet rounded PAT has decreased considerably from 7.766 to 7.642 units, while power number has only marginally risen from 0.933 to 0.935 causing a net efficiency rise from 79.5% to 81.0%.

Table 4.1, BEP summary for two stages of Optimization Stage I on the 35.3 rpm PAT

Stage	ϕ	ψ	p	η
Non-modified	0.151	7.766	0.933	79.5%
Inlet-rounded	0.151	7.642	0.935	81.0%

The hydraulic effects can be closely understood using the percentage analysis chart plotted in Figure 4.2. The power improvement line with respect to the modified PAT is seen to be positive throughout the operating range with excessive rise seen between no-load and part-load regions. However the percentage improvement falls to about +0.2% at the BEP line and

again increases to +0.8% to +1% in the overload region. The head reduction curve is making a visual impact, with reductions ranging from +3.5% to +1.6% for the inlet rounded PAT. The head reduction curve follows a parabolic pattern with magnified reductions in the part-load and overload regions on either side of the BEP. Due to the combined effect of the power number and head number characteristics, the efficiency rise curve shows stable gains of +1.6% to +2.5% throughout the operating range.
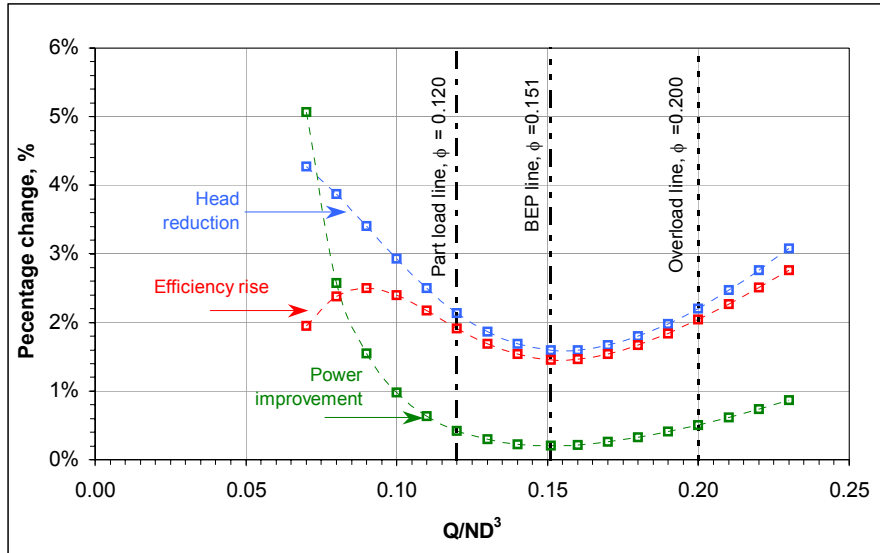

Figure. 4.2, Percentage Analysis Plot for Optimization Stage I on the 35.3 rpm PAT

The relative impacts of the head and power parameters on the efficiency at the part-load, BEP and overload lines respectively are summarized in Table 4.2. It is evident that head reduction effects are overriding the marginal power improvement effect for all the three load points analyzed.

Table 4.2, Relative study at part-load, BEP and overload lines for Optimization Stage I on the 35.3 rpm PAT

	Part-load line $\phi = 0.120$	BEP line $\phi = 0.151$	Overload line $\phi = 0.200$
Head reduction	+2.1%	+1.6%	+2.2%
Power improvement	+0.4%	+0.2%	+0.5%
Efficiency rise	+1.9%	+1.5%	+2.0%

Discussion of Results on 35.3 rpm PAT

The behaviour of the power improvement curve suggests that even though small, there are still positive hydraulic effects taking place within the impeller control volume, either with decreased hydraulic losses or increased net rotational momentum for the Inlet rounded 35.3 rpm PAT. But the behaviour of the head reduction curve suggests that only positive

hydraulics within the entire PAT zone is taking place and no increase of the net rotational momentum. Therefore the only possibility is that the losses of zone *iii* and *iv* have reduced, though marginally. But the large reductions from head number goes to suggest that even if the reductions of the zone *iii* and *iv* are included, the head number would not reduce so much. This leads to an interesting physical condition of marginal reduction of losses within the impeller, zone *iii* and *iv*, but a much larger reduction of losses in zone *ii*. Hence the inlet rounding modification for the 35.3 rpm PAT has influenced greatly the hydraulic conditions of the stationary zone *ii*, instead of the rotary impeller zone *iii-iv*.

4.1.1.1.2 Optimization Stage I - Summary

The results of optimization stage I (from section 4.1.1.1.1 and section A5.1, Appendix A) reveal that the modifications have essentially had positive effects on the 8 tested PATs. Though it may be difficult to generalize the results, an attempt is made to summarize the results under 3 categories namely, at the BEP, at part-load and overload regions.

There have been minor corrections with respect to the geometric conditions in few PATs in addition to impeller/shroud rounding. In that the optimization stage for the 45.2 rpm PAT (section A5.1.4, Appendix A) also includes the repair of the shroud section and for the 36.4 rpm PAT (section A5.1.2, Appendix A) includes the axial correction of the impeller misalignment (Figure A5.3).

1. The BEP region

Excluding the results from the 45.2 rpm and the 36.4 rpm PAT, it is seen from Table 4.3 that there are evidences of power improvement due to inlet rounding in all the tested PATs with a rise of +0.2% to +0.7%. For the same PATs it is seen that the head reduction percentages are very substantial in the range of +0.4% to +1.6%, much more than the corresponding power improvement. This behaviour clearly eliminates the change of rotational momentum within the impeller control volume (refer section 3.1.3.1.2 and 3.1.3.1.1, Chapter 3) and only refers to changes in hydraulic loss composition.

Therefore from the positive behaviour of the power improvement points +0.2% to +0.7%), it can be concluded that the hydraulic conditions within the impeller have improved with decrease of losses in zone *iii* and *iv*, which are more likely to be the reduced flow separation component ($H_{L.iii-iv.flow-sep}$, refer section 2.3.3, Chapter 2). The behaviour of the head reduction values at BEP (+0.4% to +1.6%) also improved hydraulics in zone *ii* in addition to the positive hydraulics within the impeller. The effects in zone *ii* include better interaction with sub zones 'b' and 'c' ($H_{L.ii\ b-c}$ loss component, section 2.3.2.1) and lower turbulence ($H_{L.ii-iii}$ loss component, section 2.3.2.2).

However in the mixed flow 94.4 rpm PAT, power improvement (+0.7%) is greater than head reduction (+0.4%), which indicates that the improvement of the hydraulics within the impeller

zone (zone *iii* and *iv*) is more than in zone *ii*. There could also be a condition of no improvement of zone *ii* hydraulics.

For the 36.4 rpm PAT the axial correction in addition to inlet rounding (section A5.1.2) has caused extensive improvement of hydraulics in zone *ii*,*iii* and *iv* (+3.4% power improvement and +3.3% head reduction).

It is very interesting to point out that the shroud repair in the 45.2 rpm PAT (section A5.1.4), has lead to the decrease of net rotational momentum (refer section 3.1.3.1.2 and 3.1.3.1.1, Chapter 3) with -3.5% power improvement and over +8% head reductions. The excessive head reductions also points towards an overall decrease of losses in zone *ii* ($H_{L.ii\ b-c}$ and $H_{L.ii-iii}$ components).

Table 4.3, Relative study at the BEP for the tested PATs in the Optimization Stage I

PAT	Reference Table No.	ϕ	Head reduction	Power improvement	Efficiency rise
24.5 rpm	(A5.2)	0.117	+1.2%	+0.3%	+1.1%
35.3 rpm	(4.2)	0.151	+1.6%	+0.2%	+1.5%
36.4 rpm	(A5.4)	0.185	+3.3%	+3.4%	+4.7%
39.7 rpm	(A5.6)	0.200	+1.6%	-0.5%	+0.9%
45.2 rpm	(A5.8)	0.235	+8.5%	-3.5%	+2.4%
46.4 rpm	(A5.10)	0.275	+2.0%	-0.2%	+1.4%
79.1 rpm	(A5.12)	0.480	+0.0%	+0.2%	+0.1%
94.4 rpm	(A5.14)	0.400 $_{mf}$	+0.4%	+0.7%	+0.9%

2. The Part-load region

The results of the tested PATs in the part-load region are summarized in Table 4.4. In the 35.3 rpm, 39.7 rpm, 46.4 rpm and 79.1 rpm PAT, the percentage of head reductions are 1 to 4 times greater than the percentage of power improvements, which needlessly goes to say that loss reduction in zone *ii* is more dominating than the loss reduction within the impeller control volume.

Table 4.4, Relative study at the part-load line for the tested PATs in the Optimization Stage I

PAT	Reference Table No.	ϕ	Head reduction	Power improvement	Efficiency rise

24.5 rpm	(A5.2)	0.080	+0.5%	+0.6%	+0.7%
35.3 rpm	(4.2)	0.120	+2.1%	+0.4%	+1.9%
36.4 rpm	(A5.4)	0.135	+1.8%	+6.1%	+4.8%
39.7 rpm	(A5.6)	0.140	2.0%	+0.5%	+1.8%
45.2 rpm	(A5.8)	0.170	+12.0%	-8.1%	+3.0%
46.4 rpm	(A5.10)	0.200	+1.9%	-0.1%	+1.2%
79.0 rpm	(A5.12)	0.380	+1.3%	+0.9%	+1.5%
94.4 rpm	(A5.14)	0.280 $_{mf}$	+2.2%	+8.9%	+6.8%

In the 24.5 rpm PAT the part-load point shows more gains within the impeller zone compared to the zone *ii*. The results of 36.4 rpm PAT owing mainly to axial correction shows higher power improvement compared to the head reductions. The 45.2 rpm PAT shows negative power improvement compared to head reduction due to the shroud repair (decrease of rotational momentum) than due to impeller rounding. The part-load results for the mixed flow 94.4 rpm PAT reveal that there are substantial reductions of impeller losses and practically no improvement of hydraulics in zone *ii*.

The efficiency rise in the part-load region is positive and lies in the range of +1% to +7% for all PATs, which represents a net improvement of the hydraulic conditions.

3. The Overload region

As seen in Table 4.5, the percentage of head reductions due to rounding are also much greater compared to the power improvement, even for the 94.4 rpm PAT which exhibited opposite behaviour in the part-load and BEP region respectively. This signifies a condition of greater reductions of losses within the radial clearance zone *ii* compared to improvement of reductions within the impeller zone *iii* and *iv* for all tested PATs in the overload region.

Table 4.5, Relative study at the overload line for the tested PATs in the Optimization Stage I

PAT	Reference Table No.	ϕ	Head reduction	Power improvement	Efficiency rise
24.5 rpm	(A5.2)	0.137	+1.7%	+0.6%	1.6%
35.3 rpm	(4.2)	0.200	+2.2%	+0.5%	+2.0%
36.4 rpm	(A5.4)	0.250	+6.2%	+2.1%	+5.2%
39.7 rpm	(A5.6)	0.250	+2.3%	+0.2%	+2.1%

45.2 rpm	(A5.8)	0.320	+6.6%	-3.5%	+2.4%
46.4 rpm	(A5.10)	0.320	+2.3%	-0.2%	+1.4%
79.0 rpm	(A5.12)	0.600	+0.3%	+0.0%	+0.2%
94.4 rpm	(A5.14)	0.500 mf	+1.7%	-0.1%	+1.3%

4.1.1.2   Optimization Stage II – Inlet Casing Rings

As seen in Table 3.4, Chapter 3, the optimization stage II has been implemented only on two PATs, namely, the 39.7 rpm PAT and the 79.1 rpm PAT. There are two distinct designs of inlet casing rings incorporated. The 39.7 rpm PAT uses tapered rings (Figure A5.18, Appendix A), while the 79.1 rpm PAT incorporates flat and thin rings (Figure 4.3). The results of the 79.1 rpm PAT are analyzed in detail in this section, while that for the 39.7 rpm PAT are presented in section A5.2, Appendix A. A generalized summary of the effects due to the two different types of rings is discussed later in this section.

4.1.1.2.1   79.1 rpm PAT
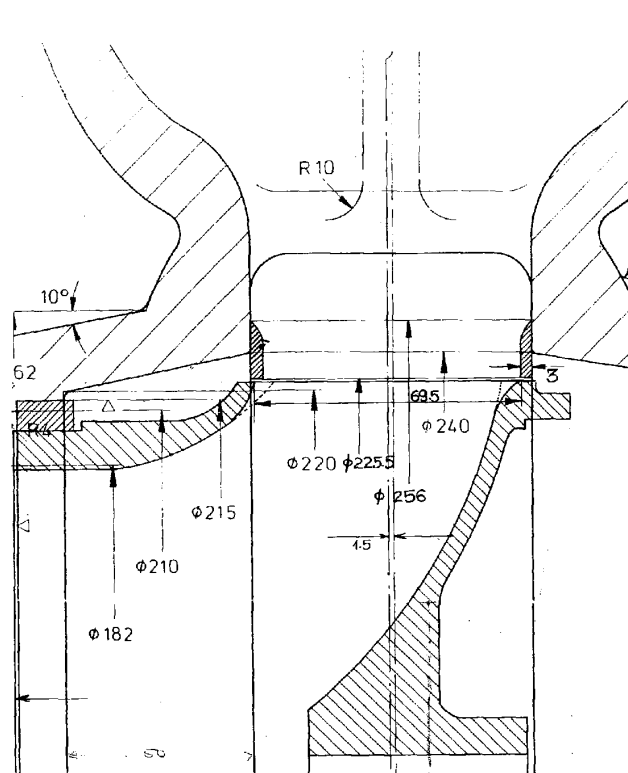
Figure 4.3, Flat rings insertion in the Optimization Stage II on the 79.1 rpm PAT

The geometric modification on the 79 rpm PAT consists of fixation of two flat rings of 3 mm thickness as shown in Figure 4.3. The ring near the front shrouds protrudes ahead blocking some flow into the impeller width. The misalignment of the impeller in the axial direction could worsen the hydraulic - geometric interface near the front shroud of the impeller.

The effects of the flat rings are studied from the dimensionless characteristics plotted in Figure 4.4. It is seen that except in the part-load region, where there is reduction of head across the modified PAT, the head number characteristics for the two stages are almost identical. On the other hand the PAT with casing rings shows greater power generation starting from the part-load region to overload region, with margins continuously rising. Due to greater influence of the power number curve there is a consistent increase of efficiency in the range of +1% to +1.5%. The BEP is compared in Table 4.6, where the power number increases from 1.771 to 1.804 units, while the power number increases from 4.883 to 4.903 resulting in a net efficiency rise of +1%, from 75.6% to 76.6%.
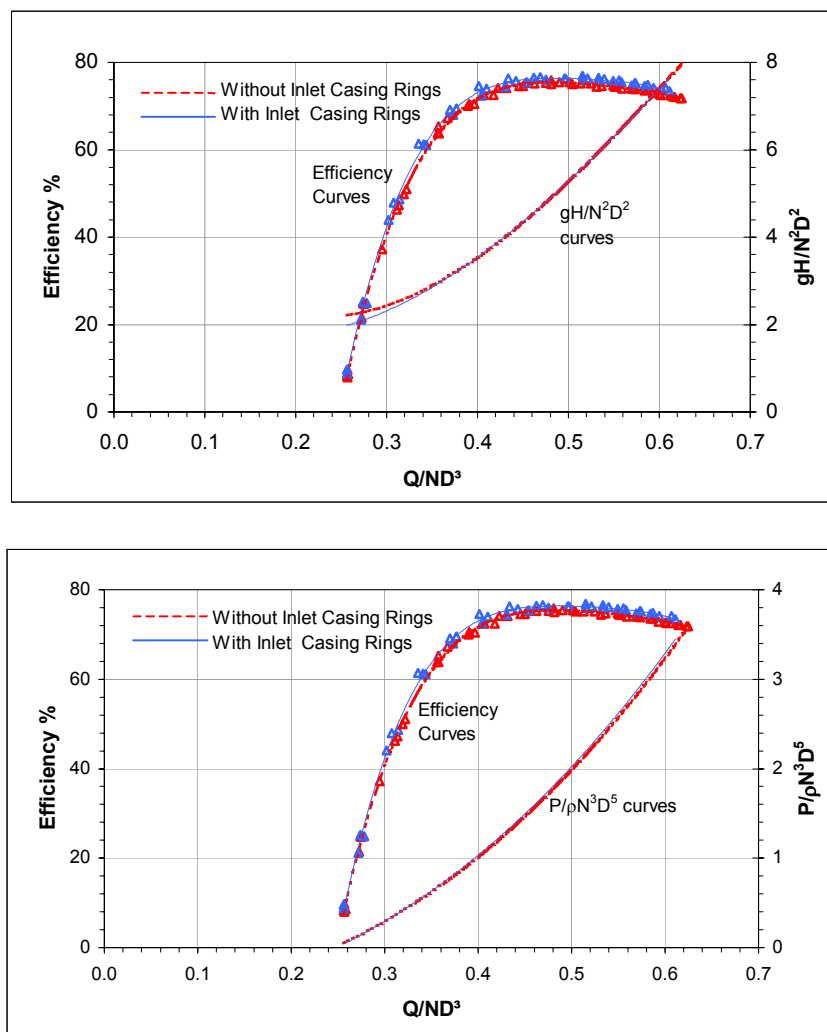

Figure 4.4, Comparisons of dimensionless characteristics for Optimization Stage II on the 79.1 rpm PAT

Table 4.6, BEP summary for two stages of Optimization Stage II on the 79.1 rpm PAT

Stage	ϕ	ψ	**p**	η
Non-modified	0.480	4.883	1.771	75.6%
Inlet casing rings	0.480	4.903	1.804	76.6%

The percentage analysis chart in Figure 4.5 reveals that the percent power improvement is fairly constant and substantial throughout the operating range with +1.5% to +2% rise. The percent head reduction curve on the other hand shows excessive reduction between the no-load and part-load line, but the reductions become negative (to about –0.5%) in the main operating region. The reductions however become positive in the overload region. There is positive efficiency rise in the entire operating range with +1.3% in the part-load line and about +1.4% in the overload region. The behaviour of the various parameters in the part-load, BEP and overload lines is summarized in Table 4.7.
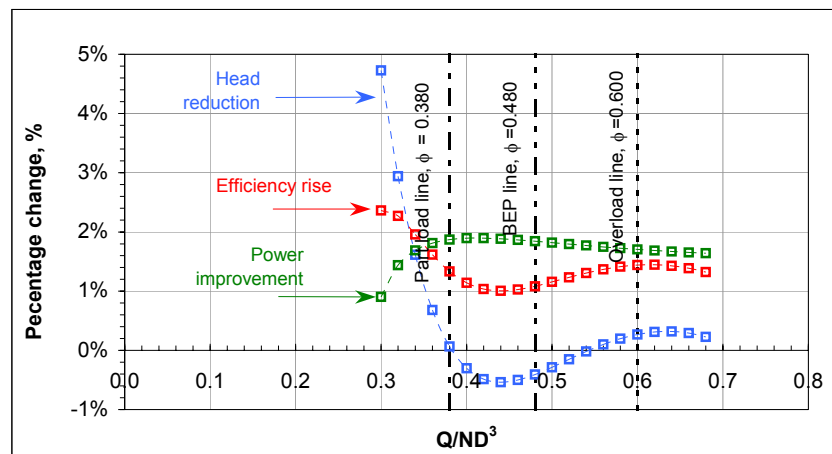
Figure 4.5, Percentage Analysis Plot for Optimization Stage II on the 79.1 rpm PAT

Table 4.7, Relative study at part-load, BEP and overload lines for Optimization Stage II on the 79.1 rpm PAT

	Part-load line ϕ = 0.380	BEP line ϕ = 0.480	Overload line ϕ = 0.600
Head reduction	+0.1%	-0.4%	+0.2%
Power improvement	+1.9%	+1.8%	+1.7%
Efficiency rise	+1.3%	+1.1%	1.4%

Discussion of Results on the 79.1 rpm PAT

Considering only the operating range after the part-load line (ϕ =0.380 to ϕ =0.550 in Figure 4.5), there has been a substantial rise of power in the modified PAT. This signifies either the possibility of decrease in the net impeller losses or increase of net rotational momentum across the impeller. On the other hand there is an increase in the head number for the modified PAT, which suggests either a rise of overall losses across the PAT control volume or rise of the net rotational momentum.

Due to the asymmetric geometric conditions of the front shroud and ring interface in Figure 4.3 a small component of loss in zone *iii* and *iv* is introduced. Further the introduction of the frictional losses due to the presence of rings in zone *ii* and the probable shock losses due to minor changes to the inlet velocity triangle, and if at all there were to be an increase of net rotational momentum, this would cause the head reduction curve to go deeper into the negative quadrant compared to what is recorded in Figure 4.5. This behaviour strongly prompts a condition of greater decrease of the losses in the PAT control volume, compared to the rise of the inlet rotational momentum component. For the PAT control volume losses to decrease there could be either a drop in one of the components in impeller zone, *iii* and *iv* or a component of the stationary zone *ii*. These loss components that decrease are having a complex relationship with the other increasing loss components. It is also very difficult to obtain the exact relationship of the various loss components and influence of the net rotational momentum component in this operating range (though there seems to be a very small presence of it).

However in the overload region (after ϕ =0.550 in Figure 4.5), the head reduction become positive which clearly indicate that there is no influence of the rotational momentum component and only the losses in the PAT control volume have decreased. The power improvement in this overload range also stands positive pointing towards better hydraulics in the impeller zone. The final outcome of the insertion of rings of flat design type has improvement the overall performance of the 79 rpm PAT.

4.1.1.2.2   Optimization Stage II - Summary

1. The BEP region

For 39.7 rpm PAT, it is shown in section A5.2.1 (Appendix A) that the positive power improvement and negative head reductions at the BEP are coming from increase rotational momentum and also increased losses in zone *ii*. While for the 79.1 rpm PAT, it has been shown that change in rotational momentum is negligible and the power improvement (+1.8% in Table 4.8) is coming mainly from improved hydraulic condition in zone *iii* and *iv*. The negative head reduction (-0.4% in Table 4.8) is due to greater increase of total losses in zone *ii* (complex interaction of various loss components in zone *ii* as seen in section 4.1.1.2.1) notwithstanding the decrease of losses in zone *iii* and *iv*.

Table 4.8, Relative study at the BEP for the tested PATs in the Optimization Stage II

PAT	Reference Table No.	Ring type	φ	Head reduction	Power improvement	Efficiency rise
39.7 rpm	(A5.16)	Tapered	0.200	-2.5%	+0.8%	-1.4%
79.1 rpm	(4.7)	Flat	0.480	-0.4%	+1.8%	+1.1%

2. The Part-load region

In the part-load region, the 39.7 rpm PAT shows a negative power improvement (-3.5% in Table 4.9) is due to increase flow separation losses (as seen in section A5.2.1, and Figure A5.21, Appendix A) due to impeller misalignment (Figure A5.18, Appendix A) compared to rise rotational momentum. For the 79.1 rpm PAT it is seen from Table 4.9, losses in zone *iii* and *iv* (with +1.9% power improvement) are much larger than the increases losses in zone *ii* (only +0.1% head reduction).

Table 4.9, Relative study at the part-load line for the tested PATs in the Optimization Stage II

PAT	Reference Table No.	Ring type	φ	Head reduction	Power improvement	Efficiency rise
39.7 rpm	(A5.16)	Tapered	0.140	-2.0%	-3.5%	-4.0%
79.1 rpm	(4.7)	Flat	0.380	+0.1%	+1.9%	+1.3%

3. The Overload region

The overload summary as shown in Table 4.10 reflects the same behaviour as in the BEP region discussed earlier (Table 4.8).

Table 4.10, Relative study at the overload line for the tested PATs in the Optimization Stage II

PAT	Reference Table No.	Ring type	φ	Head reduction	Power improvement	Efficiency rise
39.7 rpm	(A5.16)	Tapered	0.250	-5.2%	+3.1%	-1.6%
79.1 rpm	(4.7)	Flat	0.600	+0.2%	+1.7%	+1.4%

4. Summary

The optimization stage of casing rings have brought about different hydraulic effects in the two PATs considered. The cause could be attributed to the different design approaches considered for the inlet casing rings. While on the 39.7 rpm PAT, the greater taper on the rings resulting in higher flow contraction effects. In this PAT it was also seen that there was a velocity triangle rearrangement (Figure A5.21, Appendix A) at the inlet causing greater transfer of rotational momentum. The contraction also caused excessive losses in zone *ii*. The net head was found to increase across the PAT due to the increased rotational momentum and other forms of losses and subsequently bringing down the overall efficiency. Hence this modification with tapered rings has had a negative impact on the PAT's performance.

On the 79.1 rpm PAT the rings were flat and hence the contractions effects were minimal. It was also seen that there was a substantial positive effect inside the impeller (lower losses in zone *iii* and *iv*) contributing to increased power and resulting a more or less unchanged net head (since total losses in zone *ii* have increased, but not much as in 39.7 rpm PAT). However the results of the 79.1 rpm PAT did not give evidence of the influence of rotational momentum effects. The overall efficiency in the 79.1 rpm PAT increased by +1% to +1.5% which shows the modification procedure with flat rings has had a positive outcome.

4.1.1.3   Optimization Stage III – Suction Eye Enlargement

The optimization stage III is performed on the two PATs, namely, the 24.5 rpm PAT and the 35.3. rpm PAT, that had a peculiar design of the suction, zone *vi* (This design is mainly related to the shortened axial eye length, $L_{s.e}$ and a sharper contraction from the plane '2' to plane 's' in Figure A4.3 and Table A4.2). The results of the suction eye enlargement on the 24.5 rpm PAT are analyzed in this section, while that of the 35.3 rpm PAT are presented in section A5.3, Appendix A.

4.1.1.3.1   24.5 rpm PAT

This optimization stage comprises of modification carried out on the eye region of the impeller and casing as explained in section 2.5 of chapter 2. While the impeller eye was conically expanded, the casing eye was given a single constant diameter enlargement. Therefore this modification cause complete alteration to the *vi* of the PAT control volume and the subsequent draft tube zone *vii*.

The characteristics of the two stages are analyzed in Figure 4.6 where is it is seen that the head number for the modified PAT has considerably dropped in the whole of the no-load and part-load region. However within the main operating region there is no head reduction and two characteristics merge. In the overload region the head number for the modified PAT is seen to slightly increase. The power number curve for the modified PAT also shows signs of

greater generations only in the part-load region and no change in the BEP region, while in the overload region the power begins to slightly drop. The part-load efficiency has increased in the range of +8% to +10%, mainly owing to the combined effect of head number and power number. However at the BEP the efficiency remains unchanged. In Table 4.11, the BEP point is summarized where it seen that head number decreases from 11.333 units to 11.307 units while the power number drops from 0.9764 units to 0.9744 units.
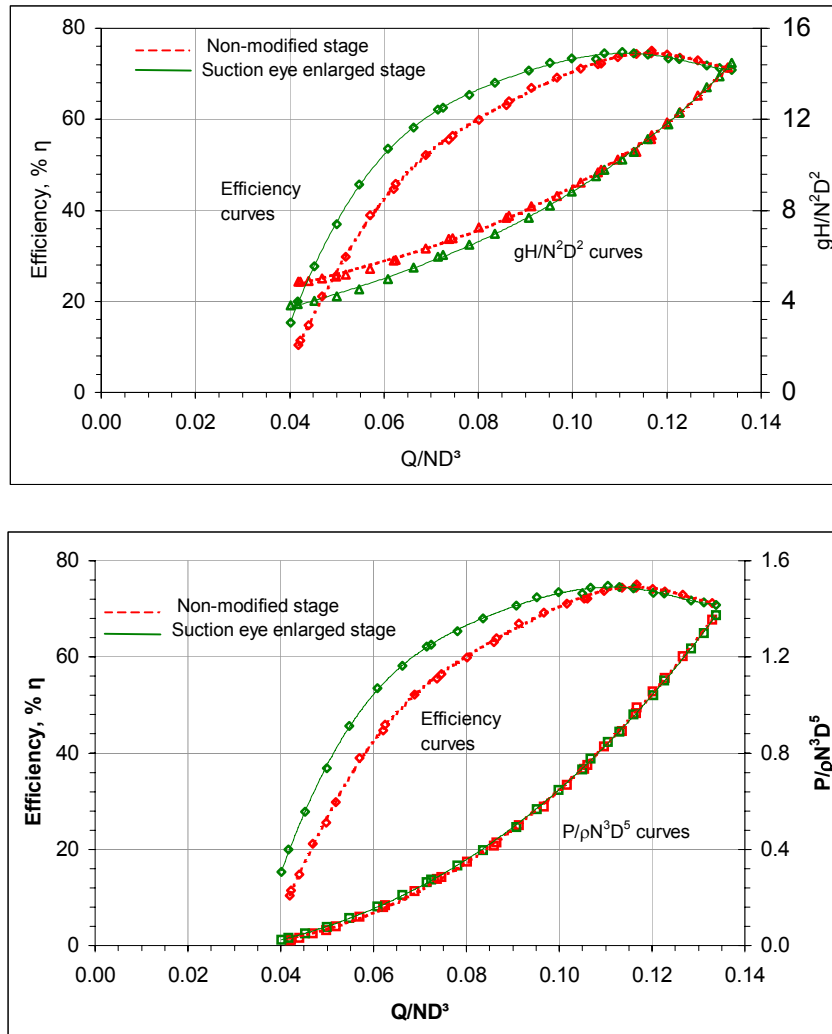

Figure 4.6, Comparisons of dimensionless characteristics for Optimization Stage III on the 24.5 rpm PAT

Table 4.11, BEP summary for two stages of Optimization Stage III on the 24.5 rpm PAT

Stage	ϕ	ψ	**p**	η
Non-modified	0.117	11.333	0.9764	73.6%
Suction eye enlarged	0.117	11.307	0.9744	73.7%

The internal effects of this modification can be understood from the percentage analysis in Figure 4.7, where power improvement of +3% to +10% is recorded within the part-load region and subsequently begins to decrease and becomes negative near the BEP. It continues to be negative throughout the overload region in the range of –0.5% to –2%. The head reductions on the other hand too display tremendous gains in the part-load region (+6% to +8% reductions) and the gains slowly diminish in the BEP and overload regions. However deep in the overload region the head reductions begin to become positive. The efficiency rise curve is positive till the BEP line and then becomes negative owing more to the power number drop. The relative gains of the various parameters in the part-load line, the BEP and the overload line are respectively summarized in Table 4.12.
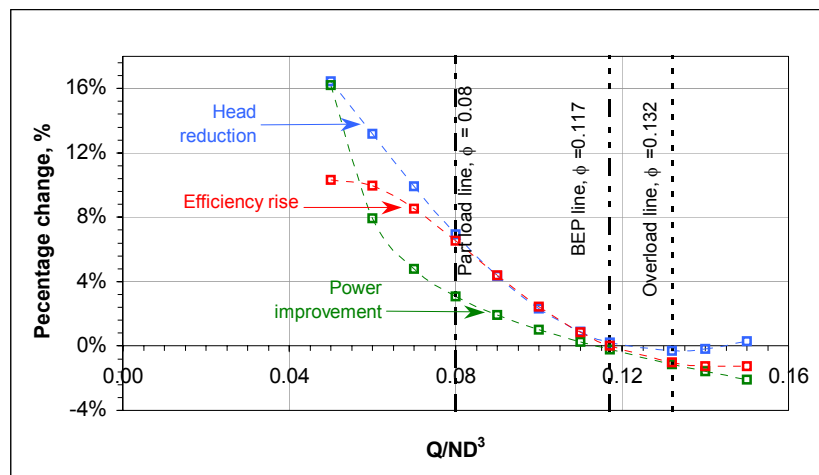
Figure 4.7, Percentage Analysis Plot for Optimization Stage III on the 24.5 rpm PAT

Table 4.12, Relative study at part-load, BEP and overload lines for Optimization Stage III on the 24.5 rpm PAT

	Part-load line $\phi = 0.080$	BEP line $\phi = 0.117$	Overload line $\phi = 0.132$
Head reduction	+6.9%	+0.2%	-0.3%
Power improvement	+3.1%	-0.2%	-1.1%
Efficiency rise	+6.6%	0.0%	-1.0%

Discussion of Results on the 24.5 rpm PAT

The modification on zone *vi* has had a great influence on the power number behaviour, in which there is an improvement in the whole region from no-load to BEP. This suggests that either the hydraulics within impeller zone *v*, *iv* and *iii* have improved or there is an decrease of the exit rotational momentum giving a net increase of the rotational momentum across the impeller. In the same operating range, the head reductions are also positive and very

substantial, which means that there is no influence of rotational momentum effects and the entire transformation can be attributed only to loss mechanisms in various zones.

This suggests that the impeller zone losses have tremendously dropped, which are also reflected head number curve. But the reductions in the head number curve are so much that there is a certain possibility of losses in zone *vi* also decreasing. Therefore the part-load region of the characteristics symbolizes with reduction of losses in zone *vi* and impeller zone *v*, *iv* and *iii*.

The continuous negative trend of the power improvement curve towards the BEP and overload region directly indicates that impeller losses have begun to increase considerably with loading. However the head reductions have not gone into the negative quadrant, which mean that there is a certain positive hydraulic in zone *vi* that is negating the increased impeller losses.

Therefore the suction eye enlargement for the 24.5 rpm PAT has decreased the losses in zone *vi* throughout the operating range, while the impeller zone losses have decreased only in the part-load region, which subsequently changed its trend and started to increase in the BEP and overload region. This modification has shown no evidence of changes to the rotational momentum across the impeller.

4.1.1.3.2   Optimization Stage III - Summary

1. The BEP region

It is seen from Table 4.13 at BEP that there is no change in the efficiency for the 24.5 rpm PAT, with marginally positive head reductions and negative power improvement. The 35.3 rpm PAT shows +1.7% improvement in power with negative head reduction of –3.4% (detailed causes in section A5.3.1, Appendix A) causing a drop in the efficiency.

Table 4.13, Relative study at the BEP for the tested PATs in the Optimization Stage III

PAT	Reference Table No.	ϕ	Head reduction	Power improvement	Efficiency rise
24.5 rpm	(4.12)	0.117	+0.2%	-0.2%	0.0%
35.3 rpm	(A5.18)	0.151	-3.4%	+1.7%	-1.3%

2. The Part-load region

The part-load point region shows significant gains in terms of efficiency for both the PATs. While the 24.5 rpm PAT shows both a considerable positive head reduction and power improvement, the 35.3 rpm PAT shows a marginal head reduction.

Table 4.14, Relative study at the part-load line for the tested PATs in the Optimization Stage III

PAT	Reference Table No.	ϕ	Head reduction	Power improvement	Efficiency rise
24.5 rpm	(4.12)	0.080	+6.9%	+3.1%	+6.6%
35.3 rpm	(A5.18)	0.120	+0.4%	+2.7%	+2.3%

3. The Overload region

Both the PATs show a fall in the operating efficiency at the corresponding overload point (Table 4.15). While both the head reductions and power improvement are negative for the 24.5 rpm PAT, the power improvement for the 35.3 rpm PAT is still positive indicating rotational momentum's influence.

Table 4.15, Relative study at the overload line for the tested PATs in the Optimization Stage III

PAT	Reference Table No.	ϕ	Head reduction	Power improvement	Efficiency rise
24.5 rpm	(4.12)	0.137	-0.3%	-1.1%	-1.0%
35.3 rpm	(A5.18)	0.200	-2.1%	+1.3%	-0.5%

4. Summary

The suction eye enlargement has had different effects on the two PAT tested. However there are some similarities in the results, mainly in the part-load region, where reductions of impeller control volume losses and also the eye zone losses is recorded. The overall PAT operating efficiency in the part-load region has been enhanced due to this effect, which is a positive development due to the modification.

One of the phenomenon found to occur in the 35.3 rpm PAT is with respect to consistent increase of power generation. Here it was found that in addition to the decrease of impeller losses there was also influence of the change in rotational momentum effects. The rotational momentum has also affected the head number curve (making head reduction negative) accordingly. Though the results in the BEP-overload region also indicate that there could be a decrease of the zone *vi* losses. This rise of rotational momentum is strongly linked to the decreased velocity conditions due to eye enlargement.

However no evidences of rotational momentum effects were found in the characteristics of 24.5 rpm PAT, despite the lowered velocities at the eye. In fact within the BEP-overload region, there were evidences to show that impeller losses have increased on one hand and the losses in zone *vi* have decreased substantially on the other hand.

As far as the overall performance is concerned there are no major gains in the BEP and overload regions for both the tested machines, in fact the overall efficiency drops by over 1% for the 35.3 rpm.

4.1.1.4 Optimization Stage IV – Effect of Casing Eye Rib

The optimization stage has been carried out on the 4 PAT test units namely the 36.4 rpm, 39.7 rpm, 46.4 rpm and 79.1 rpm PATs. Internal flow measurements mainly associated with swirl flow at the measurement plane 'e' were performed only on the 36.4 rpm, 39.7 rpm and the 46.4 rpm PATs. The results pertaining to the 39.7 rpm PAT is discussed in detail this section while results for the 36.4 rpm PAT, 46.4 rpm PAT and the 79.1 rpm PAT are presented in section A5.4, Appendix A.

4.1.1.4.1 39.7 rpm PAT

4.1.1.4.1.1 Overall Performance Comparison

Figure 4.8 shows the geometry of the casing rib along with the zone *vi*. The dimension of the rib is considerable in comparison to the eye cross-section and is placed very close to the interface zone *v*.

The dimensionless characteristics are compared in Figure 4.9 in which the head characteristics of the CRA stage has dropped considerably throughout the operating range with greater reductions in the part-load region. The reduction in the BEP region is present but small. The power curve for the CRA stage on the other hand shows increased generation towards the BEP and overload region. Owing to the decreased head consumption and increased power generation, there is a consistent improvement of efficiency of +1% to +1.5% at all load points.

The BEP point analyzed in Table 4.16 sees a decrease of head number from 6.843 to 6.807units while the power rises from 1.120 to 1.130 units causing a rise of efficiency from 81.8% to 83%.
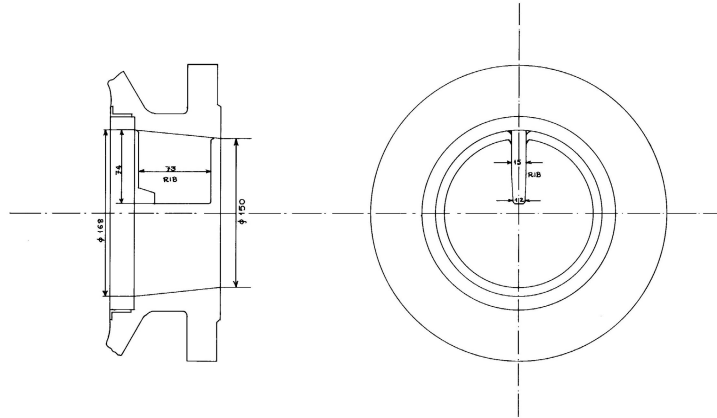
Figure 4.8, Geometry of the casing eye rib for the 39.7 rpm PAT

Table 4.16, BEP summary for two stages of Optimization Stage IV on the 39.7 rpm PAT

Stage	ϕ	ψ	p	η
Casing Rib Present	0.200	6.843	1.120	81.8%
Casing Rib Absent	0.200	6.807	1.130	83.0%

The percentage analysis chart in Figure 4.10 shows a slight decrease of power within the part-load region (0% to -0.6%). But in the main operation region the power improvement curve is positive with a maximum gain of +1% at the BEP. The head reduction curve on the other hand is positive throughout the operating range. The head reductions are over +2% in the part-load region decreases to about +0.5% at the BEP. The efficiency rise curve is very stable with an average gain of +1.2% to +1.8%. Table 4.17 summarizes that relative gains of various parameters within the part-load, BEP and overload regions.

Table 4.17, Relative study at part-load, BEP and overload lines for Optimization Stage IV on the 39.7 rpm PAT

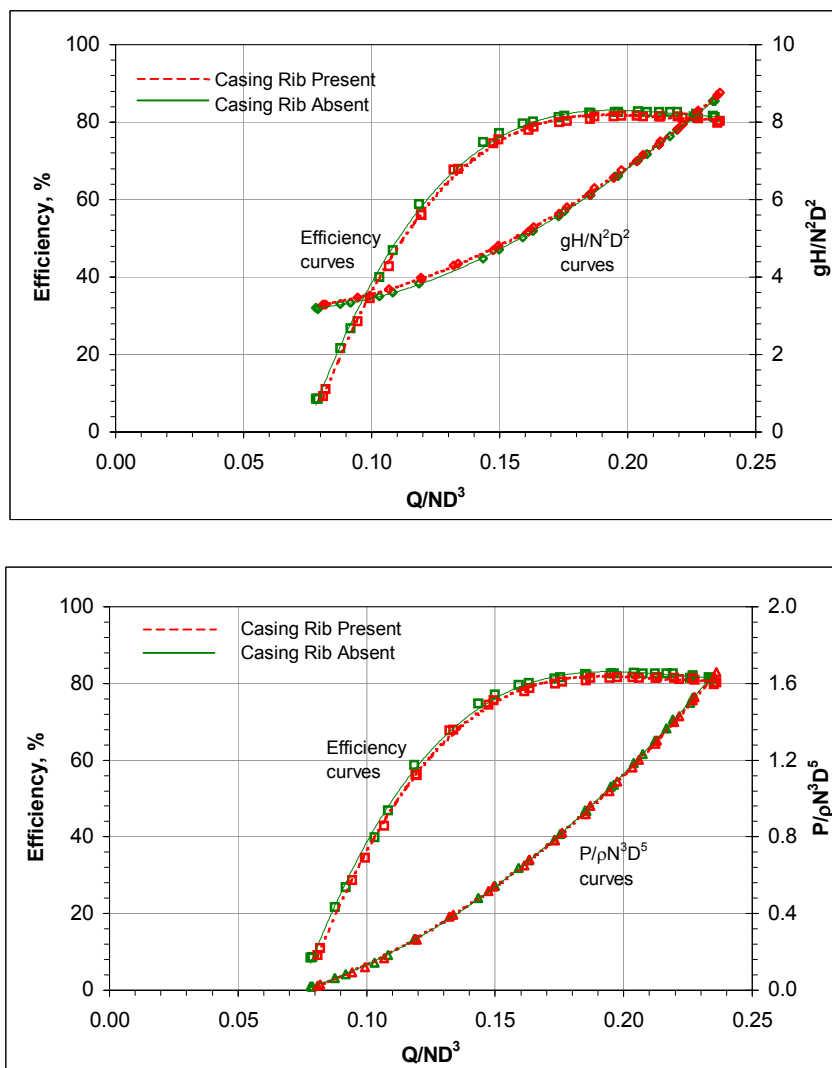|	Part-load line ϕ = 0.140	BEP line ϕ = 0.200	Overload line ϕ = 0.250
Head reduction	+2.5%	+0.5%	+1.1%
Power improvement	-0.3%	+0.9%	+0.4%
Efficiency rise	+1.6%	+1.1%	+1.2%

Figure 4.9, Comparisons of dimensionless characteristics for Optimization Stage IV on the 39.7 rpm PAT
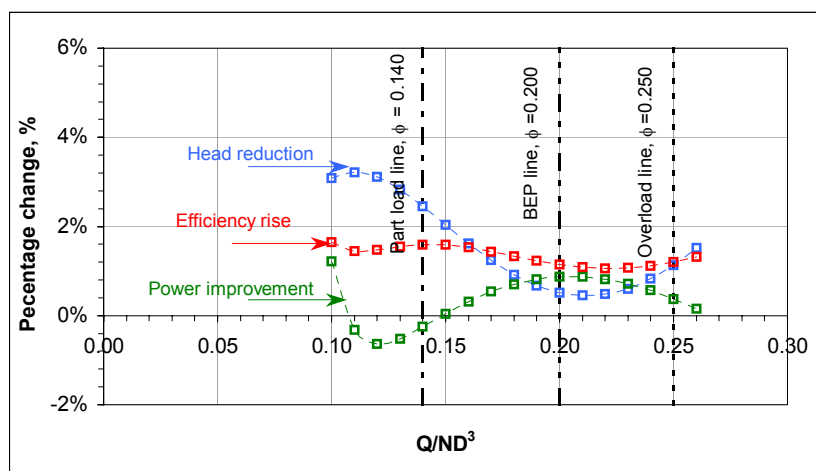

Figure 4.10, Percentage Analysis Plot for Optimization Stage IV on the 39.7 rpm PAT

Discussion of Results on 39.7 rpm PAT

In the operating range from no-load to part-load line there is a decreased power generation in the CRA stage that could be due to decreased net rotational momentum effects or some rise of hydraulic losses in the impeller zone. In the same operating range the head reductions are positive and quite substantial, which could also mean a decrease of net rotational momentum or decreased losses in PAT control volume specifically zone *vi*.

But in the main operating region the power generation for the CRA stage increases. Increased exit rotational momentum cannot be accounted here since it would decrease the power. This can only imply that the losses of the impeller zone *v* and *iv* have decreased substantially. There is a drop in the head reduction (still positive, though) towards the BEP and overload region (Figure 4.10) notwithstanding the fact that both the impeller losses and the frictional loss component of zone *vi* have decreased. Also in this range rotational momentum effects seem to be negligible. Therefore for the head reduction line to drop so much, an additional component of losses in zone *vi* could exist.

However towards the overload region the head reduction curve begins to rise (Figure 4.10) showing the influence of rotational momentum effects. It is also seen that the power begins to drop which is also coming from decreased net rotational momentum effects.

Therefore, for the 39.7 rpm PAT under optimizations stage IV, the rotational momentum effects are felt only in the part-load and overload regions. In the BEP region the impeller losses have reduced that could be associated with the position of the rib, which is too close to the impeller zone *v*. Within the same range there are evidences of another loss component in zone *vi* which is negating the frictional component and other positive effects inside the impeller to still pull the head reductions down. This new component however cannot be associated with swirl.

4.1.1.4.1.2   Internal Performance Comparison

The internal swirl profiles at reference plane '*e*' are plotted in Figure 4.11 and 4.12 for the CRP stage and CRA stages respectively at 6 load points described in Table 4.18.

Table 4.18, Definition of load points for swirl flow comparisons on the 39.7 rpm PAT

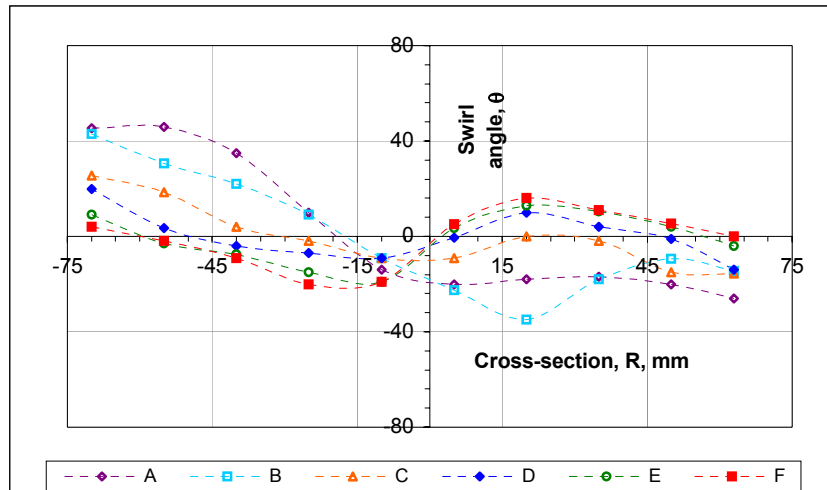| Load Point	Condition	$Q/ND^3_{(CRP)}$	$Q/ND^3_{(CRA)}$
A	No Load	0.098	0.100
B	Part-Load	0.138	0.135
C	Part-Load	0.171	0.172
D	BEP	0.196	0.194
E	Overload	0.226	0.225
F	Overload	0.242	0.242

Figure 4.11, Swirl profiles for the CRP stage of the 39.7 rpm PAT

In the swirl profiles of CRP stage (Figure 4.11) loads A, B and C do not display good symmetry while that of the BEP load, D and overload points E and F show good symmetry across the central axis. The reversal of swirl direction takes place in loads D, E and F, all of which still have positive wall swirls.
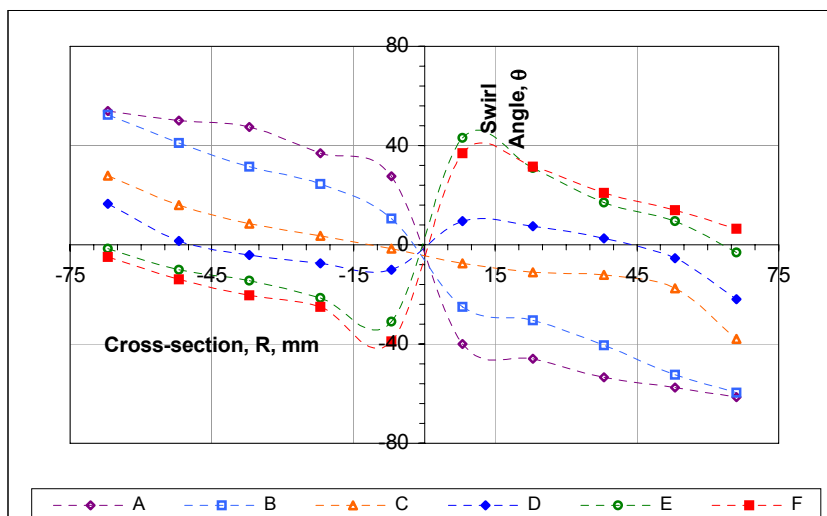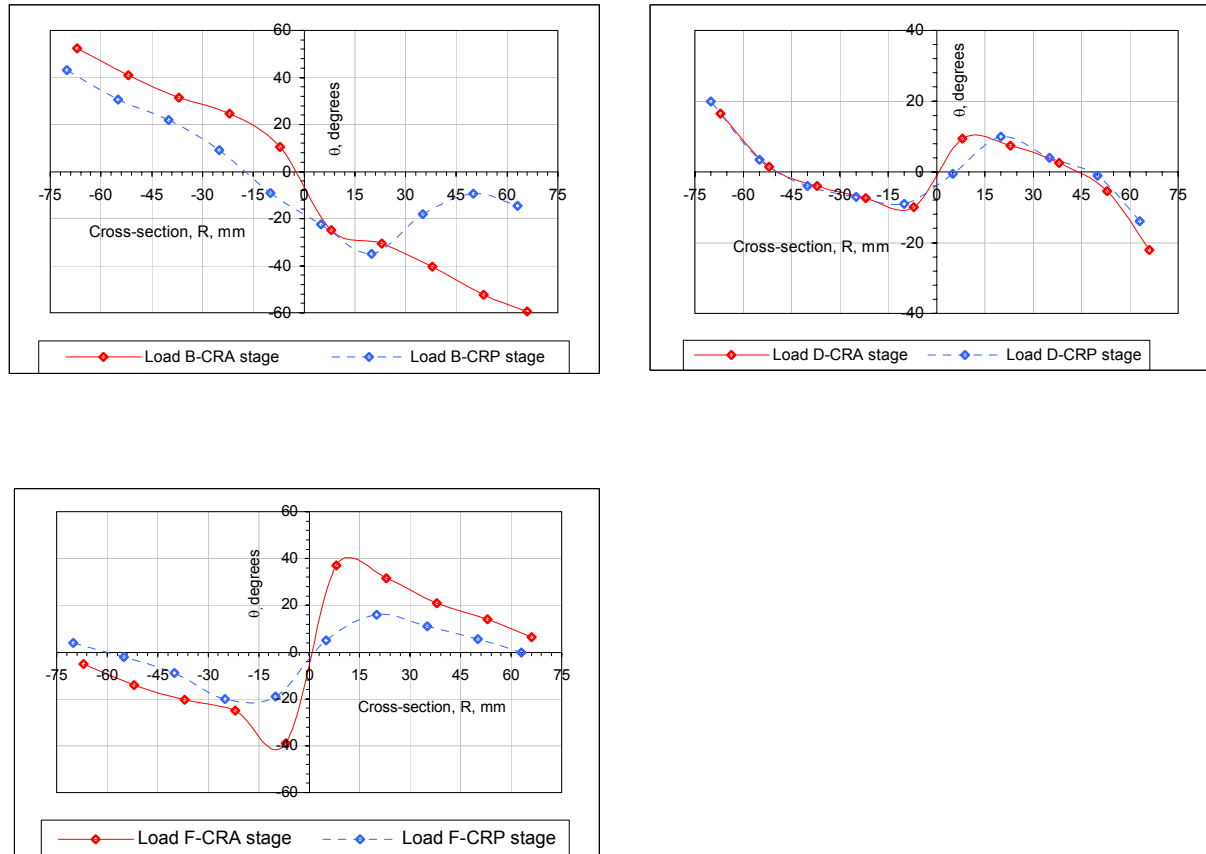

Figure 4.12, Swirl profiles for the CRA stage of the 39.7 rpm PAT

The swirl profiles for the CRA stage (Figure 4.12) show a wonderful symmetry but magnitudes (intensities) across the central axis for all loads. The profiles for load A, B and C display only positive swirls while loads E and F display complete negative swirls. The swirl directional transformation takes place at load D. The magnitude of wall swirl is highest at loads A and B (in the range of 55^0 to 60^0) while for the overload profiles the wall swirls are in the range of 0^0 to 5^0.

The swirl profile for loads B, D and F are compared for the two stages in Figure 4.13. The comparisons at load B reveal that CRA posses excessive swirl over the CRP stage (in the range of 15^0 to 20^0). At the BEP load D, the two swirl profiles nearly collapse into each other

indicating no change in the rotational momentum of the fluid. However in the overload point F, the CRA stage shows greater swirls that are in range of 10^0 to 35^0 compared to the CRP stage.

The internal performance comparisons also revalidate results from the overall comparison that the momentum effects are felt only in the part-load (ϕ = 0.140 in Figure 4.10) region and overload (ϕ = 0.250 in Figure 4.10) region.

Figure 4.13, Comparisons of the swirl profiles for the CRP and CRA stage of 39.7 rpm PAT at load B, D and F

4.1.1.4.2   Optimization Stage IV - Summary

1. The BEP region

At the respective BEPs it is seen from Table 4.19 that the 36.4 rpm PAT and 46.4 rpm PAT show negative power improvement values and positive head reductions with the efficiency dropping. The 79.1 rpm PAT shows a marginal negative head reduction and negative power improvement causing a drop in efficiency. It is only the 39.7 rpm PAT that shows an improvement in power and also positive head reduction resulting in an efficiency rise of over +1%.

Table 4.19, Relative study at the BEP for the tested PATs in the Optimization Stage IV

PAT	Reference Table No.	ϕ	Head reduction	Power improvement	Efficiency rise
36.4 rpm	(A5.20)	0.185	+1.3%	-2.3%	-0.7%
39.7 rpm	(4.17)	0.200	+0.5%	+0.9%	+1.1%
46.4 rpm	(A5.23)	0.275	+0.9%	-1.2%	-0.2%
79.1 rpm	(A5.26)	0.480	-0.2%	-0.3%	-0.4%

2. The Part-load region

The part-load performance (Table 4.20) of the 36.rpm PAT, 46.4 rpm PAT and the 79.1 rpm PAT are degraded with negative power improvement values combined with negative head reductions. However interestingly the 39.7 rpm PAT shows a significant positive head reduction (+2.5%) and a marginal decrease in power (-0.3%), still giving a part-load efficiency rise of +1.6%.

Table 4.20, Relative study at the part-load line for the tested PATs in the Optimization Stage IV

PAT	Reference Table No.	ϕ	Head reduction	Power improvement	Efficiency rise
36.4 rpm	(A5.20)	0.135	-0.5%	-0.7%	-0.7%
39.7 rpm	(4.17)	0.140	+2.5%	-0.3%	+1.6%
46.4 rpm	(A5.23)	0.200	+0.7%	-0.8%	0.0%
79.1 rpm	(A5.26)	0.380	-0.9%	0.2%	-0.5%

3. The Overload region

The behaviour in the overload region (from Table 4.21) is similar to the BEP region, with excessive power drops for the 36.4 rpm and 46.4 rpm PATs but with positive head reductions. The positive performance of 39.7 rpm PAT continues in the overload region with greater head reduction (+1.1%) compared to power improvement (+0.4%) resulting in an efficiency rise of +1.2%.

Table 4.21, Relative study at the overload line for the tested PATs in the Optimization Stage IV

PAT	Reference Table No.	ϕ	Head reduction	Power improvement	Efficiency rise
36.4 rpm	(A5.20)	0.250	+1.7%	-2.2%	-0.3%
39.7 rpm	(4.17)	0.250	+1.1%	+0.4%	+1.2%
46.4 rpm	(A5.23)	0.375	+0.4%	-1.3%	-0.6%
79.1 rpm	(A5.26)	0.600	-0.2%	-0.7%	-0.7%

The first conclusion to be made from the results of the optimization stage IV is that the rib has had an influence on the rotational momentum conditions at the interface zone *v*. This has been validated both by the behaviour of overall parameters and also using the swirl flow measurement at the draft tube entrance.

Swirl flow analysis on the 36.4 rpm (section A5.4.1.2), 39.7 rpm (section 4.1.1.4.1.2) and 46.rpm PAT (section A5.4.2.2) reveal that excessive swirls are present in the CRA stage mainly in the part-load and overload regions with minimal effects in the BEP region. But on the 46.4 rpm PAT (Load C, Figure A5.35, section A5.4.1.2) there was greater swirl associated even at BEP conditions. The increase of swirl or rotational momentum at the interface zone *v* decreases the net rotational momentum or Euler head (Equation (2.4), in section 2.2, Chapter 2) across the PAT impeller. This decrease of Euler head decreases both the power generated and net head consumed. These effects of power and head parameters have been recorded in the 36.4 rpm, 46.4 rpm and in some regions of the 79.1 rpm PAT.

The results also revealed that the overall losses of zone *vi* seem to decrease, but there are two opposing loss component, one associated with absence of rib (λ component in Equation (2.20), Chapter 2) which should decrease in CRA stage and other associated with excessive swirl velocities (ζ component in Equation (2.20), Chapter 2), which should increase. But the first component (absence of rib) appears to predominate within CRA stage of the 36.4 rpm, 39.7 rpm and 46.4 rpm PATs causing considerable head reductions. But it is very difficult to quantify the relative contribution of these loss components of zone *vi*, since they are interacting with rotational momentum effects (Equation (2.5) and (2.6)).

Another effect recorded in the CRA stage of the 39.7 rpm PAT (Figure 4.10) was the increase of power in the BEP and overload region, which could happen only with the decrease of impeller losses. This situation was not encountered in any of the other PATs. Though this is difficult to physically comprehend, it can be associated with the presence of the rib so close to the interface zone *v* and also its considerable thickness compared to the cross-section.

However quite conversely to that of the 39.7 rpm PAT, the 46.4 rpm PAT (discussed in section A5.4.2.1 and 5.4.2.2 with respect to Figure A5.32 and A5.35) showed an increase of impeller loss component between the BEP and overload region for the CRA stage, which is however very difficult to explain.

The results of the 79.1 rpm PAT (section A5.4.3, Appendix A) were inconclusive mainly with respect to the behaviour of the head curve. The zone *vi* for the 79.1 rpm PAT had a gradual expansion compared to the regular contraction in area for the other pumps. This could also alter the loss patterns. There could also be chances of erratic measurements on this PAT.

In the overall terms, the optimization stage comprising of rib removal, brought about a degradation of the performance in the 36.4 rpm PAT, 46.4 rpm PAT and 79.1 rpm PAT with 0% to 1% drop in operating efficiency and enhancement of the performance for the 39.7 rpm PAT with 1% to 1.5% rise of BEP and overload efficiency.

4.1.2 Cavitation Results

The results in this section comprises of the presentation of the mean CSHN curve for the 35.3 rpm PAT at various operating speeds under given boundary conditions associated with the draft tube designs. The CSHN curves for the other PATs are presented in section A6, Appendix A. The draft tube designs (summarized in Table B2.1) along with application examples for the cavitation study (in section B2.2) are dealt in the section B2, Appendix B.

This section also includes the summary of the necessary operating speeds required to reach the dangerous condition of cavitation (for given draft tube conditions) as defined from Dixon [10]'s criterion (Equation (2.26), Chapter 2) for each PAT.

4.1.2.1 35.3 rpm PAT

The CSHN curve for the 35.3 rpm PAT is plotted in Figure 4.14 at speeds of 900 rpm, 1000 rpm, 1100 rpm, 1200 rpm and 1300 rpm respectively and all the points are displaying very good collapsibility. In Table 4.22 it is seen that the minimum CSHN conditions occur after the BEP. The required speed for entering the critical cavitation conditions are 3350 rpm with NSPH of 7.05 m when operated at BEP and 3050 rpm with NPSH of 6.56 m when operated at the minimum CSHN conditions, respectively.

Table 4.22, Cavitation summary at the BEP and minimum CSHN conditions for the 35.3 rpm PAT

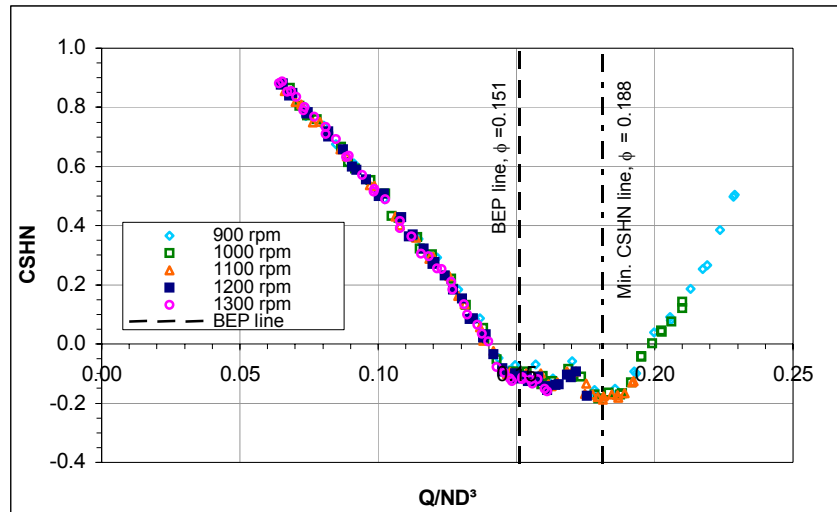| Condition	ϕ	CSHN	N_{ss} (From Dixon)	N_{cr} (rpm)	$NPSH_{cr}$ (m)
BEP	0.151	-0.120	0.63	3350	7.05
Min. CSHN	0.181	-0.118	0.63	3050	6.56

Figure 4.14, CSHN curve for the 35.3 rpm PAT

4.1.2.2   Cavitation Summary

The excellent and consistent collapsibility of the individual CSHN curves (Figure 4.14 and Figures A6.1, A6.2, A6.3, A6.4, A6.5, A6.6, A6.6 and A6.7 in section A6, Appendix A) seen for all the tested PATs vindicates the theory developed CSHN theory and approach in section 2.5.2.1, Chapter 2. It is highly encouraging result to have a single dimensionless curve to study a complicated phenomenon of cavitation in any given PAT. Therefore this approach can be used as a tool to understand and optimize the system design of PAT plants with respect to cavitation safety.

The CSHN - ϕ curve exhibits a characteristic inverted bell shape. The minimum value of the CSHN corresponds to the net combination of various parameters of the exit hydraulic is taken to be as the limiting design factor as far as cavitation is concerned. This point represents minimum pressure conditions at the dimensionless scale and therefore the corresponding discharge number becomes an important design parameter for the PAT system design. For all the radial flow PATs tested, the minimum CSHN is found to occur after the BEP and essentially in the overload region. However for mixed flow PAT of 94.4 rpm the minimum CSHN occurs before the BEP and in the part-load region (Figure A6.7, Appendix A).

For the given boundary conditions described in the Table B2.1 (section B2.1, Appendix B) for each PAT, the limiting parameters of operating speed and NPSH for the 'minimum CSHN' condition have been summarized in Table 4.23. The given PAT therefore should be operated below the critical speeds and above the limiting NPSH specified in Table 4.23.

Table 4.23, Cavitation summary at the minimum CSHN conditions for the tested PATs

PAT	$\phi_{min. CSHN}$	CSHN	N_{cr} (rpm)	$NPSH_{cr}$ (m)
24.5 rpm	0.137	-0.27	2450	5.61
35.3 rpm	0.181	-0.188	3050	6.56
36.4 rpm	0.280	-0.78	2540	4.35
39.7 rpm	0.240	-0.21	2170	6.71
45.2 rpm	0.340	-0.3	2520	6.51
46.4 rpm	-	-	-	-
79.0 rpm	0.610	-0.165	2101	7.72
94.4 rpm	0.365_{mf}	-0.047_{mf}	2350	8.26

The above analysis of limiting cavitation occurrence is restricted to the particular PATs tested and their respective boundary conditions namely the draft tube design and turbine setting. The operating speed therefore becomes the only control parameter for cavitation. However in practice, not only are the size and geometry of the PATs different but also the boundary conditions (draft tube design and turbine setting). In such cases, the CSHN characteristics of the machine need to be determined first for changed boundary conditions and subsequently the role of operating speed to study cavitation occurrence can be calculated. An application problem of such a situation is dealt in detail in the section B2, Appendix B.

4.2   Experimental and CFD Correlation

This section analyses the accurateness of the CFD model (discussed in detail in section B3, Appendix B) using the experimental results as a standard. It consists of comparing the overall characteristics and percentage analysis to determine the deviations with an objective to give a physical interpretation to these deviations with respect to the PAT control volume. The overall characteristics of the 3 PATs (24.5 rpm (Figure B3.2), 35.3 rpm (Figure B3.4) and 39.7 rpm (Figure B3.6 and B3.8) that were studied using CFD model (section B3, Appendix B) are compared with their respective experimental counterparts. For the 39.7 rpm PAT even the internal performance comprising of swirl profiles are also compared between CFD and experimental methods.

The detailed comparisons for the 24.5 rpm PAT (in section A7.1), 35.3 rpm PAT (in section A7.2) and the CRP stage of the 39.7 rpm PAT (section A7.3) are carried out in section A7, Appendix A. This section presents the results of the elaborate comparisons (both overall and internal performance) for all the CRA stage of the 39.7 rpm PAT. A detailed summary of the accurateness of the CFD model for the PATs is also presented here. This section concludes with the relative study of the Optimization Stage IV (absence of casing eye rib) from both the experimental and CFD perspectives.

4.2.1   39.7 rpm PAT - Casing Rib Absent Stage

The comparisons of the characteristics in <u>Figure 4.15</u>, reveals the CFD head number curve is consistently below the experimental curve throughout the operating range considered. The power number curve for CFD is below the experimental power curve with the margin of decrease in CFD power continuously rising from the part-load region towards the overload region. The efficiency curve for the CFD essentially remains below that of the experimental curve in the range of 1% to 4.5%. The predicted BEP point from the CFD model is also displaced with respect to the experimental BEP as summarized in <u>Table 4.24</u>.

<u>Table 4.24</u>, BEP from CFD and Experiment for the 39.7 rpm PAT (CRA stage)

	CFD	Experiment
Q/ND^3	0.180	0.200
gH/N^2D^2	5.965	7.105
$P_{hyd}/\rho N^3D^5$	0.887	1.219
$\eta_{\eta\psi\delta}$	82.6%	85.8%

The comparisons of the conditions made at the experimental BEP (Q/ND^3 = 0.200) in <u>Table 4.25</u> show that the CFD head number is lower than the experimental values while the power number prediction from CFD are much lower compared the experimental power number. The CFD efficiency is lower than the experimental efficiency due to greater influence from the drop in power number.

<u>Table 4.25</u>, Comparison of the experimental and CFD results at the experimental BEP for the 39.7 rpm PAT (CRA stage)

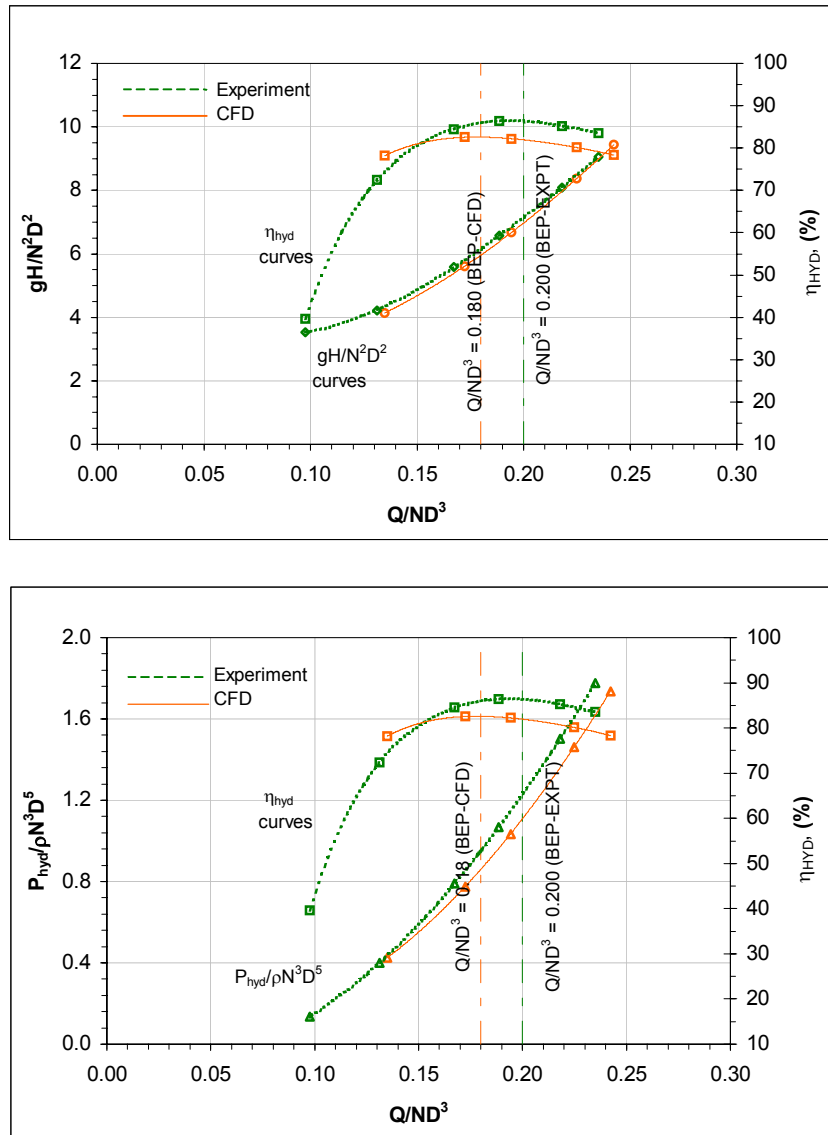| Stage	ϕ	ψ	**P**	η
Experiment	0.200	7.105	1.219	85.8%
CFD	0.200	6.971	1.143	82.0%

Figure 4.15, Comparisons of dimensionless characteristics for Experiment-CFD correlation on 39.7 rpm PAT (CRA stage)

The comparative percentage analysis chart shown in Figure 4.16 reveals that the CFD is predicting essentially the same power at the part-load line, however at the BEP line and overload line it is predicting 6% and 5% lower power respectively compared to that of the experiment. The head reduction curve is essentially positive in the considered operating range with the CFD predicting 2% lower head at the BEP while towards the overload region the head reductions diminish. The efficiency rise curve for the CFD is positive only at the part-load line and essentially remains negative in the BEP/overload region with a reduction of 3% to 4.5%.

The relative deviations between the two approaches at the part-load, BEP and overload lines are summarized in Table 4.26.
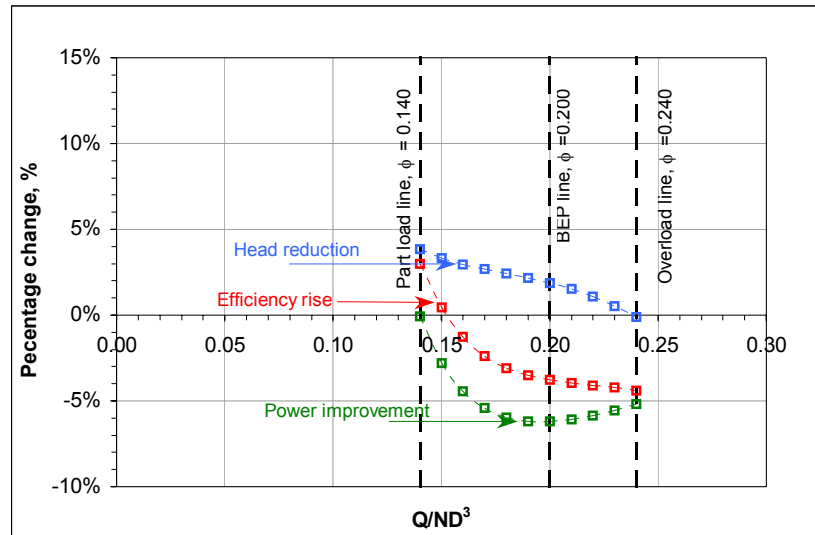
Figure 4.16, Percentage Analysis Plot for Experiment-CFD correlation on 39.7 rpm PAT (CRA stage)

Table 4.26, Relative study at part-load, BEP and overload lines for Experiment-CFD correlation on 39.7 rpm PAT (CRA stage)

	Part-load line $\phi = 0.140$	BEP line $\phi = 0.200$	Overload line $\phi = 0.240$
Head reduction	3.8%	1.9%	-0.1%
Power improvement	-0.1%	-6.2%	-5.2%
Efficiency rise	3.0%	-3.8%	-4.4%

Discussion of Results on 39.7 rpm PAT (CRA stage)

The behaviour of the power improvement curve in the part-load and BEP region can either signify that the CFD is either calculating lower net rotational momentum across the impeller or predicting greater losses in the impeller zone (analogy in section 3.1.3.1, Chapter 3) or a combination of both. The head reduction curve is positive in the same region, which suggests that the CFD could be predicting either a decreased rotational momentum or lower losses within the PAT control volume. These behaviours suggest that there is greater chance of lower determination of net rotational momentum.

Towards the overload region the head reductions become negligible and with the power improvement still being considerably negative, it becomes quite evident that the CFD, in addition to decreased rotational momentum predictions, is also miscalculating the hydraulic losses within the stationary and rotating zones in a complex distribution pattern.

Internal Performance Comparison

The swirl profiles obtained from the two approaches are compared in <u>Figure 4.17</u> at load B, D and F. At load B, it is seen that there is a reasonable similarity between the swirl profiles in the wall and main flow region of the cross section. However in the core region of the cross-section, the CFD predicts 20^0 to 50^0 greater swirl angles compared to the obtained from the experiment.
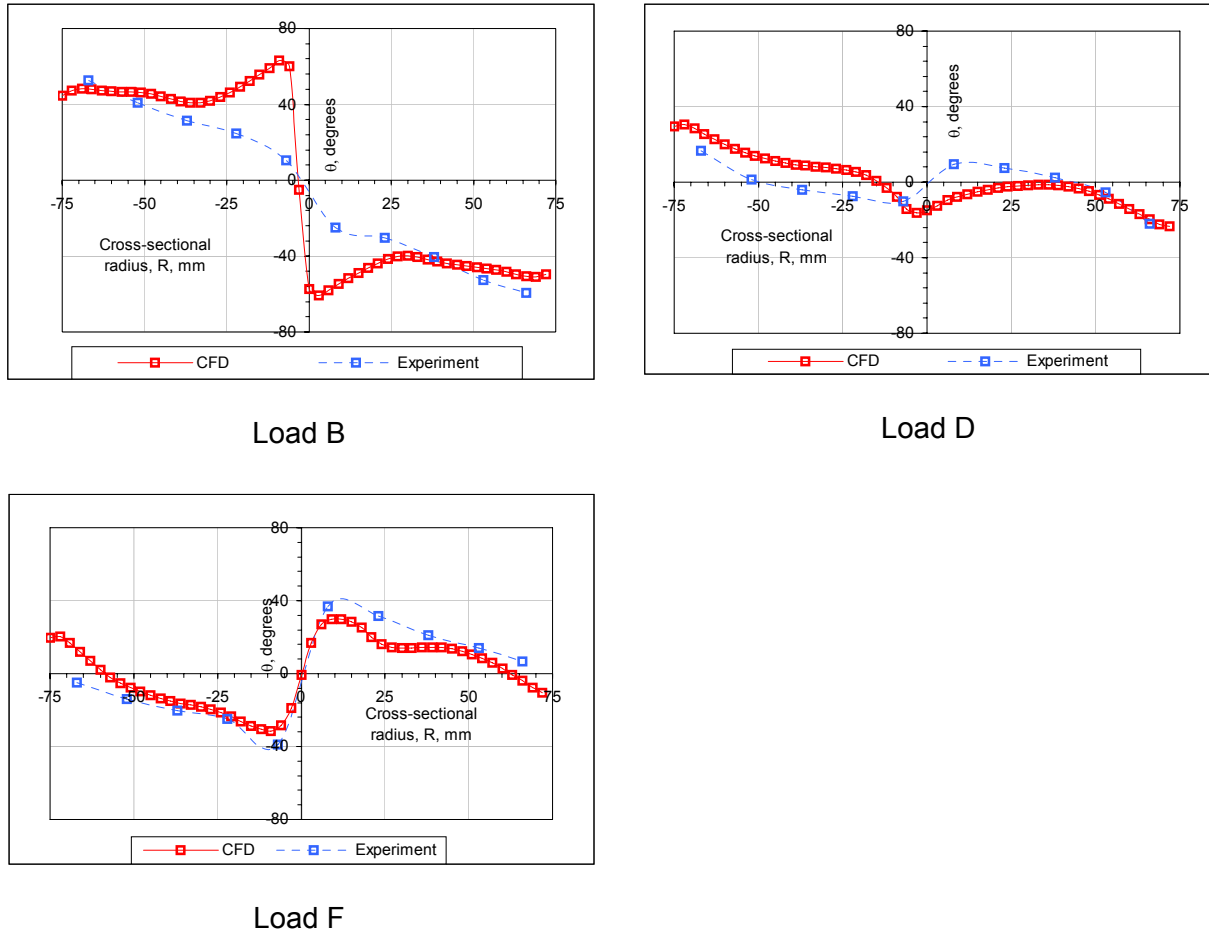

Load B

Load D

Load F

<u>Figure 4.17</u>, Comparisons of the CRA swirl profiles for the 39.7 rpm PAT at load B, D and F from Experimental and CFD approaches

At the BEP load 'D' there has been a considerable deviation between the two methods throughout the cross-section though there is good matching in the value of wall swirls. Also the CFD swirl profile is not as symmetric about the central axis compared to that of the experiment.

For the overload point there is a very good similarity in the main flow region with deviations restricted to only 5^0 to 8^0. However there appears to be considerable deviations at the wall conditions, which is over 15^0.

4.3.2   Summary of the Experimental - CFD comparisons

1. Deviations at BEP

The relative deviations at the experimental BEP of the various parameters for the PATs tested using both CFD and experimental methods are summarized in Table 4.27.

Table 4.27, Relative study at the BEP for the Experiment-CFD correlation on 24.5 rpm, 35.3 rpm and 39.7 rpm PAT

	24.5 rpm PAT	35.3 rpm PAT	39.7 rpm PAT	
			CRP	CRA
Head reduction	13.8%	12.9%	0.7%	1.9%
Power improvement	-16.8%	-23.8%	-4.4%	-6.2%
Efficiency rise	-2.8%	-10.6%	-3.1%	-3.8%

The deviations for both the stages of the 39.7 rpm PAT lies below 2% and 6% for both the head and power parameters respectively, which is an acceptable result. The predicted parameters for the 24.5 rpm PAT show an error of over ±14% for both head and power, while the 35.3 rpm PAT records a deviation of over -23% for the power parameter and +13% for the head parameter, which are essentially poor results. It is to be pointed out that only the magnitudes of the deviations are considered. The sign of the deviation has a significant physical meaning is also an issue of discussion.

It also found that the location of the individual BEPs obtained from CFD does not match well with the experiment for the PATs with respect to the discharge number (as seen in Table A7.1, A7.4 and A7.7, Appendix A). For the 24.5 rpm (Figure A7.1) and 39.7 rpm PAT (Figure A7.5 and 4.15), the BEP from CFD is found to occur in the part-load region of the experimental characteristics, while for the 35.3 rpm PAT (Figure A7.3) has its BEP prediction in the overload region. The deviations of the discharge numbers predicted at BEP are tolerable for the 24.5 rpm (3.5% deviation) and 39.7 rpm PAT (9% to 10% deviation), but for the 35.3 rpm PAT, the discharge number is displaced at least by 20% towards the overload region.

Wrong prediction of BEP can lead to many problems during system design (as will be discussed in Chapter 5 and 6).

2. Prediction of Physical conditions

The deviation in the predictions from the CFD model can be interpreted as a deviation in the prediction or calculation of the physical conditions of the PAT control volume, which comprises of variables like the net rotational momentum across the PAT impeller and individual zone losses of the PAT control volume, based on the procedure developed in section 3.1.3.1 and 3.1.3.4.2, Chapter 3. This procedure gives probability of deviations in CFD results.

In the 39.7 rpm PAT with the CRP stage (section A7.3, Appendix A) the deviation of the CFD prediction suggests that there are greater chances for the rotational momentum to be wrongly calculated, though the error in the determination of actual losses cannot be ruled out. The same PAT with CRA stage (section 4.2.1) also suggests a wrong determination of rotational momentum, but also gives evidences of miscalculation of losses in the various zones mainly towards the BEP region.

For the 35.3 rpm PAT (section A7.2, Appendix A), which displayed poor comparisons the behaviour of the power and head number suggests a greater probability of CFD predicting much lower rotational momentum compared to the experiment and a lower probability of errors in the prediction of the zonal loss distribution.

The deviations of the 24.5 rpm PAT (section A7.1, Appendix A) also suggests towards a lower determination of the net rotational momentum compared to miscalculation of hydraulic losses.

3. CFD model

The CFD model (as discussed in section B3.1, Appendix B) used for all the 3 PATs is nearly similar. All the PATs use the CFX.5 commercial code with standard k-ε turbulence model. There are minor variations in type of grid structure and the number of grid points selected. There are also small variations in the way of the boundary condition (Table B3.2, Appendix B). In that, for the 35.3 rpm and the 39.7 rpm PAT the mass flow rate is specified at the exit of the draft tube and the total pressure at the inlet of the PAT. However conversely for the 24.5 rpm PAT mass flow rate is imposed as the inlet boundary condition while static pressure is specified at the outlet of the draft tube. The differences in the CFD prediction with respect to experimental results may also remotely be associated with the application of the CFD model, which includes differences in the actual geometry and friction conditions assumed. However no verification procedures (post-results) for the CFD model for any of the PATs have been carried.

4. Uncertainties

There are many uncertainties associated with both the experimental and CFD methods. Section B5.2.1 deals in detail with the uncertainties concerning the comparisons of the experimental methods. With respect to the determination of leakage flow, the results in Table B5.5, section B5, Appendix B depict over ±3% deviation on the discharge scale for the 24.5 rpm PAT and the 35.3 rpm PAT, and only ±1.5% for the 39.7 rpm PAT at the respective BEP.

It is also seen from the determination of the overall uncertainty (including random and systematic errors) in Table A5.6, Appendix A that there are considerable uncertainties (±10%) associated with discharge measurement for the 24.5 rpm and 35.3 rpm PAT. While

for the 39.7 rpm PAT, the uncertainty on the discharge measurement is only ±1.6%. The uncertainties in discharge measurement can be compared with the deviations of the respective BEP estimation (on the discharge number scale in Table A7.1, A7.4 and A7.7). The -3.5% deviation (part-load) for the 24.5 rpm lies well within the uncertainty bands of ±9.6% (Table B5.6), while the –9% to –10% deviation (part-load) in the 39.7 rpm PAT lies outside the uncertainty bands (±1.6%, Table B5.6). The BEP dislocation for the 35.3 rpm PAT is over +20% (overload), which is definitely outside the ±10.2% experimental uncertainty (Table B5.6).

The deviations of the head and power scales (mentioned in Table 4.27) can be compared with the relative uncertainties for the same in Table B5.6. The obtained deviations for the head reduction (+14%) and power improvement (-17% to -24%) for the 24.5 rpm PAT and 35.3 rpm PAT are in no way compatible with the experimental uncertainties (which are less than ±2.1%, Table B5.5). For the 39.7 rpm PAT, the head reductions seem to be compatible, but the power improvements are way beyond the experimental uncertainties.

Though the efficiency rise values depicted in Table 4.27 lie very well in the maximum experimental uncertainties (Table B5.5), this has less significance as deviations on the head, discharge and power parameters are exceedingly large.

In a workout in section B5.2.2, Appendix B it has been pointed out that there exists a tremendous mismatch between the boundary discharge applied on the CFD model and the discharges calculated at the reference plane 'e' (using internal velocity-integration method in Table B5.7). Though it is not possible to exactly quantify the uncertainties in the CFD model, the deviations of discharges suggest possible errors within the model. This leads to the conclusion that the CFD is not error-free.

4.3.3   Optimization Stage IV – A Relative Study

This section compares the results from the experimental and CFD approaches independently relating to the effect of the casing eye rib. It combines results from section 4.1.1.4.1 and section B3.2.3, Appendix B.

1.   Head reduction line

Experiment	CFD
The greater head reduction in the part-load and overload region of Figure 4.9 and 4.10, which reveal that the CRA head curve is coming under greater influence from the rotational momentum effects.	The head reduction line of Figure B3.13 and B3.14 also demonstrate the identical trend of greater head reduction in the part-load region, but lower reduction in the overload region.

2.   Power improvement line

Experiment	CFD
Though rotational momentum has some influence on the CRA power characteristics, there is a stronger indication of major reduction of losses in the impeller control volume (from <u>Figure 4.9</u> and <u>4.10</u>) mainly in the BEP and overload region. This loss could be associated with position of rib being very close to the impeller interface zone '*v*'	The CFD results also shows an evidence of the improvement of hydraulics within the CRA impeller mainly in the overload region as seen in <u>Figure B3.13</u> and <u>B3.14</u> (Appendix A). However the rotational momentum effects are felt only in the part-load and BEP region with negligible influence in the overload region.

3.   Efficiency

Experiment	CFD
The CRA stage has shown a rise in the efficiency in the range of +1% to +1.8% in the BEP and overload region.	The CFD however shows only a rise in the range of +0.4% to +1.2% for the CRA stage.

Therefore both the experimental and CFD methods are independently suggesting similar kind of hydraulics within the PAT control volume, which is extremely positive and reinforcing result. This suggests that both the methods are justifying each other and at a relative scale they are able to sense small but identical changes within the hydraulics due to the absence of casing eye rib.

The identical effects sensed by both the methods are summarized below,

1. Greater influence of rotational momentum effects in the part-load region for the CRA stage.

2. Improvement of the impeller hydraulics in the BEP and overload region of CRA stage.

3. Decrease of the rotational momentum's influence towards the overload region and introduction of an additional loss component in zone *vi*, which is seen to rise for the CRA stage.

5. Theory of PAT Application

5.1 Background

5.1.1   Available PAT Application Methods

One of the most serious problems (as briefly mentioned in section 1.1.2 and 1.1.4 of Chapter 1) hindering the implementation of PAT technology is the inaccuracy and uncertainty with respect to the prediction techniques developed so far. Section B1 of Appendix B deals with the comparison of these prediction techniques with the experimental results, which shows inconsistency and mediocre conformity. All these techniques that are discussed in section B1 deal only with the evaluation of the 'best efficiency point' in turbine mode.

Very few methods have been developed that actually determine the entire turbine mode characteristics of a pump. Kittredge [28] developed the first of these methods using model characteristics of 4 pumps both in pump mode and turbine mode. His method was based on the assumption that two pumps of identical pump mode dimensionless characteristics would essentially have similar turbine mode characteristics. Kittredge himself agreed that a usual degree of accuracy should not be expected from these methods and extreme care should be exercised during interpolation. Subsequently Acre American Inc. [1] developed a computer programme essentially based on Kittredge's method in which a database of pump and turbine mode characteristics for specified number of pumps is loaded. This programme compares the known pump's characteristics with that of the proposed pump and provides an estimate of the turbine mode performance.

Williams [57] made a detailed review of both the Kittredge [28]'s and Acre American Inc. [1]'s methods. He suggested some changes to Kittredge's method, as it had not incorporated changes in pump mode efficiencies for the model and the proposed pumps. In the Acre American Inc. [1] he found some errors with respect to the scaling factors. Though Williams [57] found that Kittredge's method after correction gave more sensible solution he was not convinced of Acre American Inc. [1]'s methods as its predictions were completely out of range. He concluded that despite the complexity of these methods they hardly gave more accurate results compared to those obtained by the simple 'Best Efficiency Point' prediction methods. Williams himself developed a new method for PAT predictions based on the concept of Area Ratio defined by Anderson [3]. In that he evaluated the turbine mode performance at two points namely the shock free entry and swirl free exit, based on the geometrical relationship of the throat area to that of the net impeller flow area at turbine mode inlet. He also showed and claimed that the 'Area Ratio' method was more accurate than most of the methods published in the literature. However the concept of 'Area Ratio'

has not been validated further by other researchers and this concept remains an issue of controversy amongst pump designers and academia.

Cohrs [6] using his exhaustive and comprehensive equation developed for turbine mode head, power and efficiency respectively, demonstrated an extremely good resemblance between calculated and measured points. However the requirements for his model are tremendous in terms of the geometrical data and other constants. His model also evaluated the limiting operating conditions of the PAT namely the runaway, locked rotor (zero speed) and the starting torque conditions. His work also paved way for the development of another computer programme in collaboration with University of Hamburg-Harburg and Thyssen, applicable only for radial flow pumps of pump specific speeds in the range of 10 rpm to 50 rpm.

Therefore from the above considerations, any new development work on a prediction model of turbine mode performance should justify the cause. Evolving of a new theoretical model would make less sense. This is not only because of existing independent theoretical models by Williams [57] and Cohrs [6], but also due to fact that such models comprise of parameters that are subjected to practical uncertainties. Especially with the model developed by Cohrs [6], it has come to notice that it would need inputs like approximations of slip in PATs (which is still not correctly understood), assumptions related to internal impeller circulation (also uncertain), and other factors for leakage and disc friction.

5.1.2 The Cordier Diagram

With accurate experimental data available for over 8 PATs, it would make more sense to develop an overall selection cum performance chart based on principles of application in general turbo-machinery. One of the earliest and widely accepted approaches is that developed by the German engineer Otto Cordier [9] who brought all types of turbo-machines under a common platform, comprising of the interdependence of two dimensionless numbers, namely the specific speed number and specific diameter number. He displayed this complex interdependence on a chart, which became popularly known as the Cordier diagram. The Cordier diagram consists of plotting the BEP specifications of respective turbo-machines on a chart characterized by dimensionless specific speed as the ordinate and the dimensionless specific diameter as the abscissa. He did not make any distinction between machine types and included fans, pumps and blowers.

The data points were plotted on a logarithmic scale with constant head number ψ_c lines superimposed. Cordier showed that the loci of dimensionless specific speed σ and specific diameter Δ (both defined at BEP) for all machines followed a unique negative slope. Different classes of machines (radial, axial and mixed flow) occupied different regions of the loci.

The constants defined by Cordier need to be represented in terms of those constant used throughout the dissertation. The head number ψ_c and discharge number ϕ_c from Cordier's principle are represented as,

$$\psi_c = \frac{2gH}{u^2} = \frac{2}{\pi^2}\frac{gH}{N^2D^2} = \frac{2}{\pi^2}\psi \qquad (5.1)$$

$$\phi_c = \frac{4Q}{\pi D^2 u} = \frac{4}{\pi^2}\frac{Q}{ND^3} = \frac{4}{\pi^2}\phi \qquad (5.2)$$

Subsequently the specific speed number, σ and specific diameter number, Δ are represented as follows,

$$\sigma = \frac{\phi_c^{1/2}}{\psi_c^{3/4}} = \frac{\left(4/\pi^2\right)^{1/2}\phi^{1/2}}{\left(2/\pi^2\right)^{3/4}\psi^{3/4}} = 2^{1/4}\pi^{1/2}\frac{\phi^{1/2}}{\psi^{3/4}} \qquad (5.3)$$

$$\Delta = \frac{\psi_c^{1/4}}{\phi_c^{1/2}} = \frac{\left(2/\pi^2\right)^{1/4}\psi^{1/4}}{\left(4/\pi^2\right)^{1/2}\phi^{1/2}} = \frac{\pi^{1/2}}{2^{3/4}}\frac{\psi^{1/4}}{\phi^{1/2}} \qquad (5.4)$$

The relationship between the dimensionless specific speed and the SI definition of specific speed is given by,

$$\sigma = \frac{2^{1/4}\pi^{1/2}}{g^{3/4}\,60}\frac{NQ^{1/2}}{H^{3/4}} = 6.3383\times10^{-3}N_q \qquad (5.5)$$

5.2 Selection and Performance Charts

The development of the selection and performance chart for radial and mixed flow PATs is in accordance with the objectives (objective no. 6.i and 6.ii, section 1.2, Chapter 1) and problem outline (problem 2, section 1.3.2, Chapter 1) of the dissertation. The experimental results of both radial and mixed flow PATs are separately treated through Cordier principle (section 5.1), following which the overall selection and performance charts would be evolved.

5.2.1   Radial Flow PATs

In addition to the 7 radial flow PATs tested in the laboratory, 2 more radial flow PATs, namely a 21 rpm PAT and a 61.3 rpm PAT, have been considered for the selection and performance chart. The BEP results in turbine mode of the 21 rpm PAT from Singh et al[48] and a 61.3 rpm PAT from Warrilow [56] along with others PATs are summarized in Table B1.2 (Appendix B).

The turbine mode head numbers, ψ_t, and discharge numbers ϕ_t, of <u>Table B1.2</u> are reduced in terms of the Cordier coordinates, namely specific speed number, σ and specific diameter, Δ using Equations (5.3) and (5.4) respectively and plotted on the logarithmic scale of in <u>Figure 5.1</u>. It is seen that the loci of all the points is a straight line with a negative slope and lies between the loci of ψ_c = 1 and the ψ_c = 2 lines. The equation of the mean experimental line is given by,

$$\sigma = 1.2249 \, \Delta^{-1.2882} \qquad\qquad (5.6)$$

However this equation cannot be guaranteed for all radial flow PATs. It is therefore safer to set tolerance band for this mean line. The tolerance bands are set by varying the constant term (1.2249) of the Equation (5.6) and retaining the original slope depending of confidence levels. The constant displacement selected here in <u>Figure 5.1</u> is $\pm$ 8%.

The application of the Cordier diagram begins with the determination of the range of impeller diameters for given boundary conditions from site namely, head (H), discharge (Q) and operating speed (N). With given H, Q and N, specific speed number σ can be calculated from Equation (5.5). The intersection of σ with the mean experimental line and the tolerance bands gives the three specific diameters, namely Δ_{mean}, Δ_{lower}, and Δ_{upper} respectively. The dimensionless specific diameters can be reduced to absolute scale to get the range of impeller diameters (outer peripheral) to suit the given boundary conditions.
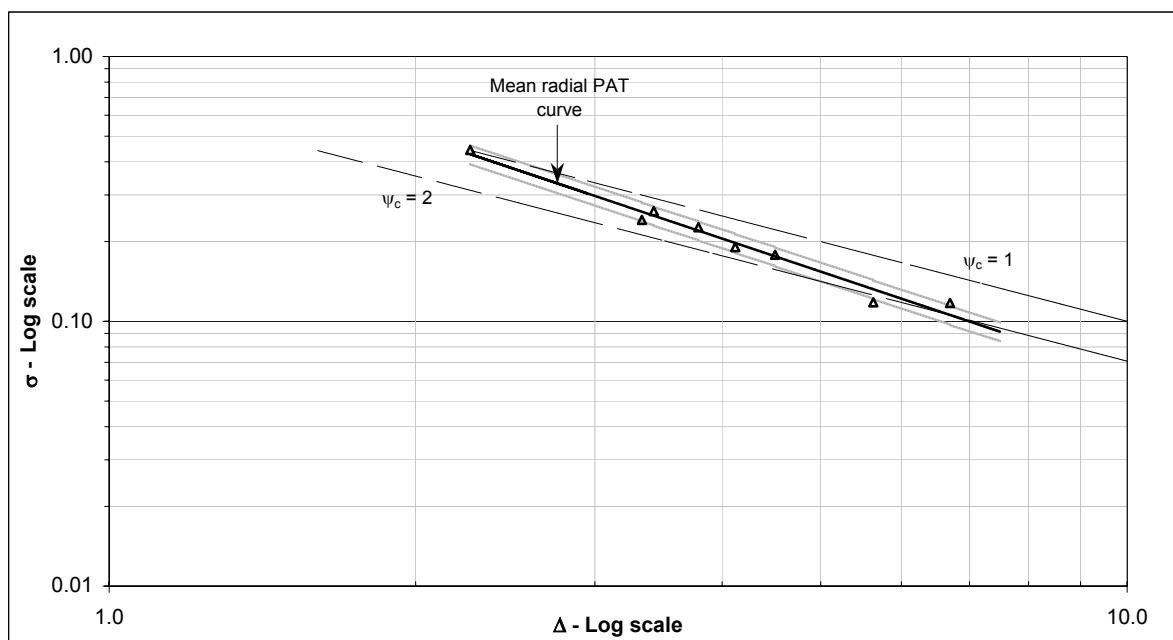

Figure 5.1, The Cordier line for radial flow PATs from experimental results

To proceed with the ultimate goal of first the selection and further the synthesis of the complete operating characteristics of the PAT an additional technique needs to be developed. Ensslinger [13] published the performance characteristics of 4 pumps of different specific speeds namely 33 rpm, 46 rpm and 78 rpm on the common abscissa of discharge number, Q/ND^3 and ordinates of head number, gH/N^2D^2 and efficiency, η. These pumps had identical blade angle and the corresponding dimensionless curves got distributed in a systematic pattern. Taking cues from Ensslinger's effort a new plot for experimentally tested radial flow PATs is presented in Figure 5.2 with ψ - ϕ curves and η - ϕ curves.

The pump specific speeds considered are 21 rpm, 24.5 rpm, 35.3 rpm, 36.8 rpm, 39.7 rpm, 45.2 rpm, 46.4 rpm, 61 rpm and 79 rpm PATs. This plot is representative only for the radial flow PATs whose diameter at the outer peripheral edge is constant (i.e. between the front shroud and read shroud). It is seen from Figure 5.2 that the there is a wonderful distribution of the ψ - ϕ curves, with the lower specific speed curves concentrated towards the left of the plot and for subsequent higher specific speeds the ψ - ϕ curves also move incrementally towards the right. The lower specific speed ψ - ϕ curves also posses greater slope compared to the higher specific curves. The individual PATs have different values of maximum operating efficiencies, which are more related to the size of the machine and the scaled hydraulics within it.

The loci of all the ψ and ϕ points defined at the BEP is also plotted in Figure 5.2, which is seen to follow trend of a power curve, however with a rather poor regression coefficient of 0.6. This result indicates the difficulty in obtaining the exact location of the BEP, i.e. the ψ_{BEP} and ϕ_{BEP}. It is also to be mentioned that all the PATs display high efficiencies on either side of the BEP covering a range of discharge numbers (i.e. on the part-load and overload region). It seen from the η - ϕ in Figure 5.2 that the range of peak operating efficiencies for higher specific speed PATs is much greater than for lower specific PATs. However it is reasonable to assume that the mean experimental trend line is the natural BEP for the PATs. Similar to the BEP line the no-load line is plotted, which also displays a reasonable fit. The no-load line is also used as a reference for building the characteristics of the PATs to be investigated.

The ψ - ϕ characteristics are enlarged and plotted separately in Figure 5.3. It also shows the plots of tolerance bands for the $(\psi$ - $\phi)$ $_{BEP}$ trend line on the part-load and the overload sides respectively. The no-load line has also been plotted along with its respective tolerance bands. The pump mode and turbine mode specific speeds are mentioned on the respective curves. Some characteristic features of the plot are illustrated below.

1. The ψ - ϕ curves for the 35.3 rpm and 36.4 rpm PATs are considerably displaced from each other even though their specific speed suggests that they have identical geometry and characteristics.

2. The ψ - ϕ curves for 45.2 rpm and 46.4 rpm PATs intersect each other and don't display the behaviour of incremental patterns.

3. It is also interesting to point out that the turbine mode specific speeds for the 21 rpm and 24.5 rpm PATs are identical ($N_{q\,t}$ - 18.5 rpm and 18.6 rpm respectively) but their ψ - ϕ characteristics are considerably displaced and diverging. This is due to the large variation in the head number and discharge numbers at the respective BEP points.

The above features suggest that the parameter, specific speed, either the pump mode or the turbine mode cannot be blindly used in obtaining and generalizing the characteristics of a new PAT. The specific speeds are no doubt helpful but at the most they can be used as a reference to make early assessment. The Figures 5.2 and 5.3 are together called the selection and performance chart for radial flow PATs. These charts are the secondary stage of the application after initial calculations from the Cordier diagram have been carried out.
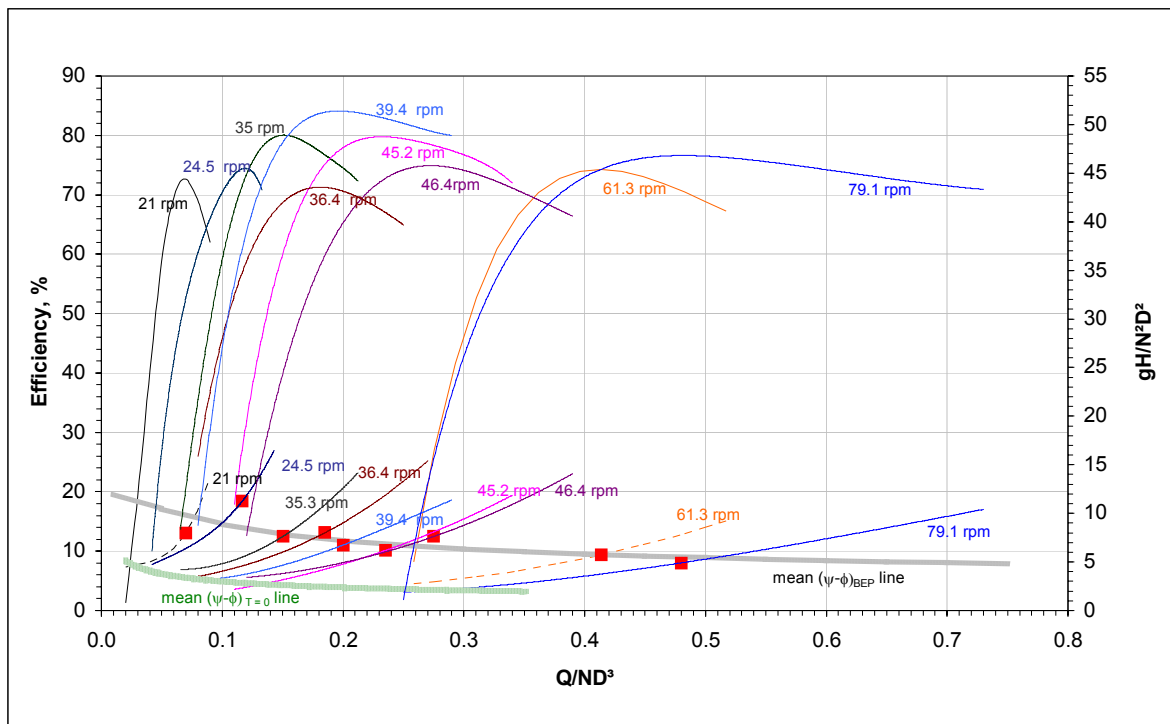

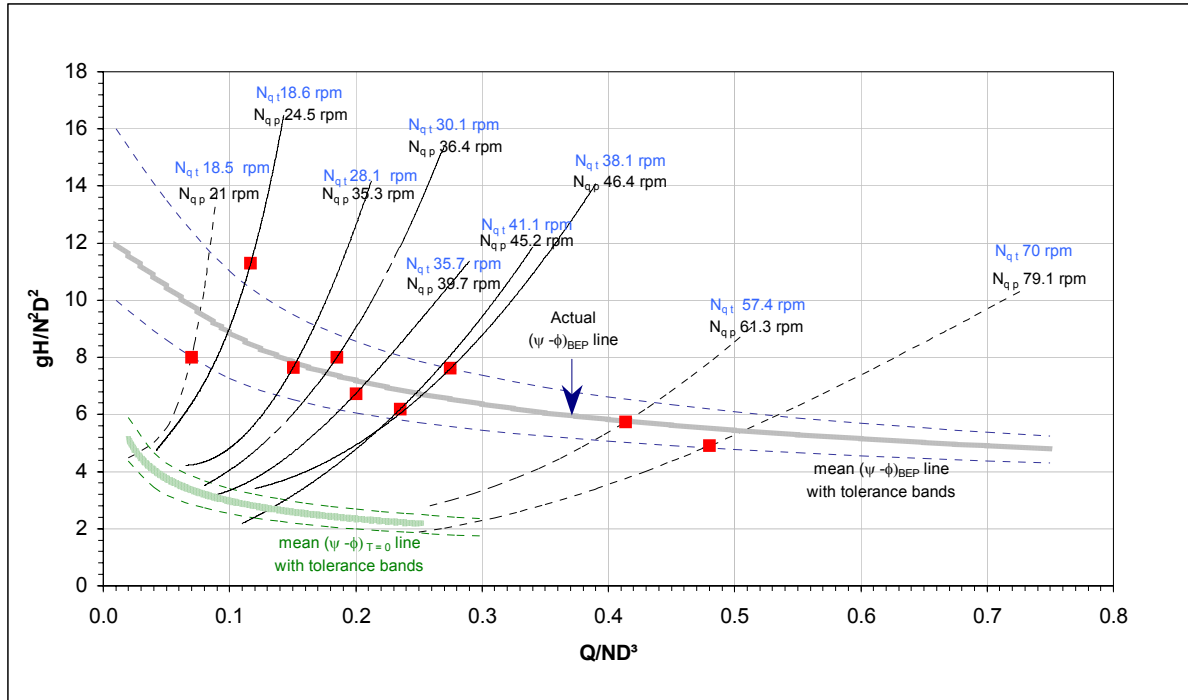Figure 5.2, Overall Selection and Performance chart of radial flow PATs

Figure 5.3, Overall ψ-ϕ chart of radial flow PATs with mean BEP and no-load line

5.2.1.1 Procedure for Selection and Synthesis of Characteristics

Step 1: Diameter Selection

The Cordier diagram as seen provides a range for the reference diameters (synonymous to D_1 - Table 3.1, Chapter 3) of the PATs that would probably suit the site boundary conditions. With this range available the pump manufacturers catalogue should be referred and the nearest diameter that lies within this range preferably nearer to the mean diameter should be selected. Once the tentative selection of the diameter of a standard pump is done, there is a two-fold procedure that needs to be carried out.

1. To find out if the selected pump would perfectly suit the head and discharge conditions.

2. And if the selected pump clears the above condition test then the synthesis of the complete characteristics needs to be done.

Step 2: Range of Specific Speeds (operating speeds)

With the selected diameter, the specific diameter Δ, can be determined whose value gets frozen for the entire calculation programme. The intersection of the Δ line with experimental PAT line of Figure 5.1 along with the tolerance bands gives 3 specific speeds namely, the mean specific speed σ_{mean}, the lower specific speed σ_{lower} and the higher specific speed σ_{upper}. For each of these specific speed numbers, 3 different operating speeds (N in rpm) can

be obtained. The SI units of specific speeds, N_q (from Equation (5.5)) can be subsequently obtained which also gives a fair idea of what kind of turbine is needed.

Step 3:   Range of Head numbers and Discharge numbers
The next important calculation is the determination of the head number, gH/N^2D^2 and discharge number, Q/ND^3 for the given boundary conditions of design head (H) and design discharge (Q) respectively along with the selected reference diameter (D) and the three operating speeds (N) from <u>step 2</u>. These are called the 'boundary' numbers.

The 3 different head number and discharge number combinations (mean, lower and upper) become important parameters of subsequent analysis. The intersection of the mean head number line with the mean BEP line (in <u>Figure 5.3</u>) will lead to the approximate operating discharge number for the selected PAT. This discharge number is referred to as the 'required' discharge number.

Step 4:   Suitability of the selected PAT
The next step is to verify if the given PAT hydraulics suit the boundary conditions. There are two requirement criteria to be evaluated. It is necessary for both the criteria to be approximately satisfied.

1. Boundary discharge to be fully utilized
The 'required' discharge number for the PAT is now compared to the mean 'boundary' discharge number for conformity. In general the mean 'boundary' discharge number should be never go under-utilized. This is only a preliminary verification.
The lower and upper boundary discharge numbers are used only as a reference range and cannot be directly compared to the 'required' discharge number.

2. Verification of head and discharge ratios between turbine and pump modes
This stage involves the approximate determination of the required range of turbine mode-pump mode head (ψ_t/ψ_p) and discharge ratios (ϕ_t/ϕ_p) for the selected PAT. The selected ratios should necessarily ensure that the PAT would at least operate in the overload region if not the ideal BEP point. The given PAT needs to be studied with respect to the various model PAT specifications illustrated in the section B1, Appendix B. This is a very crucial verification and it does not serve the purpose to compare the specific speed alone. The other parameters of pump mode, namely discharge number and head number (both at BEP) also need to be compared. It is also worthwhile to check the pump mode efficiencies, and the relative sizes of the selected and model PAT for future synthesis operation.
The outcome of this procedure is to obtain the range of head ratios and discharge ratios with reasonable confidence.

Step 5:   Selection of the final operating point, ψ_t and ϕ_t
This step deals with the selection of the BEP, with a certain degree of freedom. However the

final selection needs to be made after evaluating all perspectives and using proper discretion.

In this step, the calculated 'boundary' head and discharge numbers (step 3) are plotted on the selection and performance chat in Figure 5.3. This helps to locate the approximate region in the Figure 5.3 where the real PAT characteristics would be located. The respective head ratios (ψ_t/ψ_p) and discharge ratios (ϕ_t/ϕ_p) from the three boundary conditions are compared to the corresponding ratios for the selected pump proposed in step 4. During the evaluation it is also necessary to bring in the 'required' discharge number from step 3 independently. All these criteria should be thoroughly contemplated and the final design head number (ψ_{BEP}) and discharge number (ϕ_{BEP}) at the BEP should be fixed.

It may not be possible to satisfy all the conditions, but the objective is make a solution nearest to the conditions. It may be sometimes a compromise.

Step 6: Synthesis of the complete operating characteristics

The first step in determining the overall characteristics is the shape of the ψ - ϕ curve for the given PAT. The ψ - ϕ curve is essentially on the Figure 5.3 drawn by freehand passing through the fixed points ψ_{BEP} and ϕ_{BEP} (from step 5). Care should be taken in selecting the slope of curve, which should be similar to the slope of the ψ - ϕ curve of the geometrically similar PATs situated in the vicinity of the selected PAT's BEP. The curve is drawn from the proposed no-load line (Figure 5.3) proceeding through the above best efficiency points and extended into the overload region up to a reasonable extent corresponding to that of the other PATs.

Once the ψ - ϕ characteristic line is drawn, the second sep is to synthesis the efficiency curve. The efficiency line is also hand drawn between the limits set, namely, the no-load point where efficiency is 0%, the BEP where efficiency is maximum and the overload limit where the efficiency takes a decreasing trend. It is necessary to fix the correct value of the efficiency at the BEP for the PAT under investigation. This value is selected based on geometrical consideration and approximate size of the PAT in comparison with the respective model machines described in section B1, Appendix B. It will also be useful to verify the pump mode efficiencies of the PAT to arrive at the valve of the BEP in turbine mode. To be on a safer side a slightly lower value of efficiency can be assumed. The efficiency curve is sketched following the loci of the other PAT efficiency curves, which essentially are seen to be following a systematic trend in Figure 5.2. In the overload region the decreasing slope of the efficiency curve should be adjusted with respect to the slope of the other efficiency curves and considering size/geometric factors.

With the construction of the ψ - ϕ and the η - ϕ characteristics the machine's complete behaviour on a dimensionless scale is essentially fixed. The power characteristics can be eventually evaluated from the head and efficiency characteristics. However these are only mean synthesized characteristics and are subjected to uncertainties discussed below.

Step 7: Uncertainties

Though the above method of laying out the characteristics is based on the conventional principles, there are a number of uncertainties mainly related to the slope selected of the ψ - ϕ curve, the shape of the η - ϕ curve and the value of BEP assigned. There are also uncertainties within the Cordier diagram analysis for the experimental PAT line though the tolerance bands have dealt with this level of uncertainty. The reference data for the model machines also suffer from uncertainties. To add to these there are many uncertainties associated with pump design parameters like, the volute design, impeller blade angles, clearance between stationary and rotary systems, blade number, impeller eye and casing eye geometries. The relative influences of these uncertainties may not be possible to be directly determined. Therefore to cover all these uncertainties it is necessary to establish fresh tolerance bands for this mean ψ - ϕ synthesized curve.

The uncertainty bands are obtained by simply shifting the mean ψ - ϕ and the η - ϕ curve along the abscissa by a constant '$\Delta\phi$'. This value of $\Delta\phi$ depends on the respective confidence levels, however it is recommended to have this value to equal to $\pm$ 5% to $\pm$10% of the ϕ_{BEP}. The values of the, ψ and η do not change with corresponding, $\phi_{Lower} = \phi + \Delta\phi$ and, $\phi_{Upper} = \phi - \Delta\phi$. This results in the formation of the two parallel bands across the mean ψ - ϕ curve and the subsequent displacement of the η - ϕ curve. This technique is very relevant and makes the synthesis method more realistic and complete.

Step 8:   Muschel characteristics

Muschel characteristics are the total characteristics of a machine which comprises of the constant speed curves, constant efficiency curves, constant output curves and no-load line and zero-speed line (locked rotor) plotted between the abscissa of absolute discharge and the ordinate of absolute head. Muschel characteristics are developed based on the mean ψ - ϕ and η - ϕ curves.

Step 9:   Final selection of operating speed

The system resistance line or the site curve is integrated on the muschel characteristics to evaluate all possible operating points. Intensive studies from both the optimum hydraulic conditions and load transmission criterion needs to be carried out in tandem along with the boundary head and discharge conditions, to determine the most suitable speed of operation.

Step 10:   Uncertainty analysis at design speed

At the final selected speed it is necessary to evaluate the range of the variation in terms of discharges, operating heads and output powers. This is obtained by integrating the system resistance line with the single speed characteristics and its respective tolerance bands. The range of operating parameters should be verified with the guaranteed specifications of the PAT power output. If they the deviations are outside the allowable tolerance limits, the selection of the PAT may have to be redone.

If the economics of the project allow, the testing of the selected PAT could be done to determine the actual characteristics.

5.2.2   Mixed Flow PATs

The mixed flow PATs that have been considered for the selection and performance chart are the 94.4 rpm PAT (tested during the dissertation course) and 72.8 rpm PAT (test report from Kirloskar [24]). The details (i.e. ψ_t and ϕ_t) at the BEP for these two PATs are summarized in Table B1.2 (section B1, Appendix B).

The dimensionless specific speed, σ and dimensionless specific diameter, Δ defined at the BEP conditions are determined from Equation (5.3) and (5.4) and plotted on the Cordier diagram in Figure 5.4. It is seen that one of the points lies outside the $\psi_c = 1$ line and other between $\psi_c = 1$ and $\psi_c = 2$ lines. Though two points are not enough to determine the mean trend line for this class of PATs, a representation is made based on the following equation.

$$\sigma_{mf} = 3.1091 \Delta_{mf}^{-2.1091} \tag{5.7}$$

The slope of this mean trend line (m = -2.1091) is much greater than the slope of the constant head number, ψ_c (m = -1.0) lines. Two tolerance bands are also plotted similar to the procedure in radial flow PATs in section 5.2.1.

The selection and performance chart for the mixed flow PATs is plotted in Figure 5.5, with gH/N^2D^2 and η as the ordinates and the Q/ND^3 as the abscissa. The trend line joining the ψ_{BEP} and ϕ_{BEP} points for the two PATs along with the upper and lower tolerance bands representing are plotted in Figure 5.5. The loci of the two no-load points are also plotted.

The Figure 5.5 signifies the behaviour of series of mixed flow PATs only and the reference diameter used in the calculation procedure is the greater of the two diameters at the turbine mode inlet (as described in Table 3.1, Chapter 3)
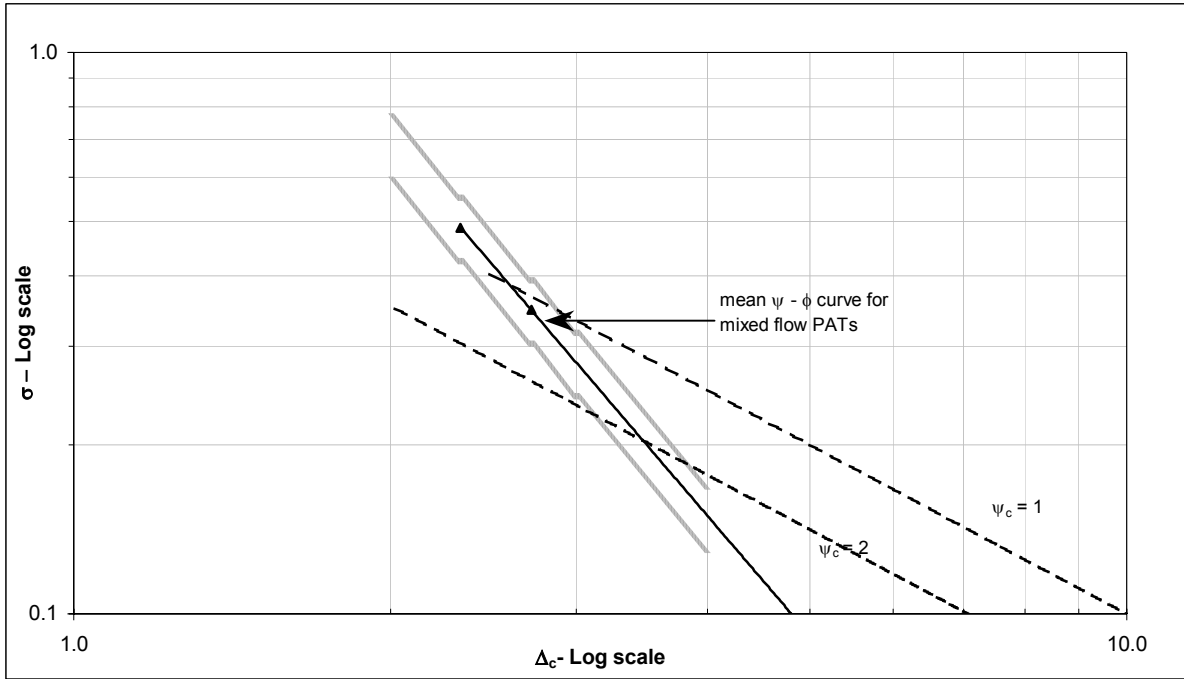
Figure 5.4, The Cordier line for mixed flow PATs from experimental results

5.2.2.1 Procedure for Selection and Synthesis of Characteristics

The selection of a suitable mixed flow PAT to suit site boundary conditions and synthesis of the characteristics is carried out based on the identical procedure illustrated for the radial flow PATs (in section 5.2.1.1).
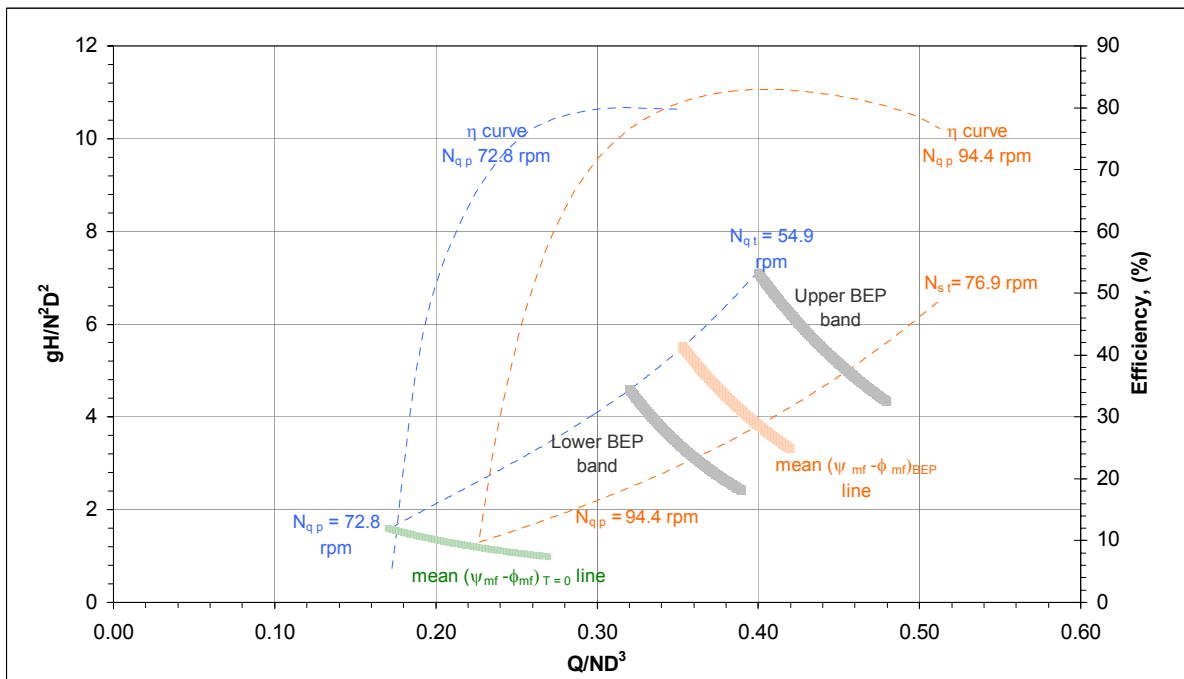

Figure 5.5, Overall Selection and Performance chart of mixed flow PATs

5.3 Four Quadrant Analysis of Pumps

The four-quadrant analysis of pumps needs to be discussed in pursue of the objectives of handling runaway problems (objective no. 6.iv, section 1.2, Chapter 1) and some issues concerning the optimization of the system design (problem 3, section 1.3.3, Chapter 1). The introduction to the four-quadrant representation of pump characteristics is elaborately dealt in section A8.1, Appendix A. The accepted sign convention used in these charts along with those operating quadrants that are of specific interest to a micro hydro application scenario are also discussed in section A8.1.

5.3.1　　Radial Flow Pumps

Stepanoff [52] presented the complete characteristics of a radial flow pump tested by Knapp [29] shown in Figure 5.6. The lower half of the diagram (Figure 5.6) with negative speed ordinate signifies the turbine mode operation. The quadrant formed by –Q abscissa and –N ordinate is the one applicable to the micro hydro PAT. The constant head curves intersect the –Q abscissa at discharge greater in magnitude than the discharge when it intersects the no-load, T = 0 line. The H = 0 line (locked rotor) is formed between the +Q and –N.
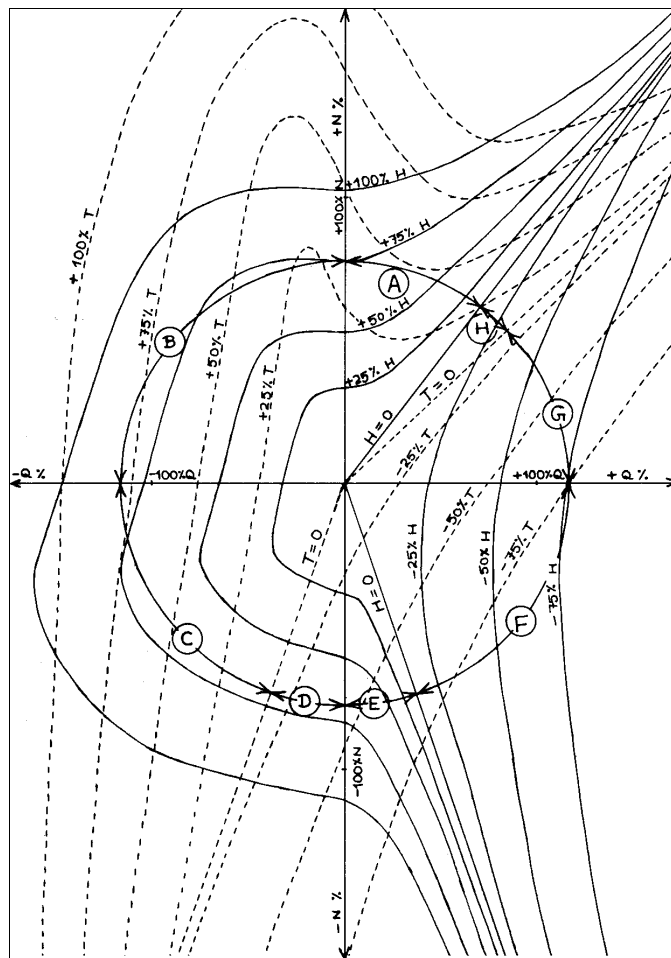

Figure 5.6, 4-quadrant characteristics for a medium specific speed radial flow PAT

Transposing the behaviour of the characteristics in this quadrant into the H-Q co-ordinate system in Figure 5.7 (note the sign convention is based on turbine mode operation), it is seen that the no-load line, T = 0 displays an exponential behaviour with greater slope with respect to the discharge abscissa as compared to the zero-speed line, N = 0. The constant speed curves begin from the no-load line and extend with increasing heads and discharges asymptotically to the zero-speed line. The field of constant speed curves generally lies between the T = 0 and N = 0 lines.

In the quadrant D, it is seen that at Q = 0, that the operating head is positive but smaller than the head at the T = 0 line. Therefore for radial flow PATs the constant speed curves fall backwards towards the ordinate axis (Head).

No-load line, T = 0

The no-load line signifies the runaway characteristics for the radial flow PAT. The movement from a load condition (positive torque) in quadrant C towards the T = 0 line is more often characterized by increasing heads and decreasing discharges along with the natural increase of speed. However this movement needs to be studied along with the system resistance curve for a given site.
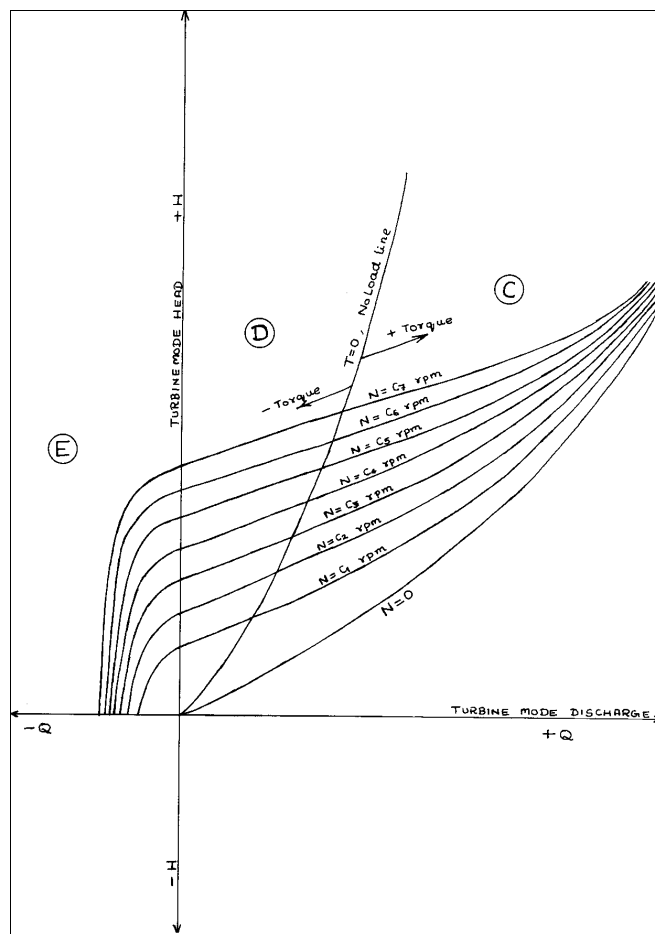

Figure 5.7, Quadrant C, D and E for a radial PAT on H-Q co-ordinates

5.3.2   Mixed Flow Pumps

Mixed and axial flow PATs show more or less an identical behaviour as reported by Stepanoff [52]. Figure 5.8 displays the 4-quadrant characteristics of a typical mixed flow pump. The quadrant of micro hydro PAT is formed as usual between the –Q abscissa and the – N ordinate. An important and characteristic behaviour observed is that the constant head curves intersect the N = 0 line at a discharge much lesser in magnitude compared to the discharges at the intersection with the H = 0 line. Another feature of the mixed flow PAT is the characteristic behaviour of the N = 0 line and the T = 0 line. The no-load line T = 0 has a much smaller slope with the discharge abscissa and the H = 0 line is placed in the same quadrant (i.e. between the –Q abscissa and the –N ordinate). These behaviours are distinctly different from that of the radial flow PAT.

Due to the above changes the plot of the characteristics in the H-Q co-ordinate system is totally different from normal radial flow characteristics (seen in Figure 5.7). The H-Q plot for the mixed flow PAT in Figure 5.9 shows that the T = 0 line has a much smaller slope with respect to the discharge abscissa compared to the N = 0 line. (An effect completely opposite to that of the radial flow PAT).
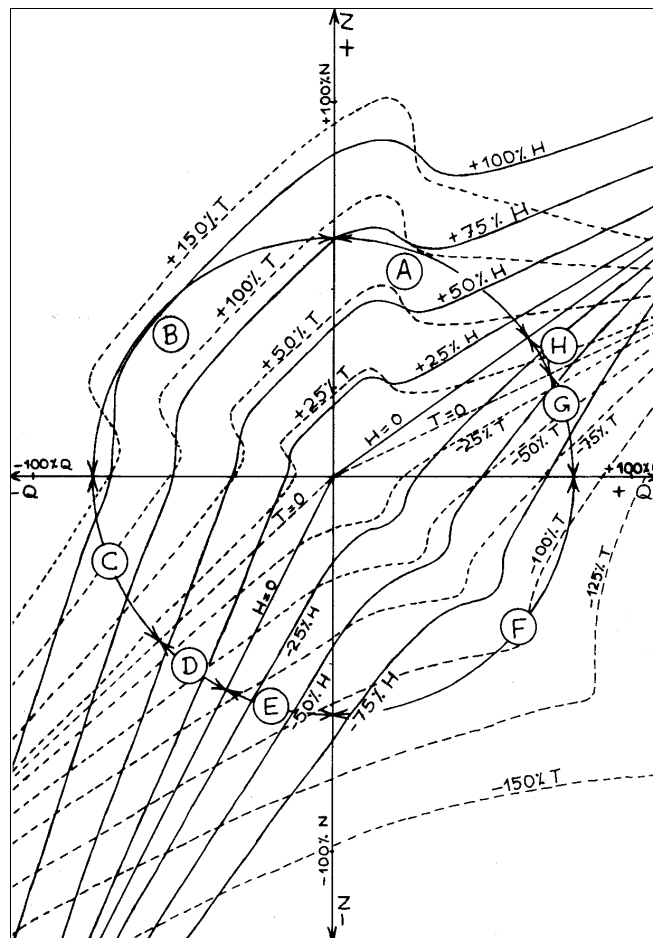
Figure 5.8, 4-quadrant characteristics for a mixed flow PAT

The constant speed curves as usual originate from the no-load line and proceed into the quadrant C with rising slope compared to the T = 0 line. The quadrant D for the mixed flow PAT (which is bound by the T = 0 line and the H = 0 line) translates on the H-Q quadrant as the region between the T = 0 line and the Q abscissa. Therefore the constant speed curves move backwards towards the Q abscissa and intersect the H = 0 line at a fixed magnitude of discharge.

The constant speed curves move further below the abscissa and cut the –H ordinate at fixed values which forms the quadrant E. Further the movement of the constant speed curves takes the PAT into zone F.

No-load line, T = 0

The shift of the operating point from a load condition to the no-load (T=0) line, as seen from Figure 5.9 causes a decrease in operating head but a rise in the discharge capacities within the PAT. However the speed shows its natural behaviour and tends to increase. The exact behaviour can be determined only with the help of system resistance curve of a given site.

The movement of the operating point towards the no-load line for a mixed flow PAT is distinctly different from that of a radial flow PAT.
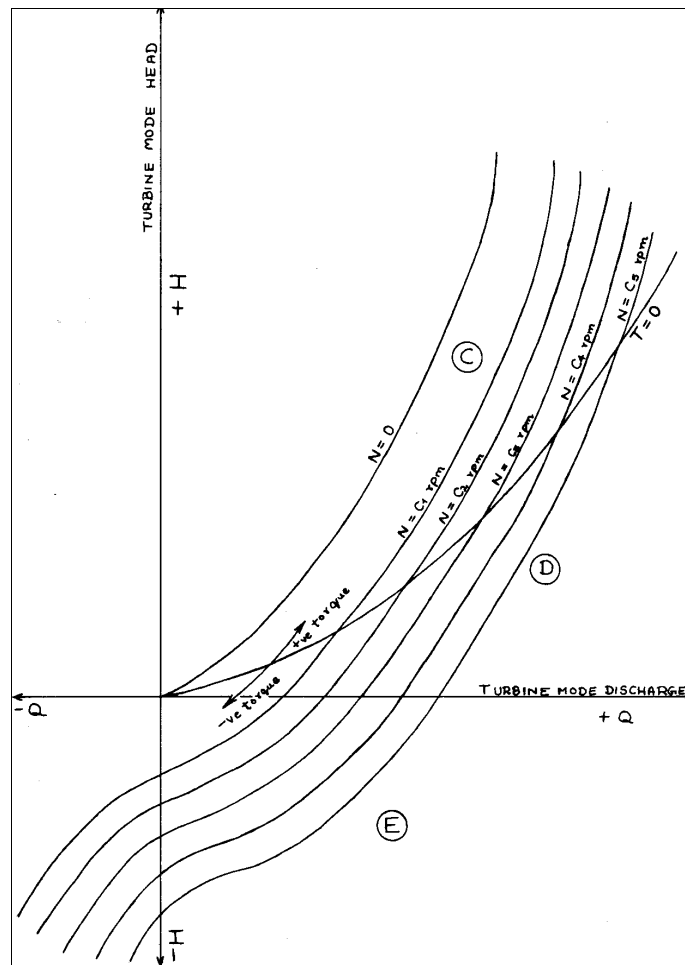

Figure 5.9, Quadrant C, D and E for a mixed flow PAT on H-Q co-ordinates

5.4   Runaway Problems in PATs

It is seen from the 4-quadrant analysis that there are different behaviours for the runaway conditions in radial flow (Figure 5.7, and section 5.3.1) and mixed flow (Figure 5.9, and section 5.3.2) PATs respectively. The behaviour in radial flow PATs is more dangerous as the runaway is essentially associated with increase of operating head on the PAT compared to the actual operating head when it is in load condition. The rise of head is dependent on the design of the pump and the extent of devastation depends on the operating and system characteristics. Nevertheless the sudden change in the flow due to runaway will initiate the water hammering in the penstock. Quick operation of the valve will further complicate the water hammering effects and can have fatal impacts on the penstock and civil structures near the powerhouse. Added to the penstock problems, runaway conditions are accompanied by rise of operating speed. The speed rise is once again associated with the PAT characteristics and also the system boundary conditions. The mechanical problems associated with shaft, bearing and other rotating components at higher speeds needs to be verified.

The mixed flow PAT on the other hand shows a drop in the operating head at runaway conditions, which therefore will not result in pressure surging in the penstock. This is great advantage unlike the radial flow runaway condition. However the runaway condition in the mixed flow PAT will be accompanied by increasing speeds which would have identical mechanical problems and would entail verification.

Therefore whatever be the PAT, the machine needs to be brought to safe operating speeds within short time duration.

5.4.1   Handling of the Runaway Condition

The methodology of handling the runaway and associated problems in micro hydro projects based on both the radial flow and mixed flow PATs is crucial design feature. Especially for the radial flow PATs, which have pressure surging problems the design becomes more a challenging. Though the intention is to have a foolproof design, it may not be all that easy. Following are few methods proposed to handle runaway problems in PAT systems.

5.4.1.1   Forebay Valve

This is an ideal option but may not be easy for manually operated plants because the distance to be covered may be large. An automatic system to operate this valve can also be considered, but the economics may not necessarily justify this option.

5.4.1.2 Mechanical Braking

This option helps to restore the operating speeds of the machine to safe limits. A manual brake or even an automatic system, if the economics allow can be considered. But this option will not be able to handle the hydraulic conditions within the penstock. The mechanical braking without reducing the inlet head on the PAT will lead to problems with overloading as understood from the 4-quadrant analysis.

5.4.1.3 Closed Bypass Design

This design comprises of the installation of a bypass line across the main inlet valve to the turbine. The main purpose of this closed bypass design is mainly to assist the startup, where it ensures that the slice type valve (used as the main inlet valve) opens with no pressure difference across it. Following a runaway condition the bypass valve is first opened and subsequently the main inlet valve is closed. The bypass valve is later closed to eliminate any possible discharge. This methodology only ensures valve safety, but only marginally handles the pressure surges and associated problems.

5.4.1.4 Open Bypass Design

The open bypass design is the chief method presented in the dissertation to handle runaway conditions in PATs. This method not only helps in controlling the pressure surging conditions but also balances the speed conditions on the electro-mechanical machinery. This method comprises of installing a simple open bypass with one end connected to the main penstock line and other end open to the atmosphere. In short the operation consists of opening the bypass valve fully in case of runaway situation. The open bypass must essential have the least possible hydraulic resistance to allow maximum discharge. The increased flow through the bypass reduces the pressure in the penstock line. This reduction of the pressure should not only prevent the excessive pressure surging to occur but also restores the operating speed of the PAT unit. The main inlet valve is subsequently closed after the machine has reached safe operating conditions.

The design features, which is dealt in detail comprises of hydraulic design, bypass valve characteristics and the governing boundary conditions.

5.4.1.4.1 Hydraulic Design

The hydraulic design comprises of accurately determining the hydraulic resistance of different components of a typical micro hydro system, namely

Main penstock line

This comprises of the piping section from the forebay tank and the junction point (before the bifurcation to the bypass and turbine manifold line).

Bypass line

This line comprises of section between the junction point and the atmospheric exit and is inclusive of the valve.

Turbine manifold line and Draft tube

All components between the junction point till the turbine inlet and entire draft tube section.

PAT runaway line

The hydraulic resistance of the runaway line is an important input parameter to be determined. This needs to be represented as a function of discharge and can be obtained from the muschel characteristics of the PAT explained in section 5.2.

In the event of the bypass valve getting fully opened, the main flow Q divides into Q_{PAT} and Q_{bypass}. Therefore the first governing equation is given by,

$$Q = Q_{PAT} + Q_{bypass} \tag{5.8}$$

Series of equations are obtained by applying the Bernoulli's between the various sections. The first section considered is between the forebay tank and the junction point.

$$\frac{p_{junction}}{\rho g} = z_{junction} - h_{L\,penstock} - \frac{v^2_{junction}}{2g}$$

$$\frac{p_{junction}}{\rho g} + \frac{v^2_{junction}}{2g} = z_{junction} - K_j Q^2 \tag{5.9}$$

The second section is between the junction point and the bypass exit.

$$\frac{p_{junction}}{\rho g} + \frac{v^2_{junction}}{2g} + z_{bypass} = \frac{v^2_{exit\,bypass}}{2g} + h_{L.bypass}$$

$$\frac{p_{junction}}{\rho g} + \frac{v^2_{junction}}{2g} = \frac{v^2_{exit\,bypass}}{2g} + K_{bypass} Q^2_{bypass} - z_{bypass} \tag{5.10}$$

The third section is between the junction point and the draft tube exit.

$$\frac{p_{junction}}{\rho g} + \frac{v^2_{junction}}{2g} = \frac{v^2_{exit\,PAT}}{2g} + \left(K_{PAT} + K_{runaway}\right) Q^2_{PAT} - z_{PAT}$$

$$\tag{5.11}$$

The ratio of the Q_{PAT} and Q_{bypass} can be obtained by solving the Equations (5.10) and (5.11). There are two conditions with respect to the input discharge that need to be considered for the behaviour of the bypass.

1. Unlimited Input Discharge – Q

The first condition is with respect to discharge Q, which becomes temporarily unlimited through a huge capacity of the forebay tank. This is the general condition in all micro hydro plants, where unlimited conditions need to be assumed. This condition is the worst condition and the safety design should be based on this. This discharge Q can be obtained by substituting the discharge ratio in Equation (5.8) and solving Equation (5.9). Subsequently the individual discharges through the bypass and the turbine are obtained. The runaway conditions of the PAT, namely the speed and operating head, can now be evaluated based on the Q_{PAT} flowing through it from the muschel characteristics.

2. Limited Input Discharge – Q

The second condition consists of limited input discharge, Q, which occurs in micro hydro plants with minimum forebay tank capacities and run off the stream situation. The individual discharges through the PAT and the bypass lines are evaluated from equation (5.8). The discharge ratio found earlier does not change for the limited input discharge condition. With the given discharge through the PAT, the no-load speed and operating head can be obtained.

The PAT runaway speed calculated from the above procedure should be essentially below safe running speeds for the all the machines. Another consideration should be with respect to the pressure condition within the penstock. The objective is to bring down this pressure to prevent any kind of surging.

5.4.1.4.2   Bypass Valve Characteristics

The selection of the bypass valve should be based on several factors like the total time of operation, cavitation characteristics of the valve, mechanical considerations like starting and operating torque and finally the overall valve stability. Since the bypass valve operation is one time-full opening, simple valve solutions like gate/sluice valve and butterfly valves can be adopted. The butterfly valves in certain boundary conditions (greater pressure difference) may need high operating torques to open, which may be replaced by sluice valves that can be opened with reasonable levels of torques but have disadvantages of long opening and closing times.

However the poor cavitation characteristics of simple valve types can also pave way for more complicated solutions like needle discharge valve and jet/cone discharge valves. These valves have cavitation free operation and are also simple to control, but extremely expensive.

5.4.1.4.3   Operating Boundary and Limiting Conditions

As in the analysis of the open bypass, the input boundary system conditions like system head, discharge and output boundary conditions essentially comprising of the machine specific runaway characteristics play a decisive role in the design for runaway condition. The limiting conditions like the strength of the penstock and other joints to withstand pressure surging and mechanical damage caused by speed rise needs to be meticulously assessed.

It is recommended to incorporate the open bypass design for micro hydro power plants based on both radial flow and mixed flow PATs.

5.5 D Quadrant Operation of PATs

The D quadrant analysis of a PAT becomes a very significant issue of consideration during complex system design when two PATs are mechanically coupled to each other (problem 3, section 1.3.3, Chapter 1). It is seen from Figure 5.6 and 5.8 (section 5.3.1 and 5.3.2) that the operation in the D quadrant occurs when the PAT is rotating dry (in air) and positive discharge from the penstock line comes into contact with this running impeller (in context of micro hydro scenario). With positive net head across the turbine and flowing discharge, the PAT becomes a net energy dissipater. Both radial flow (Figure 5.7) and mixed flow (Figure 5.9) PAT are seen to display different types of behaviours in the D quadrant, but in principle there are negative torque effects common to both the types of machines.

In radial flow PATs from Figure 5.6 and 5.7 for constant speed operation, the torque continuously increases in the negative direction, beginning from the T = 0 line till the –N ordinate (Q = 0 line) where the quadrant D ends. Though the negative torques increases further into quadrant E, the behaviour here is not relevant in the micro hydro scenario. Therefore the maximum negative torque condition corresponds to Q = 0 line. Also on the Q = 0 line, the magnitude of the negative torque increases with rise of turbine speed.

On the other hand the mixed flow PAT operating at constant speed, as shown in Figure 5.8 and 5.9, the torque continuously increases (in the negative direction) from the T = 0 line till the H = 0 line where the quadrant D ends. The constant speed curve is seen to enter the quadrant E, below the H = 0 line with the negative torques increasing further. The maximum negative torque occurs along the Q = 0 line for a given speed. Both the quadrants D and E are relevant in the micro hydro scenario. With increasing speeds the negative torque corresponding to the Q = 0 line also increases in magnitude.

Therefore for either type of machines, the magnitudes of negative torque or the magnitudes of energy absorbed change depending on the operating condition. In practical projects the problems will arise when two or more PATs are running together in synchronization and if one of the PAT units happens to enters the quadrant D, it will start absorbing power and act as load on the other PAT units decreasing the net plant output. In addition to power absorption it also adds transients and instability, which can be dangerous for the normal

operation. The objective is to prevent this operation and if there is no alternative to operate in this quadrant, the magnitude of negative torques at corresponding speeds should not be allowed to increase to dangerous limits. The magnitude of negative torques at a given speed can be controlled by altering the discharge flow rates through the respective PATs (either a radial flow or a mixed flow machine). However the physics of this control is slightly different for the two types.

5.6 Solutions to Part-load PAT Operation

One of the main disadvantages sighted in section 1.1.4, and subsequently the most critical objective of the dissertation (Objective no. 6.iii, section 1.2, Chapter 1) was with respect to the part-load operation of PATs. The two fold problem (briefly discussed in problem 3, section 1.3.3, Chapter 1) created with PATs operating in the part-load region at constant speed is corresponding lower operating efficiency and lower net head utilization, which causes the overall output from a PAT to decrease.

It is also generally found that a single speed operation is the most economical operation in terms of the system design of a micro hydro power plant and popular one too. No doubt variable speed operation of PATs can also be foreseen for certain PAT applications, but these are only for specific applications. Therefore the focus is to find solutions for the part-load operation of PATs will be mainly for single speed operating schemes.

It was also mentioned in section 1.3.3, Chapter 1 that the probable ways handling the part-load condition could be either by operating parallel and independent PAT units or an innovative idea of synchronizing different PAT units on single load (electrical or mechanical). The option of variable speed is also briefly dealt in this section. However the prime focus of the theory would be on the design and development for synchronized PAT operation with the 4-quadrant physics and mechanical design, which covers shaft, bearing design along with critical speed analysis.

5.6.1   Single Speed Operation

The cause and need for single speed operation is due to extensive and popular use of synchronous generators in decentralized power generation, which operates only at the given synchronous speed.

5.6.1.1   Independent Operation of PAT Units

This option is incorporated for systems whose electrical distribution network can be divided into various sectors or for schemes that use independent mechanical power units. This option calls for dividing the output load system into 2 or more separate entities depending on

the number of PATs required to handle the part-load operation optimally or the output load requirement. Each load line would then be powered from individual PAT units.

The hydraulic design for the PATs would comprise of a central or the main penstock line that is divided into manifold lines for each PAT unit. If the length between the PAT and the source is small, independent penstock lines can also be contemplated. Each PAT unit would be then coupled to its own load, either mechanical or electrical. The coupling can be direct or indirect using a gearbox or a belt drive system.

The mechanical design calculations would involve verification of shaft and bearing loads on both the driver and driven machines due the influence of drive forces (bending) and torsional loading. Critical resonance determination for both the lateral forces and the torsional forces need to be carried out on all individual units.

An economic study should also be undertaken that includes the costs involved for the individual PAT units, load system, distribution lines, mechanical drive systems, mounting structures and not forgetting the individual hydraulic manifold lines along with the draft tubes. Such systems have their own advantages and disadvantages.

5.6.1.2   Synchronized Operation of PAT Units

The synchronized operation is defined as the simultaneous operation of 2 or more PAT units on a single load, generally an electrical generator. This operation becomes inevitable when a single mechanical or electrical unit limitation is imposed. This can also arise when independent PAT units with divided distribution network cannot be practically implemented or such schemes with independent units become economically unviable.

This operation is achieved by having a long counter shaft for the generator and the individual PATs connected to their countershaft through belt drive systems. The single counter shaft would be a common link between all the driver machines (PATs) and therefore would form a self-regulating mechanism. The constant speed of the counter shaft would ensure that the PAT units also adopt their respective speeds (depending on the speed ratio of the drives). Changes to any of the sub-system would cause changes to all the interconnected drive systems. Therefore the entire synchronized system is sensitive to the smallest change in the any of the sub-system. The mechanical power transmission between the PAT units and the generator shaft is occurring at only one speed of the countershaft and the active powers from different units would mathematically add up.

There is, however a special problem associated operation with single driven shaft illustrated in section 5.5. This occurs when one PAT is fully loaded, transmitting power at the generator synchronous speed and the second interconnected PAT that is also running at identical speed conditions, but dry and needs to be loaded as well. If the valve is opened in this condition and discharge passed through the PAT, it would necessarily cause the PAT to enter the quadrant D irrespective of the type of PAT. But within the D quadrant the physics is

peculiarly different as far as the radial flow PATs and mixed flow PATs are concerned and hence should be separately treated.

5.6.2.1.1 Special operating problem in Radial flow PATs

As seen from the 4-quadrant analysis in Figure 5.6 and 5.7 (section 5.3.1), the contact of discharge with a running impeller would take the PAT into the quadrant D at constant speed (corresponding to the generator shaft) and if the discharge quantities are small a high degree of negative torque (-40% to -60% of the rated torque) is imposed. This physically implies a sudden brake or jerk to the system. If the two PATs are of comparable capacities, and if one of the PAT is operating at 100% rated torque, the situation can be very dangerous with more that 50% of the torque taken over by the new PAT.

The dynamics of the system is simply impossible to predict. There may be a transient effect and stability could subsequently return to the system if the discharge on the new PAT is increased further. Addition to the loss of power, it is the jerk that is created in the beginning is dangerous or even fatal to all the motive parts. Therefore this does not classify as a good method for loading a radial flow PAT within a synchronized system.

5.6.2.1.2 Special operating problem in Mixed flow PATs

The physics involved in mixed flow PAT is totally different. The contact of discharge with the dry running impeller will take the PAT into the quadrant E (Figure 5.8 and 5.9, section 5.3.2). Again here with small magnitudes of flow and with rated operating speed, a tremendously high degree of negative torque (as high as 100% to 150% of the rated torque) is created and imposed on to the entire system. The operating head also becomes negative (inlet head is less than the exit head) as seen in Figure 5.8 and 5.9. With a large negative torques the mixed flow machine exerts a sudden braking effect and under severe circumstances it can effectively bring the entire system to a stand still. This can result in serious mechanical damage to the energy generating PAT, which has been previously operating at the rated head and discharge, and several other components.

This special problem of starting up a PAT in running load condition is the most lethal thing that can happen to a synchronized PAT system. Though the dangers to the mixed flow PATs is greater than the radial flow PATs, the startup technique during load conditions should never be attempted for any type of synchronized PAT system.

5.6.2.1.3 Starting up of the synchronized PAT systems

A simplified methodology for the startup of a twin PAT synchronized system is proposed, which essentially comprises of negotiating the magnitude of the torques on the PATs (+ve or

–ve) along with the buildup of operating speed. The procedure consists of first bringing the two PATs to their respective no-load speed (corresponding to the generator synchronous speed) and then loading each of the PATs independently. The operational procedure with respect to the radial and mixed flow PATs is illustrated below.

1. Radial flow PATs – (Figure 5.7)

As mentioned to bring the two PATs (assuming that they are identical) to their respective no-load rated speeds, the procedure of alternate incremental operation needs to be carried out. It first involves bringing one of the two PATs to rotate at a very slow speed. This PAT will essentially follow the T = 0 line. The second PAT will also begin to rotate at speed of the first PAT, but dry. Allowing discharge through the second PAT will cause it to enter the quadrant D, with a negative torque and subsequently results in the reduction of the system speed. The first PAT gets positively loaded and enters the quadrant C. Since the initial operating speed is very low, the negative torque developed is marginal and will have no dangerous fallout. The second PAT is to be brought to T = 0 line, which can achieved by increasing the discharge till the original speed (of first PAT) is reached. This critical operation will bring the two PATs nearly to the same T = 0 line.

After this, an alternate operation of the two PAT units is executed with every operation associated with only an incremental speed rise. Greater incremental steps should not be undertaken for safety. This alternate operation will eventually lead to the rated no-load speed condition of the PAT units. Once the two PATs are rotating together at rated synchronous speed, loading can begin. Considerable degree of freedom can be exercised in selecting the PAT to be loaded. One of the two PATs can be taken to the fully loaded condition in incremental steps ensuring constant rated speed is achieved at every step. The other PAT will essentially oscillate between the no-load line and the quadrant C (positive torque). Once the first PAT is fully loaded the loading of the second PAT can slowly begin. Loading the second PAT at various steps results in drop in speeds momentarily and causes the first PAT to oscillate between a specific overload point and it original operating point (when rated speed is brought back).

The shut down of the two PATs in synchronization should also be very carefully done. No PAT should be independently closed at one-go, as it would result in quick decrease of system speed and excessive overloading of the other PAT, which would subsequently move towards the N = 0 line, which is not a safe operation. Both the PATs should be slowly closed simultaneously or alternately (also in incremental steps).

2. Mixed flow PATs – (Figure 5.9)

The procedure for starting up and loading the synchronized PAT system with mixed flow machines is essentially similar to the radial flow PAT system. But internally the physics is

slightly different. During the first critical operation of bringing the two PATs in synchronization at low no-load speeds, the second PAT will first pass through the quadrant E. The negative torques in zone E would be considerable even at low speeds and may cause a momentary standstill condition. Hence this PAT should be quickly taken out of this quadrant by increasing the flow. Subsequently it should also be moved through the quadrant D and brought in the vicinity of the T = 0, when the original no-load speed of the first PAT is nearly attained. Once the two PATs are operating in the region formed near the T = 0 line, the alternate incremental procedure for speed rise needs to be followed.

All remaining loading and shutting down procedures for the mixed flow PAT system are identical to that based on radial flow PATs. However extra care should be taken to ensure that that mixed flow PAT does not spend too much time in quadrant E and D, even at no load condition.

5.6.1.2.4   Mechanical Design in Synchronized PAT systems

The mechanical design issues arising from complex situation of synchronizing two PATs needs be given special treatment (as mentioned in objective no. 6.v, section 1.2 and problem 3, section 1.3.3 of Chapter 1). The important considerations for such a design are described in section A8.2, Appendix A.

5.6.2   Variable Speed Operation

The variable speed operation with PATs has been given a detailed treatment by Surek in [51], where he proposed various ways of improving the power output compared to single speed operation. The variable speed operation is mainly foreseen in process application where the discharge and head conditions are varying. However this operation can also be considered for micro hydro application.

The system design for a variable speed application would comprise of a PAT unit coupled to an induction or asynchronous generator and frequency regulator to provide electricity at constant frequency conditions at the output load side. Surek showed that there was enhanced power generation in the range of 5% to 80%, if the PAT was to be operated at lower speeds corresponding to the drop in net head across it, compared to single speed operation. In most of these applications the discharge utilization is not an issue. Therefore a PAT system design with variable speed operation has advantages in process industries or water supply networks where the inlet pressure is continuously varying and no constraints on discharge consumption patterns are imposed.

However in micro hydro application, the efficacy of variable speed needs to be ascertained. As generally seen throughout, objective of a single PAT would be to utilize the full head available even at lower discharges with off course increased output compared to that

obtained during single speed operation. From the detailed analysis carried out in section 5.3, it can be seen that under constant head conditions, the speed should increase for radial flow PAT (<u>Figure 5.6</u> and <u>5.7</u>) and decrease for a mixed or axial flow PAT (<u>Figure 5.8</u> and <u>5.9</u>) if the discharge through the PAT units is lowered. The power output for this new operating speed should be evaluated and compared the output at the same flow and original speed. If there is significant power rise and if it can be economically justified, micro hydro application can also be designed for variable speed operations. A similar evaluation needs to be carried out on greater discharge conditions. The prime requisite for evaluating a micro hydro PAT for variable speed application is the muschel or total characteristics (Few examples of muschel characteristics are provided in section B4, Appendix B).

6.   Case Study – Ambootia Micro Hydro Project

The unparalleled outcome of the hard and intensive research programme has been to install a working example a PAT system (objective no. 7, section 1.2 and problem 4, section 1.3.4 of Chapter 1) in a rural atmosphere and especially where it would be needed the most (a fully decentralized system). The entire energy of the body, soul and mind is to implement this project incorporating all the features extending from appropriate selection, synthesis of performance characteristics, internal optimization, and optimum system design to handle the part-load problem entailed throughout the dissertation. The problem would also involve the challenging implementation, commissioning along with an unbiased evaluation. The evaluation would need to question the selection of the machine, accuracy of the synthesized characteristics and other issues concerning the hydraulic and mechanical stability of synchronized PAT operation. The rural atmosphere is a tea garden in the hills of Darjeeling situated in the northeastern part of the Indian subcontinent, where the idea is put to test.

6.1   Background

The background information regarding the Ambootia micro hydro project is provided in section A9.1, Appendix A. The design phase of the project began in January 2004 and was eventually commissioned in August 2004.

6.2   System Boundary Conditions

6.2.1   Design Input Conditions

6.2.1.1   Maximum available Head

The available elevation between the free surface of the forebay tank and the tailrace level is 95.3 m. There is however an envisaged 8% to 10% head in the penstock and various hydraulic components (discussed in section 6.3).

6.2.1.2   Approximate Discharge Pattern

The water available for power generation is only for 6 to 7 months a year. Table 6.1 summarizes the approximate discharge pattern for the entire year. Unfortunately there was no accurate hydrological study carried out or flow duration curve determined for the given site. Therefore the designed system would need to be highly flexible in terms of discharge range to be handled.

<u>Table 6.1</u>, Seasonal discharge pattern for the Ambootia site

Type of flow	Duration	Months of Year	Discharge
Lean Flow	2 months	March, April	40 l/s – 50 l/s
Steady or Mean Flow	4 – 5 months	May, June, August, September, October	100 l/s – 120 l/s
Peak Flow	0.5 – 1 month	July	200 l/s – 220 l/s

6.2.2   Output Load Requirement

The demand criterion from the Tea factory cum Estate specified by the authorities is summarized follows.

1. To provide peak electrical output of 100 KW_{elec}, however intermittently (2 hours at a stretch).

2. An Intermediate load of 70 to 75 KW_{elec}

3. A base load operation of 50 KW_{elec} continuously.

4. A guaranteed 20 KW_{elec} during lean flow periods.

6.2.3   Design Configuration

To meet the availability and demand criterion a multiple PAT system needs to be selected. These PATs are to be coupled together onto a single shaft with belt drives with only one generator (dealt in detail in subsequent sections) to handle with the various part-load operations efficiently. The configuration of PAT units selected is summarized below.

1. 2 identical PAT units delivering at least 50 KW of electrical power operating individually, called PAT1 and PAT2.

2. 1 single PAT delivering 20 KW electrical power, called PAT3.

There exist three combinations of the synchronized operations, namely,

1. PAT1 and PAT2, producing a net output of at least 100 KW_{elec}.

2. PAT1 and PAT3, generating a net output of 70 to 75 KW_{elec}.

3. PAT2 and PAT3 also producing a net output of 70 to 75 KW_{elec}.

Therefore three PAT units are selected to meet the demand with only 2 of the 3 PAT units envisaged to operate simultaneously. However an alternate combination of all three PATs in synchronization could also be theoretically attempted, but with no increase in the net output.

6.3 Penstock, Manifold Lines and Draft Tube System

The entire piping system of the project is divided in three segments namely, the main penstock line, the turbine manifold lines and the individual draft tubes. The main penstock line is common to all the PAT units. The inlet of each PAT unit is connected to the main penstock line through independent pipelines, called the manifold line. The draft tubes are incorporated leading the exit of every PAT to the tailrace tank. Detailed configuration and calculation of the hydraulic losses for every segment of the piping can be found in the detailed project report from Nestmann and Singh [37].

6.3.1   Main Penstock Line

The main penstock line comprises of all the sections beginning from the forebay tank till the turbine building. This includes the bell mouth and shutoff sluice valve at the forebay tank, cast iron pipe segments (8 m length and ϕ272 mm diameter), PVC pipe segments (which form chief component of the main penstock line with a total length of 367 m and inner diameter of ϕ272 mm) and bend segments (6 nos. in total). The PVC pipes are joined together using ring (rubber) fit joints while the joining of metal-PVC pipe interfaces are accomplished using mechanical expansion joints. The total hydraulic loss in the main penstock line for the given discharge range (100 l/s to 250 l/s) is approximated to the following equation with Q in m^3/s.

$$\text{Main penstock loss equation} = 425.2Q^2 \qquad\qquad (6.1)$$

6.3.2   Manifold Lines

The layout of the different manifold lines of each of the PAT units is shown in Figure 6.1.

6.3.2.1   Manifold Line 1

The manifold line 1 comprises of main junction joint, mild-steel pipe segment of inner diameter ϕ310 mm, reducer (ϕ310 mm to ϕ205 mm), another mild-steel section of inner diameter ϕ205 mm and a bend of ϕ205 mm and finally reducer (ϕ205 mm to ϕ150 mm) leading to the inlet of PAT1. Figure 6.1 and 6.2 give an idea of the construction of manifold line 1, whose hydraulic loss equation is approximated to $52.8Q^2_{PAT1}$. The total system resistance equation for PAT1 is given by,

$$= 425.2Q^2 + 52.8Q^2_{PAT1} \qquad\qquad (6.2)$$

6.3.2.2 Manifold Line 2

The manifold line 2 comprises of essentially the similar components as in manifold line 1, but with an extended length of the ϕ205 mm pipe section as seen in Figure 6.1 and 6.2. The loss equation of this line is approximated to $61.8Q^2_{PAT\,2}$ and the total system resistance line is given by,

$$= 425.2Q^2 + 61.8Q^2_{PAT2} \qquad (6.3)$$

6.3.2.3 Manifold Line 3

The manifold line as seen in Figure 6.1 and 6.3 is third branch line and it combined with the open bypass line. Since the volute inlet to the PAT3 is only ϕ80 mm, the manifold comprises of systematic pipe reductions and a sluice valve of ϕ150 mm. The loss equation of manifold line 3 is approximated to $569.2Q^2_{PAT3}$. Hence the total system resistance line can be then written as,

$$= 425.2Q^2 + 569.2Q^2_{PAT3} \qquad (6.4)$$
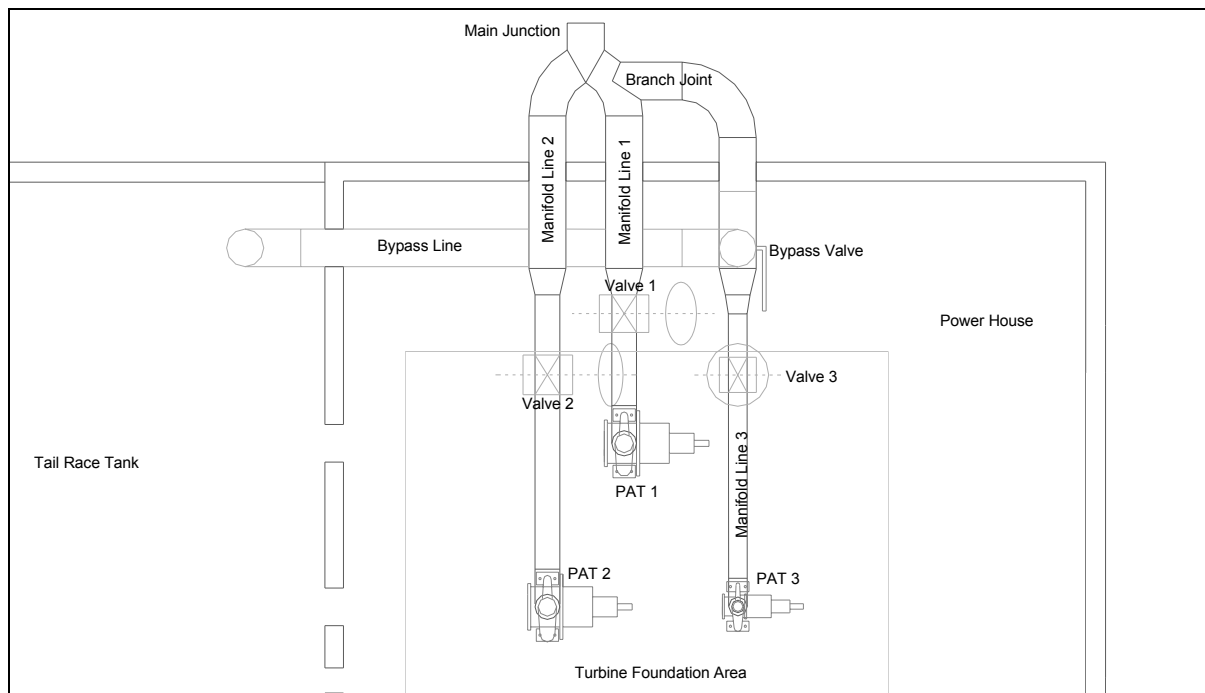
Figure 6.1, Layout of the penstock and bypass system for the Ambootia project
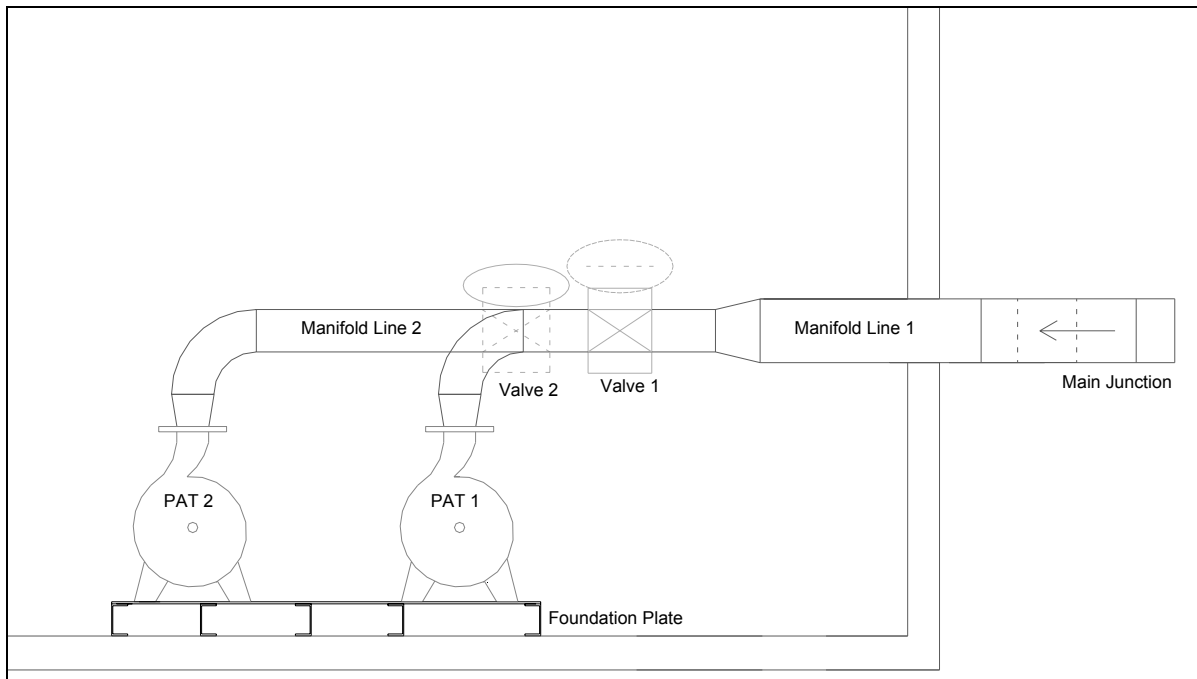
Figure 6.2, Side view of the manifold line 1 and 2 along with foundation plate
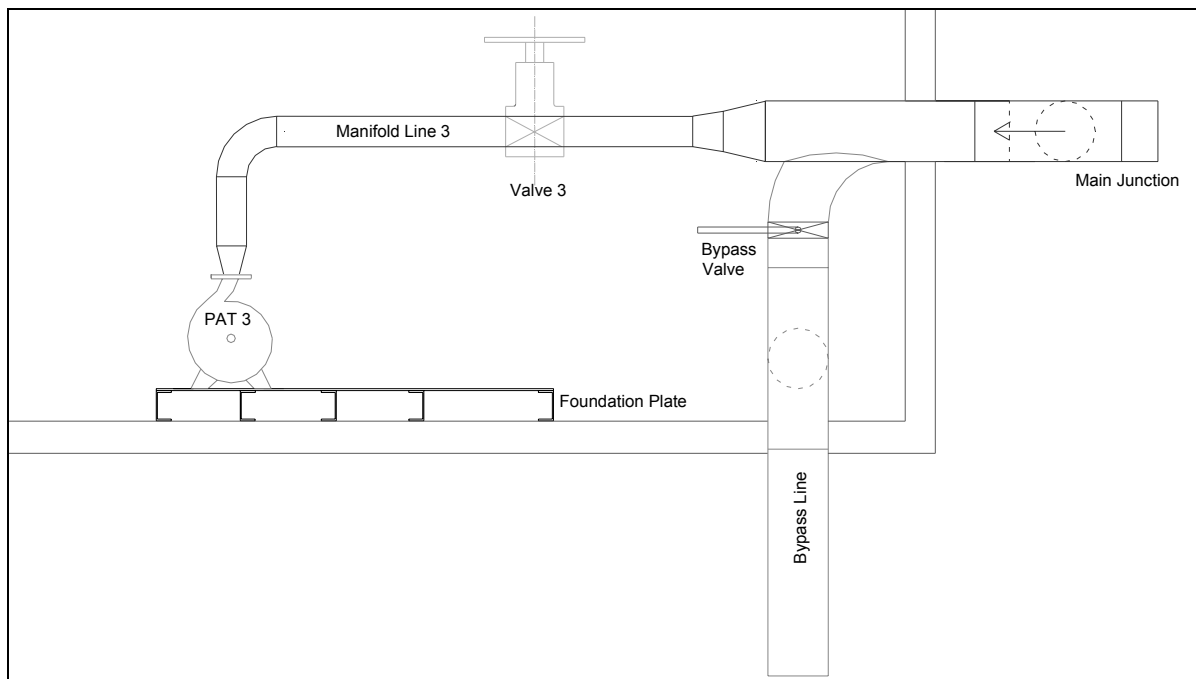

Figure 6.3, Side view of the manifold line 3 and the bypass line

6.3.3   Draft Tubes

All the PAT units have independent draft tubes of specific designs based readily available components. Figure 6.4 gives the overall plan of the draft tube sections of all the three units.

6.3.3.1   Draft Tube 1

As seen in Figure 6.4 and 6.5 comprises of $\phi205$ mm pipe section, an expander from $\phi205$ to $\phi310$ mm, a horizontal section, a bend and a vertical section (all with $\phi310$ mm diameter). The hydraulic loss within the draft tube 1 assuming non-swirling flow is $21.6Q^2_{PAT1}$, while the net velocity head gain (from $\phi205$ to $\phi310$ mm) is $41.4Q^2_{PAT1}$. The static elevation between the PAT centerline and tailrace weir is 1.5m.

6.3.3.2   Draft Tube 2

The draft tube for PAT2 essentially comprises of the same components of the draft tube 1 except that it has a shortened horizontal pipe segment as in seen Figure 6.4 and 6.5. The hydraulic loss for non-swirling flow is represented as $21.3Q^2_{PAT2}$, while the velocity head gain is given as $41.4Q^2_{PAT2}$. The static elevation remains the same as in draft tube 1 at 1.5m.

6.3.3.3   Draft Tube 3

The draft tube 3 as seen in Figure 6.4 and 6.5 consists an expander ($\phi125$ to $\phi205$ mm), two $\phi205$ mm bends combined together forming 'S' shape, a horizontal and vertical section of $\phi205$ mm constant diameter. The hydraulic loss for draft tube is represented as $191.8Q^2_{PAT3}$, while the velocity head is given by $287Q^2_{PAT3}$. The static elevation PAT centerline and tailrace weir is 1.44m.
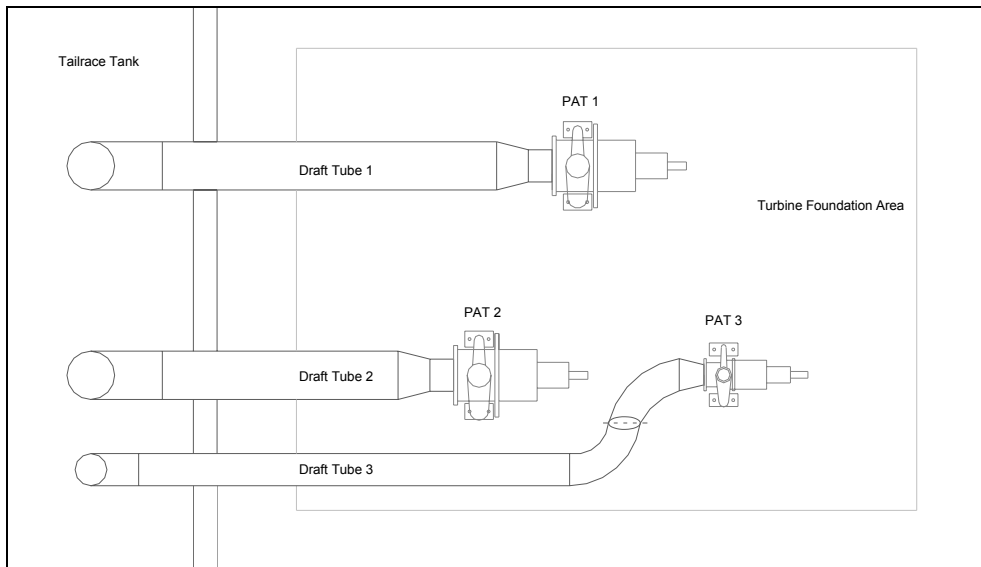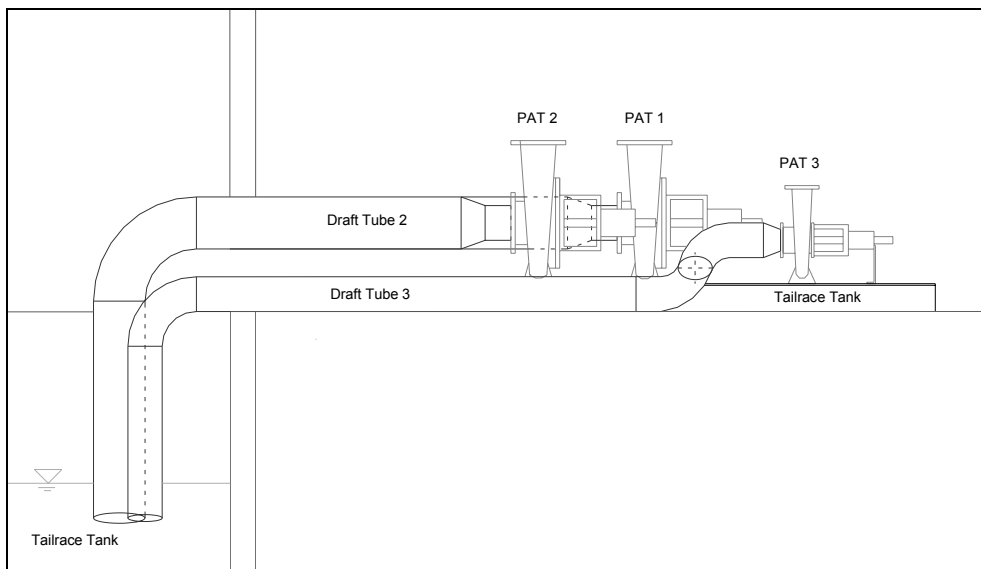
Figure 6.4, Plan of the draft tube 1, 2 and 3

Figure 6.5, Front view of the draft tube 2 and 3

6.4 Design of the Turbine System

6.4.1   PAT1 and PAT2

The boundary conditions for the design and selection of the PAT for unit 1 and 2 are summarized in Table 6.2, which specifies the design net head, the design discharge, the

operating speed and the specific speed (both SI (N_q) and Cordier (from Equation (5.3), Chapter 5).

Table 6.2, Boundary condition for the selection and design of PAT1

Design Net Head	H	77	m
Design Discharge	Q	130	l/s
Operating speed	N	1200	rpm
Specific speed (SI)	N_q	16.6	rpm
Specific speed (cordier)	σ	0.106	

The selection of the above parameters is governed by the input as well as the output boundary condition discussed in section 6.2. However some approximation and freedom is exercised here, especially in terms of operating speed selection. The $\sigma = 0.106$ line is plotted on the Cordier diagram for radial PATs as shown in Figure 5.1 to obtain 3 specific diameter numberss, Δ_{mean}, Δ_{lower}, and Δ_{upper} respectively that are summarized in Table 6.3 along with the diameters in terms absolute terms.

Table 6.3, Specific and reference diameter range for the selection of PAT1

Δ_{mean}	6.708		D_{mean}	438 mm
Δ_{lower}	6.279		D_{lower}	410 mm
Δ_{upper}	7.130		D_{upper}	465 mm

Step 1:   Diameter Selection

From the catalogues of Kirloskar [23], a radial pump of outer impeller diameter of ϕ449 mm is found that comes within the range required from Cordier consideration. The pump duty point at 1450 rpm is defined at a discharge of 92.8 l/s and net head of 62 m with and operating efficiency of 79.5%.

Step 2:   Range of Specific Speeds (operating speeds)

Based on the selected diameter ϕ449 mm, the dimensionless specific diameter Δ is determined from Equation (5.4) to be equal to 6.881. The $\Delta = 6.881$ line is superimposed on the radial PAT cordier diagram as shown in Figure 6.6. The intersection with mean curve and its tolerance bands gives a range of dimensionless specific speed numbers, σ. Table 6.4 summarizes the ranges of both the specific speed numbers and absolute operating speeds.
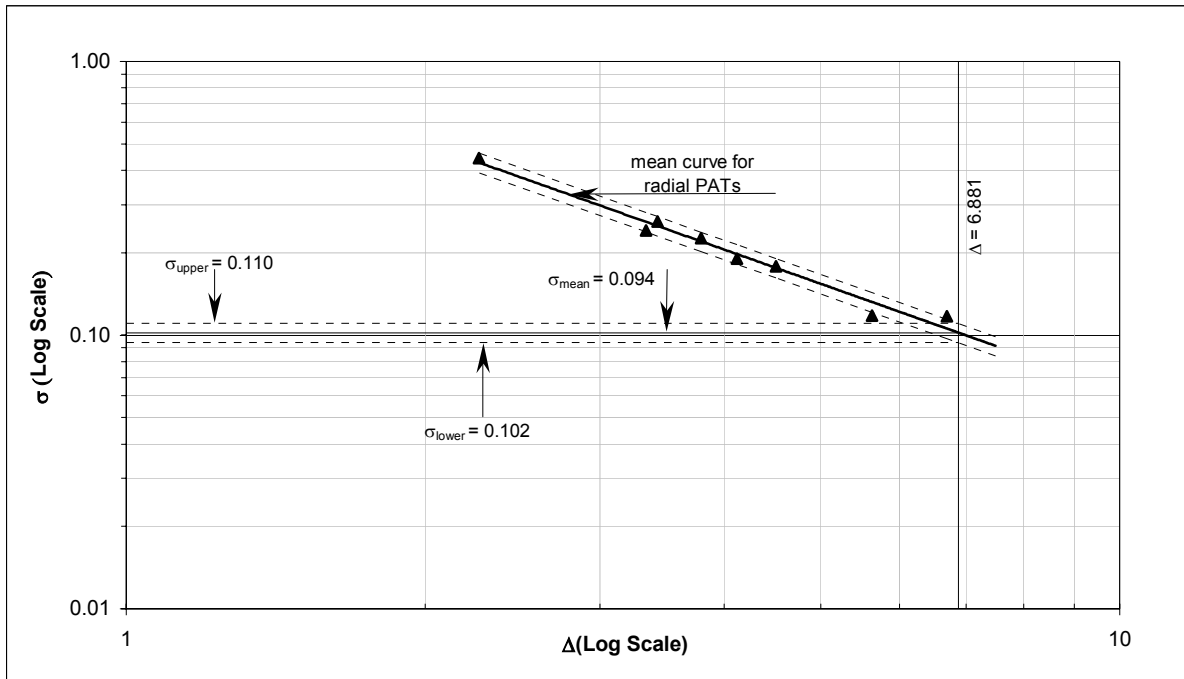
Figure 6.6, Interaction of the constant specific diameter line with Cordier lines for design of PAT1

Table 6.4, Specific and operating speed range for the selected PAT1

σ_{mean}	0.102		N_{mean}	1161 rpm
σ_{lower}	0.094		N_{lower}	1067 rpm
σ_{upper}	0.110		N_{upper}	1256 rpm

Step 3:   Range of Head numbers and Discharge numbers

The range for the head numbers and discharge numbers ('boundary' numbers) based on the full utilization of the boundary parameters (77 m and 130 l/s in Table 6.2) and the operating speed range (obtained in Table 6.4) are determined and summarized in Table 6.5.

Table 6.5, 'Boundary' head number and Discharge number range

$(gH/N^2D^2)_{mean}$	10.000		$(Q/ND^3)_{mean}$	0.074
$(gH/N^2D^2)_{lower}$	11.860		$(Q/ND^3)_{lower}$	0.081
$(gH/N^2D^2)_{upper}$	8.550		$(Q/ND^3)_{upper}$	0.069

The mean 'boundary' head number $\psi_{mean} = 10.000$ intersects the mean $(\psi - \phi)_{BEP}$ trend line of Figure 5.3 at $\phi_{mean} = 0.078$ ('required' discharge number).

Step 4:   Suitability of the selected PAT

1. Boundary discharge to be fully utilized

The boundary conditions specify that the mean discharge number should be 0.074 as to 0.078 obtained from the requirement criterion of the PAT curve from the mean $(\psi - \phi)_{BEP}$ trend line (Figure 5.23). However the $(Q/ND^3)_{mean}$ from both the boundary and requirement conditions are nearly similar and it can be seen that the boundary discharge conditions are not going underutilized.

2. Verification of head and discharge ratios between turbine and pump modes
The dimensionless numbers of the selected pump at BEP is given in Table 6.6. The turbine mode dimensionless 'boundary' numbers based on mean, lower tolerance and upper tolerance limits (provided in Table 6.5) need to be compared to the pump mode BEP condition. The comparisons are carried out in Table 6.7.

Table 6.6, Pump mode ψ, ϕ and $N_{q\,p}$ at the BEP for PAT1

ψ_p	5.166
ϕ_p	0.042
$N_{q\,p}$	20.0 rpm

Table 6.7, Range of head number and discharge number ratios for PAT1

	ψ_t/ψ_p	ϕ_t/ϕ_p
Mean conditions	1.94	1.75
Lower tolerance limit	2.30	1.90
Upper tolerance limit	1.65	1.62

The characteristics of the selected pump ($N_{q\,p}$ 20 rpm) should be situated in the vicinity of the characteristics of the 21 rpm and 24.5 rpm PATs within the selection and performance chart shown in Figure 5.2 and 5.3, Chapter 5. The discharge ratios and head ratios at the respective turbine and pump mode BEP points for these pumps (provided in Table B1.2, section B1, Appendix B) are summarized in Table 6.8.

Table 6.8, Head and discharge ratios for the 21 rpm and 24.5 rpm PATs

Parameters	21 rpm PAT (ϕ225 mm)	24.5 rpm PAT (ϕ258 mm)
ϕ_t/ϕ_p	1.85	1.9
ψ_t/ψ_p	1.78	2.1

Since the selected pump ($N_{q\,p}$ 20 rpm) has a specific speed closer to the tested 21 rpm pump, there is a strong possibility that their hydraulics are similar. But before a blind assumption of the characteristics is made, it is crucial to see if these pumps have identical pump characteristics or operating duty points. Table 6.9 compares the dimensionless pump mode duty points of the 20 rpm and 21 rpm pumps.

Table 6.9, Comparison of the pump mode duty points for the 20 rpm and 21 rpm PATs

Parameters	20 rpm pump	21 rpm pump
ϕ_p	0.042	0.038
ψ_p	5.166	4.500

The comparison of the pump mode duty points is very interesting in that, the lower specific speed pump, i.e. 20 rpm pump has a greater ϕ_p = 0.042 compared to ϕ_p = 0.038 of the 21 rpm pump, while head number ψ_p = 5.166 is greater compared to ψ_p = 4.500 of the higher specific speed pump. It is only due to this greater head number that specific speed of the selected pump has dropped. Therefore once again it is seen that it's not always right to rely only on specific speed numbers for selection and performance prediction.

Step 5:   Selection of the final operating point, ψ_t and ϕ_t

From all the considerations, the final ψ_{BEP} and ϕ_{BEP} for the selected PAT is assumed to be lying between the mean and the upper tolerance condition that has been illustrated in Table 6.5. Table 6.10 summarizes the BEP point along with head and discharge ratios of selected 20 rpm PAT. It is also seen that the head and discharge ratios are also compatible with the illustration in Table 6.8. This point has also been plotted in the selection and performance chart for radial flow PATs in Figure 6.7.

Table 6.10, Final selection of the ψ_t and ϕ_t at BEP for PAT1

ϕ_t	ψ_t	ϕ_t/ϕ_p	ψ_t/ψ_p
0.072	9.370	1.69	1.81
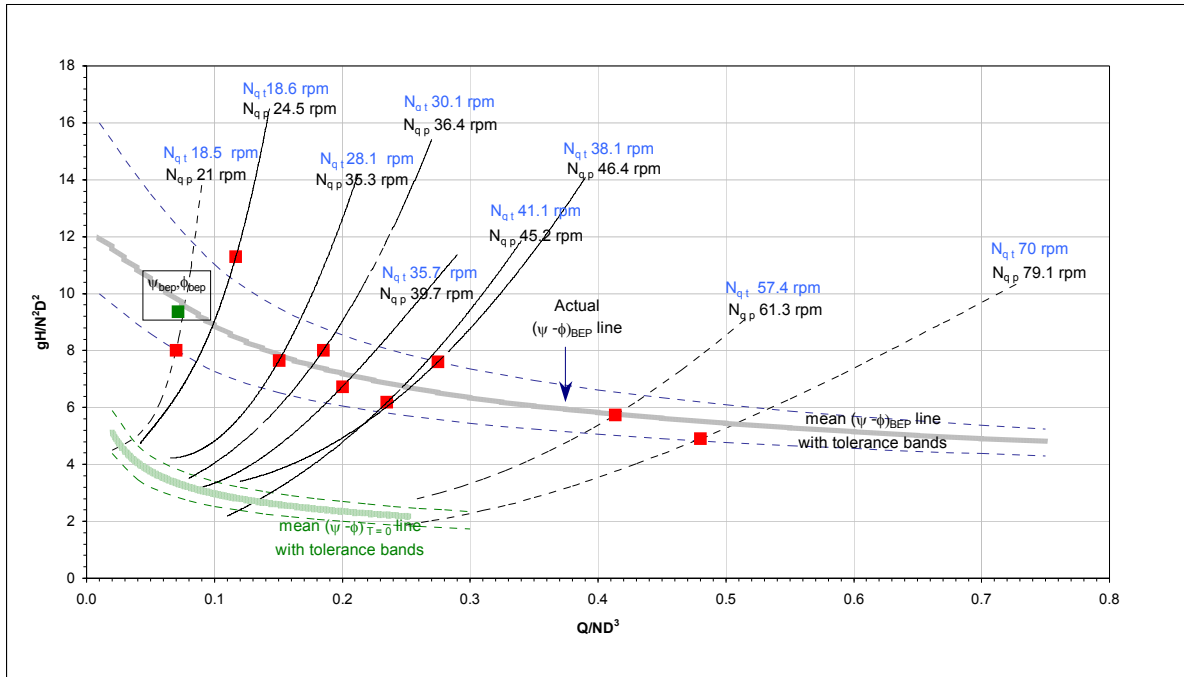
Figure 6.7, Locating the selected ψ_t and ϕ_t on the overall ψ-ϕ characteristics for radial PATs

Step 6:   Synthesis of the complete operating characteristics

The (ψ - ϕ) curve for the selected PAT is constructed following the procedure illustrated in Chapter 5, section 5.2.1.1, step 6, passing through the BEP point (fixed in Table 6.10) and mean no-load field of the radial flow PATs (Figure 5.3 and 6.7). The overload limit is also suitability fixed. The slope of the (ψ - ϕ) characteristics is selected accordingly shown in Figure 6.8, where the characteristics of 21 rpm and 24.5 rpm PAT have also been plotted.

The (η - ϕ) characteristics is also plotted following the locus of the 21 rpm (η - ϕ) curve between the no-load and overload limits of previously synthesized (ψ - ϕ) curve. The magnitude of the best efficiency assigned to it is 76.5%, which is moderate value, considering its size and geometry.
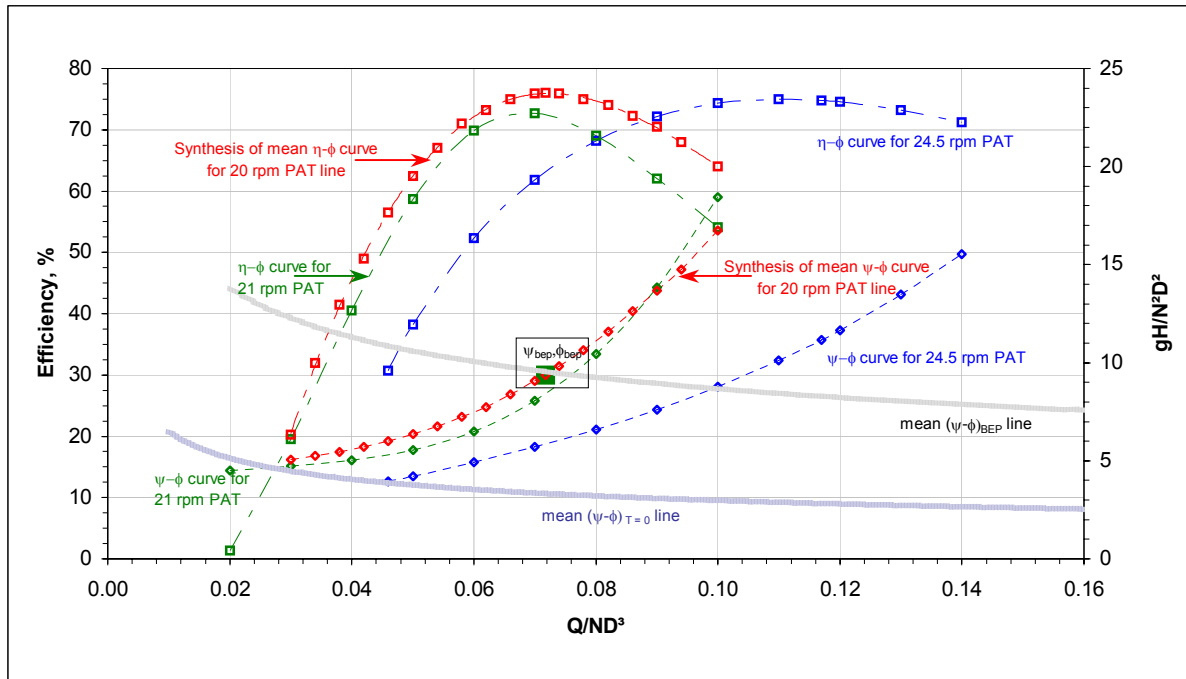
Figure 6.8, Synthesis of the ψ-ϕ and η-ϕ characteristics for the PAT1

Step 7:   Uncertainty Bands

The displacement for the discharge number $\Delta\phi$ selected is 0.008, which represents a deviation of ±11% at BEP (±0.008/0.072). The mean synthesized curves (for ψ - ϕ and η - ϕ characteristics) along with the tolerance bands are plotted in Figure 6.9.
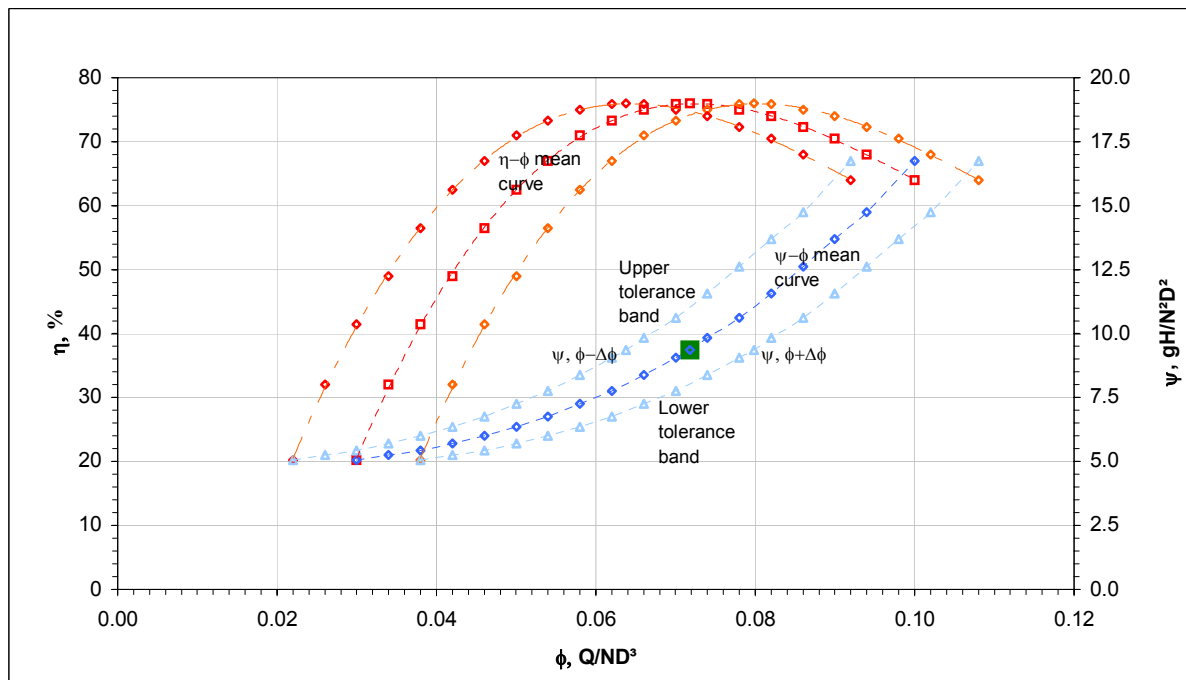

Figure 6.9, Uncertainty bands for the ψ-ϕ and η-ϕ characteristics of the PAT1

Step 8: **Muschel characteristics**

The muschel curves are developed based on the mean synthesized curves and plotted in Figure 6.10. The muschel curves are seen to follow the trend of radial flow PATs (as in section 5.3.1 and Figure 5.8). These characteristics include the following curves.

1. Constant speed curves: The speeds considered here are, 1000 rpm, 1100 rpm, 1200 rpm, 1300 rpm and 1400 rpm.

2. Constant power curves: consist of the 10 kW, 20 kW, 30 kW, 40 kW, 50 kW, 60 kW, 65 kW, 70 kW, 75 kW, 80 kW, 85 kW and 90 kW lines.

3. Constant efficiency curves: comprise of the following efficiency lines - 40%, 50%, 60%, 70%, 74% (part-load), BEP (76%), and 74% (overload).

4. T = 0, No-load or Runaway line.

5. System Resistance curve determined by Equation (6.2) or (6.3).
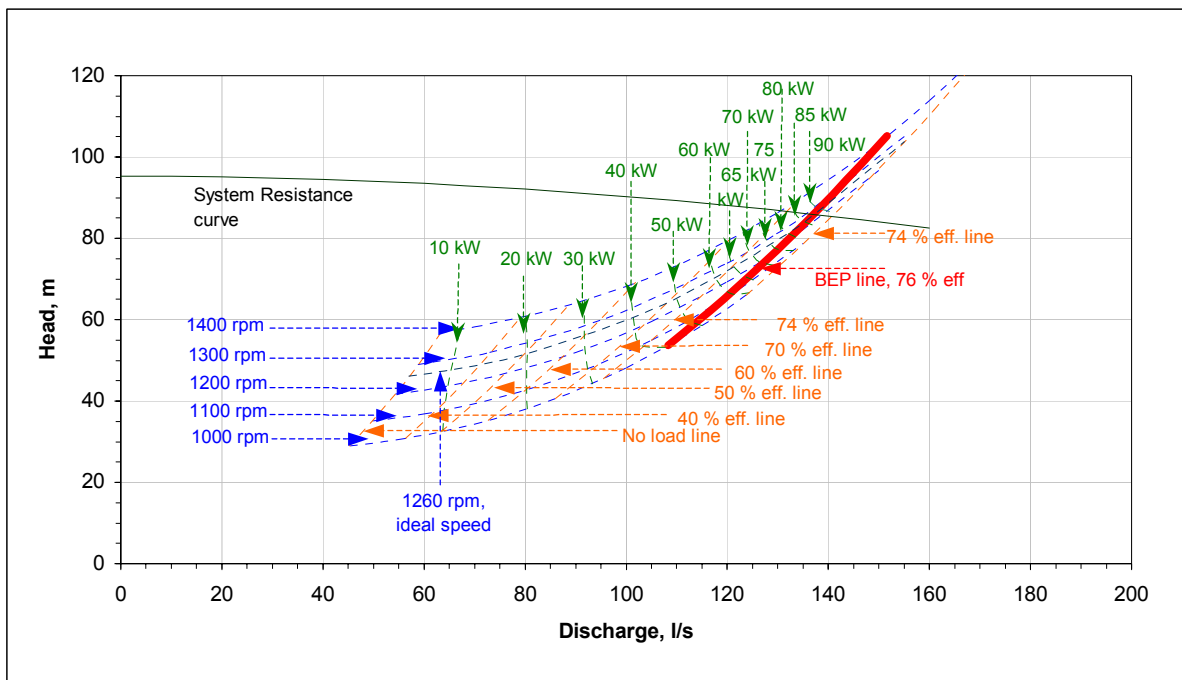
Figure 6.10, Muschel characteristics for PAT1 with system resistance line

Step 9: **Final selection of operating speed**

After studying the intersection of the site curves with the constant speed curves in Figure 6.10 very closely, 1260 rpm is selected as the design operating speed.

Step 10: **Uncertainty analysis at design speed**

Figure 6.11 displays the mean characteristics at 1260 rpm along with the two tolerance bands and the site curve. It cuts the constant speed curves at three points, which refer to the probable operating points. Table 6.11 illustrates the large variations of the operating

parameters at all the three probable points. The expected power output would lie in the range of 81.1 KW to 93 KW.
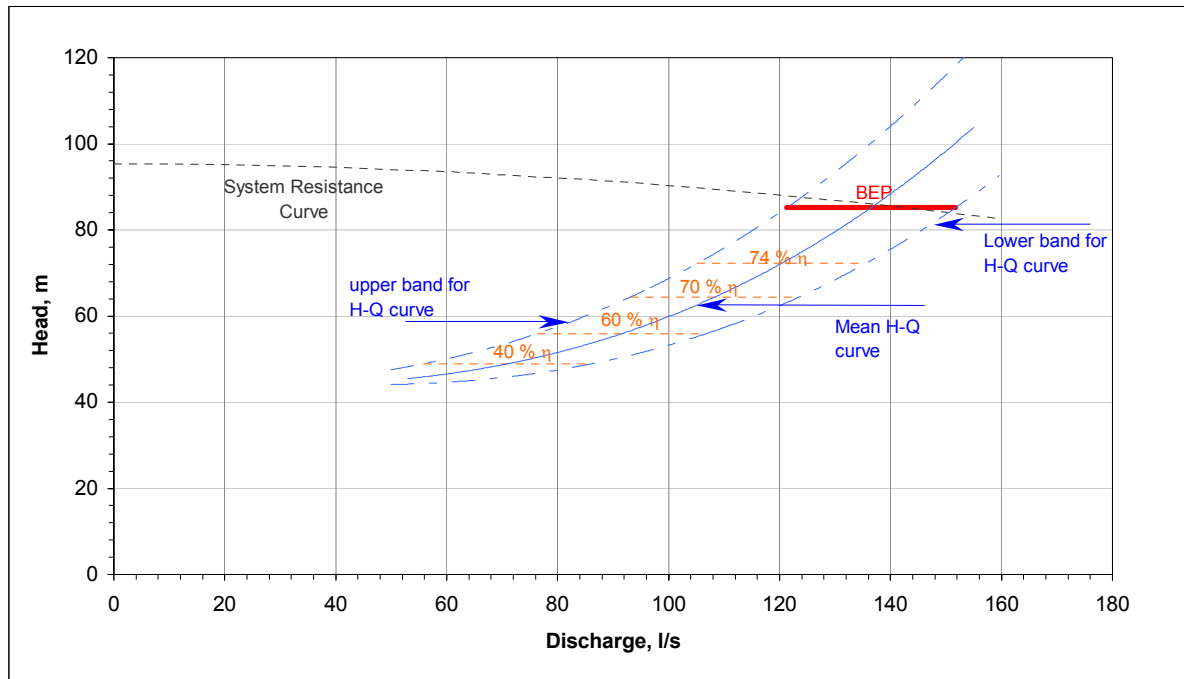

Figure 6.11, Uncertainty bands for the constant speed (design) H-Q curve of PAT1

Table 6.11, Maximum operating range of PAT1 considering uncertainties

	H	Q	P_{mech}
Upper Band	87.6 m	124.0 l/s	81.1 KW
Mean	85.9 m	137.3 l/s	88.0 KW
Lower Band	83.3 m	149.6 l/s	93 KW

6.4.2   PAT3

The procedure for the selection of a PAT for unit 3 and synthesis of characteristics is essentially similar to that PAT1 and PAT2 (in section 6.4.1) and is elaborated in section A9.2, Appendix A.

6.4.3   Internal Optimization on PATs

There were only two stages of optimization that were implemented on the three PAT units selected namely,

1. Optimization Stage I – Inlet Impeller Rounding

The blade profiles and the shroud edges were systematically rounded in accordance to the procedure described in section 2.4.1, Chapter 2.

2. Optimization Stage IV – Casing Eye Rib Removal

The casing eye region of all the PATs that comprised of a single rib was removed (section 2.4.4, Chapter 2).

6.4.3.1   Summary of the PAT Design

No intensive design study of the PATs was carried out. However the chief design parameters of the machines are summarized in Table 6.12.

Table 6.12, Design features of PAT1, PAT2 and PAT3

	PAT 1 and PAT 2	PAT 3
Inlet Volute (turbine mode) Diameter	ϕ150 mm	ϕ80 mm
Outer Impeller Diameter	ϕ449 mm	ϕ329 mm
Casing Eye Diameter	ϕ200 mm	ϕ125 mm
Number of Blades	5	5

6.5 System Design

6.5.1   Single Generator Criterion

One of the chief considerations for the layout is criterion of a single generator for the plant. Due to this criterion, all the 3 PAT units have to be inevitably linked or connected to that single generator. This link is established by an extension to the generator shaft called the main shaft system.

6.5.2   Layout

The single generator and the forthcoming necessity of an extension shaft calls for many other optimizations steps to complete the layout. The important blocks that go into the layout are identified and dealt as follows.

6.5.2.1   Positioning of PAT units

The simplest procedure to extend the generator shaft and directly couple it to another shaft called, the main shaft. This eliminates all secondary drive systems, which are not recommended. The main shaft hence incorporates the drive system for the individual PAT units, namely PAT1, PAT2 and PAT3. The positioning or placements of the three PATs needs the following considerations.

1. To have the smallest shaft length as possible. Long shafts lead to other mechanical problems and also increase the space utilization.

2. To have optimum hydraulics for the draft tube, with the minimum bends and shortest length.

3. To allow space for the operator to handle all the three valves from the same platform.

4. To allow easy access to every part of the system and

5. And to have the highest degree of flexibility, for maintenance, repair etc.

Based on the above considerations two options for the layout are foreseen.

OPTION 1: All PAT units are inline and on one side of the main shaft

This option would result in an extremely long shaft (approximately 4 m), which is not an economical option in any sense. Also the inline placements would cause unfavorable draft tube hydraulics, in that a bend section directly emerges out of the eye region of the PAT. The draft tube requirements and clearance between draft tube section and drive of preceding PAT also cause a further increase of shaft length.

To have unequal drive length (or center to center distances) for the PAT units in order to improve the draft tube conditions and to shorten the shaft length is not recommended due to mechanical problems associated with of extensive drive lengths. This also creates difficulties in managing the PAT manifold lines and issues concerning layout flexibility. Therefore this option is not very suitable and hence rejected.

OPTION 2: PAT units on either side of the main shaft

In this option two PAT units are placed on one side of the main shaft and the third PAT on the other side of the main shaft as illustrated in <u>Figure 6.12</u>. The PAT units are to be positioned so that the draft tubes of the two main PATs, i.e. PAT1 and PAT2, are proceeding straight (without any bend). To achieve this, PAT1 and PAT2 are placed on either side of the main shaft but with a lateral displacement needed for accomplishing the safe drive system and hence causing unequal draft tube lengths. This design helps in reduces the length of main shaft to below 1.8 m as against 4 m from the option 1.

The third PAT, i.e. PAT3 can either be placed inline with PAT1 or PAT2. It is chosen to position it behind PAT2 because of the interference its draft tube would cause with the proposed bypass line and space for the operator, if placed behind PAT1. In order to achieve

the identical drive lengths for PAT2 and PAT3, the draft tube for PAT3 will be skewed to negotiate the path towards the common discharge tank. This 'S' formation of the PAT3 draft tube is not optimum for the draft tube hydraulics. However the maximum operating head on PAT 3 envisaged is only a little over 85 m and the loss of head in the draft tube is acceptable.

The option 2 also allows space and good access for the operator and his platform is situated between manifold lines of PAT1 and PAT3. The layout based on option 2 is accepted for the project.
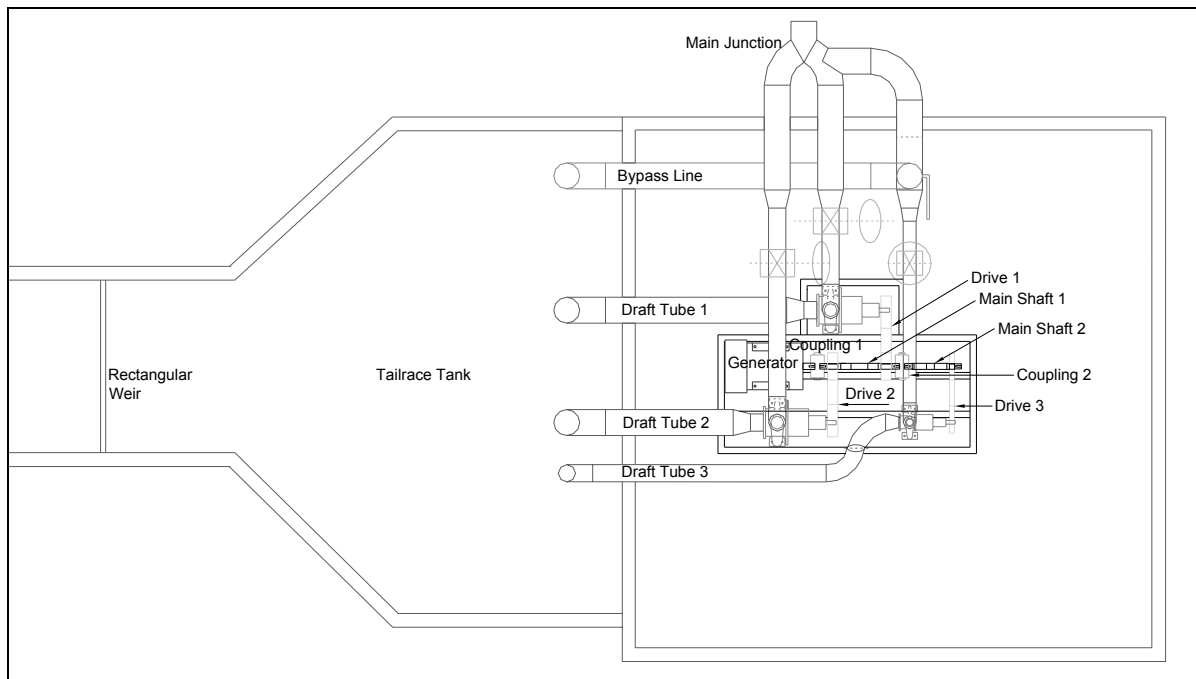

Figure 6.12, Layout evolved after system design considerations (also refer to Figure B6.24, B6.25 and B6.26, Section 6.3, Appendix B)

6.5.2.2   The Main Shaft

The main shaft would experience a combined loading from the bending and torsion. The bending load arises due to the belt thrusts acting perpendicular to the shaft axis. The main shaft should transmit the power from the PAT units to the generator with minimum prorogation of bending stress. The propagation of the torsional shear stresses in inevitable, but the propagation of the bending stress can be reduced by splitting the main shaft. In addition to the advantages of stress distribution, the splitting of the main shaft has other advantages.

1. It allows optimum allocation for the pair of bearing blocks on the two shaft units instead of one shaft unit.

2. It increases the flexibility of mechanical handling as,

   a. It allows the assembly/disassembly of the belts and pulleys.

   b. It allows the disengaging of the main shaft 2 when drive of unit 3 is not in use.

The primary shaft unit is coupled to the generator and holds the drive for PAT1 and PAT2 respectively, called main shaft 1. The secondary shaft unit (main shaft 2) is connected to the primary shaft via coupling and holds the drive for the PAT3. Therefore there are two couplings in system, both of which are of flexible type and easily mountable. The main shaft 1 needs to be always coupled to the generator shaft while the main shaft can be disengaged when the PAT3 is not required for operation.

The shaft length cannot be indefinitely decreased due to the subsequent reduction of the distance between the bearing blocks on the shaft. Smaller distances tend to increase the forces at the bearing supports. This would result in difficulties in bearing selection and increase of costs. Therefore a balance needs to be struck and shaft length should be reduced as far as possible till the operating forces allow for the selection of readily available bearings for a minimum of 10-year lifetime.

6.5.2.3 Drives and Belt Tensioning

The center-to-center distances between the respective axes of the PAT shafts and the axis of the main shaft system is maintained at 650 mm. Longer distances are not recommended for both space limitation and mechanical problems.

The layout (Figure 6.17) shows no scope for tensioning the belts by shifting the generator axis using slide rails. Therefore this would necessitate the use of idler or jockey rollers to achieve the appropriate belt tensions. Due to the placements of the PAT units on either side of the shaft and also due to the fixed direction of rotation of the PAT impellers with respect to the rotation of the shaft, the slack sides of the drive are different. For PAT1, the slack side would form on the upper section of the drive, while for the PAT2 and PAT3 the slack side would correspond to the lower drive section. The idler rollers should be appropriately designed and placed to allow easy tensioning and operational safety.

6.5.2.4 Bypass Line

The bypass system is conceived with the following requirements.

1. Quick accessibility

2. To be situated inside the powerhouse for reasons of safety.

From the above, it was found that the only place where the bypass can be built is on the manifold line of the PAT3. The bypass line is efficient from the hydraulic resistance point of view (dealt in section 6.5.3). But due to the fact that it is placed on the manifold line 3 and

not the main penstock line, it does act as a very efficient flush for the debris and stones during the initial loading of the penstock.

6.5.2.5 Foundation system

The foundation system consists of a 12 mm surface plate welded to a grid comprising of 150 mm 'C' channels. A view of the foundation system is seen in Figure 6.2 and 6.3. The 'C' channel grid and the surface plate have holes that allow 27 foundation bolts to pass through and fastened at the top surface plate. The generator, the PAT units, the bearing supports, and all other supports are fastened directly on to the surface plate.

6.5.3 Bypass System

The runaway behaviour experienced under the given boundary condition for the respective PAT units is analyzed in Table 6.13. It is found that operating head on the various PAT units increases from 75 - 85 m range to over 93 m. The runaway speed on PAT1 and PAT2 is 1815 rpm while that for PAT3 is 2250 rpm. This translates to generator speed of over 2250 rpm. These speeds are however still in the tolerance range of both the PAT and generator specifications. Though the runaway behaviour is not alarming, the given rise of operating head and speed are not favourable and cannot be left untreated.

Table 6.13, Summary of the runaway conditions of PAT1, PAT2 and PAT3

	PAT1	PAT2	PAT3
Q_{PAT}	68.5 l/s	68.5 l/s	17.4 l/s
H_{PAT}	93.1 m	93.1 m	94.7 m
N_{PAT}	1815 rpm	1815 rpm	2250 rpm
$N_{GEN.}$	2160 rpm	2160 rpm	2250 rpm

To deal with the runaway problems, an open bypass design is chosen that has been described in section 5.4.1.4, Chapter 5. The bypass line comprises of the all the components between the main junction point and the tailrace tank. Figures 6.1 and 6.3 describe the line, which is linked to the manifold line for PAT 3. The total resistance of the hydraulic line (from Nestmann and Singh [37]), is given by,

$$= 24.05 Q_{bypass}^2 \qquad (6.5)$$

Table 6.14 summarizes the various constants that are needed for the solution of the open bypass design, comprising of the hydraulic resistance and runaway coefficients for different PAT units.

Table 6.14, Summary of the various coefficients for the open bypass design

$K_{penstock}$	$Z_{junction}$	K_{bypass}	Z_{bypass}	PAT1		PAT2		PAT3	
				$K_{runaway}$	$K_{manifold\ PAT}$	$K_{runaway}$	$K_{manifold\ PAT}$	$K_{runaway}$	$K_{manifold\ PAT}$
(6.1)	(m)	(6.5)	(m)		(6.2)		(6.3)		(6.4)
425.2	3.5	24.05	3.5	19900	52.8	19900	61.8	314200	569.2

The constants from Table 6.14 are used in Equations (5.8), (5.9), (5.10) and (5.11) (of Chapter 5) to obtained the ratios of discharges, the actual discharges through the bypass system and the respective PAT units, following which the speed conditions at no load conditions are obtained. Table 6.15 summarizes the runaway analysis with the open bypass design for the unlimited input discharge conditions.

Table 6.15, Summary of the operating conditions after the opening the bypass line

	PAT1	PAT2	PAT3
Q_{PAT}/Q_{bypass}	0.035	0.035	0.009
Q_{bypass}	446 l/s	446 l/s	457.3 l/s
Q_{PAT}	15.6 l/s	15.6 l/s	4.1 l/s
H_{PAT}	4.8 m	4.8 m	5.3 m
N_{noload}	413 rpm	413 rpm	530 rpm

The bypass valve selected is of butterfly type with manual operating lever. Opening the valve with a net head difference of the order of 10 bar is not going to be an easy task as torque requirements would be very high. However economics did not allow the use of sophisticated valves like needle or cone discharge valves. Fortunately the runaway conditions are not so dangerous. However to improve the reaction time it is recommended to close the main inlet valve simultaneously while the bypass valve is being closed.

6.5.4   Combined PAT Operation Table

The combined operation of the all the 3 PAT units in synchronization for the input discharge ranging from 0 l/s to 240 l/s is listed in Table 6.16. The salient features of the operational table are,

1. In the discharge range between 25 l/s and 55 l/s, PAT3 is the only unit that will have optimum operation delivering a maximum of 25 KW$_{elec.}$.

2. In the range from 100 l/s to 140 l/s, the individual operation of PAT1 or PAT2 is most optimal with an output of 50 KW$_{elec}$ to 72.5 KW$_{elec}$.

3. The synchronized operation of PAT1 or PAT2 and PAT 3 for the range from 160 l/s to 200 l/s generates 74 KW$_{elec}$ to 85 KW$_{elec}$.

4. Over the discharge of 220 l/s and below 240 l/s, the combined operation of PAT1 and PAT2 produces an output between 85 KW$_{elec}$ and 100 KW$_{elec}$.

Table 6.16, Combined operational table for PAT1, PAT2 and PAT3

Input	PAT1				PAT2				PAT3				Total	Total	Total
Q	H	Q	P$_{mech.}$	η	H	Q	P$_{mech.}$	η	H	Q	P$_{mech.}$	η	Q	P$_{mech.}$	P$_{elec.}$
(l/s)	(m)	(l/s)	(KW)	(%)	(m)	(l/s)	(KW)	(%)	(m)	(l/s)	(KW)	(%)		(KW)	(KW)
55	-	-	-	-	-	-	-	-	86.4	55	33.1	71.1	55.0	33.1	26.7
80	-	-	-	-	-	-	-	-	86.4	55	33.1	71.1	55.0	33.1	26.7
100	59.9	100.0	38.5	65.6	-	-	-	-	-	-	-	-	100.0	38.5	31.5
120	72.0	120.0	63.0	74.3	-	-	-	-	-	-	-	-	120.0	63.0	51.8
140	85.9	137.3	88.0	76.1	-	-	-	-	-	-	-	-	137.3	88.0	72.7
160	83.0	134.0	83.0	76.1	-	-	-	-	48.6	26.0	5.8	46.8	160.0	88.8	73.4
180	80.4	131.0	78.5	76.0	-	-	-	-	72.3	49.0	24.7	71.1	180.0	103.2	85.8
200	77.2	127.0	72.7	75.6	-	-	-	-	76.5	51.0	27.3	71.4	178.0	100.0	83.1
220	73.4	122.0	65.7	74.8	58.9	98.0	36.4	64.2	-	-	-	-	220.0	102.1	84.9
236	70.6	118.0	60.3	73.8	70.6	118.0	60.3	73.8	-	-	-	-	236.0	120.6	100.2

The selected PAT units and their synthesized performance characteristics are found to comply fully with all the four output load criteria imposed in section 6.2.2.

6.6 Mechanical System

The detailed design of the mechanical system for this synchronized PAT project is carried out in Nestmann and Singh [37]. However the salient features of the design is summarized in section A9.3, Appendix A.

6.7 Field Testing and Evaluation

The field testing comprises of individual load tests on PAT2 and PAT3 along with the synchronized test of PAT2 + PAT3. The tests were performed till the saturation of the input pressure conditions was attainted. Individual tests on PAT 1 could not be carried out.

The net head on the respective PAT units is determined from the measured inlet static pressure, the theoretically determined exit pressure (from section 6.2.3), the velocity heads and elevations. The discharge is calculated using the standard Rehbock formula (from IEC code in [20]) for the rectangular weir. The electrical output power consumed by the ballast loads is determined from the average ballast voltage across the three phases and approximate resistance of the coils. The operating speed is measured using inductive sensors interfaced with perforated discs on the respective shafts. This calculation leads to the overall efficiency, and subsequently turbine efficiency is determined from the given generator characteristics.

6.7.1   Testing of PAT2

During the testing of PAT2, the impeller was severely damaged (see Figure B6.27, section B7, Appendix B) due to contact with debris. Three of the five vanes were broken near the inlet impeller (zone *iii* and *iv* of PAT control volume). A piece of the back shroud plate was also ripped off. However complete load testing was carried out on the damaged impeller. Table 6.17 summarizes the results of the actual constant speed load test.

Table 6.17, Field test results of PAT2

Load Point	H_{net} (m)	Q (l/s)	$P_{elec.}$ (KW)	N (rpm)	$\eta_{overall}$ (%)	η_{PAT} (%)
1	44.2	56.2	0	1235	0	0
2	52.5	63.3	15.8	1310	48.5	60.1
3	48.4	63.3	16.4	1262	54.7	67.8
4	65.2	86.2	33.2	1237	60.2	74.6
5	75.8	102.8	45.6	1237	59.7	73.9
6	81.2	111.5	51.2	1237	57.6	71.3
7	85.6	120.4	57.0	1237	56.4	69.8

The field H-Q curve at constant speed of 1237 rpm is plotted with synthesized H-Q curve (with tolerance bands) at the same speed in Figure 6.13. The field curve is shifted to left of the predicted zone in the entire operating range except in the no-load region.
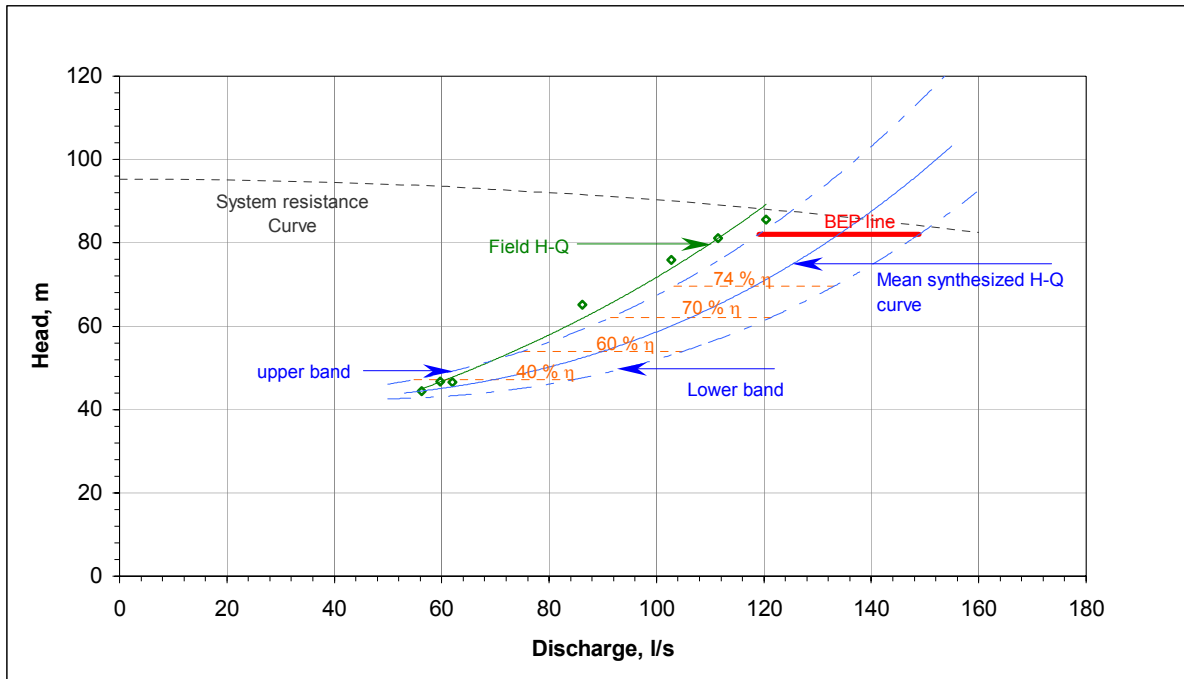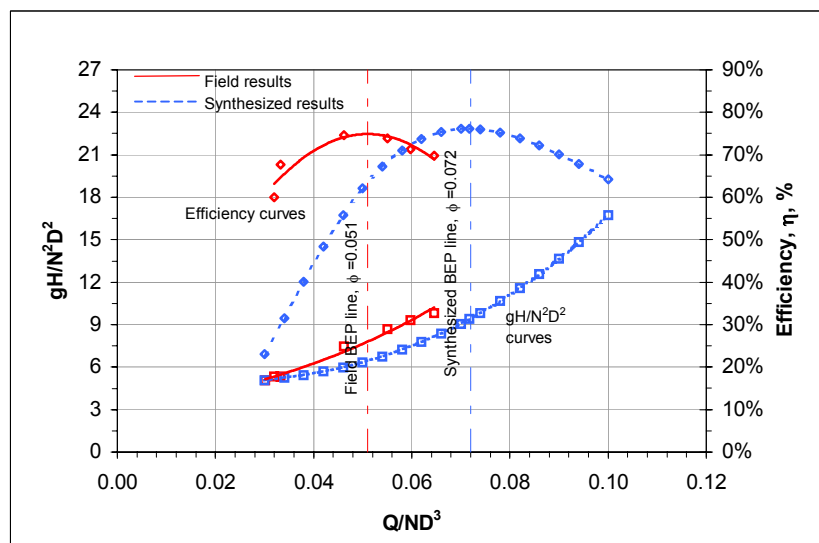
Figure 6.13, Comparison of the field and synthesized H-Q characteristics for PAT2

The comparison at the dimensionless scale between the field and the mean synthesized characteristics is carried out in Figure 6.14. It is clearly found that there are large displacements in the head number and power number characteristics. The field head number curve lies above the mean head number curve and the margin of rise magnify in the BEP and overload region. On the other hand the field power number curve also lies above that of the synthesized curve with considerable displacement. This results in a completely displaced efficiency curve. The field BEP is found to occur at $\phi_{BEP} = 0.051$, as to the synthesized $\phi_{BEP} = 0.072$, which represents a deviation close to 30%.
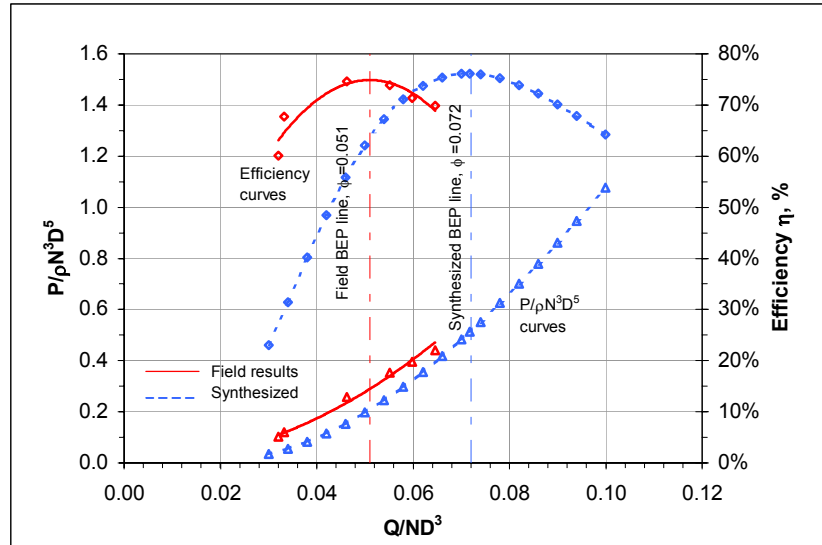
Figure 6.14, Comparison of the dimensionless field and synthesized characteristics for PAT2

6.7.2 Testing of PAT3

The testing on the PAT3 was carried out with the drive of the PAT2 unit active. Also the weir height and subsequently the discharge could not be determined. Therefore the interpretation will be focused on head, power and speed parameters. To determine the net head on the PAT the velocity head has been approximated. The results of the tests are summarized in Table 6.18.

To compare the synthesized mean characteristics with the field characteristics another approach is employed. This approach involves the use of dimensionless numbers based on constant head criterion, i.e. power co-efficient $P/(\rho D^2(gH)^{3/2})$ and speed co-efficient $ND/(gH)^{1/2}$. Figure 6.15 compares the power coefficient curves from the field and the synthesized results.

Table 6.18, Field test results of PAT3

Load Point	H_{net} (m)	N (rpm)	$P_{elec.}$ (KW)	$P_{mech.}$ (KW)
1	28.4	1468	1.9	2.5
2	45.1	1471	5.7	7.4
3	61.2	1472	11.4	15.9
4	66.4	1472	12.8	17.7
5	71.6	1472	14.3	19.6

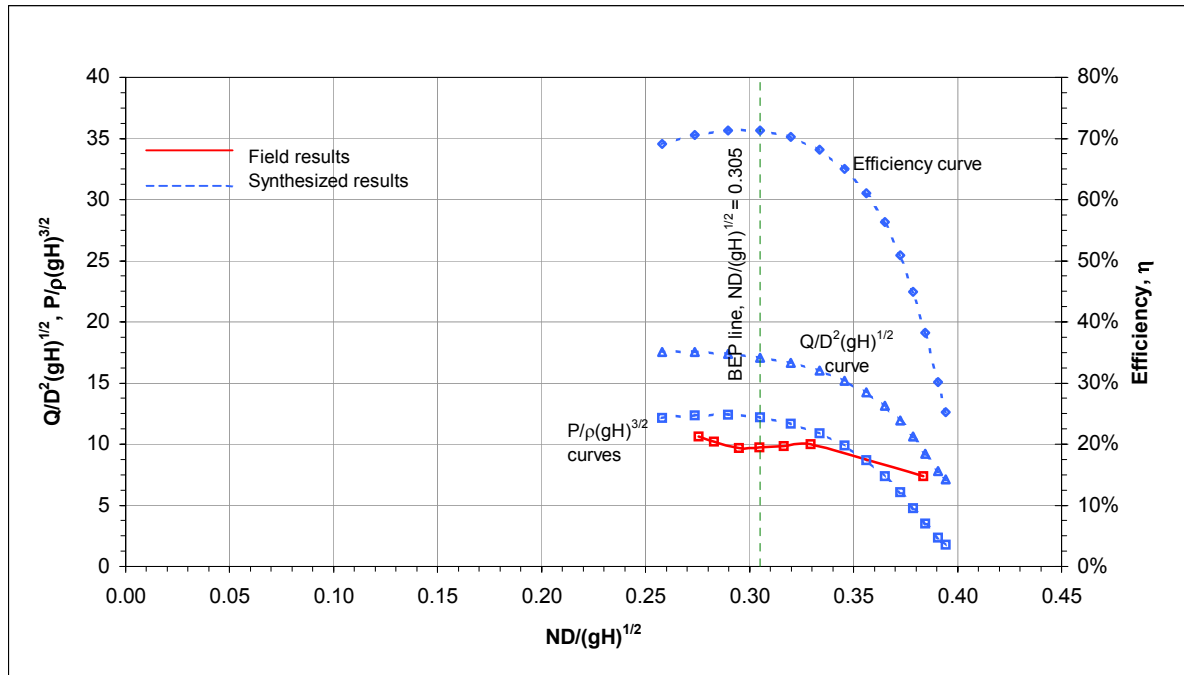|				
6	76.7	1476	15.8	21.6
7	83.6	1477	19.1	26.0
8	86.1	1460	20.9	28.3

Figure 6.15, Comparison of the dimensionless field and synthesized characteristics for PAT3

The field power co-efficient curve is seen to be unstable and does not match well with mean synthesized curve. The power coefficients from field results are at least 15% to 20% below that of the mean predictions in the BEP and over load regions. The discharge coefficient $Q/D^2(gH)^{1/2}$ cannot be plotted for the field results and hence cannot be compared its counterpart. Subsequently the field efficiency curve cannot be determined. Therefore with the currents results it is difficult to comment on the discharge behaviour of PAT 3 in the BEP and overload region. But it is clear from the behaviour power coefficient curves that measured power is below the expected power.

6.7.3   Testing of PAT2 + PAT3

The synchronized test of PAT2 and PAT3 was initiated after carefully bringing the two PATs to no-load synchronous speed of the generator. During the no-load synchronization procedure PAT2 was the first to be started at a low speed and when PAT3 was started, no evidence of jerking or drop in speed was observed. The valves of the two PATs were alternately operated upon to reach 1500 rpm of the generator or main shaft speed. Loading of the PAT3 was accomplished first and subsequently PAT2 was loaded. The entire

operation of synchronization was smooth and there were no problems with respect to hydraulic or mechanical instability.

The test results synchronized load test of PAT2 and PAT3 are illustrated in Table 6.19, where it is observed that an electrical output of 76.4 KW$_{elec.}$ was generated at maximum load point consuming a total discharge of 168.6 l/s.

Table 6.19, Field test results of the synchronized operation of PAT2 and PAT3

Load	PAT 2		PAT 3		Q$_{TOTAL}$	Total P$_{elec.}$
Point	H$_{net}$	N	H$_{net}$	N		
	(m)	(rpm)	(m)	(rpm)	(l/s)	(KW)
1	44.2	1237	66.8	1472	78.3	24.7
2	54.6	1237	75.1	1472	120.4	40.4
3	61.1	1237	78.3	1473	139.0	58.8
4	70.7	1237	77.3	1473	148.6	63.2
5	78.2	1237	77.3	1473	168.6	76.4

The comparisons of the field measurements with the synthesized results are carried out with respect to the discharge consumed and the power generated. Table 6.20 compares the total synthesized discharges through PAT2 and PAT3 at the similar net head and speed conditions as measured in field trials with the measured discharges. It is observed that the synthesized discharge is consistently greater than the measured at all load points having over 10% prediction errors.

Table 6.20, Comparison of the field and synthesized discharges in the synchronized operation of PAT2 and PAT3

Load	PAT 2		PAT 3		Synthesized Q	Measured	Deviation
Point	H$_{2\,net}$	Q$_{Syn\,2}$	H$_{3\,net}$	Q$_{Syn\,3}$	Q$_{Syn\,2}$ + Q$_{Syn\,3}$	Q	
	(m)	(l/s)	(m)	(l/s)	(l/s)	(l/s)	(%)
1	45.5	**63.0**	66.8	**46.5**	**109.5**	78.3	-39.9
2	54.6	**92.0**	75.1	**50.7**	**142.7**	120.4	-18.5
3	61.1	**105.0**	78.3	**52.1**	**157.1**	139.0	-13.0
4	70.7	**120.0**	77.3	**51.7**	**171.7**	148.6	-15.5
5	78.2	**129.5**	77.3	**51.7**	**181.2**	168.6	-7.5

The synthesized and measured powers are compared in Table 6.20 where it is again seen that the total synthesized power is greater than the measured power in the range of 10% to 18%.

Table 6.21, Comparison of the field and synthesized output powers in the synchronized operation of PAT2 and PAT3

Load Point	PAT 2		PAT 3		Synthesized P	Measured P	Deviation
	$H_{2\,net}$ (m)	$P_{Syn\,2}$ (KW)	$H_{3\,net}$ (m)	$P_{Syn\,3}$ (KW)	$P_{Syn\,2} + P_{Syn\,3}$ (KW)	P (KW)	(%)
1	45.5	**7.0**	66.8	**15.2**	**22.2**	24.7	10.0
2	54.6	**24.4**	75.1	**21.6**	**46.0**	40.4	-13.8
3	61.1	**35.9**	78.3	**23.4**	**59.3**	58.8	-0.8
4	70.7	**51.6**	77.3	**23.1**	**74.7**	63.2	-18.3
5	78.2	**65.4**	77.3	**23.4**	**88.8**	76.4	-16.2

The large deviations seen in the Table 6.20 and 6.21 are obvious since in section 6.7.1, it was found that the ψ-ϕ curve of PAT2 to be displaced causing its BEP point to shift to the left of the synthesized characteristics. There have also been some deviations with respect to PAT3's power characteristics however extent of deviation in discharge could not be ascertained.

6.7.4 Uncertainty Analysis

The detailed uncertainty analysis for the field measurements (net head, discharge and electrical power) is carried out in section A9.4, Appendix A. It is seen that the measurements have been of mediocre quality with large uncertainties (Table A9.23 and A9.24) associated with the variables.

6.7.5 Discussion

The field results can be viewed from many perspectives. The first perspective is related to the direct comparison of the field results with synthesized results, while the second perspective is concerning the uncertainties existing in the methodology of recording the various parameters. As seen the measurement techniques (section A9.4, Appendix A) have been crude and it is not possible to draw any firm conclusions as far as the accurate performance comparisons are concerned. However broad conclusions based on intuitive skills could be drawn.

Other features of the project namely, dealing with the boundary criteria and part-load operation, the selection of the PATs, the accuracy of the synthesis model, the synchronized operation, mechanical and hydraulic stability, bypass, internal optimization techniques are also discussed.

6.7.5.1 Performance of PAT2

As seen the full load test on PAT2 is the only test that could be fully analyzed from all perspectives. Figure 6.13 shows that the field H-Q curve is completely deviating from the synthesized H-Q curve. Before blindly blaming the selection or the synthesis model employed for this deviation, a further investigation needs to be pursued. In Figure 6.14 it is seen that displacement of the field head number curves are similar to that in Figure 6.13 (absolute scale). But interestingly the power number curve for the field results has risen tremendously over that of the synthesized results. The field efficiency characteristics have gotten laterally displaced with the BEP point occurring at 25% lower discharge number.

To discuss the results the damaged conditions of the impeller (as mentioned in section 6.7.2) needs to be kept in mind. This condition of the PAT2 impeller is similar to that of the 45.2 rpm PAT (in Figure A5.9, section A5.1.4, Appendix A), in which it was found that a broken shroud piece resulted in an increased power production. This particular behaviour in the 45.2 rpm PAT was linked to the change with respect to the net rotational momentum across the impeller. An identical effect may also be occurring in the PAT2 impeller as well. The proposed rise in the net rotational momentum is causing the rise in the power generation and simultaneously increasing the net head consumed by the PAT2 as seen in Figure 6.14. The hydraulic losses in zone *ii* and *iii* would also increase for the damaged impeller, which naturally adds on to the further increase on net head consumed (from Equation (2.5) in Chapter 2). The increased losses in zone *iii* would reduce the net power output, but the rotational momentum effects seem to have dominating effects on the net power output. Though the conditions of the impeller are affecting the field characteristics, the magnified deviations cannot be fully owed to the damaged impeller only.

From the perspective of the uncertainties, Table A9.23 (Appendix A) shows over $\pm 15\%$ to $\pm 20\%$ with respect to the discharge measurement alone and another ± 7 to $\pm 10\%$ with respect to the power determined. The deviations in Figure 6.14 could also be directly a result of degree of these uncertainties. For concurrence of the field and the synthesized curves, the discharge measurement should have been underestimated causing the shift of the head number and power number curves to shift to the right along with a probable overestimation or underestimation of power measured.

The deviations in the field results could also be a result of inaccuracy in the synthesis model. It appears that the allocation of the head number at the BEP (section 6.4.1, step 5) is all right, but the allocation of the discharge number may be slightly exaggerated. Subsequently

there could also be a mistake in the construction of the mean ψ-ϕ and η-ϕ curves, with a different BEP (section 6.4.1 and <u>step 6</u>).

Therefore the field results for the PAT2 and the subsequent deviations could be combination of the possible errors in the synthesis model, damaged conditions of the impeller and the prevailing uncertainties of the measured parameters. To a realistic estimate of the accuracy of the synthesis model, it is recommended to replace the PAT2 impeller and improve the accuracy of the measurement methodology.

6.7.5.2   Performance of PAT3

The testing on PAT3 has been incomplete as seen in section 6.7.2, with non-availability of discharge measurements. With only the speed, net head and power output the comparisons between the field and synthesized results have been carried out in <u>Figure 6.15</u>. The power coefficient curve for the field results has fallen below the synthesized curve. These deviations could be only discussed from the perspectives of the accuracy of the model and the uncertainties in the measured parameters.

From the perspectives of the uncertainties, the concurrence can be caused only by the underestimation of the power. With maximum errors of $\pm 10\%$ near the BEP region (from <u>Table A9.24</u>, Appendix A), the role of uncertainty cannot be ruled out. The accuracy of the model cannot be easily determined with the discharge utilization patterns not available. However one of the possible scenarios can be considered, in which no uncertainties exist in the power measurements and the efficiency curves for the two methods being nearly identical.   This scenario could only mean that there is decreased discharge utilization through the PAT 3. This directly represents an inaccuracy of the synthesis model with respect to a higher discharge number assigned at BEP (section 6.4.2, <u>step 5</u>) and also questions the construction of mean ψ-ϕ curve (section 6.4.2, <u>step 6</u>).

The overall deviations in PAT 3 can be termed as combination of small inaccuracies in the synthesis model and various uncertainties in measurements. To get a true assessment of the synthesis model, the testing needs to be carried out with measurement of all parameters using more accurate methods.

6.7.5.3   Fulfillment of Demand Criterion

From the demand criterion listed in section 6.2.2, condition 2, i.e. a guaranteed output of 70 to 75 KW_{elec} seems to be easily achieved from the results of synchronized PAT2 and PAT3 operation where over 76 KW_{elec} was generated (section 6.7.3).

Condition 3 (of section 6.2.2) also appears to be easily achieved from individual testing of PAT2, in which a maximum of 56.4 KW_{elec} was produced. The condition 3 (of section 6.2.2)

for lean flow season also seems to negotiated with over 20 KW_{elec} easily generated by PAT3 even though the discharge utilization could not be confirmed.

Though the condition 1, i.e. of 100 KW_{elec} could not be verified, the fulfillment of condition 2, 3 and 4 only goes to say that the selection of the PATs are genuine and appropriate.

6.7.5.4 Accuracy of Synthesis Model

It has come notice during the analysis of field results for both PAT2 and PAT3 there are some evidences of the synthesized performance characteristics estimating a greater discharge through the PAT units. But the exact extent of the deviations could not be ascertained as the field results have considerable uncertainties associated with them.

The positive aspect is that the maximum conditions of the synchronized operation of PAT2 and PAT3 as measured is defined by 168 l/s and 76.4 KW_{elec} (Table 6.18, section 6.7.3) is fitting very well with the range of 160 to 180 l/s and 73.4 to 85.8 KW_{elec}, as proposed by the combined operational table based on the synthesized results (in Table 6.15, section 6.5.4). This can be termed as a success for the synthesis model developed.

6.7.5.5 Synchronized PAT Operation

The smooth and trouble-free operation of the synchronized operation of the PAT2 and PAT3 proves that such a design is hydraulically and mechanically stable. However safety of such designs can be guaranteed only if a thorough startup and shut off procedure is meticulously followed. Since both PAT2 and PAT3 are radial flow PATs, only quadrant to be negotiated is 'D' before the operation energy generation quadrant 'C' and the intensities of negative torques in quadrant D at low speeds are so negligible that not a single jerking effect was felt during synchronizing the two PATs at no-load speeds.

6.7.5.6 Mechanical Design

The intensive mechanical design calculation (section A9.3, Appendix A) can be justified, as it was important to study the load patterns, stress involved and the approximate resonating conditions of the system. The fact that under operating conditions of 1500 rpm of the generator, with individual and synchronized operation of PAT2 and PAT3 no evidence of resonance or dangerous vibrations were observed clearly validate the calculations and justifies the rigorous design process.

6.7.5.7 Internal Optimization of Geometry

Though two (optimization stage I and II) of the four internal optimization stages (section 6.4.3) of the PAT research programme were implemented on all the PAT units of the project, its actual influence could not be ascertained, as no reference data on non-modified stages was available. These optimizations stages comprising of Inlet impeller rounding and casing rib removal would have definitely have influenced the performance.

6.7.5.8 Bypass and Runaway Design

Since no situation of runaway occurred during the entire field-testing the validity of this open bypass design (section 6.5.3) for managing runaway could not be physically verified. However one major deficiency was observed with respect to the bypass valve. The butterfly design chosen needed extremely high torques to open under maximum pressure (9.5 Bar) conditions on the upstream side and could not be opened by hand. Also at this semi-opened valve position, tremendous noise due cavitation was heard, which is an obvious phenomenon in such operating conditions in butterfly valves. Therefore quick opening of the butterfly valve under runaway may prove a tough task. It is recommended to find a solution to the valve operation under these conditions.

7. Hydro-Economics of PAT Systems

One of the chief objectives of the dissertation programme (as seen from objective no. 8, section 1.2, Chapter 1) is to evaluate the hydro-economics of the micro hydro projects that are based on the PATs. The term hydro-economics in this context is associated with the resource utilization and the output delivered. The efficacy with which a system utilizes the two resource parameters namely the constant head and the variable discharge on one hand, and correspondingly how efficiently it converts the utilized resources to deliver the output power on the other hand, are the two guiding phenomena that define the hydro-economy of the given system.

As seen time and again throughout the dissertation (problem 3, section 1.3.3 of Chapter 1 and section 5.6 of Chapter 5) that the part-load operational problem in PATs is symbolized with not only with a drop in efficiency but also decreased utilization of the constant resource parameter, i.e. the available head. Therefore a PAT system under part-load conditions signifies a poor condition of hydro-economy. However before generalizing this condition, it is important to quantify the hydro-economic condition as a parameter and evaluate this parameter for different PAT options. To study the merits of such systems it often preferred to have a defined criterion for this parameter based on acceptable levels hydro-economy.

Based on the defined criterion of hydro-economy, it will be an interesting exercise to study all PAT options namely (single or multiple units) in comparison with a conventional turbine option. This analysis, however does not involve cost economics and relates only to the hydraulic characteristics of respective machines.

7.1 Weighted Average Efficiency

Small and micro hydro projects cannot be directly compared to the established criterion of hydro-economy for large hydro projects. To study the merits of small and micro systems some of the institutions have evolved their own criteria. UREDA [55] one such institution has prescribed the use of a pre-defined value of 'weighted average efficiency' as a hydro-economic criterion. The weighted average efficiency is determined from the conditions at 3 load points namely, the 100% load (100%P), 80% load (80%P) and 60% load (60%P) and defined by,

$$WAE = \left(WF_{100} \times \eta_{t\,100} \times \eta_{G\,100}\right) + \left(WF_{80} \times \eta_{t\,80} \times \eta_{G\,80}\right) + \left(WF_{60} \times \eta_{t\,60} \times \eta_{G\,60}\right) \quad (7.1)$$

where, WF_{100}, WF_{80} and WF_{60} are the 'weight factors' for the WAE equation at 100%P, 80%P and 60%P load points. UREDA has specified the following values for the weight factors.

$$WF_{100} = 0.6, WF_{80} = 0.2, WF_{60} = 0.2, \qquad (7.2)$$

with $WF_{100} + WF_{80} + WF_{60} = 1.0$.

The value of the weighted average efficiency, according to [2] should not fall below 60% or 0.6, for any micro hydro system. Therefore the criterion can be defined as,

$$WAE \geq 0.6 \text{ or } 60\% \qquad (7.3)$$

η_{t100}, η_{G100}, η_{t80}, η_{G80}, η_{t60}, η_{G60} are efficiencies of the turbine and generator unit at 100%, 80% and 60% of rated outputs. Any shortfall in the WAE attracts severe penalties and may also lead to rejections. The hydro-economic criterion as defined by UREDA in Equation (7.3), hence can be used as the means of analyzing the merits of all PAT systems.

The turbine mode efficiencies for the different load conditions, i.e. 100%P, 80%P and 60%P points, should be calculated based on the rated head (100%H) at 100% load point and not on the local operating head on the PAT.

7.2 Application of Hydro-Economic Criterion

The hydro-economic criterion, i.e. the weighted average efficiency is applied on different PAT options, namely the simple single PAT unit and the more sophisticated multiple PAT unit (developed to deal with the part-load problem, section 1.3.3, Chapter 1). Even within the single PAT option, different specific speeds/designs needs to be considered. This weighted average efficiency is subsequently also applied to an ultimate option of a conventional turbine, i.e. a model Francis turbine.

Two single PAT options from the PAT test programme (Table 3.4, section 3.2, Chapter 3) are chosen for the hydro-economic evaluation, namely the radial flow 39.7 rpm PAT and the mixed flow 94.4 rpm PAT. The multiple PAT system developed in the Case Study of Chapter 6 is also subjected to the hydro-economic evaluation.

7.2.1 Single PAT unit

7.2.1.1 39.7 rpm PAT system

The hydro-economic criterion for the 39.7 rpm PAT system is analyzed in Table 7.1, with the rated condition defined by a mechanical power (100%P) of 22.8 KW, head (100%H) of 30.3

m and discharge (100%Q) of 92 l/s. The rated condition selected in this case is corresponding to the BEP at an operating speed of 1500 rpm.

Table 7.1, Summary of the hydro-economic criterion for the 39.7 rpm PAT

Percent Load	Load (KW)	H_{net} (m)	Q (l/s)	η_t (%)	$\eta_{t\,rated}$ (%)	η_G (%)	$\eta_t * \eta_G$ (%)
100%P	22.8	30.3	92	83.4%	83.4%	86.0%	71.7%
80%P	18.2	26.8	84	82.6%	73.1%	84.0%	61.4%
60%P	13.7	23.2	75	80.1%	61.4%	83.5%	51.2%

Then the weighted average efficiency, based on Equation (7.1) is given by,

$$WAE = (0.6 \times 83.4\% \times 86\%) + (0.2 \times 73.1\% \times 84\%) + (0.2 \times 61.4\% \times 83.5) = 65.5\% \qquad (7.4)$$

This value of WAE for the given radial flow PAT is greater than 60% criteria set by UREDA [55]. However it is important to study the operating ranges of the heads and discharges at these load points with respect to the rated conditions.

It is seen from Table 7.2 that operating heads extend from 76.6%H to 100%H and discharges vary from 81.5%Q to 100%Q for 60% to 100% load conditions. This result signifies that the PAT cannot utilize nearly 24% of the rated head at 60% load condition (which is essentially getting throttled through the control valve). On the discharge side, it implies that the PAT would still require 81.5%Q to operate at 60% load point.

Table 7.2, Range of the head utilization and discharge requirement for the 39.7 rpm PAT at different loads

Percent Load	Head Utilization	Discharge Requirement
100%P	100.0%H	100.0%Q
80%P	88.4%H	91.3%Q
60%P	76.6%H	81.5%Q

7.2.1.1   94.4 rpm PAT system

Table 7.3 summarizes the hydro-economic analysis for the 94.4 rpm mixed flow PAT. The rated condition (corresponding to the 100% load) is chosen to be in the overload region, with a net head (100%H) of 10.4 m, a discharge (100%Q) of 115 l/s, a mechanical power (100%P) of 9.7 KW and operating at a speed of 1200 rpm.

Table 7.3, Summary of the hydro-economic criterion for the 94.4 rpm PAT

Percent Load	Load (KW)	H_{net} (m)	Q (l/s)	η_t (%)	$\eta_{t\,rated}$ (%)	η_G (%)	$\eta_t * \eta_G$ (%)
100%P	9.7	10.4	115	82.7%	82.7%	86.0%	71.1%
80%P	7.8	8.9	106.8	83.2%	71.2%	84.0%	59.8%
60%P	5.8	7.4	97	82.7%	58.8%	83.5%	49.1%

$$WAE = (0.6 \times 82.7\% \times 86\%) + (0.2 \times 71.2\% \times 84\%) + (0.2 \times 58.8\% \times 83.5) = 64.4\% \qquad (7.5)$$

The weighted average efficiency of 64.4% is above the acceptable criterion of 60%. From Table 7.4 it is seen that the mixed flow PAT is not utilizing nearly 29%H and it still needs over 84%Q to produce 60% of the rated power output.

Table 7.4, Range of the head utilization and discharge requirement for the 94.4 rpm PAT at different loads

Percent Load	Head Utilization	Discharge Requirement
100%P	100.0%H	100.0%Q
80%P	85.6%H	92.9%Q
60%P	71.2%H	84.3%Q

7.2.2   Multiple PAT unit

As mentioned the multiple PAT system of Ambootia micro hydro project would be used as an example to study the hydro-economic criterion. It is also seen from section 6.7, Chapter 6 that the field tests were incomplete with the no results were available for the synchronization test of PAT1 and PAT2. Therefore for the application of the hydro-economic criterion, the synthesized results from Table 6.16 (section 6.5.4, Chapter 6) would be used. Table 7.5 summarizes the results at 5 five different load points (including 20%P and 40%P loads).

The rated head condition (100%H) is defined as the static pressure at the main junction (shown in Figure 6.1, section 6.3, Chapter 6) corresponding to the total flow through the main penstock line at every load point. The rated load (100%P) is fixed at 120.6 KW$_{mech}$ and rated system discharge (100%Q) at 236 l/s.

<u>Table 7.5</u>, Summary of the hydro-economic criterion for the multiple PAT system

Load	Load	$H_{junction}$	PAT 1			PAT 2			PAT 3			Q_{total}	$\eta_{t\,rated}$	η_G	$\eta_t * \eta_G$
			H_{net}	Q	P	H_{net}	Q	P	H_{net}	Q	P				
(%)	(KW)	(m)	(m)	(l/s)	(KW)	(m)	(l/s)	(KW)	(m)	(l/s)	(KW)	(l/s)	(%)	(%)	(%)
100%P	120.6	71.6	70.6	118.0	60.3	70.6	118	60.3	-	-	-	236.0	72.7%	88.0%	64.0%
80%P	96.5	82.6	82.1	133.0	81.5	-	-	-	58.6	40	15.0	173.0	68.8%	87.0%	59.9%
60%P	72.4	88.5	77	126.8	72.4	-	-	-	-	-	-	126.8	65.8%	86.0%	56.5%
40%P	48.2	90.3	64.5	108.5	48.2	-	-	-	-	-	-	108.5	50.2%	85.0%	42.7%
20%P	24.1	94.3	-	-	-	-	-	-	71.5	48.6	24.1	48.6	53.7%	84.0%	45.1%

The weighted average is determined as ever based on 100%, 80% and 60% loads from Equation (7.1).

$$\mathrm{WAE} = \left(0.6 \times 72.7\% \times 88\%\right) + \left(0.2 \times 68.8\% \times 87\%\right) + \left(0.2 \times 65.8\% \times 86\%\right) = 61.2\% \qquad (7.5)$$

The weighted average efficiency (61.2%) of the multiple PAT system is lower compared to both that of the single PAT options of 39.7 rpm and 94.4 rpm PAT system. However, it is still greater than the acceptability criterion of 60%.

<u>Table 7.6</u>, Range of the discharge requirement for the multiple PAT system at different loads

Percent Load	Discharge Requirement
100%P	100.0%Q
80%P	73.3%Q
60%P	53.7%Q
40%P	46.0%Q
20%P	20.6%Q

The greater advantage of this multiple PAT system is the optimal operation even at 20%P and 40%P points. <u>Table 7.6</u> gives a picture of the range of operating discharges for the different load points. It can be seen that the complete system needs only 53.7%Q at the 60%P point. Even at 20%P point, the entire system requires only 20.6%Q, which is necessarily demonstrates the effective discharge savings of this type of system at part-loads.

7.2.3   Francis Turbine

The Francis turbine (of specific speed N_q = 70.2 rpm) used for the hydro-economic evaluation (Table 7.7) is model machine named Bayano, manufactured by Riva-Hydroart [40]. The rated load (100%P) corresponds to the BEP (η_t = 90.3%) with a head (100%H) of 4.64 m, discharge (100%Q) of 308 l/s, power output (100%P) of 12.7 KW and operating at a speed of 400 rpm.

Table 7.7, Summary of the hydro-economic criterion for the 70.2 rpm Francis turbine

Percent Load	Load (KW)	H_{net} (m)	Q (l/s)	η_t (%)	$\eta_{t\ Rated}$ (%)	η_G (%)	$\eta_t * \eta_G$ (%)
100%P	12.7	4.64	308	90.3%	90.3%	86.0%	77.7%
80%P	10.1	4.44	264.5	87.9%	84.1%	84.0%	70.7%
60%P	7.60	4.34	215	83.0%	77.6%	83.5%	64.8%

$$WAE = (0.6 \times 90.3\% \times 86\%) + (0.2 \times 84.1\% \times 84\%) + (0.2 \times 77.6\% \times 83.5\%) = 73.7\% \qquad (7.6)$$

With weighted average efficiency equal to 73.7%, the Francis turbine classifies a better option compared to any of the options of the PAT system considered. Also from Table 7.8, it can be seen that the Francis turbine's head utilization factor is extremely good. Even at 60%P point the turbine manages to utilize up to 93.5%H, which is very encouraging result. From discharge requirement criterion, the Francis turbine would need nearly 70%Q at the same 60%P conditions.

Table 7.8, Range of head utilization and discharge requirement at different loads for the 70.2 rpm Francis turbine

Percent Load	Head Utilization	Discharge Requirement
100%P	100.0%H	100.0%Q
80%P	95.7%H	85.9%Q
60%P	93.5%H	69.8%Q

7.3   Discussion

The discussion on hydro-economic issue can be pursued in many directions. However, firstly the most crucial result is pertaining to the single PAT system, which has always been considered to be highly disadvantageous in terms of its part-load performance. This myth seems to have been eliminated especially after the two single PAT options, the radial flow 39.7 rpm PAT and the mixed flow 94.4 rpm PAT, easily satisfying the hydro-economic criterion (with WAE equal to 65.5% and 64.4% respectively).

7.3.1   Comparisons of Weighted Average Efficiencies

The weighted average efficiency along with the combined turbine-generator efficiencies at the three load points is compared in <u>Table 7.9</u> for all the four turbine options.

The 39.7 rpm radial PAT and 94.4 rpm mixed flow PAT were the best of the 8 PATs that were experimentally tested. However it is the radial PAT, which seems to have a greater hydro-economic value mainly due to higher combined $(\eta_t * \eta_G)$ efficiencies at all part-load points (80%P and 60%P) and hence a slightly higher weighted average efficiency (WAE = 65.5%) compared to the mixed flow PAT (WAE = 64.4%).

The multiple PAT system seems to have the lowest weighted average efficiency, but it still early to make any conclusions. The weighted average efficiency for this system has taken a shortfall mainly due to lower operating efficiencies of PAT1 and PAT2 at the 100%P point. However, some positive features are observed with respect to the high values of combined turbine-generator efficiency $(\eta_t * \eta_G)$ at lower loads compared to the single PAT options. At the 60%P point the multiple PAT system has a $\eta_t * \eta_G$ = 56.5% compared to 51.2% for the 39.7 rpm PAT and 49.1% for the 94.4 rpm PAT.

The Francis model turbine however stands out as the best machine with the highest weighted average efficiency of 73.7%. This is an obvious result due to the specialized design consideration of casing, runner and draft tube along with the most important feature of varying the orientations of the guide vanes.

<p align="center">Table 7.9, Summary of the weighted average efficiency for all options</p>

	39.7 rpm PAT	94.4 rpm PAT	Multiple PAT	Francis Turbine
$(\eta_t * \eta_G)$ at 100% load	71.7%	71.1%	64.0%	77.7%
$(\eta_t * \eta_G)$ at 80% load	61.4%	59.8%	59.9%	70.7%
$(\eta_t * \eta_G)$ at 60% load	51.2%	49.1%	56.5%	64.8%
Weighted Average Efficiency	65.5%	64.4%	61.2%	73.7%

7.3.2   Head Utilization and Discharge Requirement

The weighted average efficiency gives a reasonable picture of the hydro-economic value of the system. However it does not explicitly talk about two important parameters, namely the head utilization and the discharge requirement at different load points, though within itself it accounts for the above two parameters.

The objective is to have a system that can utilize the maximum available head and requires minimum discharge at respective part-load operations. Therefore the comparison of two systems based on the head utilization and discharge requirement values can also be used as another tool for evaluating the hydro-economic criteria.

7.3.2.1   Head Utilization

Table 7.10 compares the head utilization factors only for the three options of 39.7 rpm PAT, 94.4 rpm PAT and the Francis turbine at 80%P, 60%P, 40%P and 20%P points respectively. Since it is very difficult to determine the accurate head utilization for multiple PAT system, they are excluded from the summary of Table 7.10.

It is observed that the radial flow PAT (39.7 rpm) has consistently shown better head utilization factors at all part-load points compared to that of the mixed flow PAT (94.4 rpm). The Francis turbine again displays excellent head utilization rates (over 90%H) for the 80%P and 60%P points, but the head utilization drops dramatically for the 40%P and 20%P points. At the 20%P point the head utilization of the Francis turbine is only 44.2%H compared to 54.5%H for the 39.7 rpm PAT.

The poorer head utilization comparisons at the 60%P and 80%P points of the PAT units essentially point towards greater percentages of head dissipation through the flow control units of the PAT systems compared to the superlative Francis turbine.

Table 7.10, Summary of the head utilization range at different loads for all single unit options

Load	39.7 rpm PAT	94.4 rpm PAT	Francis Turbine
80%P	88.4%H	85.6%H	95.7%H
60%P	76.6%H	71.2%H	93.5%H
40%P	65.0%H	56.7%H	78.7%H
20%P	54.5%H	40.4%H	44.2%H

7.3.2.2 Discharge Requirement

The discharge requirement rates unlike the head utilization rates can be summarized for all the 4 turbine options in Table 7.11. The comparisons are carried again at all load points, namely 80%P, 60%P, 40%P and 20%P points.

It should be noted that the multiple PAT system, which had the poorest weighted average efficiency of all the options, displays a remarkable change in terms of discharge requirement pattern. In that it requires the lowest discharge at each load points in comparison with all the turbine options (even the Francis turbine option).

It is interesting to see that at a marginal load of 20%P, the multiple PAT system requires only 20.6%Q, while the Francis turbine requires at least 51.6%Q. Therefore from the perspectives of the discharge requirement patterns the multiple PAT system stands unmatchable.

Table 7.11, Summary of the discharge requirement range at different loads for all options

Load	39.7 rpm PAT	94.4 rpm PAT	Multiple PAT	Francis Turbine
80%P	91.3%Q	92.9%Q	73.3%Q	85.9%Q
60%P	81.5%Q	84.3%Q	53.7%Q	69.8%Q
40%P	70.1%Q	74.8%Q	46.0%Q	58.4%Q
20%P	56.5%Q	63.0%Q	20.6%Q	51.9%

The Francis turbine option in comparison with the other single PAT options requires lower discharge rates at all the load points. But is has to be mentioned that the discharge requirement patterns for Francis turbine are not very encouraging at the 80%P and 60%P points with relatively higher discharge requirements (85.9%Q and 69.8%Q respectively - Table 7.11) compared to its head utilization rates at corresponding loads (96%H and 94%H respectively - Table 7.10).

Between the two single PAT options it is observed that the percentage discharge requirements at part-load points for the 39.7 rpm radial PAT are lower compared to that of the mixed flow PAT, which again proves that the radial PAT has a overall better performance compared to the mixed flow PAT. This result cannot be generalized for all radial flow and mixed flow PATs and refers to the specific machines under study.

7.3.3 New Hydro-Economic Criteria

If the hydro-economic criterion defined by Equation (7.2) is going to be used as the basis for judging micro hydro power plants, then PATs (even with a single unit) easily qualify as promising options. However more stringent conditions could be imposed on the Equation

(7.1) and (7.3) especially by increasing the factors WF_{80} and WF_{60} along with considerations for lower load conditions as compared to the 80%P and 60%P points.

Any new hydro-economic criterion method evolved should be applied consistently irrespective of the type of machine and evaluated holistically. However a new hydro-economic criterion will only influence the absolute numbers and may not change the relative values for the different turbine options evaluated using Equation (7.1) and (7.3).

8. Conclusions and Recommendations

The structured control volume and zonal loss distribution approach has given an interesting direction to the understanding of the hydraulic energy transfer in PATs. The 'percentage analysis plots' of measuring the head reduction, power improvement and efficiency rise has provided a good platform for getting a complete picture with respect to the changes in the hydraulic behaviour within the various zones under modified geometric conditions (i.e. during optimization stages).

The optimization programme developed has reconfirmed the fact that zone *ii*, *iii* and *vi* are the most critical zones for energy transfer in PAT.

The optimization stage I, which comprised of rounding of the inlet impeller region (mainly zone *ii* and partly into zone *iv*) has consistently improved the overall performance of all the tested PATs with an efficiency rise of 1% to 2.5% in the BEP and overload region. From the 'percentage analysis plots' it could be concluded that this modification has reduced losses not only within zone *iii* but also in the neighbouring zone *ii*. There were two other important geometric effects that were recorded during this optimization stage. The first one was the axial placement of the impeller within the casing width, which was found to have a tremendous influence on the losses in zone *ii*, *iii* and *iv*. The other one was the back shroud plate that has transformed both the net rotational momentum and the hydraulic loss composition (on the 45.2 rpm PAT).

The optimization stage II that essentially blocked the radial clearance (zone *ii*) using different ring designs has been implemented on only two PATs. The flat ring (on the 79.1 rpm PAT) has caused a tremendous reduction of losses with zone *iii* instead of zone *ii*. Though the interaction component ($H_{L.ii\,b-c}$) of losses in zone *ii* has reduced, the frictional loss component due to solid rings has increased. The flat rings have improved the efficiency in the range of 1.2% to 1.4% in the BEP and overload region. The tapered ring design (on the 39.7 rpm PAT), showed evidences of altered rotational momentum (changed inlet velocity triangle) and particularly, an increase of losses in zone *ii* (severe contraction effects) with an efficiency drop of 1.4% to 1.6% in the BEP-overload region.

The optimization stage III comprising of a systematic expansion of the impeller and casing eye has been carried out on two PATs. This technique essentially increased the part-load performance with the decrease of losses in zone *iv*, *v* and *vi*. In the BEP-overload region the performance marginally dropped for both the PATs. While the 24.5 rpm PAT showed proof of increase of losses in zone *iv-v* and reduction of losses in zone *vi*, the 35.3 rpm PAT in fact displayed an contrasting effect with the presence of increased rotational momentum in addition to the decrease of losses in the zone *iv-v* and zone *vi*. This increased rotational momentum was linked to the net decrease of velocity due to an expanded eye. However the similar modification on 24.5 rpm PAT showed no evidence of increase in rotational momentum.

The optimization stage IV that comprised of studying the influence of the casing eye rib using both global and internal variables on 4 PATs. In the 36.4 rpm PAT and the 46.4 rpm PAT there were evidences of reduced net rotational momentum and decrease in losses in zone *vi*. There was also some evidence of a marginal increase of impeller losses. This complex combination resulted in a decrease of BEP and overload efficiency by 0.5% to 0.7%. The 79.1 rpm with an expanding eye design also showed changes in rotational momentum but no evidences of loss redistribution. The most interesting result was on the 39.7 rpm PAT in which the overall efficiency improved by 1.1% to 1.3% mainly due to decrease in losses within the impeller zone *iv-v* despite the presence of reduction of rotational momentum, which was associated with the considerable cross-sectional area occupied by the rib and its position (in close proximity to the impeller eye).

The internal performance studies showed great symmetry of swirl profiles for the CRA stage across the cross-sectional axis at different load points. The CRA stage also showed enhanced swirls (corresponding to greater rotational momentum) compared to CRP stage, but mainly in the part-load and overload regions.

The uncertainty analysis at BEP showed larger uncertainties associated with discharge and efficiency values for the 24.5 rpm, 35.3 rpm and 45.2 rpm PATs ($\pm4\%$ to $\pm7\%$). However for the other PATs the uncertainties in efficiency values were below $\pm2\%$. These uncertainties would affect only the absolute magnitudes of the variables and would have limited influences on the analysis of the optimization stages (which is only a relative study).

From the individual conclusions of the optimizations stages, following recommendations are made.

i.   The optimization stage I, which is extremely simple should be necessarily implemented on all PATs.

ii. The optimization stage II, can also be considered but the design of the external rings is very critical. This stage may be difficult to implement on smaller pumps and also needs good mechanic skills. However the economic value may need to be considered first.

iii. The optimization stage III can be considered for PATs with smaller eye length and greater contraction but with essentially no performance enhancement. However, this modification has another practical value of sediment flushing and can be very useful.

iv. The optimization stage IV can be implemented if the rib has a considerable geometry (thickness), otherwise removing the rib may just drop the performance slightly.

The CSHN analysis developed has demonstrated its technical completeness to predict the pressure near the suction eye of given PAT for any condition of operating speed and draft tube design including the turbine setting. The Dixon's criterion, which is based on the availability conditions, along with CSHN analysis has proven to be a cost effective and useful methodology to study the critical cavitation in PATs.

The absolute comparisons of the experimental and CFD results for the 3 PATs showed large deviations except for the 39.7 rpm PAT. These deviations could be a result of errors in the modeling technique, since no verification procedure on the CFD model was carried out. The deviations could also be a result of uncertainties that exist in the experimental methods (leakage flow and other variables). However on a relative scale the experiment and CFD are independently predicting a similar behaviour during the optimization stage IV on the 39.7 rpm PAT, which a very encouraging result. It is further recommended to make comprehensive verification procedures on the respective CFD models and carryout other experimental optimization stages to check if similarities exist on a relative platform.

The selection and synthesis approach developed for both radial flow and mixed flow PATs is quite satisfactory. The evaluation studies on PAT2 (Case Study-Ambootia, Chapter 6) based on field measurements showed considerable deviation mainly with respect to discharge requirement, however power outputs and efficiency displayed good correlation. This deviation could be associated to three major factors. Firstly, the damage caused to the impeller may have shifted the entire characteristics. Secondly, the influence of uncertainties could also be present. Finally the model itself may be overrating the discharge number at BEP for PAT2 and subsequently plotting wrong characteristics.

The system design of the PAT system to deal with part-load operation is necessarily incorporated with multiple PAT units either as parallel isolated units or synchronized units. The option of synchronized units has advantages from the perspectives of single load distribution line. But from the hydro-mechanical perspective problems could be encountered. The operating point of any PAT may be shifted into the D and E quadrants (which are the energy dissipation zones) and can be very dangerous or even fatal if precautions are not properly followed during the startup and shutdown of two or more synchronized PAT units. The general mechanical designs of the drive and shaft system needs to be exhaustively carried out for such systems. The experience of the operation of synchronized PAT units in field has been overwhelming with absolutely no negative effects encountered during the critical sequences of startup and shutdown.

The next challenge of PAT system design (irrespective of single or multiple units) is runaway problem. Especially for radial machines the runaway problem is associated with both hydraulic problems due to sudden change of discharge (40% to 60% of the operating discharge) along with increase of net head, which leads to both water hammering in penstock and mechanical problems due to higher operating speed. The mixed flow machines are less prone to hydraulic problems however encounter mechanical problems of higher speeding. A simple design of an open bypass is proposed to deal with both hydraulic and mechanical stability along with excessive rise of operating speed. This bypass design was implemented in the Case Study-Ambootia (Chapter 6), however its performance could not be tested. The runaway issue needs to be overemphasized and taken as a critical design parameter for application of PATs.

It has been quite a revelation that even single PAT units have passed the hydro-economic criterion, the weighted average efficiency (WAE), defined for 3 loads (100%P, 80%P and

60%P). The WAE for the best model PAT (i.e. the 39.7 rpm PAT) is 65.5%, which is not far from the WAE of a medium specific speed Francis turbine (with 73.7%). It has also come to clear notice that the multiple PAT system has an enormous advantage with lower part-load discharge requirement compared to that of a fully regulated Francis turbine. Between the various PAT designs, radial flow PATs seem to have an edge over mixed flow PATs with better head utilization and lower discharge requirement at identical loading points.

With encouraging results from the laboratory and positive feedback from the field, the philosophical journey of 'doing small things in a big way instead of big things' using PATs has just begun on an honest and humble note. Although time will determine how long and how well this journey sustains and flourishes, concerned souls can still make a difference in shaping this journey.

9. References

[1] Acre American Inc. 1980, Small Hydro Plant Development Program; Vols. I, II and III, subcontract No. K-1574, U.S. Department of Energy, Idaho National Engineering Laboratory, Available from National Information Service, U.S. Department of Commerce, Springfield, VA 22161.

[2] Alatorre-Frenk, C. 1994, Cost Minimisation in Micro-Hydro Systems using Pumps-As-Turbines, PhD Thesis, University of Warwick, pp 85-89, pp 142-150.

[3] Anderson, H. H. 1980, Centrifugal Pumps; Trade and Technical Press, 3rd edition, England.

[4] Arndt, R.
Farell, C.
Wetzel, J. M.
1984, Hydraulic Turbines; Chapter 6, In: Small and Mini Hydropower Systems, Edited by Fritz J.J., McGraw-Hill Book Company, New York, pp 6.1-6.62.

[5] Childs, S. M. 1963, Convert Pumps to Turbines and Recover HP; Hydrocarbon Processing and Petroleum Refiner, Vol. 41, No. 10.

[6] Cohrs, D. 1997, Untersuchungen an einer mehrstufigen rückwärtslaufenden Kreiselpumpe im Turbinenbetrieb; Verlag und Bildarchiv, Faragallah, W. H., pp 8-41.

[7] Cohrs, D. 1990, Betriebsverhalten von Kreiselpumpen im Mehrquadranten-Kennfeld; Diplomarbeit, TU Hamburg-Harburg, Arbeitsbereich Wärmekraftanlagen und Schiffmaschinen, Hamburg, Germany.

[8] Cooper, P. 2001, Centrifugal Pump Theory; Section 2.1, In: Pump Handbook, 3rd edition, Edited by Karassik, I.J. et al., McGraw-Hill Series, pp 2.34-2.36, pp 2.49-2.50.

[9] Cordier, O. 1953, Aehnlichkeitsbedingungen für Strömungsmaschinen; BWK (Brennstoff-Wärme-Kraft) Bd. 5, Nr. 10, October, pp 337-340.

[10] Dixon, S.L. 1978, Fluid Mechanics, Thermodynamics of Turbomachinery; 3rd edition, Pergamon Press, Oxford.

[11] Dresig, H.
Holzweissig, F.
2004, Maschinendynamik; 5 Aufl., Springer-Verlag, pp 220-238.

[12] Engel, L. 1932, Die Rücklaufendrehzahlen der Kreiselpumpen; Ph. D Thesis, Technical University of Braunschweig, Germany.

[13] Ensslinger, J. 1952, Wirkungsgradsteigerung von Ventilatoren radialer Bauart durch stroemunstechnisch richtige Formgebung der Fluegelraeder; M.A.N.-Forchungsheft Nr. 2, pp 59-67.

[14] Florjancic, D. 1970, Experimentelle Untersuchungen an einer Pumpe zur Feststellung der Aenderung der Saugfaehigkeit durch Oberflaechenrauhigkeit, durch Mischvorgänge am Laufradeintritt und durch Heisswasserfoerderung, Dissertation ETH Zürich.

[15] Gopalakrishnan, S. 1986, Power Recovery Turbines for the Process Industry; In: Proc. of the 3rd Int. Pump Symposium, Turbomachinery Labs. Texas A and M University, College Station, Houstan, USA.

[16] Grover, K.M. 1984, Conversion of Pumps to Turbines; GSA Inter. Corp., Katonah, New York, USA.

[17] Heninger, L. 1993, Statische und dynamische Versuche an reversiblen hydraulischen Strömungsmaschinen in einem geschlossenen Versuchskreislauf – Entwicklung der Leitechnik und automatisierten Messdatenerfassung, PhD Thesis, TU Wien, pp 47-54.

[18] Hergt, P. 1984, Die strömungstechnischen Eigenschaften von
Krieger, P. Kreiselpumpen im Turbinenbetrieb; In: Pumpentagung
Tommes, S. Karlsruhe der Fachgemeinschaft Pumpen im VDMA, Germany.

[19] Hirschberger, M. 1993, Entwicklung und Einsatz doppelströmiger
Kuhlmann, J. Kreiselpumpen als Entspannungsturbinen; In: Pumpen als Turbinen, Edited by Faragallah, W.H., Verlag und Bildarchiv, Faragallah, W. H., pp 117-132.

[20] International 1965, International Code for Model Acceptance tests of
Electromechanical Hydraulic Turbines; Publication 193.
Commission,
Geneva

[21] Karassik, I.J. 2001, Centrifugal Pumps: Major components; Section 2.2.1,
Heald, C.C. In: Pump Handbook, 3rd edition, Edited by Karassik, I.J. et al., C.C., McGraw-Hill Series, pp 2.132-2.134.

[22] Kasai, T. 1962, Cavitation aspects and Suction Performances of

	Takamatu, Y.	Centrifugal Pumps; In: IAHR Symposium, Sendai, Japan, Edited by Numachi, F.
[23]	Kirloskar Brothers Limited	2002, Catalogues Specifying the Duty Points for DB and KPD pumps; Corporate Research and Engineering Division, Pune, India.
[24]	Kirloskar Brothers Limited	2002, Test Report of MF 25-25 Pump as a Turbine; Corporate Research and Engineering Division, Pune, India.
[25]	Kirloskar Brothers Limited	2003, Report on CFD Analysis of NW4+ Pump as Turbine, Corporate Research and Engineering Division, Pune, India.
[26]	Kittredge, C.P. Thoma, D.	1931, Centrifugal Pumps Operated under Abnormal Conditions; Power, pp 881-884. (English translation of Thoma [54])
[27]	Kittredge, C. P.	1933, Vorgänge bei Zentrifugalpumpenanlagen nach ploetzichen Ausfallen des Antriebs, Diss. TH München, Mitt. d. Hydraul. Inst., TH München.
[28]	Kittredge, C. P. Cooper, P.	2001, Centrifugal Pumps: General Performance Characteristics; Sub Section 2.3.1; In: Pump Handbook, 3rd edition, Edited by Karassik, I.J. et al., McGraw-Hill Series, pp 2.376-2.389.
[29]	Knapp, R.T.	1937, Complete Characteristics of Centrifugal Pumps and Their Use in the Prediction of Transient Behaviour; Trans. ASME, vol. 59, pp 683-689.
[30]	Kovats, A. de Desmur, G.	1968 Pumpen, Ventilatoren und Kompressoren radialer und axialer Bauweise, Verlag G. Braun.
[31]	Krisam, F.	1989, Die Grenzen der Verwendarkeit von Kreiselpumpen, Technik Bd. 3.
[32]	Kumarappa, J.C.	1997, Economy of Permanence; 6th edition, Sarva Seva Sangh Prakashan, Rajghat, Varanasi.
[33]	Lobanoff, V.S. Ross, R.R.	1992, Centrifugal Pumps – Design and Application; 2nd edition, pp 85-109.
[34]	Lueneburg, R. Nelson, R.M.	1992, Hydraulic Power Recovery Turbines; In: Chapter 14 - Centrifugal Pumps – Design and Application, 2nd edition, Lobanoff, V.S. et al., Gulf Publishing Company, pp 246-282.
[35]	Mahadevan, K. Balaveera R. K.	1995, Design Data Hand Book; 3rd edition, CBS Publishers and Distributors, India, pp 384-386.

[36]   Nestmann, F.   2003, Optimization Study on Medium and Low Specific Speed
       Singh, P.   Pumps as Turbines; Sechtes Internationales Anwenderforum,
       Maskey, R.   Kleinwasserkraftwerke, Passau, pp 74-78.

[37]   Nestmann, F.   2004, Detailed Project Report, Design of Turbine and Hydro-
       Singh, P.   Mechanical System, Ambootia Micro Hydro Project,
       Darjeeling, India; Institute for Water Resources Management,
       Hydraulics and Rural Engineering; University of Karlsruhe,
       Germany, pp 1.12-1.25, 3.52-3.86.

[38]   Pfleiderer, C.   1991, Strömungsmaschinen; neubearbeitete 6. Aufl.,
       Petermann, H.   Springer-Verlag, pp 43-50, 191-203.

[39]   Raabe, J.   1989, Hydraulische Maschinen und Anlagen; 2. Aufl., VDI-
       Verlag

[40]   Riva-Hydroart   1996, Test Report on the Bayano model – Francis Turbine;
       Obtained from Voith Siemens Hydro Power Generation
       GmbH, Division – Hydraulic Laboratory, Heidenheim,
       Germany.

[41]   Rodrigues, A.   2003, Hydraulic Analysis of a Pump as a Turbine with CFD
       Singh, P.   and Experimental Data; ImechE, Seminar Proc. of 'Advances
       Williams, A. A.   of CFD in Fluid Machinery Design', London, England.
       Nestmann, F.
       Lai, E.

[42]   Schmiedl, E.   1988. Serial centrifugal pumps operating as turbines; Section
       A-6 'Pumps used as Turbines', Pump Congress, Karlsruhe,
       Germany.

[43]   Schumacher, E.F   1973, Small Is Beautiful: A Study of Economics as if People
       Mattered; Abacus, London.

[44]   Sharma, K.R.   1985, Small Hydro Electric Projects - Use of Centrifugal
       pumps as Turbines; Kirloskar Electric Company Limited,
       Bangalore, India.

[45]   Singh, P.   2004, Hydraulic Performance Optimization in Pumps as
       Nestmann, F.   Turbines; Section 8, Pump Users International Forum 2004,
       Caglar, S.   Karlsruhe, VDMA, Germany.
       Kshirsagar, J.T.

[46]   Singh, P.   2004, Experimental and Computational Studies of the Effect of
       Kshirsagar, J.T.   'Casing Eye Rib' on the Swirl Flow at the Exit of a Pump as
       Caglar, S.   Turbine; Proc. of ASME Heat Transfer/Fluids Engineering

	Nestmann, F. Natanasabapathi	Summer Conference, Charlotte, North Carolina, USA.
[47]	Singh, P.	2001, Establishment of a Test-Rig for Turbine for Micro Hydro and Detailed Testing of a Pump as Turbine; M. Tech Thesis, Centre for Energy Studies, Indian Institute of Technology Delhi, New Delhi, India, pp 24 - 26.
[48]	Singh, P. Harish Kumar, H.N. Praveen, R.N. Shankarappa, C.R.	1998, Laboratory Testing of Centrifugal Pumps as Turbines; BEng Final Year Project Report, Department of Mechanical Engineering, The National Institute of Engineering, University of Mysore, India, pp 27.
[49]	Singh, P. Kshirsagar, J.T. Nestmann, F	2003, Experimental and Numerical Studies on a Pump as Turbine; Proc. of The 7th Asian International Conference on Fluid Machinery, Fukuoka, Japan.
[50]	Surek, D.	1993, Kavitation bei rückwärtslaufenden Kreiselpumpen in Turbinenbetrieb; In: Pumpen als Turbinen, Edited by Faragallah, W.H., Verlag und Bildarchiv, Faragallah, W. H., pp 242-264.
[51]	Surek, D.	1993, Leistungsoptimierung von Kreiselpumpen im Turbinenbetrieb mittels Frequenzumrichter; In: Pumpen als Turbinen, edited by Faragallah W. H, Verlag und Bildarchiv, Faragallah W. H, pp 73-94.
[52]	Stepanoff, A. J.	1957, Special Operating Conditions of centrifugal Pumps – Chapter 13; In: Centrifugal and Axial Flow Pumps, John Wiley & Sons, Inc., pp 269-292.
[53]	Swanson, W. M.	1953, Complete Characteristic Circle Diagram for Turbo-Machinery; Trans. A.S.M.E., Vol. 75, 819-826.
[54]	Thoma, D.	1931, Vorgaenge beim Ausfallen des Antriebes von Kreiselpumpen; Mitt. Hyd. Inst. Tech. Hochschule, Muenchen, Vol. 4, pp 102-104.
[55]	UREDA	2003, Design, Supply, Erection, Testing and Commissioning of Electro-mechanical Equipments and Associated Works of 2×50 KW BANK, Micro Hydel Project in District Chamoli, Uttaranchal; Tender notice from Uttaranchal Renewable Energy Development Agency, Zila Panchayat Bhawan, Almora, pp 33 - 37.
[56]	Warrilow, J.	1993, The Turbine Operation of a Medium Head Centrifugal

		Pump; BEng Final Year Project Report, Dept of Mechanical Engineering, Nottingham Trent University, England.
[57]	Williams, A. A.	1992, Pumps as Turbines used with Induction Generators for stand-alone Micro-hydroelectric Power Plants; PhD Thesis, Nottingham Trent University, pp 51-80, pp 88-91, pp 149-153.

Appendix-A

A1   Swirl Flow Physics at PAT Exit

The flow at exit blade interface zone v of the PAT control volume (Figure 2.2 and 2.8, Chapter 2) is essentially comprises of,

i.   Peripheral velocity component, u_2

ii.   Relative velocity component, v_{r2}

iii. Meridional velocity component, v_{m2}

iv.   Swirl component, v_{u2}

v.   Absolute velocity v_2

Singh et al[46] described in detail the characteristics of the flow at the exit of medium specific speed PAT assuming a 2-dimensional frame (neglecting the radial velocity component) using both experimental and numerical studies on the swirl flow.

There are two levels at which the hydraulics should be considered. First consideration is with respect to a given load point and second with respect to different load points.

A single load point

Given a constant operating speed and at a given radius of the blade profile, the peripheral velocity u_2 is fixed. It is also well known that blade profiles at PAT exit have varying radii from the hub towards the shroud. For a given discharge Q, v_{m2} will be fixed across the entire blade profile (D_{2f} and D_{2b} of Figure A4.1, section A4). Therefore for different flow lines across the profile, the velocity triangles, with constant v_{m2} have different peripheral u_2 components and hence different absolute velocity v_2 and swirl velocity v_{u2} components as seen in Figure A1.1.

Four flow lines namely fl_1, fl_2, fl_3 and fl_4 have been analyzed. Flow line 'fl_1' represents the 'maximum' radius condition and flow line 'fl_4', the minimum radius section. The velocity triangle in Figure A1.1 is drawn based on ideal conditions of infinite blades and no shock. The swirl component is hence found to have maximum value at the far exterior point of the blade profile. Therefore the swirl velocity and its direction varies across the cross-sectional plane in the zone v, for given load point, specified by the discharge number, Q/ND^3.

Different load points

Further during loading conditions (under constant speed conditions and varying flow conditions) there are independent and unique swirl profiles associated with each load at each flow line. Figure A1.2 illustrates the velocity triangle at different load points defined at the maximum radius of the blade profile (flow line-fl_1) at three different points, namely part-load, swirl free and overload points respectively. In drawing these triangles the slip condition at the exit is neglected and infinite blades have been assumed.
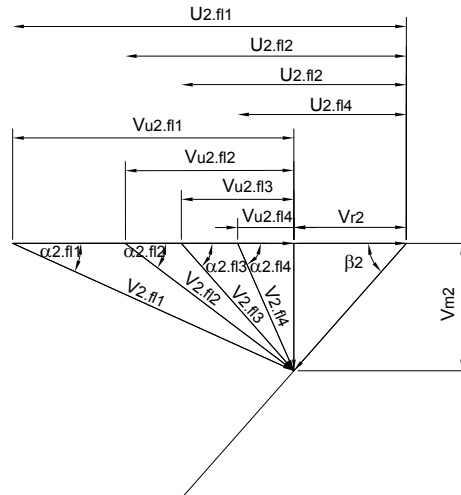
Figure A1.1, Turbine mode exit velocity triangles for different flow lines at a given load
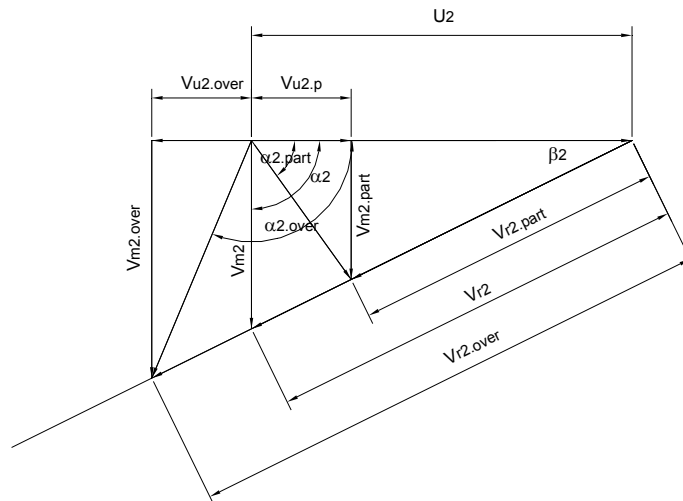
Figure A1.2, Turbine mode exit velocity triangle at different load points for a given flow line

It is observed that the swirl component v_{u2} continuously decreases as the load increases. At one load point the swirl component gets nullified and in the overload condition, the swirl component changes in direction and increases continuously at greater loads.

The study of the cross-sectional profiles of the swirl at different load points is one of the problems of the PAT research. To simplify the experimental investigation the flow in zone *vi* can be assumed to have only tangential (or swirl component) and axial components and no radial component (as recommended by Singh et al[46]). Therefore the flow can be characterized by only three components namely,

    i.   Meridional velocity component, v_{m2}

    ii. Swirl component, v_{u2}

    iii. Absolute velocity, v_2

A2   Cavtitation Theory in PATs

A2.1   Requirement based cavitation in PATs

Any study on the requirement-based cavitation should furnish what is known as the 'Net Positive Suction Head Required' or NPSHR and the subsequently the critical Thoma's factor σ_{cr}. From the textbook definition NPSHR, it is the minimum head that is to be supplied externally to overcome the losses in the critical region of the machine and to prevent cavitation.

There are two methods of determining the NPSHR. One is a detailed experimental method as specified by standardization Institutes that include either the breakdown of the H-Q curve by a preset percentage (1%, 3%, 5% or 10%), prescribed noise levels or bubble size and number. The pressure at the critical region at the breakdown point is recorded and the NPSHR evaluated for that particular flow and operating speed.

The other method of determining NPSPR is an analytical method of calculating the losses in the critical region of the PAT. This was first introduced by Pfleiderer [38] for pumps and later adapted by a host of researchers who modified the basic Pfleiderer's equation and proposed different equations for predicting NPSHR depending on their experiences.

Lobonoff [33] carried out a detailed methodology of finding out the NPSHR in pumps. It consisted of determining the frictional and shock losses at the blade entry in pump mode.

$$NPHSR = \frac{k_{m.NPSHR}v_m^2}{2g} + \frac{k_{r.NPSHR}v_r^2}{2g} \qquad (A2.1)$$

$\frac{k_{m.NPSHR}v_m^2}{2g}$ is the frictional and acceleration loss component, while $\frac{k_{r.NPSHR}v_r^2}{2g}$ represents the blade entry (shock component) losses. Lobonoff published charts for these coefficients, based on the suction area and the blade angle cum absolute flow angle respectively. $K_{m.NPSHR}$ and $k_{r.NPSHR}$ assume different proportions in different specific speed of pumps. While in low specific speed pumps the acceleration component assumes a greater proportion and in higher specific speed pumps the shock component assumes greater contribution.

Heninger [17] was one of the only researchers to do a thorough investigation on cavitation from the requirement criterion. He carried out experimentation on a radial flow pump of 33 rpm and propeller pump both in pump mode and turbine mode. On the 33 rpm radial pump he performed the 1%, 3%, 5% and 10% head-drop tests both in pump mode and turbine mode respectively.

Heninger developed specifically for radial flow pumps a host of analytical prediction equations for the NPSHR predictions based on individual equations published by researchers like Pleiderer [38], Raabe [39], Krisam [31], Kovats [30], Florjanic [14] and Kasai [22]. He also defined a new cavitation co-efficient σ_u, which is similar to Thoma's cavitation

coefficient except that the tangential velocity head at the suction blade area replaces the net head H in the Thoma's definition.

$$\sigma_u = \frac{NPSHR}{\dfrac{u_2^2}{2g}} \qquad (A2.2)$$

He categorized the various NPSHR prediction equations into two categories and then calibrated the individual coefficients $K_{m.NPSHR}$ and $k_{r.NPSHR}$ for each of those forms of the NPSHR equations using the individual results from the 1%, 3%, 5% and 10% head-drop criterion.

On the propeller pump, Heninger has restricted himself to the comparison of the obtained NPSHA values for the pump and turbine modes at identical condition. Within the radial flow PAT, he showed that the cavitation coefficient σ_u was less than 50% of that of the pump mode at respective BEPs. This gave the first evidences of excellent cavitation behaviour of pumps in turbine mode operation. On the propeller machine he reported the σ_u was still lower (80% to 90%) of the corresponding pump mode at BEP.

Surek [50] another contributor of requirement-based caviation in PATs carried out physical studies on a 20 rpm pump both in pump and turbine modes. Similar to Heninger he too published values of constants $K_{m.NPSHR}$ and $k_{r.NPSHR}$ and also agrees sum of the acceleration and the shock component at PAT exit is smaller that that in pump mode. This further reinforces Heninger's claim on less-pronounced cavitation in turbine mode operation.

Alatorre-Frenk [2] also performed simple cavitation measurement on a 36.4 rpm PAT using noise as the predefined reference parameter for calculating the cavitation coefficient. He also found that it would need drastic boundary conditions like excessive static suction elevation and high operational speeds for PAT to operate near the cavitating zone.

Therefore based on the previous research work, it can be summarized that PATs exhibit promising and safe cavitation characteristics, from requirement criterion.

A2.2 Availability based cavitation in PATs

Cavitation studies based on availability criterion by and large imply to the boundary conditions that are external to the PAT, namely the draft tube design and the established turbine setting. This study involves the determination of NPSHA for different operating conditions and comparing with the NPSHR characteristics of the machine and ensuring that NPSHA is always greater at corresponding flow conditions.

NPSHA is defined at the critical pressure region of the PAT, i.e. exit of the PAT at reference plane '2'.

$$NPSHA = H_a - H_v + \frac{p_2}{\rho g} \qquad (A2.3)$$

The value of critical pressure $p_2/2g$, is obtained from the Bernoulli's equation defined between section '2' and draft tube exit, 'a'.

$$\left(\frac{p_2}{\rho g}\right) = \left(\frac{p_a}{\rho g}\right) - \left(\frac{v_2^2 - v_a^2}{2g}\right) - z_s + \left(H_{L.vi} + H_{L.vii}\right) \quad \text{(A2.4)}$$

The determination of the $p_2/2g$ as seen from the above equation (A2.3) is based on the conditions of the downstream. However, $p_2/2g$ will also be influenced by upstream conditions of section '2', i.e. the impeller control volume, zone *iii-iv-v*, which also includes parameters like impeller flow area, blade angle, curvature and blade angle.

Analysis of every term of the right hand side of Equation (A2.4) gives a better understanding of their effects on the bahaviour of $p_2/2g$.

i. Draft tube loss, $\left(H_{L.vi} + H_{L.vii}\right)$:

As seen from section 2.3.4 and 2.3.5 (Chapter 2), the combined draft tube loss depends not only on the absolute discharge (Q) condition but also on the swirling behaviour of the flow emerging out of the PAT exit at exit plane 2. This term will always be positive. The meridional draft tube loss component can be reduced with a good draft tube design. However this term will always make the pressure p_2 more positive.

ii. Velocity gain, $\left(\frac{v_2^2 - v_a^2}{2g}\right)$:

A draft tube with good velocity gain is always recommended for all PAT installations like any other turbine installation. The velocity gain will reduce the pressure $p_2/2g$ essentially making it more negative.

iii. Suction elevation, z_s:

This is an important control parameter for the pressure $p_2/2g$. By incorporating a very large z_s, the pressure p_2 can be substantially reduced. The selection of this parameter should balance the effects of cavitation in the process of increasing the net head on the PAT unit.

The availability criterion when applied to pump mode operation would result in the following equation on $p_2/2g$.

$$\left(\frac{p_2}{\rho g}\right) = \left(\frac{p_a}{\rho g}\right) - \left(\frac{v_e^2 - v_a^2}{2g}\right) - z_s - \left(H_{L.vi} + H_{L.vii}\right) \quad \text{(A2.5)}$$

Here it can be seen that the synonymous draft tube losses $\left(H_{L.vi} + H_{L.vii}\right)$ for pump mode is negative rather than positive as in turbine mode. Therefore the critical pressure $p_2/2g$ drops

further and this prompts the further decrease of NPSHA values. Therefore the NPSHA–Q curve in pump mode possesses a greater negative slope and falls below the NPSHA curve for PATs. Thus even from the availability criterion the turbine mode operation also seems to be less susceptible to cavitation compared to the corresponding pump mode operation.

However it should be remembered that the operating discharge in turbine mode is 1.3 to 1.8 times as that of the pump mode (section B1, Appendix B) and it will be worthwhile to study the NPSHA at the corresponding best efficiency flows. Since the proportions of velocity gain and draft tube losses for the two modes will assume different magnitudes the availability comparison of pump and turbine mode may not be straightforward.

A3   Test-Rig and Instrumentation

A3.1   General Layout

The test rig is developed for carrying out experiments in the turbine mode only and is equipped with an open loop hydraulic cycle. The natural fallout of the open loop test rig, as seen from section 2.5 in Chapter 2, is that cavitation studies based requirement criterion would not be possible. Figure A3.1 illustrates the general representation of the test rig. The major components include the feed pumps, surge tank, pipelines (including the magnetic flow meter), test bed and discharge tank (or tail race tank). The test bed comprises of the test PAT along with the pressure sensors, the torque transducer shaft and the generator.

The feed pump system comprises of 4 identical pumps in parallel combination that supply the hydraulic energy through pipelines to the test PAT. A surge tank is used to maintain a maximum pressure of 15 m. After passing through the PAT, the water is discharged into the underground storage tank of a capacity of 300 m^3.
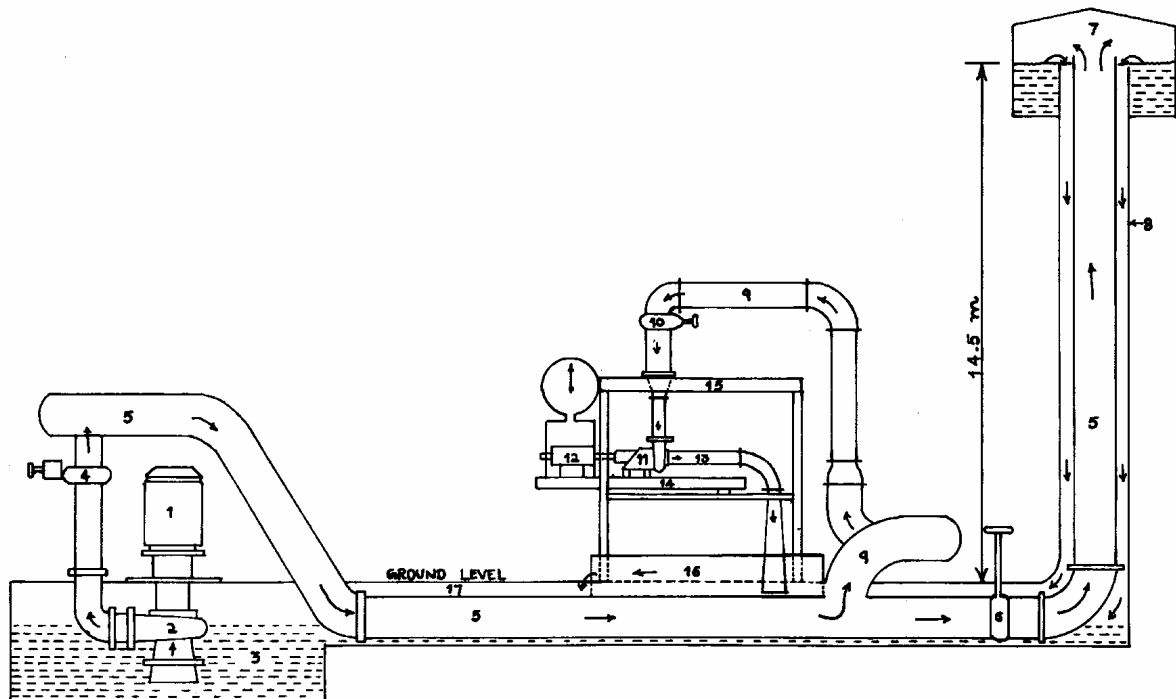
Figure A3.1, Schematic layout of the PAT test-rig

A3.2 Hydraulic and Mechanical Components

A3.2.1 Feed Pumps

The 4 feed pumps are vertically mounted with the pump units submerged in the underground storage tank as shown in Figure A3.1. These pumps are single stage pumps and of centrifugal type with duty points summarized in Table A3.1.

Table A3.1, Name plate details of the feed pump

Net Head	16 m
Discharge	140 l/s
Speed	1470 rpm
Shaft Power	27.3 KW
Efficiency	80%

A3.2.2 Piping and Valves

The piping seen from Figure A3.1 comprises of the main line with a diameter of ϕ500 mm, a branch line in which the pipe is reduced to ϕ300 mm and the remaining inlet line (known as the manifold) leading to the test turbine of essentially ϕ200mm inner diameter. Due to the space restrictions, there are many bend joints incorporated in the hydraulic circuit. The main control valve for the test rig (ϕ200 mm) is a simple gate or knife edged valve and is electrically operated. Depending on the diameter of volute entry of the PAT (i.e. at inlet plane 'i' of Figure 2.1, Chapter 2), the last pipe section is appropriately reduced from the given ϕ200 mm diameter.

A3.2.3 Mounting Bay

The mounting bay is built on an elevated platform created on 4 pillar supports. Broad 'I' beams with a modified rail system is fabricated to allow PATs of different sizes to be mounted with ease. The torque transducer shaft is also mounted on the same 'I' beam frame. The generator is mounted on a special platform on the ground level. Hence the power transmission from the PAT to the generator is accomplished through a belt drive system.

A3.2.4 Generator

A direct current generator with the specifications summarized in <u>Table A3.2</u> is used as a loading unit. The loading operation is carried out by varying the field current using an external excitation circuit and an autotransformer. The generated electricity is dissipated through a load box, which uses air-heater coils.

<u>Table A3.2</u>, Name plate details of the DC generator

Speed Range	0 -1000 rpm
Power	0 - 18 KW
Current	52.5 A at 1000 rpm
Voltage	400 V at 1000 rpm

A3.3 Operating Range of the Test Rig

The parameters that define the operating range of a test rig are mainly the H-Q characteristics of the feed pumps and the constant power line corresponding to the maximum capacity of the loading generator. However limitations on the pressure and discharge may be externally imposed from the measurement devices.

<u>Figure A3.2</u> describes the operating range of the test rig, which is built up of the characteristics of the feed pump 1 and the parallel combination of feed pump 1 and 2 along with constant generator power lines of 20 KW, 10 KW and 5 KW respectively. It is seen that the 20 KW power line lies out of the H-Q characteristics for discharges below 100 l/s. However over 100 l/s, the 20 KW line falls within the operating range. The 10 KW line is seen to be well suited for operation between 50 l/s and 150 l/s even with a single feed pump.
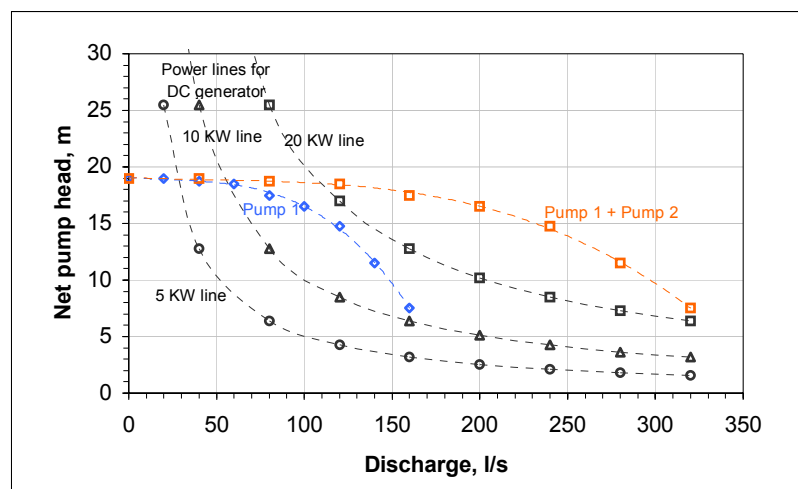
<u>Figure A3.2</u>, Operating range of the test-rig

Therefore for the PAT research programme where the generated power does not exceed 15 KW, only two feed pump configurations would suffice, namely,

    i.   The single feed pump operation or

    ii. Two pumps in parallel.

A3.4   Global Variables

A3.4.1   Net Head

The test-rig measures the static pressures at the inlet measurement plane 'i' (Figure 2.1, Chapter 2) and exit measurement plane 'e' (Figure 2.8, Chapter 2) of the PAT control volume. The static pressures are measured using two inductive type pressure transducers that are situated at the same level. This in effect cancels the elevation component of the total pressure. The mean velocity head component is determined based on the flowing discharge 'Q' and the cross-sectional areas of the respective planes. The net head is then given by,

$$H = H_i - H_e$$

$$H = \left(\frac{p_i}{\rho g} + \frac{v_i^2}{2g} \right) - \left(\frac{p_e}{\rho g} + \frac{v_e^2}{2g} \right) \qquad (A3.1)$$

These transducers measure the absolute pressure. The principle of measurement is based on the inductive property of a coil. A pressure difference causes a change in the inductance of the coil that produces a signal. The mechanical movement of the ferromagnetic core with respect to the stationary coils (which form a part of a Wheatstone bridge) causes a change of the coil's inductance. The output signal as the ratio of the input signal is taken through an amplifier and is measure of the actual pressure. Detailed description of the measurement setup can be found in Singh [47]. The summary of the technical features of the inductive pressure transducer is summarized in Table A3.3 along with that of the other instruments.

A3.4.2   Discharge

The discharge (Q) has been measured using a magnet flow meter as mentioned in section A3.1. A rectangular weir has also been built at the end of a discharge tank, but the their measurements are not used for calculations.

The magnetic flow meter is also an inductive type instrument whose measurement principle is based on Faraday's law of electromagnetic induction. The principle states that a when a conductor moves through a magnetic field, a voltage is induced perpendicular to both the direction of motion of the conductor and also the direction of the magnetic field. The water flowing has conductive property hence satisfies the Faraday's law. The voltage induced is

directly proportional to velocity of the flowing water, from which the discharge is evaluated for the given cross-sectional area. The meter's specifications are summarized in Table A3.3.

A3.4.3　Torque

The torque (T) on the PAT shaft is externally measured using a very special setup. Therefore this torque also includes the mechanical losses through the bearing, gland seals and the coupling. The torque transducer uses the principle of torsion theory, which states that a rotating shaft subjected to torque would undergo an angular deformation. This angular deformation is direct measure of torque on a shaft of defined geometry and material property.

Within the instrument, the angular deformation is felt by a sensitive strain gauge, which results in an output signal and subsequently causes the detuning of the Wheatstone bridge, which is the transformed into a measure of torque. Table A3.3 summarizes the chief features of the torque transducer.

A3.4.4　Speed

The speed, N, measurement is made possible using an optical sensor. The circuit of the sensor comprises of two components namely, an emitter that sends light (infrared) waves to the rotating body and a receiver that receives the modulated light wave. The alternate dark and bright bands on the rotating member cause a distinct modulation to the input signal (both frequency and intensity). The frequency of the output reflected signal is nothing but the frequency of the shaft. The sensor is a very simple in construction whose technical details are summarized in Table A3.3.

Table A3.3, Instrumentation specifications for the global variables

Parameter	Measurement Principle	Make	Range	Accuracy	Output Signal
Inlet Pressure (Positive)	Inductive + Wheatstone bridge	Hottinger Baldwin Messtechnik	0-2 bar	±1 % of full scale	0-8 mV/V
Exit Pressure (negative)	Inductive + Wheatstone bridge	Hottinger Baldwin Messtechnik	0-1 bar	±2 % of full scale	0-8 mV/V
Discharge	Faradays Magnetic law	Turbo	0-1000 m^3/h	±1% of full scale	0-20 mA

Torque	Wheatstone bridge	Hottinger Baldwin Messtechnik	+/-100 Nm	±0.1% of full scale	5-15 kHz
Speed	Optical counts	Self assembled		±1 rpm	Pulses

A3.4.5   Data Processing

The output signals from all the instruments are brought to an analog-digital converter, which also acts as a junction box, from where they are fed into a computer. The 'Labview' software from National Instruments is used to process the data. The objective is to carry out measurements only at steady state conditions, even though there are transitions (unsteadiness) associated within the PAT system. To accomplish this, a mean value is determined for all the variables over predefined time period of 10 seconds at any given load point of the PAT.

A3.5   Internal Variables

Section A1 of Appendix A, has dealt extensively with the internal variables, which mainly comprises of the 2-dimensional velocity swirl angle distribution along the cross-section of the plane 'e'. The internal variables consisting of the three velocity components namely, the meridional velocity component (v_{me}), the swirl component (v_{ue}), the absolute velocity (v_e) along with the absolute swirl angle, θ (where $\theta = 90 - \alpha_e$, from <u>Figure A3.1</u> and <u>A3.2</u>) are measured using a 5 hole yaw sphere. <u>Figure A3.3</u> displays a typical 5-hole sphere of which only 3 holes are used to determine the complete set of internal variables. The central hole '2' is known as the stagnation hole and holes '4' and '5' are called differential holes. The holes '1' and '3' do not come into the consideration because they are related to the measurement of radial flow components, which have been categorically neglected in the PAT study (reasons mentioned in section A1).
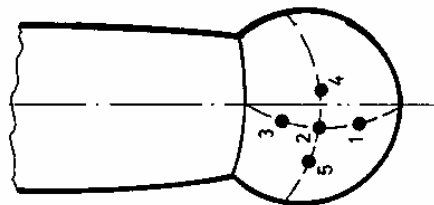
<u>Figure A3.3</u>, A 5-holed yaw sphere

The pressure on the holes are determined using inductive type differential pressure transducers with the one side of the transducer connected to the duct of the probe, while the other is left open to the atmosphere. When the pressures of holes, 4 (p_4) and 5 (p_5) are equal, then the probe gets aligned to the direction of the flow and the swirl flow angle (θ) is determined at that particular location within the cross section. The absolute velocity is then determined as follows.

$$v = \sqrt{2g(p_2 - p_4) \Big/ (k_2 - k_4)} \qquad\qquad (A3.2)$$

The yaw probe coefficients k_2 and k_4 are determined from a calibration study in a wind tunnel based on,

$$k_2 = \frac{p_2 - p_a}{\left(v^2 \big/ 2g\right)} \quad \text{and} \quad k_4 = \frac{p_4 - p_a}{\left(v^2 \big/ 2g\right)} \qquad\qquad (A3.3)$$

The coefficients k_2 and k_4 are found to be 0.96 and 0.09, respectively for a non-radial flow condition. The other velocity components, namely the axial velocity (v_m,) and swirl velocity, (v_θ) at the reference plane 'e' can be determined from the measured swirl angle (θ) and the absolute velocity (v) as seen in the velocity triangle in <u>Figure A3.4</u>.
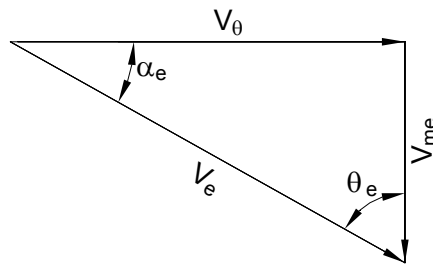
<u>Figure A3.4</u>, Velocity triangle at the exit reference plane 'e'

A4   Design of Tested PATs

A4.1   Radial Flow PATs

The major dimensions of the 7 radial flow PATs are classified into two categories, namely the impeller and volute-impeller interface dimensions respectively. Figure A4.1 and A4.2 describes general representation of a radial flow impeller along with the symbols for the various dimensions, while Figure A4.3 gives the representation of the volute-impeller interface. All the radial PATs studied have shrouds attached to both the front and rear blade profiles.
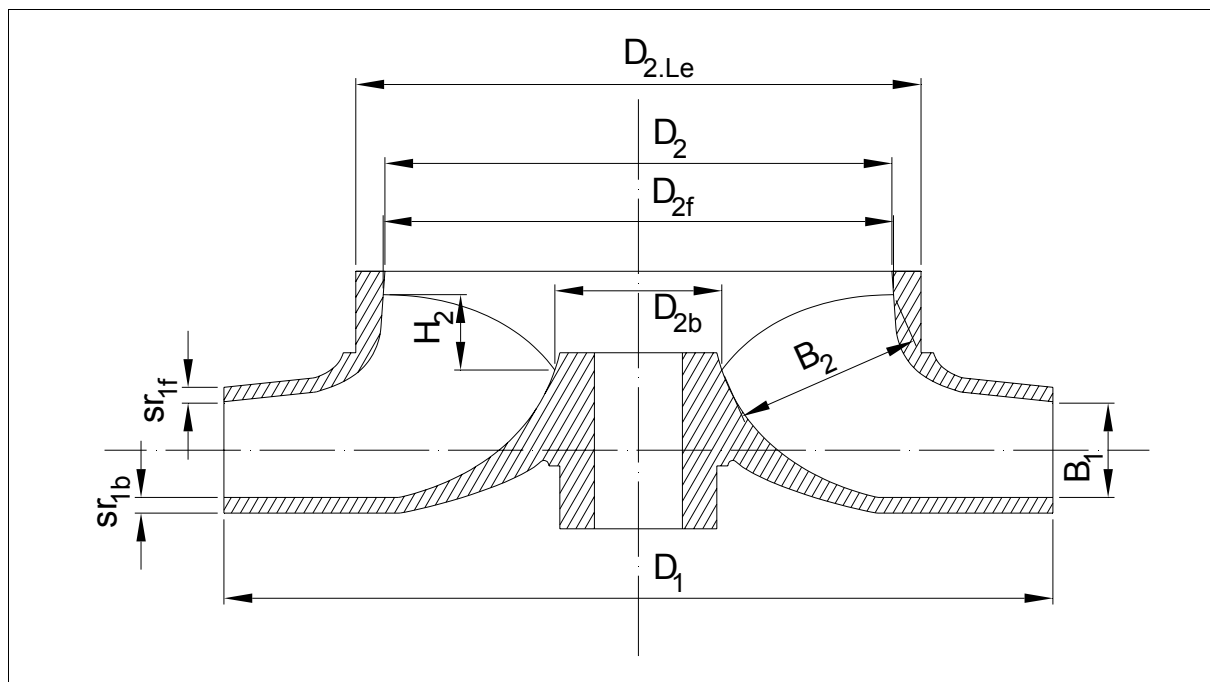
Figure A4.1, Cross-sectional view of a radial flow impeller
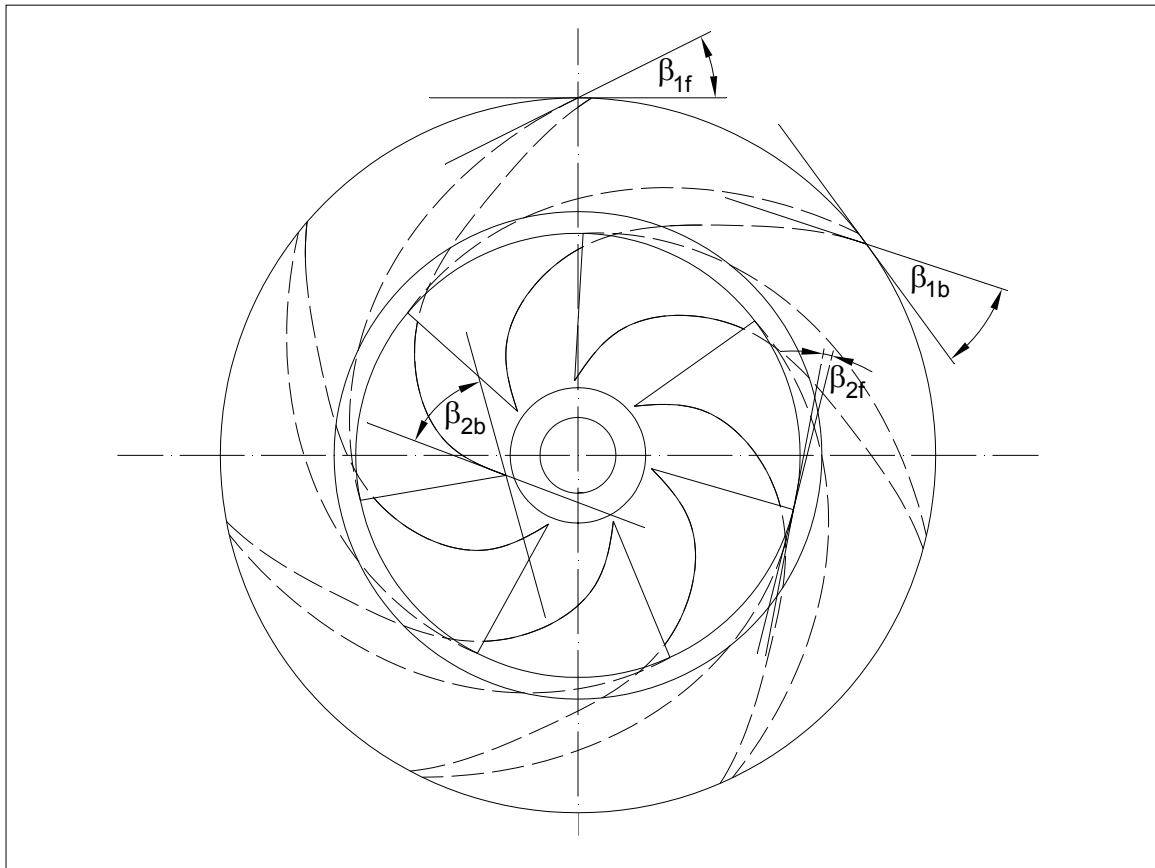
Figure A4.2, Front view of a radial flow impeller
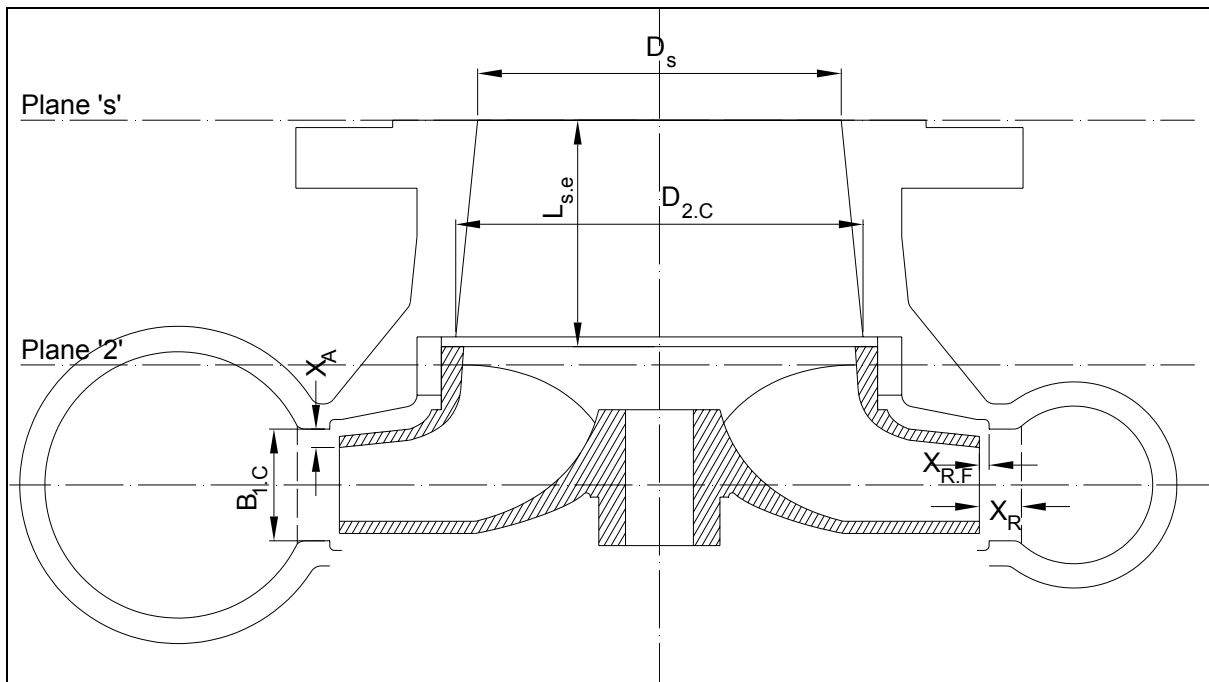
Figure A4.3, Cross-section view of the impeller and volute casing a radial PAT

Table A4.1 and A4.2 summarizes the actual dimensions on the impeller and volute-impeller interface of the radial flow PATs, which need to be studied in correspondence with Figures A4.1, A4.2 and A4.3.

Table A4.1, Summary of the impeller dimensions for the radial flow PATs

Symbol	Particulars	24.5 rpm	35.3 rpm	36.4 rpm	39.7 rpm	45.2 rpm	46.4 rpm	79.1 rpm
	Impeller							
D_1	Impeller inlet diameter (turbine)	ϕ258 mm	ϕ206 mm	ϕ139 mm	ϕ264 mm	ϕ200 mm	ϕ174 mm	ϕ224 mm
D_2	Impeller eye diameter	ϕ130 mm	ϕ118.5 mm	ϕ100.5 mm	ϕ164 mm	ϕ129.5 mm	ϕ101 mm	ϕ180 mm
D_{2f}	Impeller eye diameter (front)	ϕ132 mm	ϕ120.5 mm	ϕ100.5 mm	ϕ164 mm	ϕ129.5 mm	ϕ101 mm	ϕ180 mm
D_{2b}	Impeller eye diameter (back)	ϕ132 mm	ϕ98 mm	ϕ34 mm	ϕ52 mm	ϕ73.2 mm	ϕ37.5 mm	ϕ54 mm
β_{1f}	Inlet blade angle (front shroud)	16.4^0	36^0	17^0	39^0	34.5^0	19.5^0	39^0
β_{1b}	Inlet blade angle (back shroud)	16.4^0	36^0	21.5^0	48^0	34.5^0	30.5^0	-0
β_{2f}	Exit blade angle (front shroud)	24.3^0	8^0	3^0	2.5^0	3^0	5^0	4^0
β_{2b}	Exit blade angle (back shroud)	24.3^0	20^0	32^0	18^0	30^0	45^0	16.4^0
B_1	Inlet blade width	21.8 mm	18.8 mm	21.6 mm	30 mm	31.5 mm	18.3 mm	59.5 mm
B_2	Exit diagonal blade width	39 mm	34 mm	44 mm	60 mm	40.5 mm	40.5 mm	77 mm
H_2	Height of the exit blade	39 mm	32.3 mm	27.25 mm	22 mm	21.5 mm	21.5 mm	100 mm
t_1	Inlet blade thickness	4.25 mm	3.8 mm	3.4 mm	5.2 mm	7 mm	5 mm	7 mm
t_2	Exit blade thickness	4.25 mm	3.8 mm	2 mm	4 mm	2.5 mm	3.5 mm	1.5 mm
sr_{1f}	Front shroud thickness	7.25 mm	3.5 mm	4 mm	5 mm	4 mm	4.5 mm	9 mm
sr_{1b}	back shroud thickness	5 mm	4.5 mm	4.5 mm	5 mm	4.5 mm	4.5 mm	9 mm
n	Blade number	6	8	7	7	7	6	5

The features of the impeller dimensions of the radial flow PATs are summarized below.

i. It is observed in Table A4.1 that the 35.3 rpm PAT has highest number of blades (8 Nos.), while the 79 rpm PAT has the lowest number (only 5 blades). The exit blade profiles for all the PATs (except the 24.5 rpm PAT) exhibit identical form, with the front impeller blade diameter D_{2f} greater than the back impeller blade diameter D_{2b}. For the 24.5 rpm PAT, the two exit diameters (D_{2f} and D_{2b}) are essentially identical.

ii. It is seen that the inlet blade angles (β_{1f} and β_{1b}) at the front and back shrouds are identical for the 24.5 rpm, 35.3 rpm and the 45.2 rpm PAT. However for the other PATs there is a distinct difference in the magnitudes of the two angles with the inlet

blade angle attached to the front shroud (β_{1f}) greater than that attached to the back shroud (β_{1b}).

iii. The exit blade profiles on the other hand have been laid out in such a way that the exit blade angle at the front shroud (β_{2f}) is marginal (i.e. the front profiles at the eye region essentially merges with the segment of circle whose center corresponds to the impeller axis). The exit blade angle at the back shroud (β_{2b}) is considerable for all the PATs. However the 24.5 rpm PAT has a special design feature with the two exit blade angles essentially the same, with $\beta_{2f} = \beta_{2b} = 24.3^0$.

iv. The blade profiles for most of the PATs are 3-dimensional, while the profiles for the 24.5 rpm and the 35.3 rpm PATs are mainly a 2-dimensional representation.

v. The 79.1 rpm PAT has the maximum ratio of the inlet impeller width, B_1 (59.5 mm) to the exit impeller width, B_2 (77 mm) in comparison to all the other PATs.

Table A4.2, Summary of the dimensions of the volute-impeller interface for the radial flow PATs

Symbol	Particulars	24.5 rpm	35.3 rpm	36.4 rpm	39.7 rpm	45.2 rpm	46.4 rpm	79 rpm
	Volute-Impeller Interface							
$B_{1.C}$	Inlet volute width (turbine)	41.1 mm	35 mm	30 mm	46 mm	48.5 mm	30 mm	72 mm
X_R	Inlet radial clearance	17 mm	10.5 mm	7.5 mm	14 mm	14 mm	7.5 mm	38 mm
$X_{R.F}$	Inlet radial free clearance	5 mm	10.5 mm	3 mm	4 mm	14 mm	2.75 mm	8 mm
X_A	Inlet axial clearance	9.6 mm	8.1 mm	4.2 mm	8 mm	8.5 mm	5.9 mm	6.25 mm
$D_{2.C}$	Volute eye diameter	ϕ125 mm	ϕ101 mm	ϕ108.5 mm	ϕ168 mm	ϕ133.4 mm	ϕ101 mm	ϕ182 mm
$L_{s.e}$	Axial eye length	22.5 mm	28 mm	60 mm	90 mm	80 mm	62 mm	65 mm
D_s	Casing flange diameter	ϕ100 mm	ϕ100 mm	ϕ82 mm	ϕ150 mm	ϕ125 mm	ϕ82 mm	ϕ200 mm

The features of the volute-impeller interface are listed below (refer Table A4.2),

i. The radial clearance (X_R) and the axial clearance (X_A) in the turbine mode inlet region (that form the zone *ii* of the PAT control volume – section 2.1, chapter 2) have been summarized for all the radial PATs in Table A4.2. Both these clearances are quite considerable for each of the machines. The axial clearance (X_A) is the greatest for the 24.5 rpm PAT with over 9.5 mm on each side of the impeller shroud, while the 45.2 rpm and the 39.7 rpm PAT follow with axial clearances of over 8 mm.

ii. The radial clearance (X_R) is seen to extremely large for the 79.1 rpm PAT with a length of 38 mm, followed by 24.5 rpm PAT with 17 mm, 45.2 rpm and 39.7 rpm PAT with 14 mm each.

iii. However the most important geometric parameter, i.e. the inlet radial free clearance ($X_{R.F}$) is also summarized in Table A4.2. The radial free clearances are seen to be the highest for the 45.2 rpm and 35.3 rpm PAT with 14 mm and 10.5 mm respectively. It is also to be noted that the inlet radial clearances (X_R) and radial free clearances ($X_{R.F}$) are equal for the above to PATs. The $X_{R.F}$ is lowest for the 46.4 rpm and 36.4 rpm PAT, which is in the order of 2.5 to 3 mm.

iv. As far as the radial cross-sections of the volute casings are concerned, all the PATs have essentially circular sections, except for the 35.3 rpm PAT, which has characteristics trapezoidal sections.

v. From the perspective of the eye region (encompassing zone *v* and *vi* of the PAT control volume), it seen from Table A4.2 that the 36.4 rpm, 39.7 rpm, 45.3 rpm and 46.4 rpm PAT have similar converging design as represented in the Figure A4.3. However, the 24.5 rpm and the 35.3 rpm PATs have a peculiar suction eye design. This design is mainly related to the shortened axial eye length, $L_{s.e}$ and a sharper contraction from the plane '2' to plane 's' (also represented in Figure 2.12, Chapter 2).

vi. All the PATs display a converging eye design in some form or other, except the 79.1 rpm PAT, where it is seen from the representation in Table A4.2 that there is a gradual expansion from the volute eye diameter, $D_{2.C} = \phi182$ to casing flange diameter, $D_S = \phi200$.

A4.2   Mixed Flow PATs

Similar to the representation method for radial flow PATs, the mixed flow PAT's geometrical nomenclature is illustrated in Figure A4.4 and A4.5 for the major impeller dimensions and in Figure A4.6 for the volute-impeller interface specifications. The 94.4 rpm PAT, the only mixed flow PAT that has been included in the research programme has its dimensions summarized in Table A4.3 and A4.4.

The important features of the impeller design of the 94.4 rpm mixed flow PAT are,

i. The 94.4 rpm PAT impeller is of semi-open type, with no shrouds covering the front blade profiles as seen in Figure A4.4 and A4.6.

ii. The inlet blade edge is inclined to axis of PAT, unlike that for the radial flow PAT.

iii. The diameter corresponding to the tip of the front blade profile (D_{1f}) is considered as the reference diameter (mentioned in Table 3.1, Chapter 3) for the dimensionless

analysis carried out both in the experimental level (in section A51.7) and application procedure (Chapter 5 and 6).

iv.   At the turbine mode inlet, the blade angles β_{1f} and β_{1b} are essentially identical equal to 15^0.

v.   The 94.4 rpm PAT has only 4 blades, which leaves behind large widths of blade passages.

vi.   Within the eye region (comprising of zone *v* and *vi* of the PAT control volume) the front and the rear exit blade profiles are perpendicular to the PAT axis as seen in <u>Figure A4.4</u> and <u>A4.6</u>, casing the dimension $H_2 = 0$.

vii.   It is also seen the exit blade width B_2 is greater than inlet blade width B_1.

The features of the volute-impeller interface (refer <u>Table A4.3</u>) are summarized below.

i.   It is seen from <u>Figure A4.6</u> that the volute casing in the turbine mode inlet region (for the zone *ii*) of the 94.4 rpm PAT has an inclined entry. It is also found difficult to explicitly represent the inclined clearance (symbolic to radial clearance, X_R of Figure 3.7).

ii.   However the inclined free clearance, $X_{I.F}$ can be represented and is found to be equal to 3 mm for the given test PAT from <u>Table A4.3</u>.

iii.   The eye region of the casing (zone *vi*) is of converging design type as seen in <u>Figure A4.6</u> (the diameter changes from $\phi 172$ mm, i.e. at plane '2', to $\phi 150$ at plane 's' over the eye length, $L_{s.e} = 65$ mm).
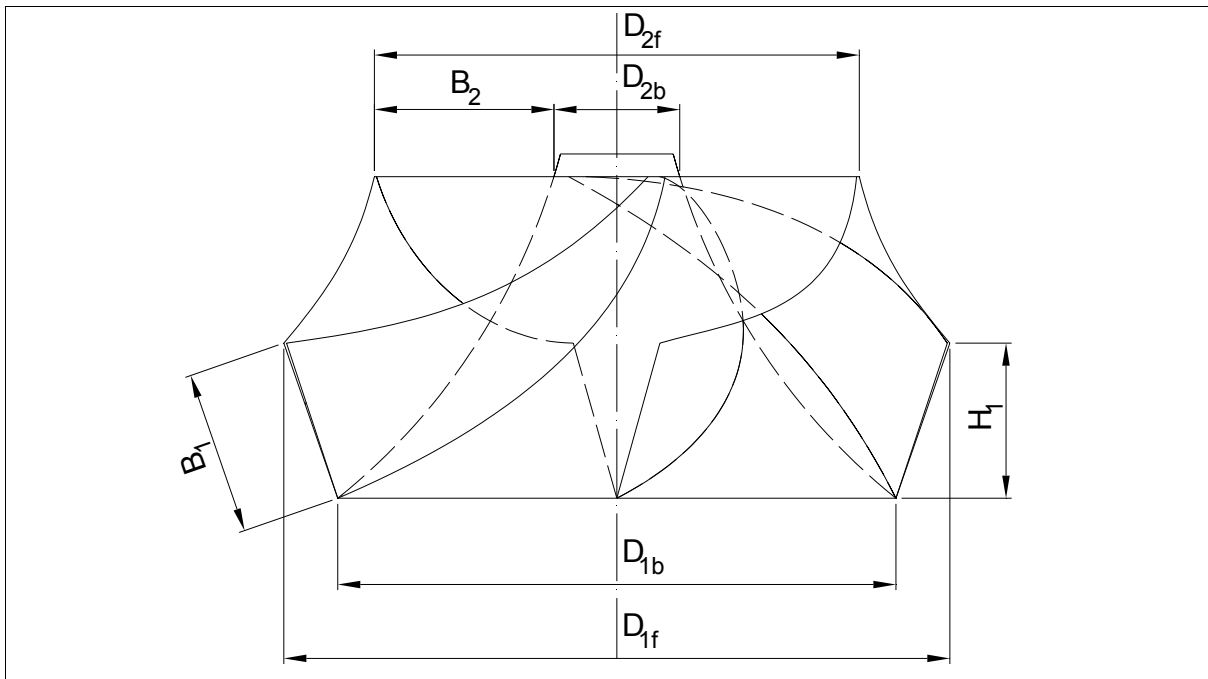
Figure A4.4, Cross-section view of a mixed flow impeller
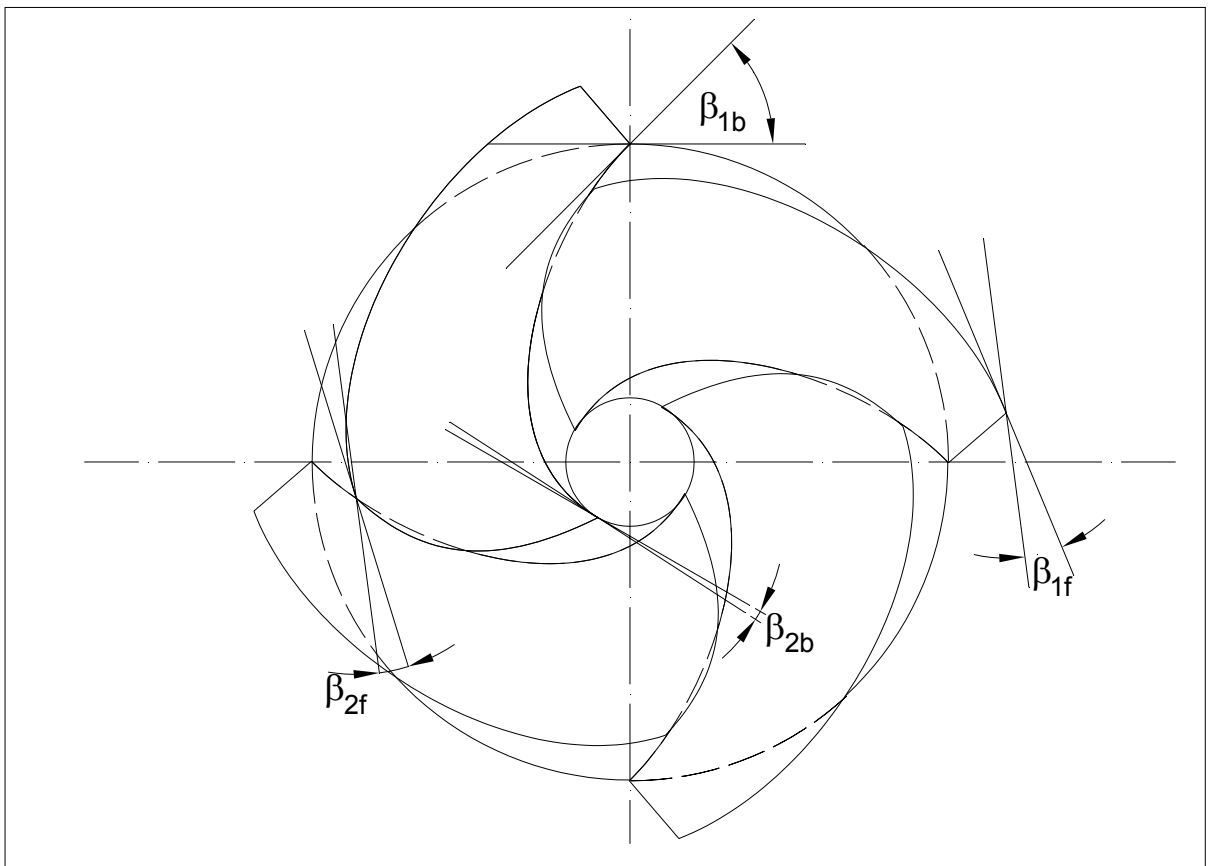
Figure A4.5, Front view of a mixed flow impeller
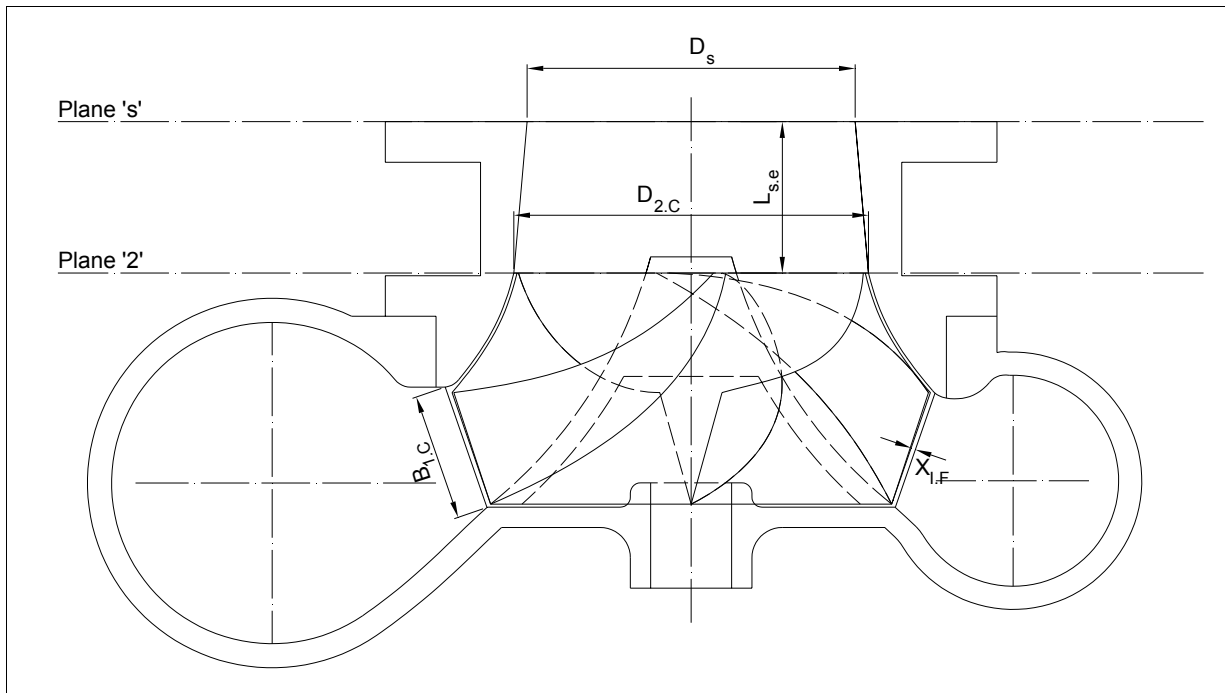
Figure A4.6, Cross-sectional view of the impeller and volute casing a mixed flow PAT

Table A4.3, Summary of the impeller dimensions for the mixed flow PAT

	Impeller	
D_{1f}	Impeller inlet diameter (front shroud)	ϕ 236 mm
D_{1b}	Impeller inlet diameter (back shroud)	ϕ 198 mm
D_{2f}	Impeller eye diameter (front shroud)	ϕ 172 mm
D_{2b}	Impeller eye diameter (back shroud)	ϕ 40 mm
β_{1f}	Inlet blade angle (front shroud)	15^0
β_{1b}	Inlet blade angle (back shroud)	15^0
β_{2f}	Exit blade angle (front shroud)	20^0
β_{2b}	Exit blade angle (back shroud)	50^0
B_1	Inlet blade width	58 mm
H_1	Height of the Inlet blade	55 mm
B_2	Exit blade width	76 mm
H_2	Height of the exit blade	0 mm
t_1	Inlet blade thickness	4 mm

t_2	Exit blade thickness	4 mm
sr_{1f}	Front shroud thickness	no shroud
sr_{1b}	Back shroud thickness	6.5 mm
n	Blade number	4

Table A4.4, Summary of the dimensions of the volute-impeller interface for the mixed flow PAT

Volute-Impeller Interface		
$B_{1.C}$	Inlet volute width (turbine mode)	62 mm
$X_{I.F}$	Inlet radial clearance	3 mm
$D_{2.C}$	Volute eye diameter	ϕ175 mm
$L_{s.e}$	Axial eye length	65 mm
D_s	Casing flange diameter	ϕ 175 mm

A5 Results of Experimental Optimization Study

This section deals with presentation of the results on the optimization stage I, II, III and IV for the corresponding PATs that are used in Chapter 4 (Results and Discussion) of the main dissertation for an overall summary of respective optimization stages.

A5.1 Optimization Stage I

As mentioned in section 4.1.1.1, Chapter 4, the detailed presentation of the results of optimization stage I on the 24.5 rpm, 36.4 rpm, 39.7 rpm, 45.2 rpm, 46.4 rpm, 79.1 rpm and 94.4 rpm PAT are made in this section.

A5.1.1 24.5 rpm PAT

The modification on the 24.5 rpm PAT comprises of the rounding of both the blade and shroud profiles are detailed out in section 2.4.1, Chapter 2. The dimensionless characteristics for this optimization stage are summarized in Figure A5.1 for the 800 rpm test. There is decrease in the head number consumption for the inlet rounded PAT over the entire operating range with magnified effects in the part-load and BEP-overload regions. The power number line for the modified PAT lies above that for the non-modified stage over the entire range. Due to the combined effect of the reduction of head number and rise of power number, the efficiency curve of the inlet rounded PAT is superlative with highest gains in the BEP and overload region with an efficiency rise of +1.5% to +2%.

The BEP is summarized in Table A5.1 where it is seen that the head number for the inlet-rounded stage decreases from 11.307 to 11.173 units, while power number increases from 0.974 to 0.978, resulting in a rise of efficiency from 73.7% to 74.8%.

Table A5.1, BEP summary for two stages of Optimization Stage I on the 24.5 rpm PAT

Stage	ϕ	ψ	**p**	η
Non-modified	0.117	11.307	0.974	73.7%
Inlet-rounded	0.117	11.173	0.978	74.8%
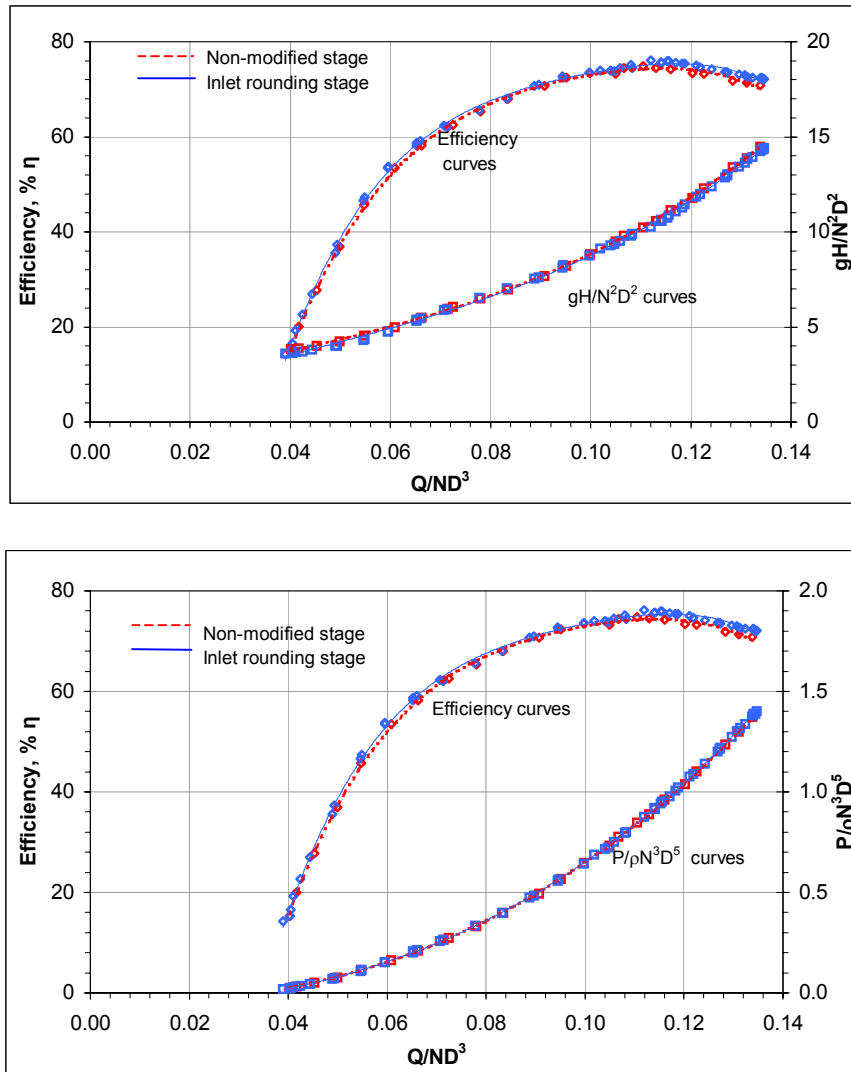
Figure A5.1, Comparisons of dimensionless characteristics for Optimization Stage I on the 24.5 rpm PAT

The percentage analysis of the various dimensionless parameters is carried out in Figure 4.2. The head reduction curve for inlet rounded PAT remains positive throughout the operating range. The head reduction decrease from +3.5% in the no-load region to +0.5% at the part-load line and the reductions continuously rises toward the BEP and overload line to +1.5% to +2%. The power improvement curve too is above the abscissa signifying the increase of power generation for the inlet rounded PAT. The improvements are relatively constant at the part-load and overload line (+0.5% to +0.8% rise), however near the BEP line the power gain is +0.3% to +0.4%.

Table A5.2 compares the relative changes of various parameters (head number, power number and efficiency) at the part-load BEP and overload lines respectively, where it is seen that the reduction of head is much more than improvement of power.
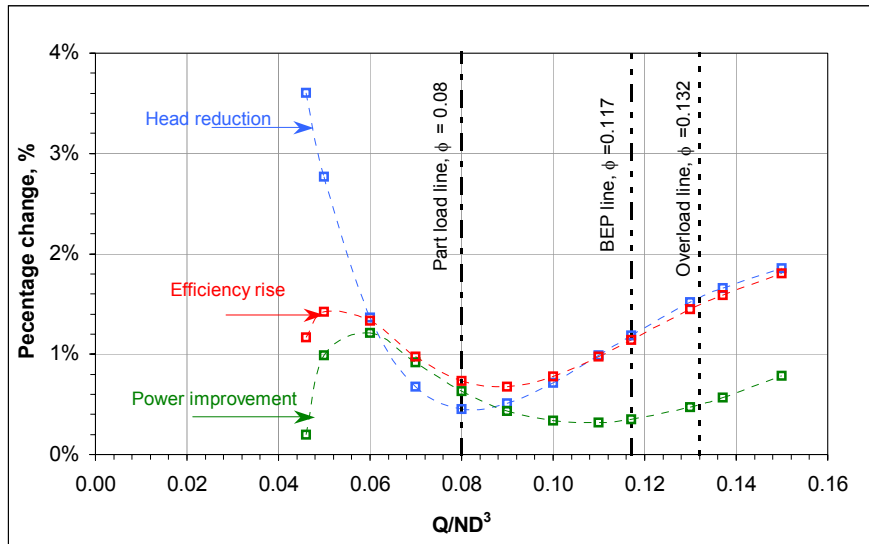
Figure A5.2, Percentage Analysis Plot for Optimization Stage I on the 24.5 rpm PAT

Table A5.2, Relative study at part-load, BEP and overload lines for Optimization Stage I on 24.5 rpm PAT

	Part-load line ϕ = 0.080	BEP line ϕ = 0.117	Overload line ϕ = 0.137
Head reduction	+0.5%	+1.2%	+1.7%
Power improvement	+0.6%	+0.3%	+0.6%
Efficiency rise	+0.7%	+1.1%	+1.6%

Discussion of Results on the 24.5 rpm PAT

The behaviour of the power improvement curve signifies two possibilities namely, the reduction of losses within the impeller control volume or the rise of the net rotational momentum, (Euler Head - $gH_{Eu.slip}$) across the impeller for the modified PAT (based on the methodology in section 2.1 and 2.2 of Chapter 2 and section 3.1.3.1, Chapter 3). On the other hand the behaviour of the head reduction curve signifies that the hydraulic losses within the entire control volume inclusive of the impeller have decreased. Since the reductions are positive throughout the operating range, the net rotational momentum cannot increase as a possibility pointed by the power improvement curve. Therefore the combined behaviour of the power and head number can be owed to only the loss mechanisms in the PAT control volume.

Also, the percentage head reductions are consistently greater in magnitude compared to the power improvement. The loss reductions within the impeller zone (zone *iii* and *iv*) are incorporated in the head reduction curve as seen in Equation (2.5), Chapter 2. However it is not possible for the loss reductions in zone *iii* and *iv* to cause such large reductions of head

as recorded in the BEP region and overload regions. This means another loss component within the PAT control volume is also affected due to inlet rounding, which can be only the clearance zone *ii*. The reduction of losses of zone *ii* are seen more in the no-load region and towards the BEP-overload region as seen in Figure A5.2, with little reduction in the part-load region. The loss reductions of zone *iii* are more or less constant throughout the operating range.

The reduction losses in zone *iii* and *iv* are mainly associated improved flow entry and separation effects. The loss component of zone *ii* that has changed is related to turbulence and shock loss effects. Therefore the inlet rounding on the 24.5 rpm PAT has caused decrease to the losses in zone *ii*, *iii* and part of zone *iv* as well and thus improving the overall performance of the machine.

A5.1.2   36.4 rpm PAT

There has been another level modification carried out on the 36.4 rpm PAT along with the traditional rounding of the blade edges and shrouds surfaces. This modification comprises of the correction of the axial misalignment between the impeller and volute casing centre lines that is of the order of nearly 3 mm as shown in Figure A5.3. Therefore the modified characteristics will also include the effects due to axial correction.
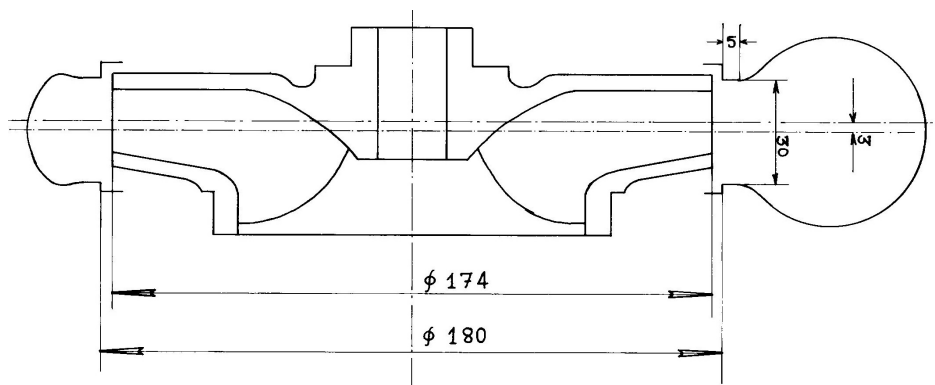
Figure A5.3, Cross-sectional view of the impeller-casing interface for the non-modified 36.4 rpm PAT

Figure A5.4 describes the dimensionless characteristics of the two test stages. The comparison of the head number characteristics reveals that there are significant head reductions over the entire operating range and the magnitude of the reductions continuously magnifies starting from the part-load region towards the overload region. The power number characteristics on the other hand show that the inlet rounded PAT is producing greater output of nearly constant magnitude throughout the characteristics. Due to this excellent combination of power number and head number effects the efficiency improvement of over +4% to +5% is recorded. Table A5.3 describes the BEP for the two stages, where the head number for the modified PAT falls from 8.278 to 8.001, while the power number increases from 1.017 to 1.052, which causes an efficiency rise from 66.4% to 71.1%.
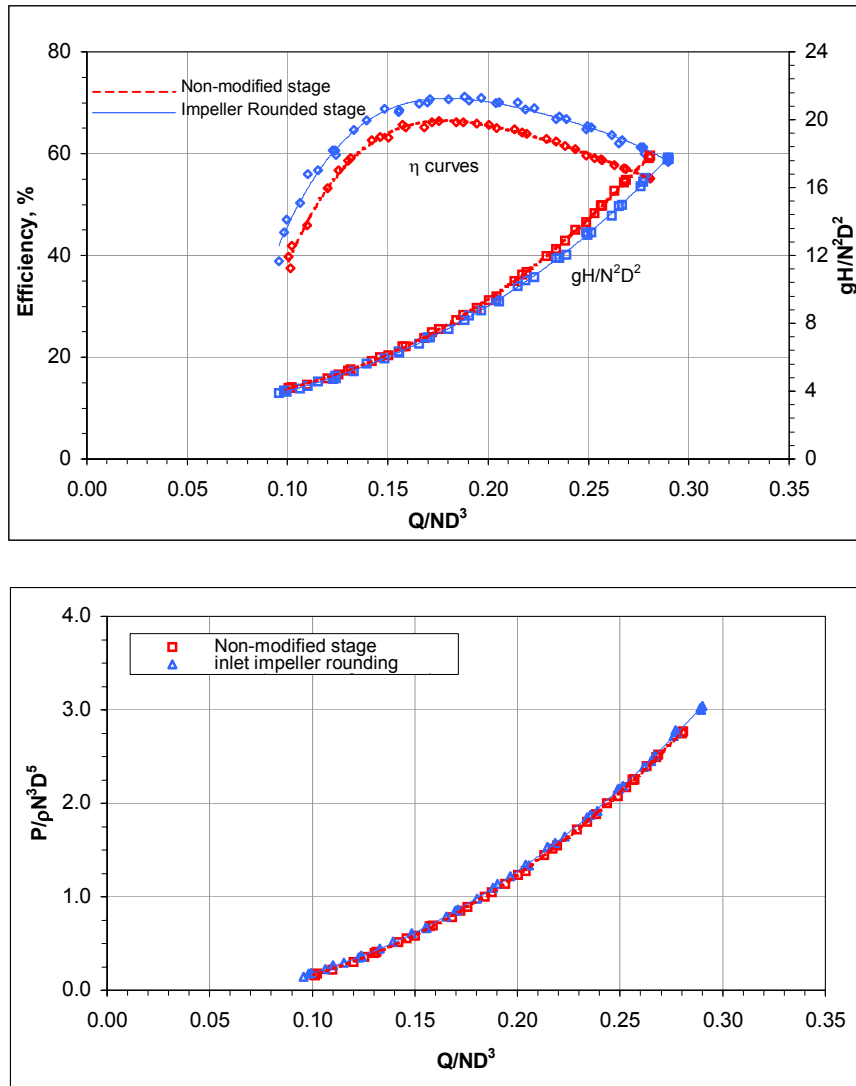
Figure A5.4, Comparisons of dimensionless characteristics for Optimization Stage I on the 36.4 rpm PAT

Table A5.3, BEP summary for two stages of Optimization Stage I on the 36.4 rpm PAT

Stage	ϕ	ψ	$\mathbf{p}$	η
Non-modified	0.185	8.278	1.017	66.4%
Inlet-rounded	0.185	8.001	1.052	71.1%

The internal hydraulic effects due the present modification can be better understood from Figure A5.5. The power improvement curve with respect to the modified PAT is positive throughout the operating range. In the part-load region a power improvement of +6% to +7% is seen which slowly reduces to +1.6% to +2.5% towards the BEP and overload region. The percentage of head reduction on the other hand rises continuously from the part-load region with +2% reductions to overload region with as much as +7% reduction. The rise of efficiency is more or less constant in the entire operating range with 4.5% to 5%.

The contribution to the rise in efficiency within the part-load region is coming from mainly power improvement. However in the BEP and overload region head number reductions play a dominating effect on the overall efficiency rise compared to power number effects.

The relative contributions to the overall efficiency from the head and power parameters are summarized at the part-load, BEP and overload lines respectively in <u>Table A5.4</u>.
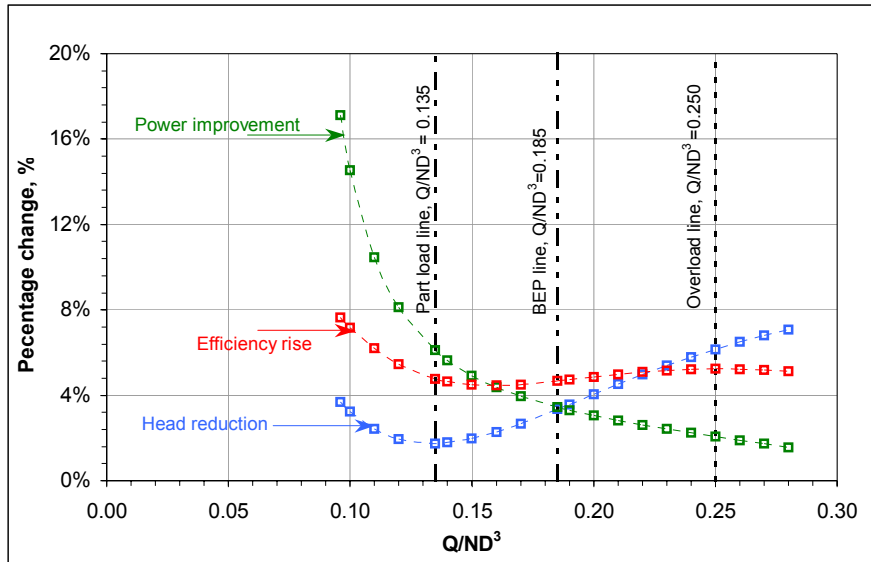
<u>Figure A5.5</u>, Percentage Analysis Plot for Optimization Stage I on the 36.4 rpm PAT

<u>Table A5.4</u>, Relative study at part-load, BEP and overload lines for Optimization Stage I on the 36.4 rpm PAT

	Part-load line $\phi = 0.135$	BEP line $\phi = 0.185$	Overload line $\phi = 0.250$
Head reduction	+1.8%	+3.3%	+6.2%
Power improvement	+6.1%	+3.4%	+2.1%
Efficiency rise	+4.8%	+4.7%	+5.2%

Discussion of Results on the 36.4 rpm PAT

The rise of power within the modified impeller and the simultaneous reduction of head indicate that the there is no role for the rotational momentum changes within the impeller control volume. Therefore the improvement of the power number symbolizes with only the reduction of loss components in zone *iii* and zone *iv*. The percentage of improvement suggests that some major reductions of losses associated within these zones. On the other hand the continuous magnification of head reductions in the BEP and overload regions suggest that inclusive of the optimum hydraulics in zone *iii* and *iv*, there is also another major

reduction of losses in zone *ii*, which may be arising due to the correction of the axial misalignment. Especially in the overload region when the effects of zone *iii* and *iv* begin to decrease and effects in zone *ii* begin to drastically improve the local hydraulic conditions.

Addition to the rounding effects on the impeller the axial correction has also a major role to play towards the behaviour of the flow zone *ii*, *iii* and *iv*. While the major effects in the zone *ii* may be associated with the symmetry of the volute and impeller, the effects in zone *iii* and *iv* can be linked to both the rounding and symmetry conditions. Rounding on the other hand would also have its influences on zone *ii*. However the relative magnitude of the influence of the axial correction cannot be exactly quantified.

A5.1.3 39.7 rpm PAT

The modification of the 39.7 rpm PAT comprises of rounding the inlet blade profiles and shroud surfaces only. As shown in Figure A5.6, there existed an axial misalignment between the centerlines of the impeller and casing, which was however not corrected.
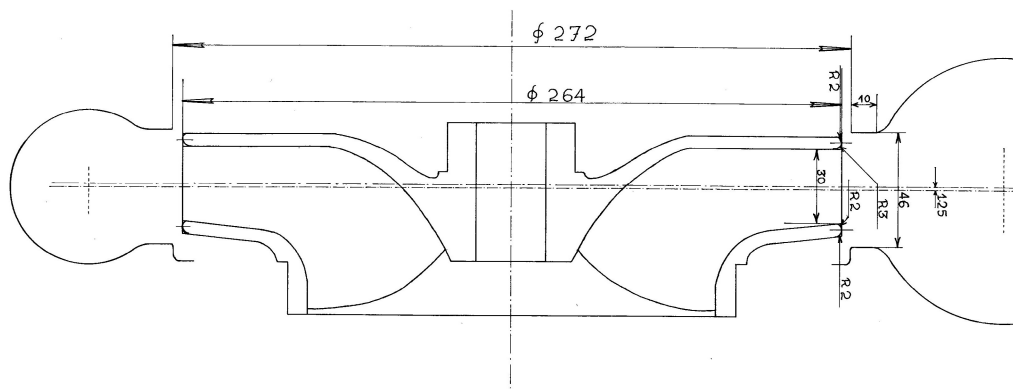
Figure A5.6, Cross-sectional view of the impeller-casing interface for the modified 39.7 rpm PAT

The optimization effects are studied at a constant speed of 900 rpm in Figure A5.7. The head number characteristics of the inlet rounded PAT runs below that of the non-modified PAT with extent of head reduction more or less uniform in absolute terms. In the region between the part-load and BEP region the head reductions have slightly reduced. The power number characteristics of both stages on the other hand seem to be very similar with the trend lines collapsing into each other. There is however some increased power productions for the inlet rounded PAT within the no-load and part-load region. The resulting efficiency curve of the inlet rounded PAT has shown an uniform rise of +1% to +1.5% over the entire range mainly coming from the head number effects.

The BEP for both the PATs are analyzed in Table A5.5, where the head number of the modified PAT decreased from 6.807 units to 6.699 units while the power number has a marginal drop 1.130 to 1.124 result in a net efficiency rise of +0.9% from 83% to 83.9%.

<u>Table A5.5</u>, BEP summary for two stages of Optimization Stage I on 39.7 rpm PAT

Stage	ϕ	ψ	**P**	η
Non-modified	0.200	6.807	1.130	83.0%
Inlet-rounded	0.200	6.699	1.124	83.9%
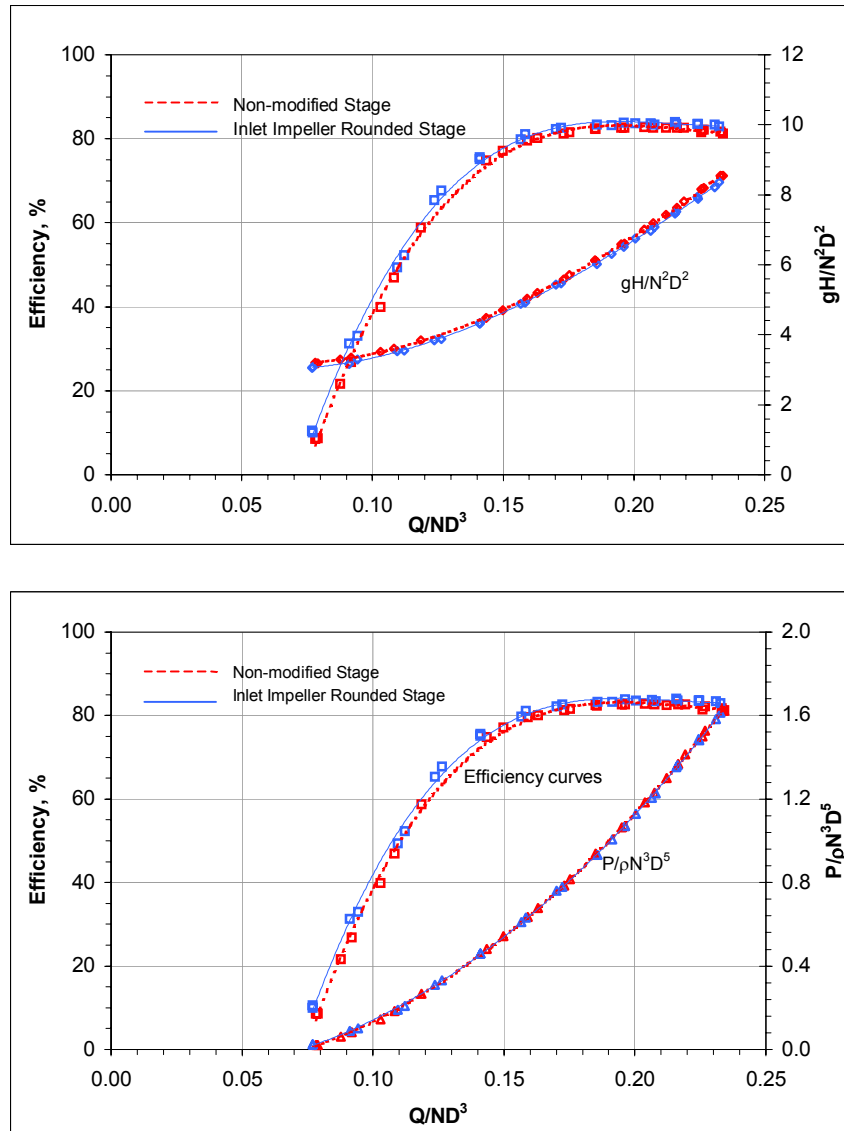
<u>Figure A5.7</u>, Comparisons of dimensionless characteristics for Optimization Stage I on the 39.7 rpm PAT

The percentage analysis of this optimization stage is carried out in <u>Figure A5.8</u>. The percentage power improvement curve shows a very different behaviour in that it enters the negative quadrant in the BEP region only, signifying a slight drop in the power production (0% to +0.5%) within the inlet rounded PAT. However in the overload region the power improvement curve once again becomes positive. The head number reductions on the other

hand is positive throughout the operating range with magnified reductions towards the part-load and overload regions. The head reductions drop from +2% at part-load line to +1.6% at the BEP line. The head reductions continue to magnify in the overload region over +2%. The efficiency rise over the entire characteristics is positive but the rise is slightly pulled down due to the negative behaviour of the power number curve. <u>Table A5.6</u> summarizes the percentage analysis of the various parameters at part-load BEP and overload lines.

<u>Table A5.6</u>, Relative study at part-load, BEP and overload lines for Optimization Stage I on 39.7 rpm PAT

	Part-load line $\phi = 0.140$	BEP line $\phi = 0.200$	Overload line $\phi = 0.250$
Head reduction	+2.0%	+1.6%	+2.3%
Power improvement	+0.5%	-0.5%	+0.2%
Efficiency rise	+1.8%	+0.9%	+2.1%
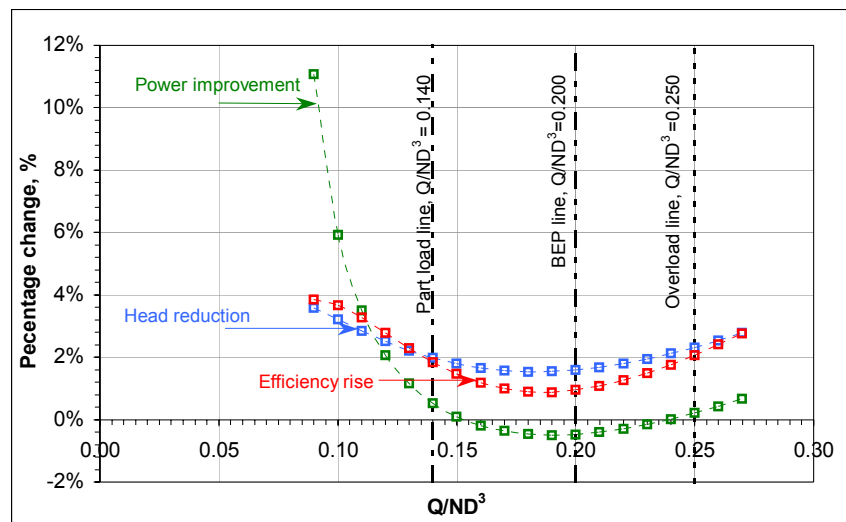
<u>Figure A5.8</u>, Percentage Analysis Plot for Optimization Stage I on the 39.7 rpm PAT

Discussion of Results on the 39.7 rpm PAT

The drop in power in the main operating region of the inlet rounded PAT is an interesting behaviour. This drop can only signify two possibilities namely either the increase of losses within the impeller control volume or decrease of the net rotational momentum across the impeller, from Equation (2.6), Chapter 2. The behaviour of the head reduction curve reveals that either the overall losses have reduced or the net rotational momentum has dropped, from Equation (2.5), Chapter 2. Drop in rotational momentum is a common factor between the effects of power and the head parameters. Therefore there could be a possibility of change in the $gH_{Eu.slip}$, for which to happen the inlet velocity triangle should be altered.

Though the other possibility of increase of losses within the impeller is difficult to explain it should be considered as well. This could be related to the axial displacement of the impeller combined with some non-uniform rounding. On the other hand the behaviour of the head reduction curve reveal that the overall PAT control volume losses have considerably reduced despite the probable increase of the losses of zone *iii* and *iv*. It is interesting to point out that the head reduction curve has been pulled down within the identical operating region where power drop has occurred.

It is difficult to exactly determine the decrease in angular momentum and increase of losses within the impeller, which are simultaneously occurring. Irrespective of the above, there is considerable evidence for reduction of losses within zone *ii* and overall improvement of the modified PAT's performance.

A5.1.4   45.2 rpm PAT

In addition to the rounding of the inlet blade profiles and shrouds, this optimization stage also includes the repair of a small broken piece of rear shroud. The effect of this modification is studied using the dimensionless plot in Figure A5.9. The first sight of comparison of the characteristics reveals a very odd behaviour as far as the power number characteristics are concerned. While the head number curve for the modified PAT has taken a major divergence with very large reductions throughout the operating range, the power number curve for the same modified PAT has also fallen below that of the non-modified stage. This is a very unexpected result especially with the rounding and shroud repair carried out.

The drop of the reduction is so large compared to the decrease in power production that the efficiency characteristics of the modified PAT have still improved considerably over the entire operating range. Table A5.7 summarizes the BEP for both the stages. While the head number has decreased from 6.757 units to 6.183 units, the power number drops from 1.219 to 1.161 with a resulting efficiency rise from 76.8% to 79.9%.

Table A5.7, BEP summary for two stages of Optimization Stage I on the 45.2 rpm PAT

Stage	ϕ	ψ	**p**	η
Non-modified	0.235	6.757	1.219	76.8%
Inlet-rounded	0.235	6.183	1.161	79.9%
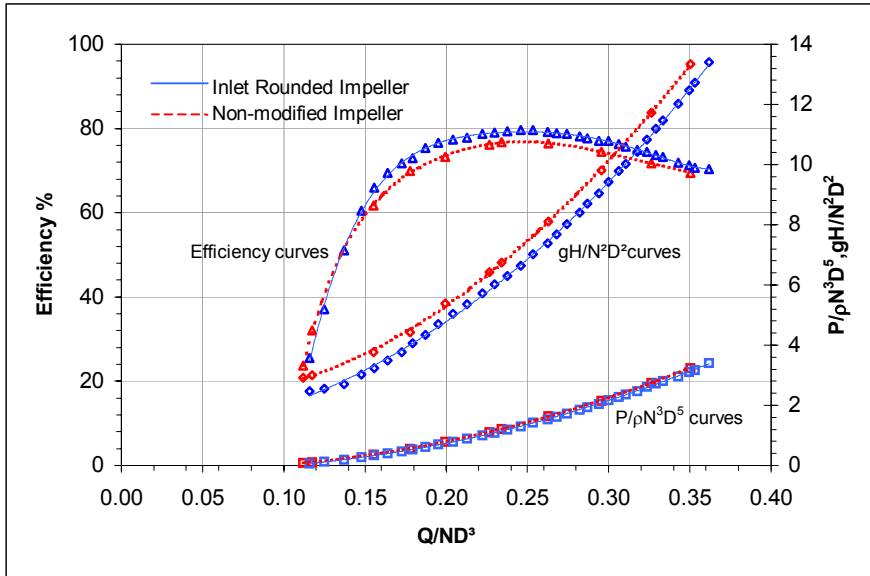
Figure A5.9, Comparisons of dimensionless characteristics for Optimization Stage I on the 45.2 rpm PAT

To get a clearer picture of the power number and head number effects the overall percentage analysis chart is plotted in Figure A5.10. The power improvement has dropped below the abscissa for the entire range. The drop of power is as much as -9 % in the part-load region and slowly improves to a -3% to -3.5% drop towards the overload line. The head reduction curve is positive throughout with +12% reduction in the part-load region to about +6% to +7% reductions in the overload region. Due to the increase influence of the head reductions the overall efficiency rise curve is positive throughout in the range of +3% in the part-load and BEP region and decreases to about +2% in the overload region. Table A5.8 analyses the relative behaviour of the various parameters at part-load, BEP and overload lines respectively.
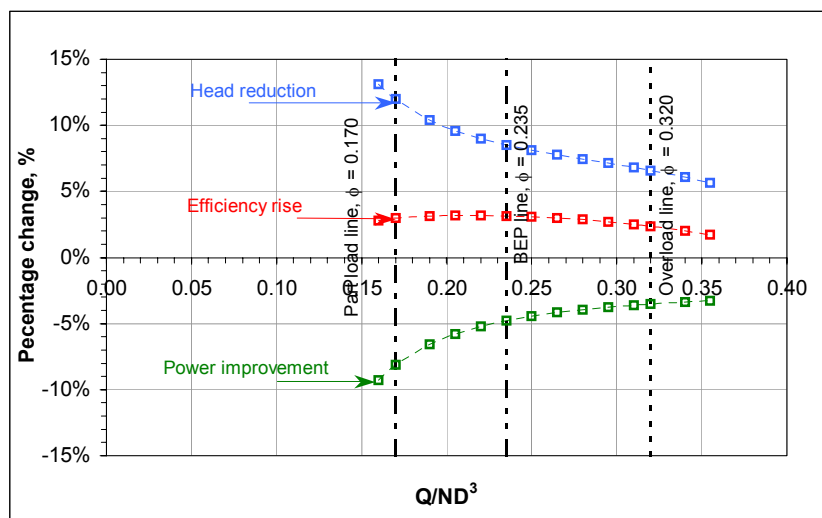
Figure A5.10, Percentage Analysis Plot for Optimization Stage I on the 45.2 rpm PAT

Table A5.8, Relative study at part-load, BEP and overload lines for Optimization Stage I on 35.3 rpm PAT

	Part-load line $\phi = 0.170$	BEP line $\phi = 0.235$	Overload line $\phi = 0.320$
Head reduction	+12.0%	+8.5%	+6.6%
Power improvement	-8.1%	-4.8%	-3.5%
Efficiency rise	+3.0%	+3.1%	+2.4%

Discussion of Results on the 45.2 rpm PAT

The decrease of power number can only suggest either increase in the impeller losses or decrease of the net rotational momentum, $gH_{Eu.slip}$ (defined in Equation (2.6), Chapter 2). Similarly the reduction of the head number curve indicates either a decrease in the losses within the PAT control volume or decrease of the net rotational momentum (defined in Equation (2.5), Chapter 2). From the behaviour detailed out in Figure A5.9 and A5.10 and given the above conditions, it can be quite confidently said that the net rotational momentum across the impeller has decreased, causing the head number curve to decrease and also the power number curve for the modified stage. This drop in the rotational momentum is obviously not coming from the inlet rounding effects and can be only due to the repair of the shroud plate. No doubt that the inlet rounding is also having positive impacts head number curve causing further reduction, which has been consistently observed in the head reduction curve in Figure A5.10. This impact can be directed to the decrease of losses more specifically in zone *ii*. Further it appears that the behaviour of power improvement curve is influenced only by the decrease of the net rotational momentum and not to the probable decrease in the loss composition within the impeller control volume.

To summarize this modification of repair of shroud plate and inlet rounding on the 45.2 rpm PAT has affected the net rotational momentum developed across the impeller and losses only in zone *ii* and probably leaving the loss distribution in zone *iii* and *iv* intact.

A5.1.5   46.4 rpm PAT

The modification carried out on the 46.4 rpm PAT is restricted only to rounding on the blade profiles and shrouds surfaces respectively. The effects optimization is analyzed in Figure A5.11, where it is seen that head number characteristics for the inlet rounded PAT has dropped below that of the non-modified PAT and as expected with greater reduction margins in the part-load and overload region. Between the part-load region and the BEP region the margins of reductions are slightly decreased. However there is no observable distinction between the power number characteristics for the two PATs, which nearly collapse into each

other. The resulting efficiency curve for the inlet rounded PAT shows a uniform rise beginning from the part-load region towards the BEP and overload regions in the range of 1.5% to 2%. This enhancement of efficiency is coming solely from head number effects.
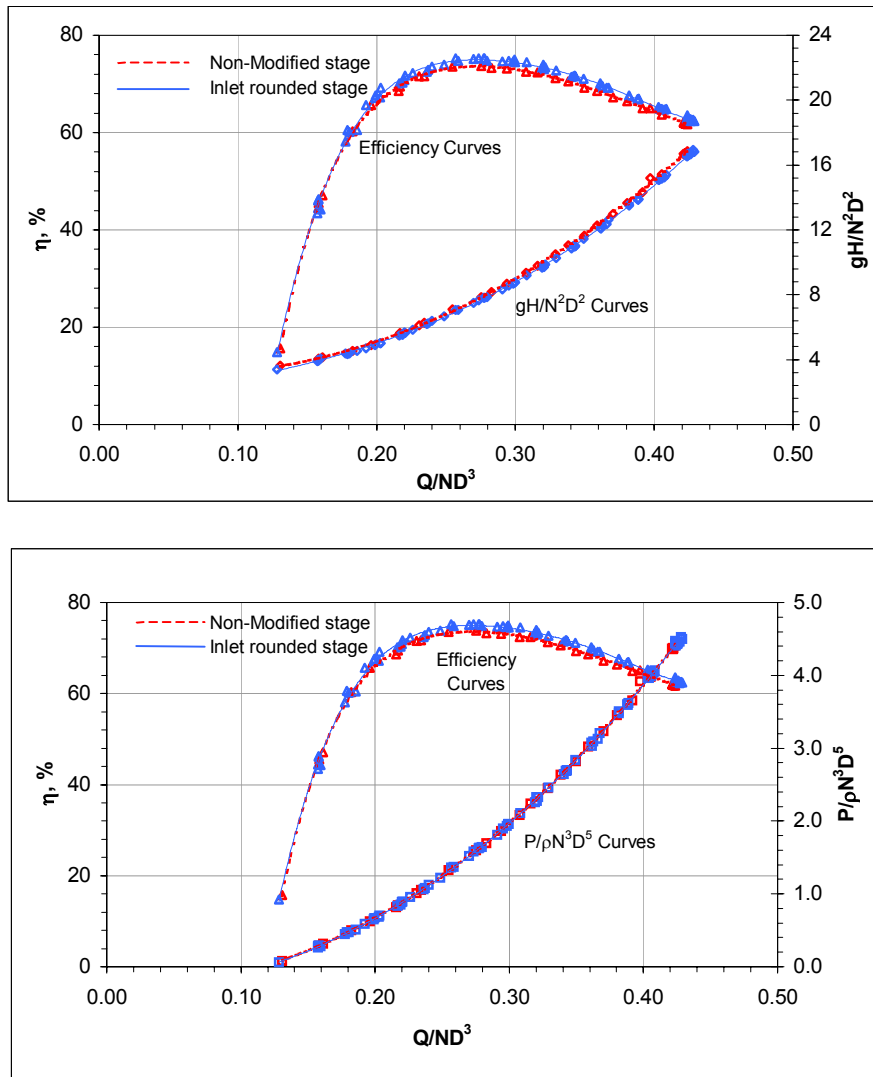
Figure A5.11, Comparisons of dimensionless characteristics for Optimization Stage I on the 46.4 rpm PAT

The BEP point has been analyzed in Table A5.9, in which there is decrease of head number from 7.819 to 7.663, while the power has marginally decreased from 1.592 to 1.589 with overall efficiency increasing from 74% to 75.4% a rise of +1.4%.

Table A5.9, BEP summary for two stages of Optimization Stage I on the 46.4 rpm PAT

Stage	ϕ	ψ	**P**	η
Non-modified	0.275	7.819	1.592	74.0%
Inlet-rounded	0.275	7.663	1.589	75.4%

From the percentage analysis chart in <u>Figure A5.12</u>, the head reduction curve is positive throughout the operating range. The head reductions rise from +1.8% in the part-load region to +2.3% in the overload region and then begin to decrease. The power number improvement line is only marginally negative which means that there is slightly decrease of power generation with in the inlet rounded PAT. However the decrease of power is mainly between 0 to +0.2% and can be neglected. Owing to the positive effect of the head number curve the efficiency rise curve is positive with a +1.2% rise in the part-load region to +1.5% in the main operating region and drops to +1.1% deep in overload region. The relative influences of the head and power parameters towards the efficiency changes at the part-load, BEP and overload lines are summarized in <u>Table A5.10</u>.

<u>Table A5.10</u>, Relative study at part-load, BEP and overload lines for Optimization Stage I on 46.4 rpm PAT

	Part-load line $\phi = 0.200$	BEP line $\phi = 0.275$	Overload line $\phi = 0.320$
Head reduction	+1.9%	+2.0%	+2.3%
Power improvement	-0.1%	-0.2%	-0.2%
Efficiency rise	+1.2%	+1.4%	+1.5%
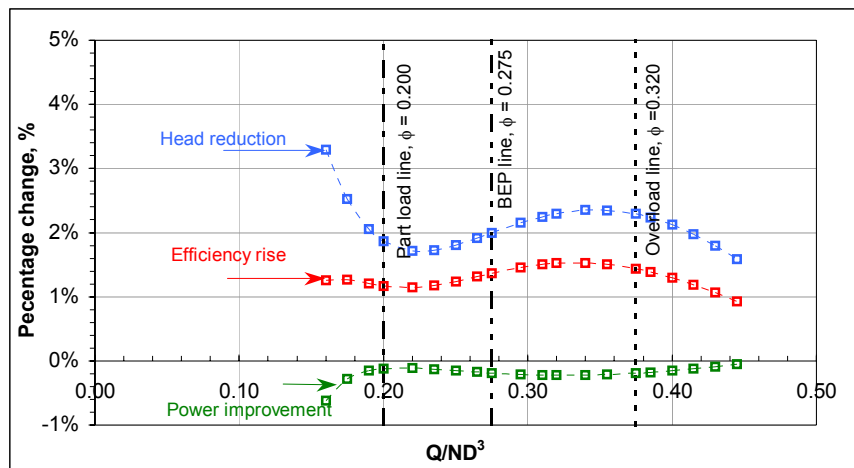
<u>Figure A5.12</u>, Percentage Analysis Plot for Optimization Stage I on the 46.4 rpm PAT

Discussion of Results on the 46.4 rpm PAT

There is clear evidence of no improvement in the power characteristics of the inlet rounded PAT. In fact there is power drop of -0.2%, which is though negligible must be attributed either to the increasing losses in the impeller control volume or drop in the net rotational momentum. However there is less probability of reduction of losses within the zone *iii* and *iv*.

The consistent head reduction patterns indicate more towards the decrease of losses within the PAT control volume, however there could be small influences of any changes in the net rotational momentum effects. Since the impeller losses have not changed, the only possibility is that losses in the zone *ii* have decreased.

A5.1.6   79.1 rpm PAT

The modification on the 79.1 rpm PAT comprises of rounding only on the impeller blade profiles. The inner surfaces of the front and rear shrouds had been previously widened and rounded. The impeller centerline of this stage has an axial misalignment of nearly 1.5 mm with respect to the volute casing's centerline as seen in Figure A5.13.
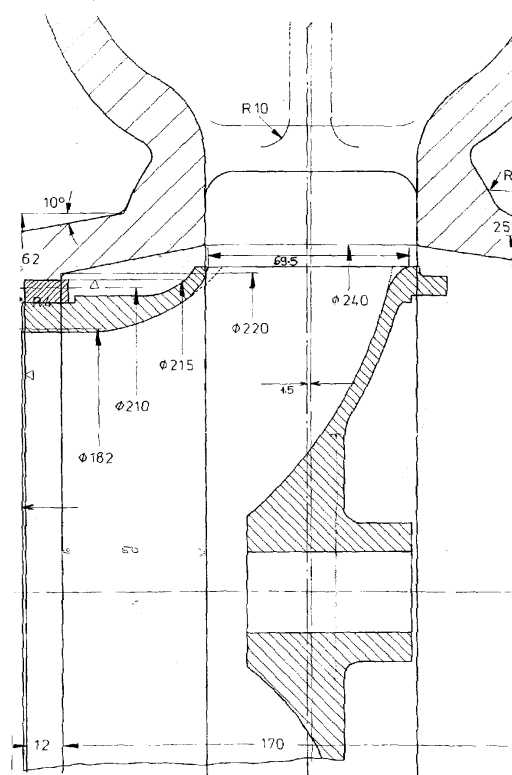
Figure A5.13, Cross-sectional view of the impeller-casing interface for the non-modified 79.1 rpm PAT

Figure A5.14 summarizes the dimensionless characteristics for this optimization stage. The head number characteristics of the modified PAT practically show no difference within the main operating region. However the head number curve drops in the part-load and overload region. On the other hand the power number characteristics for the two stages look essentially the same except for minor improvements in the part-load region for the modified stage. Owing to the joint contribution from the head reductions and power improvements in the part-load region the efficiency has shown a rise in the range of +1.5% to +2%. However in the main operating region of the BEP and overload region there is no improvement in efficiency. The BEP point for the optimization stage is summarized in Table A5.11 shows

that the head number for the inlet rounded PAT rises from 4.880 to 4.883 while the power number rises marginally from 1.768 to 1.771 with efficiency changing marginally from 75.5% to 75.6%.

Table A5.11, BEP summary for two stages of Optimization Stage I on the 79.1 rpm PAT

Stage	ϕ	ψ	**p**	η
Non-modified	0.480	4.880	1.768	75.5%
Inlet-rounded	0.480	4.883	1.771	75.6%
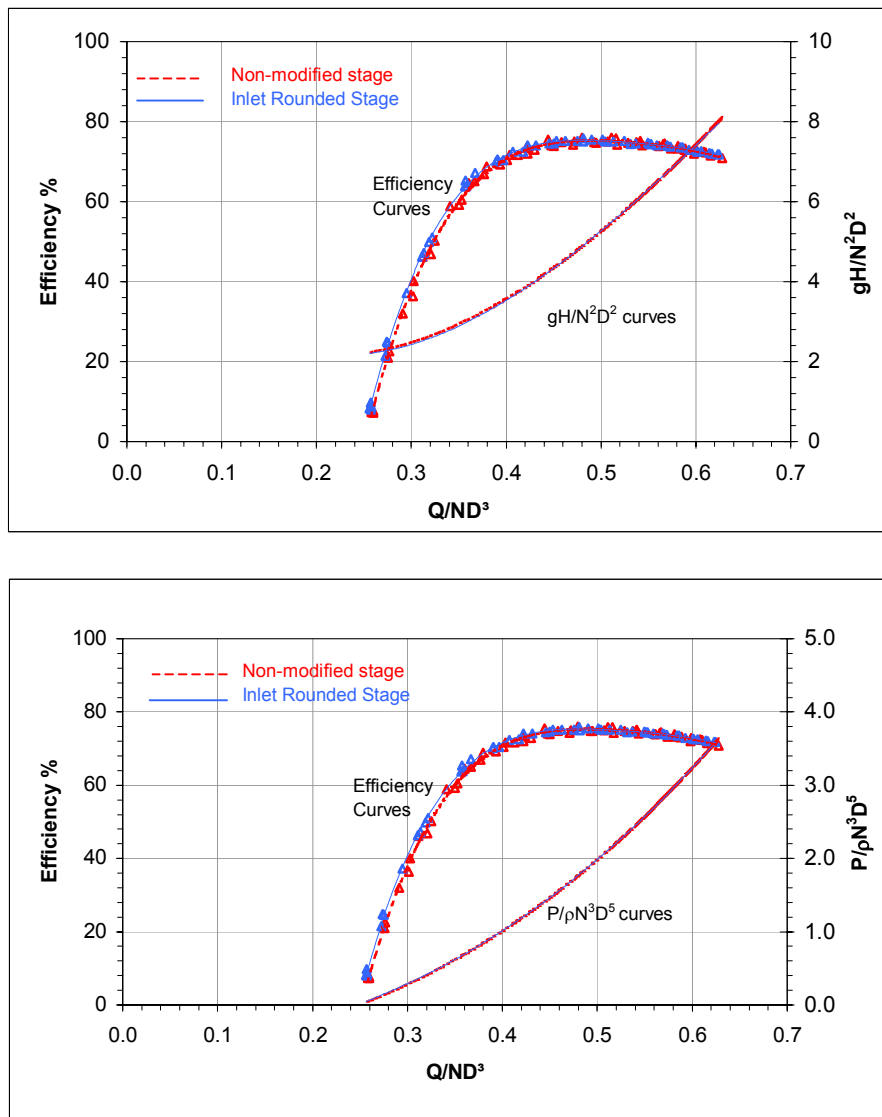
Figure A5.14, Comparisons of dimensionless characteristics for Optimization Stage I on the 79.1 rpm PAT

From the percentage analysis in Figure A5.15, it is seen that the percent power improvement line for the modified PAT is positive throughout the operating range. The power improvement

is +1.5% in the part-load region, which gradually reduces to +0.2% in the BEP and diminishes in the overload region. The percent head reduction line remains positive in the part-load region and overload region but falls below the abscissa in the BEP region to -0.2%, which is a negligible rise for the inlet rounded PAT. Subsequently, there is positive efficiency rise of +1.5% in the part-load region, and no noticeable rise in the BEP region, however towards the overload region a small efficiency rise is recorded. The part-load, BEP and overload points are analyzed in <u>Table A5.12</u> with respect to the head reductions, power improvements and efficiency rise.

<u>Table A5.12</u>, Relative study at part-load, BEP and overload lines for Optimization Stage I on the 79.1 rpm PAT

	Part-load line $\phi = 0.380$	BEP line $\phi = 0.480$	Overload line $\phi = 0.600$
Head reduction	+1.3%	+0.0%	+0.1%
Power improvement	+0.9%	+0.2%	+0.0%
Efficiency rise	+1.5%	+0.1%	+0.1%
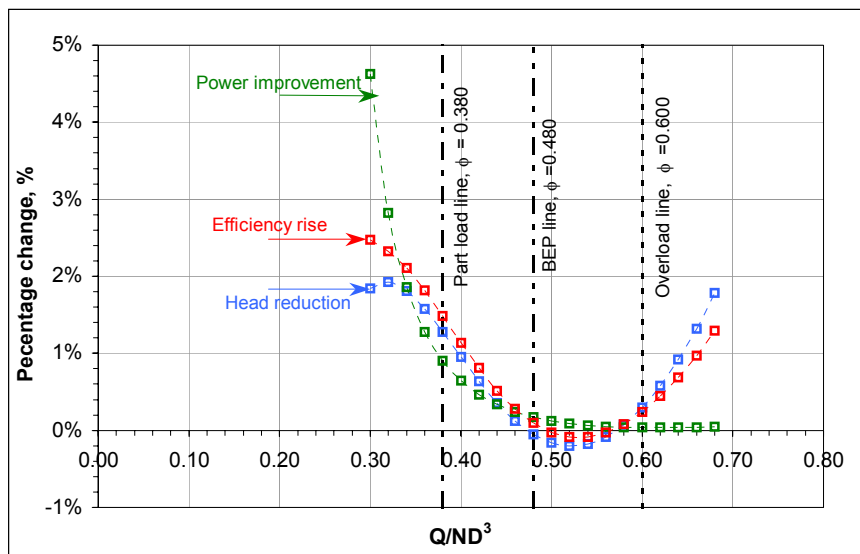
<u>Figure A5.15</u>, Percentage Analysis Plot for Optimization Stage I on the 79.1 rpm PAT

Discussion of Results on the 79.1 rpm PAT

Within the operating region between the no-load line and BEP line as defined in <u>Figure A5.15</u>, the modified PAT shows greater power production. This could mean either a reduction of impeller control volume losses or a rise in rotational momentum. Within the same region there is a positive head reduction, which can happen only with reduction of losses within the PAT control volume. This suggests that there is no change in rotational

momentum across the turbine. Therefore part of the head reduction is coming from lower losses in the zone *iii* and *iv* and another part from the zone *ii*.

However within the main operating region, the head reduction become negative, which indicate a net increase of PAT control volume losses. This is despite a marginal loss reduction within the impeller zone *iii* and *iv*. This suggests that one component of losses in zone *ii* has increased throughout the range, which could be associated with some other external influence or impeller misalignment. This increased component is nullifying the reduction of the other loss component associated with rounding effects in zone *ii*.

In the overload region, a very marginal improvement of power is recorded but a very substantial reduction of head, which is continuously rising. Therefore the losses in zone *ii* have decreased by a larger extent signifying that the loss component due to blade rounding has a dominating effect compared to the negative effect of the external loss component. There is also negligible but noticeable drop of the losses in zone *iii* and *iv*.

To summarize, it is seen that the inlet blade rounding on the 79.1 rpm PAT has marginally improved the performance in terms of efficiency. However it clearly demonstrates positive hydraulics in the impeller zone *iii* and *iv*. It also shows that there are two component of losses associated with zone *ii*, one attributed to rounding effects and other to external influences. The loss component due to rounding has showed it's greater presence in the part-load and overload region only. The external loss component is playing dominating role in the BEP region.

A5.1.7   94.4 rpm PAT

The modification on the mixed flow 94.4 rpm impeller consists of rounding the inlet, inclined blade profiles only. As seen in section A4.2, Appendix A, the impeller of 94.4 rpm PAT is semi-open. The characteristics are plotted in Figure A5.16, where it is found that the head number characteristics for the inlet rounded has fallen below that of the non-modified stage throughout the operating range with larger reductions in the part-load and overload region and marginal reduction in the BEP region. The power characteristics for the modified display enhanced productions till the BEP region and towards the overload region the power curves collapse together. Deep in the overload region, once again an increased power generation is recorded. Due to the above, the efficiency curve for the inlet rounded PAT shows gains throughout the range with +1% to +1.2% in the BEP region.

The BEP point for the two stages is analyzed in Table A5.13, sees an increase of power number from 1.264 to 1.273, while the head number decreases from 3.823 to 3.807 causing a net efficiency rise from 82.7% to 83.6%.
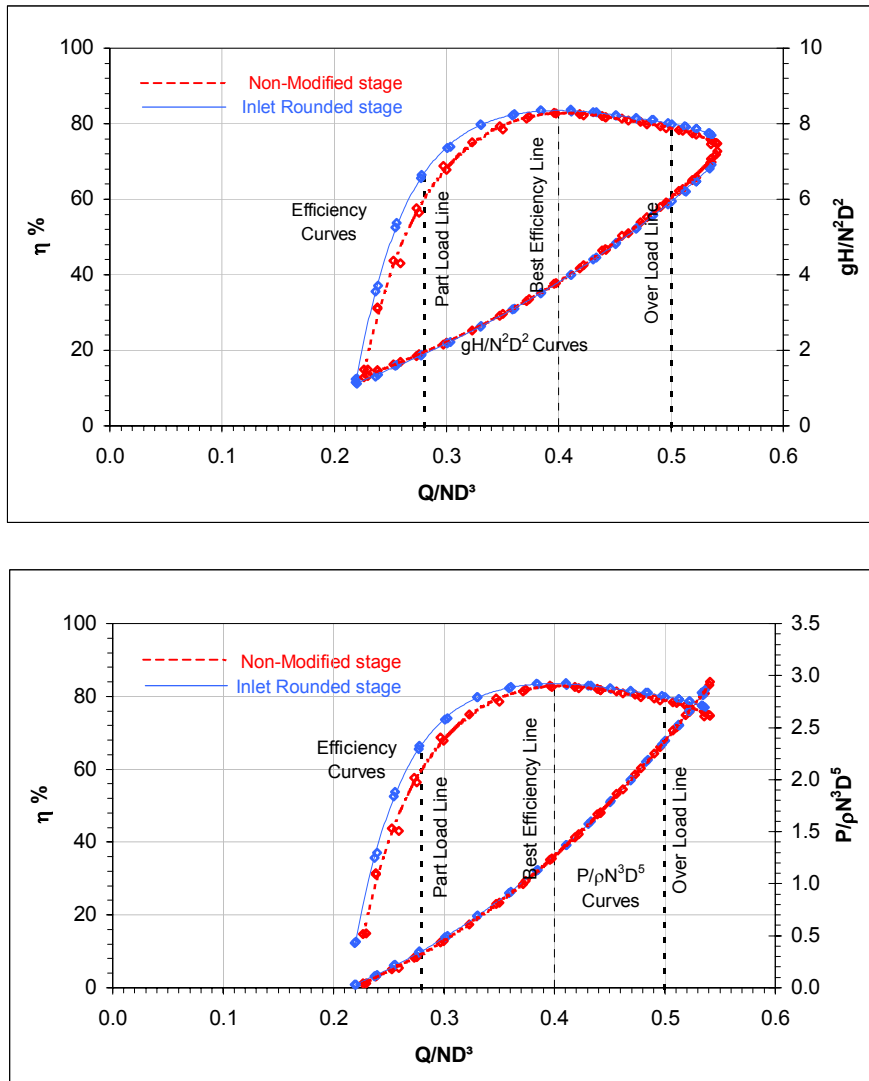
<u>Figure A5.16</u>, Comparisons of dimensionless characteristics for Optimization Stage I on the 94.4 rpm PAT

<u>Table A5.13</u>, BEP summary for two stages of Optimization Stage I on the 94.4 rpm PAT

Stage	ϕ_{mf}	ψ_{mf}	$\mathbf{P}_{mf}$	η
Non-modified	0.400	3.823	1.264	82.7%
Inlet-rounded	0.400	3.807	1.273	83.6%

It is seen from the percentage analysis plot in <u>Figure A5.17</u> that there is excessive power generation for the modified PAT in the part-load region in the range of +6% to +2% and this decreases towards to the main operation region. The power improvement curve actually falls below the abscissa in the overload region before it begins to rise up again. The percentage head reduction curve remains positive throughout the operating range with maximum reductions in the part-load region (+2.2%) and overload region (+1.7% to +3%), while at the BEP the percentage reduction is only +0.4%. The efficiency rise in the part-load region is mainly coming from power number effects and slightly from head number effects, but the

overload efficiency rise is mainly coming from head number effects. <u>Table A5.14</u> summarizes the situation of various parameters at the part-load, BEP and overload region respectively.

<u>Table A5.14</u>, Relative study at part-load, BEP and overload lines for Optimization Stage I on the 94.4 rpm PAT

	Part-load line $\phi_{mf} = 0.280$	BEP line $\phi_{mf} = 0.400$	Overload line $\phi_{mf} = 0.500$
Head reduction	+2.2%	+0.4%	+1.7%
Power improvement	+8.9%	+0.7%	-0.1%
Efficiency rise	+6.8%	0.9%	+1.3%
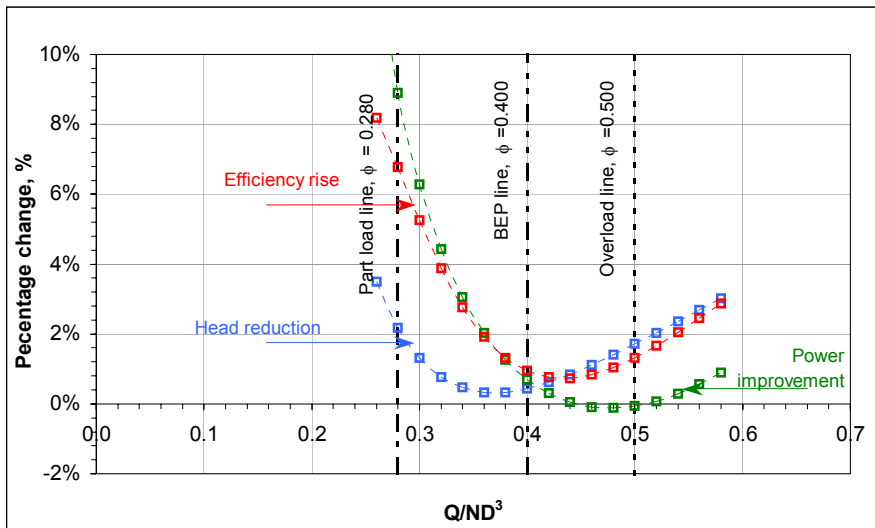
<u>Figure A4.17</u>, Percentage Analysis Plot for Optimization Stage I on 94.4 rpm PAT

Discussion of Results on the 94.4 rpm PAT

The behaviour of the head reduction curve clearly indicates that the rotational momentum effects have not been altered. Therefore only the loss mechanisms are to be considered. The power rise recorded in the part-load region can only indicate that the losses in zone *iii* and *iv* have been reduced for the inlet rounded PAT. But within a small operating range in the overload region these losses don't change. After the overload line, the impeller zone losses once again show signs of reduction.

The head reduction in the part-load region is coming mainly from reduction of losses in the impeller zone *iii* and *iv*. There does not seem to be any loss reductions in the stationary zone *ii*. With such a large reduction of losses in zone *iii* and *iv* and the head reduction curve not rising as much, there may be possibility of increase of losses in zone *ii*. However in the BEP and overload region, the continuous rise of head reduction curve and the marginally

improvement of power only go to say that zone *ii*'s losses have dropped considerably. Therefore this modified PAT indicates that within the part-load region there greater reduction of impeller losses and within the overload region there is increased reduction of losses in zone *ii*.

A5.2   Optimization Stage II

A5.2.1   39.7 rpm PAT

This optimization stage comprises of the installation of two tapered rings within the radial clearance zone *ii* as shown in Figure A5.18. This modification has therefore completely transformed the geometry of zone *ii*. The existing axial displacement of the impeller (around 1.25 mm) has however not been corrected, which therefore results in a non-symmetric interface of the two rings with respect to the impeller width. The ring on the rear side projects itself ahead of the impeller shroud slightly reducing the impeller flow area.
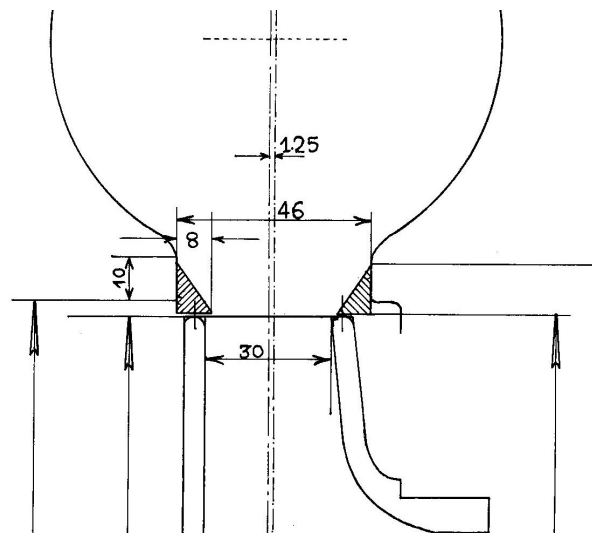
Figure A5.18, Tapered rings insertion in the Optimization Stage II on the 39.7 rpm PAT

The dimensionless characteristics for the two stages plotted in Figure A5.19, shows that the head number for the modified PAT has undergone a complete transformation with increased head consumption patterns throughout the operating range. The margin of increase tends to magnify in the BEP and overload region. The power characteristics for the modified PAT on the other hand display two different behaviours, one in the part-load and the other in the BEP/overload regions. In the part-load region the modified PAT shows decreased power production but the it increases in the BEP and overload region.

Due to the combined effect of the increased head number and lower power production, there is steep fall of the part-load efficiency (-3% to -5%) for the modified PAT. The difference between the two efficiencies reduces in the BEP region (-1% to -1.5%) mainly due to increased power in the modified PAT, but the efficiency is still lower than the non-modified

PAT. Table A5.15 shows that at the BEP, the head number increases from 6.699 units to 6.869 units for the modified PAT stage, while the power number rises from 1.124 to 1.134 still causing the net efficiency to decrease from 83.9% to 82.5% representing a fall of -1.4%.

Table A5.15, BEP summary for two stages of Optimization Stage II on the 39.7 rpm PAT

Stage	ϕ	ψ	**p**	η
Non-modified	0.200	6.699	1.124	83.9%
Inlet casing rings	0.200	6.869	1.134	82.5%
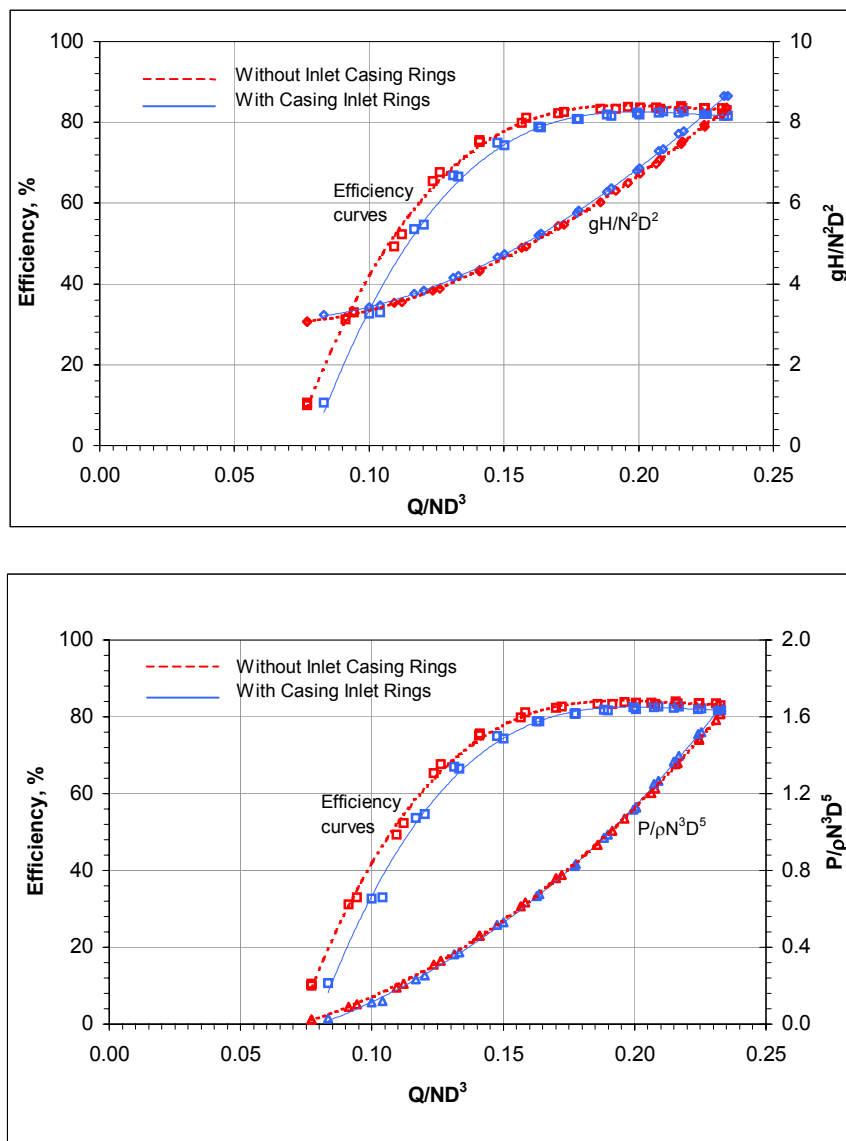
Figure A5.19, Comparisons of dimensionless characteristics for Optimization Stage II on the 39.7 rpm PAT

The percentage analysis chart in <u>Figure A5.20</u> shows that the head reduction curve is negative throughout the operating range. With head reductions of –2% in the part-load region, it continuously drops to –5% towards the overload region. The percent power improvement curve is negative in the part-load region with a drop in the range of -3% to -5%. The curve transforms itself and there is a continuous increase of power productions in the range of +1% to +4% in the BEP and overload region. The efficiency rise curve is below abscissa with consistent drop -4% in part-load region and -1.5% in the BEP and overload region.
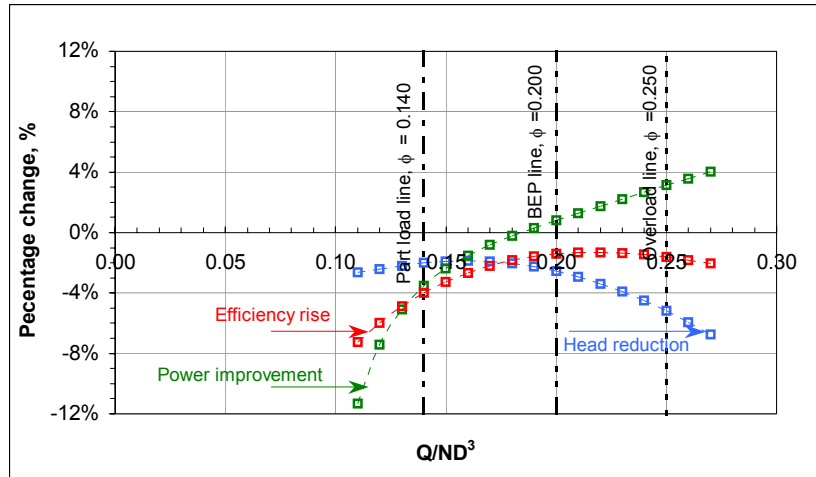
<u>Figure A5.20</u>, Percentage Analysis Plot for Optimization Stage II on 39.7 rpm PAT

In the main operating region the power number and head number show two distinctive and diverging behaviour, which is an issue of discussion. <u>Table A5.16</u> summarizes the relative effects of the various parameters in the part-load, BEP and overload lines.

<u>Table A5.16</u>, Relative study at part-load, BEP and overload lines for Optimization Stage II on the 39.7 rpm PAT

	Part-load line $\phi = 0.140$	BEP line $\phi = 0.200$	Overload line $\phi = 0.250$
Head reduction	-2.0%	-2.5%	-5.2%
Power improvement	-3.5%	+0.8%	+3.1%
Efficiency rise	-4.0%	-1.4%	-1.6%

Discussion of Results on 39.7 rpm PAT

The addition of inlet casing rings especially of the tapered design has brought an overall degradation to the machine's performance. The decrease of power in the part-load region off course represents increase of losses within the impeller. But the behaviour of the power

improvement line in Figure A5.20, i.e. from −11% to 0% suggests that there could be an influence from the net rotational momentum effect as well. In that rotational momentum is increasing continuously to negate the increase of impeller losses (Equation (2.6), Chapter 2). Simultaneously in this range the head reduction is negative, which could mean that there is an overall increase of losses across the PAT control volume or increasing rotational momentum (Equation (2.5), Chapter 2).

In the BEP/overload region the continuous rise of the power improvement line in the positive quadrant proves that the increased rotational momentum effect is playing a role. There could also be a situation of decrease of losses within the impeller. While on the other hand the negative trend of head reduction (Figure A5.20) also proves the increasing effect of rotational momentum and increased PAT control volume losses. However the increased losses in the PAT control volume are so large compared to the increased momentum effects that the efficiency drops throughout the operating range.

The physics of behaviour of the zone losses in tandem with the probable rotational momentum influence is discussed in two parts concerning the power and head curves respectively.

Part 1 – Power improvement curve

The protrusion of the rear casing ring in Figure A5.18, causes continuous flow separation especially at the inner surface of the rear shroud. This represents one component of losses in zone *iii* and *iv* that will be present throughout the operating range.

There is another effect that is influencing the power number, which can be attributed to the rotational momentum of the inlet velocity triangle. The addition of the tapered rings has caused greater contraction of the flow area as compared to the condition without casing rings. This contraction would cause an increase in absolute flow velocity entering the impeller zone and to maintain identical merdional velocities there is a decrease of flow angle α_1 for both the part-load and overload conditions as seen from Figure A5.21. This rearrangement of velocity triangles causes an increase in the rotational momentum ($v_u u$) for both the part-load and overload regions.

The increased $v_u u$ continuously interacts with the flow separation loss component in zone *iii* and *iv*. In the part-load region, the flow separation effect is dominating over the momentum effect, causing the power of the modified PAT to decrease. However the rotational momentum effects gains in magnitude and outweighs the flow separation loss component in the BEP/overload region, casing an increased power generation for the modified PAT.

Part 2 – Head reduction curve

The zone *ii*, in this optimization stage, is the region where many simultaneous are effects taking place. One of the hydraulic effects is the increased frictional losses which gets

magnified in the modified PAT not only due to increased velocity of flow but also due to greater friction that the solid rings offers compared to the water interface without rings. With increasing velocities at higher load conditions (Figure A5.21) these losses also increase.

Another important hydraulic effect is with respect to the shock velocities. Due to the alternation of velocity triangle the magnitude of the shock loss component v_{sh} also changes for different load conditions as seen in Figure A5.21. In the part-load region the shock component decreases and hence the loss component $v_{sh}^2/2g$ will also decrease. Therefore in the part-load region, the head number for the modified PAT comprises of a decreased shock loss component, which is negating an increased friction loss component, along with the increased momentum and causing only small increase of head (-2% to -3% from Figure A5.20). However in the overload region the shock component rises as seen from Figure A5.21. This increased shock losses adds to the already increased frictional losses combined with the rise of the rotational momentum and causes a continuous increase of the head number (-2% to -7% from Figure A5.20) for the modified PAT.

Part-load condition

Overload condition
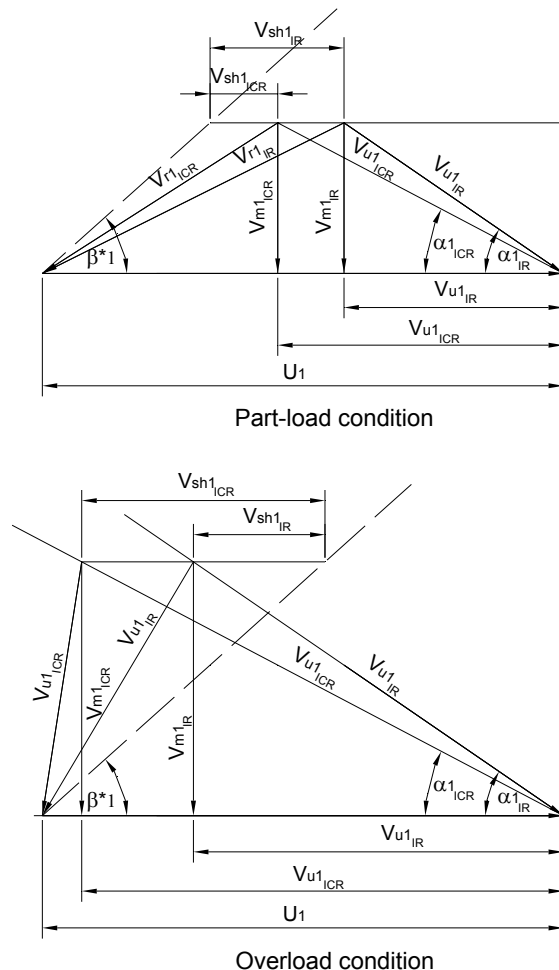
Figure A5.21, Velocity triangle formation at part-load and overload regions due tapered rings insertion on 39.7 rpm PAT

A5.3 Optimization Stage III

A5.3.1 35.3 rpm PAT

The modification carried out on the 35.3 rpm PAT is similar to that of the 24.5 rpm with diffusing impeller eye and an enlarged casing eye. The comparison of the characteristics in Figure A5.22 reveals that there are two distinctive patterns of behaviour of the head number curve for the modified PAT. While in the part-load region there is decreased head number consumption, in the BEP and overload region the head number curve rises above that of the non-modified stage. The power number curve for the modified PAT shows a constant increase of power throughout the operating range. Owing to the decreased head number and increased power, the part-load efficiency for the modified PAT has enhanced. But in the BEP and overload region the efficiency has dropped by at least 1%. Even though greater power production is consistently recorded, the increased head number is so large that efficiency drops.
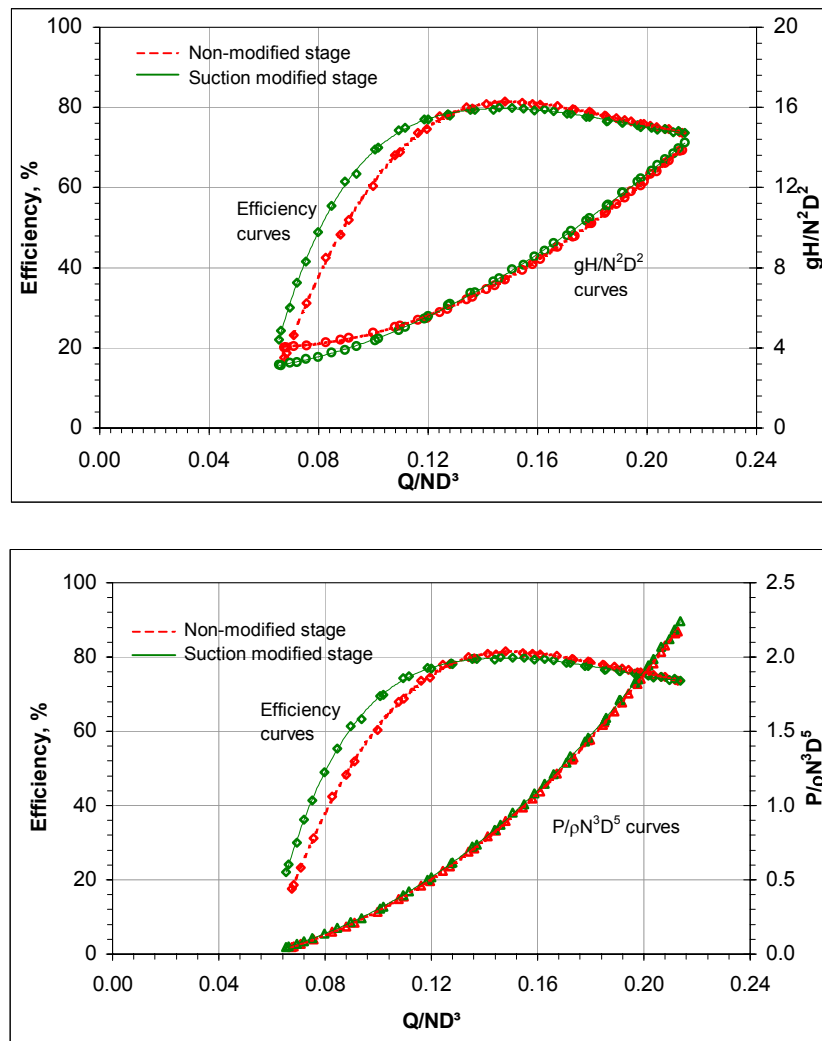
Figure A5.22, Comparisons of dimensionless characteristics for Optimization Stage III on 35.3 rpm PAT

The analysis in <u>Table A5.17</u> reveals that though the power has considerably increased from 0.9347 units to 0.9508 units, the efficiency drops from 81% to 79.7% due to the excessive rise of head number from 7.642 units to 7.899 units.

Table A5.17, BEP summary for two stages of Optimization Stage III on the 35.3 rpm PAT

Stage	ϕ	ψ	**p**	η
Non-modified	0.151	7.642	0.9347	81.0%
Suction eye enlarged	0.151	7.899	0.9508	79.7%

The percentage analysis chart in <u>Figure A5.23</u> shows a consistent improvement of power in the modified PAT with +3% improvement in the part-load region and +1.5% to +2% rise in the BEP and overload region. The head reductions are however positive only in the part-load region and become negative immediately after the part-load line. The trend continues and reaches to about –4% and later gets back to the abscissa only after the overload line. Greater influences from the negative head reduction patterns cause a fall in the efficiency, even though there is a rise of power throughout. <u>Table A5.18</u> summarizes the part-load, BEP and overload conditions with respect to relative change of the parameters.
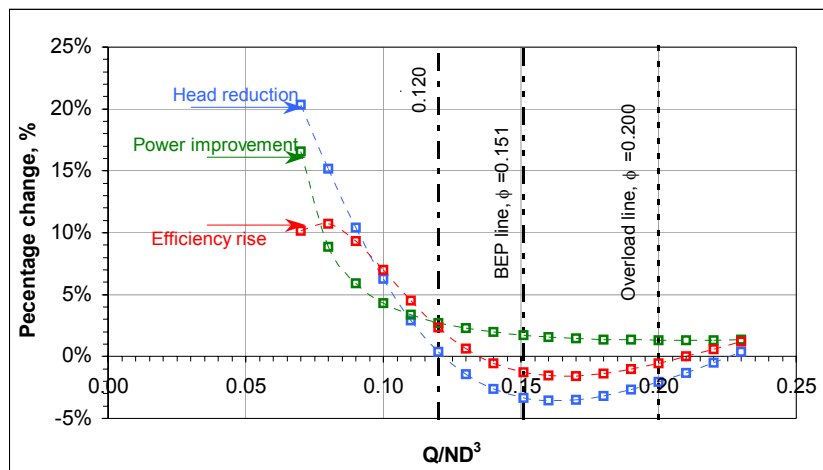
Figure A5.23, Percentage Analysis Plot for Optimization Stage III on the 35.3 rpm PAT

Table A5.18, Relative study at part-load, BEP and overload lines for Optimization Stage III on the 35.3 rpm PAT

	Part-load line $\phi = 0.120$	BEP line $\phi = 0.151$	Overload line $\phi = 0.200$
Head reduction	0.4%	-3.4%	-2.1%
Power improvement	2.7%	1.7%	1.3%
Efficiency rise	2.3%	-1.3%	-0.5%

Discussion of Results on 35.3 rpm PAT

Till the part-load line, both the trend lines for the power improvement and the head reduction are positive. This signifies that there has been significant decrease of losses within the impeller zone *v*, *iv* and *iii* as well as the eye zone *vi*. However, even if rotational momentum effects are present they are very marginal seeing the tremendous reductions of the head.

The behaviour of the head reduction curve between the part-load line and overload line in Figure A5.23, prove that there is either a condition of excessive rotational momentum effect or increased losses in the entire PAT control volume. On the other hand the consistent positive gains from the power curve in this region can either signify that the impeller losses have decreased or the rotational momentum has increased or a combination of both. There is also a strong situation of decreased losses in zone *vi*, due to enlarged area and reduced velocities. Therefore with increased probability of losses of the losses in zone *vi* to decrease, the head reductions for the modified PAT can become negative only with an increased rotational momentum component.

An interesting behaviour of the head reduction curve is in the overload region, where it tends to cross the abscissa and enter the positive quadrant despite the rotational momentum effects across the PAT. This can happen only with a significant reduction of losses in zone *vi* and the impeller zone.

The presence of a increased rotational momentum component can be directly linked to the decreased velocity conditions prevailing in the eye due to the enlargement of cross sectional area.

A5.4   Optimization Stage IV

A5.4.1   36.4 rpm PAT

A5.4.1.1   Overall Performance Comparison

Figure A5.24 describes the geometry of the zone *vi* which is of contracting design along with the rib. The contraction is quite large with from a diameter of ϕ115 mm at the plane '2' to ϕ82 mm at the plane 's'. The measurement plane 'e' is situated at an axial distance of 45 mm from the plane 's'.

The characteristics of the to stages are compared in Figure A5.25, where it is found that the head number curve for the rib absent stage is consistently lowered beginning from the part-load region and with magnified margins towards the overload region. The power characteristics also show a decreased production beginning from the part-load region and proceeds into the overload region with increased power drops. Therefore there is a condition of decreased power production along with lower head consumption. The overall efficiency

slightly drops at the BEP (by 1%) owing to greater power drop compared to the decrease in head as seen from Table A5.19.
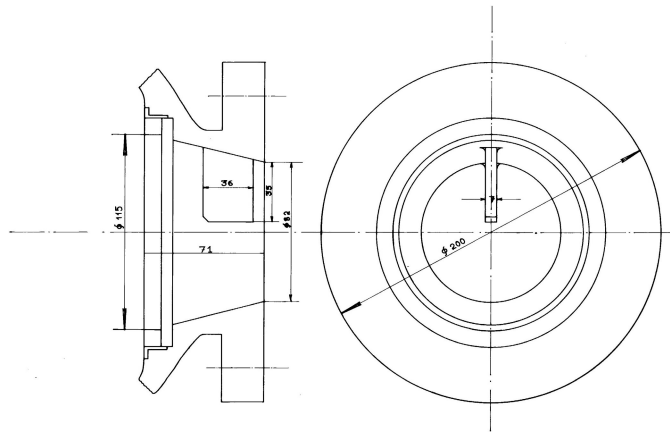

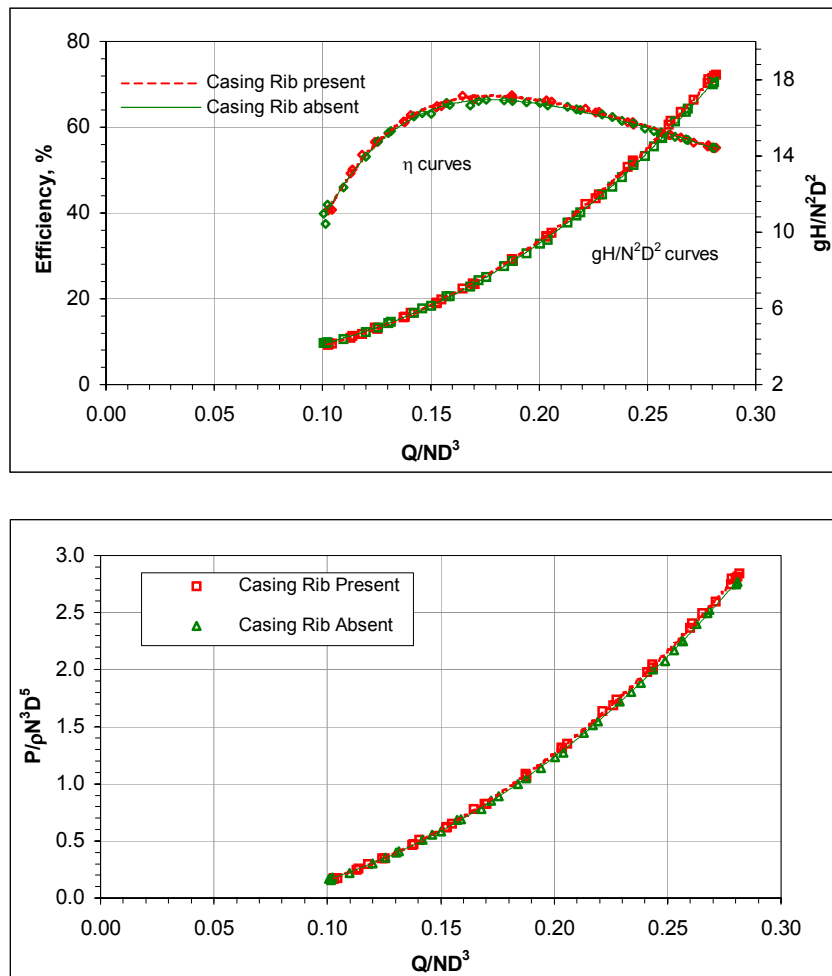Figure A5.24, Geometry of the casing eye rib for the 36.4 rpm PAT

Figure A5.25, Comparisons of dimensionless characteristics for Optimization Stage IV on the 36.4 rpm PAT

Table A5.19, BEP summary for two stages of Optimization Stage IV on the 36.4 rpm PAT

Stage	ϕ	ψ	**p**	η
Casing Rib Present	0.185	8.367	1.040	67.2%
Casing Rib Absent	0.185	8.278	1.017	66.4%

The percentage analysis chart in Figure A5.26 clearly demonstrates that the power improvement line is moving into the negative quadrant after the part-load line in the range of –1% to –2.4%. On the other hand the head reduction curve shows positive gains in the main operating region in the range of +0.5% to +1.8%. However between the no load and part-load line there is greater power production combined with greater net head across the PAT. The relative influence of the various parameters at part-load, BEP and overload regions is summarized in Table A5.20.
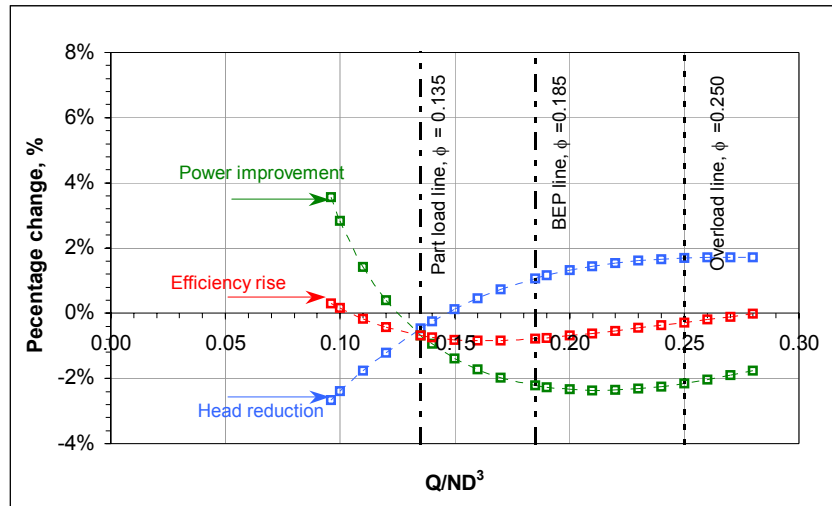
Figure A5.26, Percentage Analysis Plot for Optimization Stage IV on the 36.4 rpm PAT

Table A5.20, Relative study at part-load, BEP and overload lines for Optimization Stage IV on the 36.4 rpm PAT

	Part-load line ϕ = 0.135	BEP line ϕ = 0.185	Overload line ϕ = 0.250
Head reduction	-0.5%	+1.3%	+1.7%
Power improvement	-0.7%	-2.3%	-2.2%
Efficiency rise	-0.7%	-0.7%	-0.3%

Discussion of Results on the 36.4 rpm PAT

From the overall comparisons in Figure A5.25 and percentage analysis it Figure A5.26, the decreased power generation in the main operating region can signify either of the two effects; one associated with increased net rotational momentum and the other with the increased impeller control volume losses. The head reductions in the corresponding range are quite considerable. However these reductions cannot be owed to a possibility of decrease of loss component associated with the absence of the casing rib. Therefore, there is for certain a reduction of net rotational momentum across the PAT, owing to greater exit rotational momentum due enhanced swirl without casing rib. Within zone *vi*, in addition to the loss component attribute to frictional effects of the rib (λ component in Equation (2.20), Chapter 2) there is another loss component associated with swirl in the absence of the rib (ζ component in Equation (2.20), Chapter 2). The increased swirl loss components are countering the decreased frictional loss component.

The behaviour within the no-load and part-load region where the CRA stage shows greater power generation and higher operating net head, is however very difficult to explain.

A5.4.1.2   Internal Performance Comparison

The swirl profiles for the CRP and the CRA are plotted in Figure A5.27 and A5.28 at 5 load points described in Table A5.21. Care is taken to ensure that the 5 load points are almost identical.

Table A5.21, Definition of load points for swirl flow comparisons on 36.4 rpm PAT

Load Point	Condition	$Q/ND^3_{(CRP)}$	$Q/ND^3_{(CRA)}$
A	No Load	0.101	0.102
B	Part-load	0.137	0.140
C	BEP	0.187	0.193
D	Overload	0.238	0.236
E	Overload	0.272	0.273
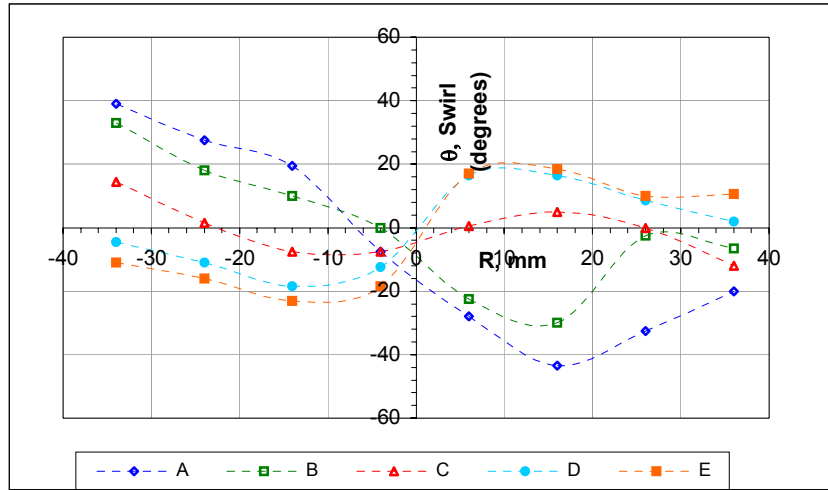
Figure A5.27, Swirl profiles for the CRP stage of the 36.4 rpm PAT

The swirl profiles for the CRP stage plotted in Figure A5.27 show that profiles for load A and B are not symmetrical, while for loads C, D and E show a relatively good symmetry about the central axis. Swirl intensity is highest at load A and reduces at load B and C. Load D and E have increasing swirls but in the negative direction (opposite to that of the PAT rotation). The BEP load point C shows only marginal swirl (less than 10^0) and displays a characteristic change of direction within the cross sectional plane.
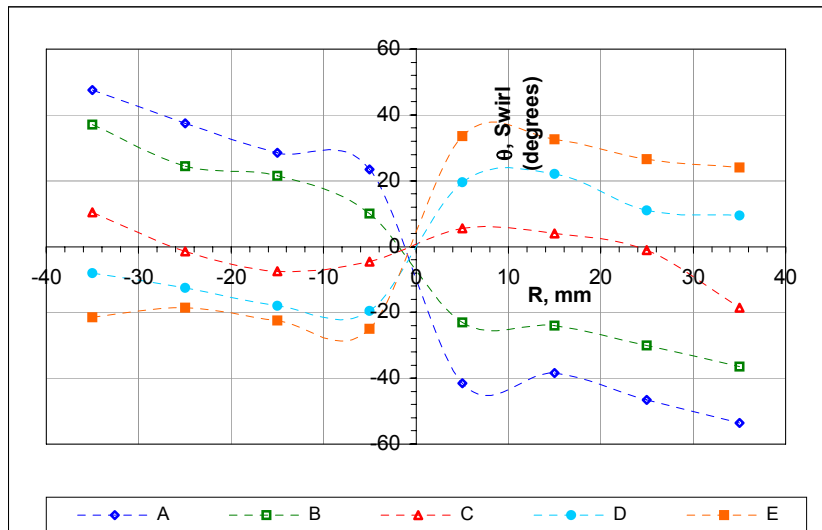
Figure A5.28, Swirl profiles for the CRA stage of the 36.4 rpm PAT

The swirl profiles for the CRA stage (Figure A5.28) show a very good symmetry consistently at all load points. It is also seen that the individual swirl profile intersects the central axis of the cross-section at 0^0 swirl. However the magnitude of the swirl in this stage is generally found to be larger compared to the corresponding load points of CRP stage.
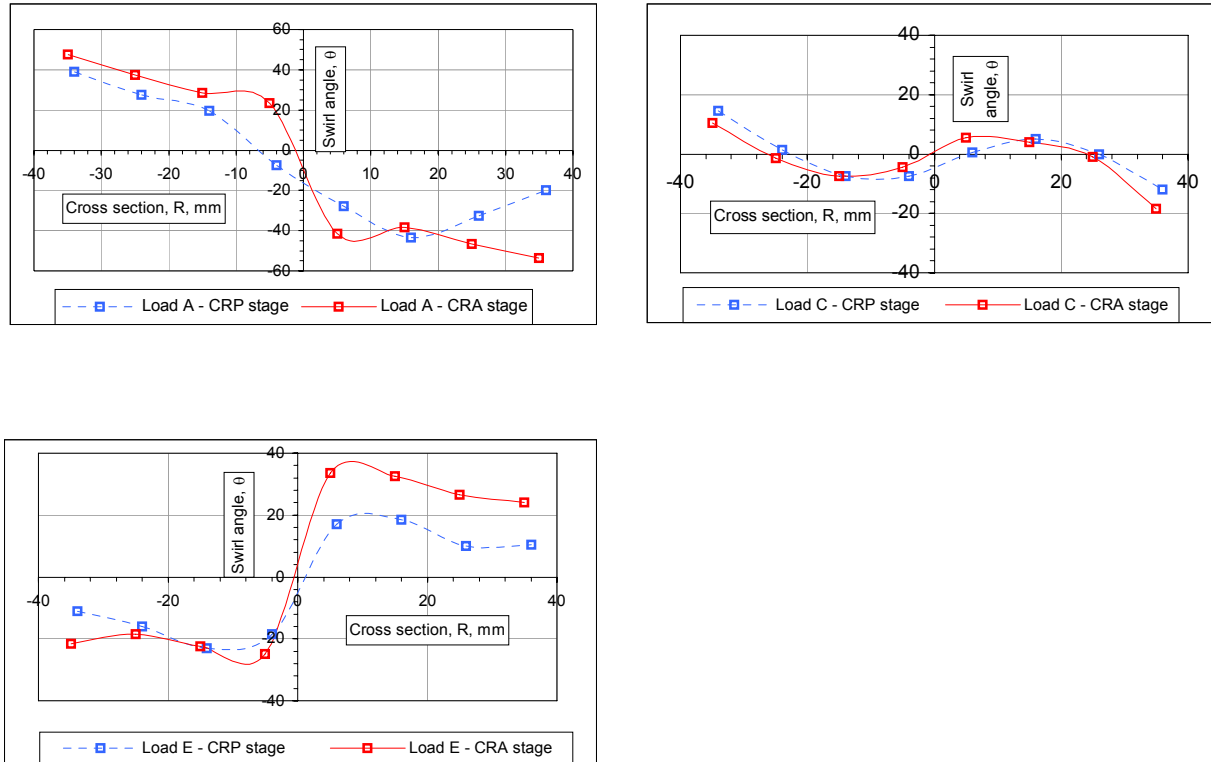
Figure A5.29, Comparisons of the swirl profiles for the CRP and CRA stage of the 36.4 rpm PAT at load A, C and E

The swirl comparisons are carried out three load points namely the no-load point A, the BEP load C and the overload point E in Figure A5.29. At load A, the swirl intensities for the CRA stage is consistently greater than that for the CRP stage through out the cross section by a margin of 8^0 to 20^0. The swirl intensities at load C are more or less identical but there seems to be a displacement of the CRP profile across the central axis. At the overload point E, the CRA stage shows excessive swirl intensities and particularly in the positive half cross section in the range of 10^0 to 18^0.

The BEP is discussed from both perspectives namely the overall comparison (Table A5.19) and internal comparison (load C in Figure A5.29). The overall comparisons revealed that there is power drop of approximately –2%, which signified excessive rotational momentum in the zone *v* and *vi* for the CRA stage. But the swirl comparisons at load C do not signify large change in the rotational momentum component.

However both the internal and overall comparisons reveal excessive rotational momentum at zone *v* for the overload point E. But there is controversy at the no-load point A where overall comparisons (Figure A5.25 and A5.26) reveal decreased exit swirls (increase of net rotational momentum), while the internal comparisons reveal increased exit swirls.

A5.4.2 46.4 rpm PAT

A5.4.2.1 Overall Performance Comparison

Figure A5.30 describes the zone *vi* of the 46.4 rpm PAT along with the rib geometry. The zone *vi* is similar to that of 36.4 rpm with a contracting design.
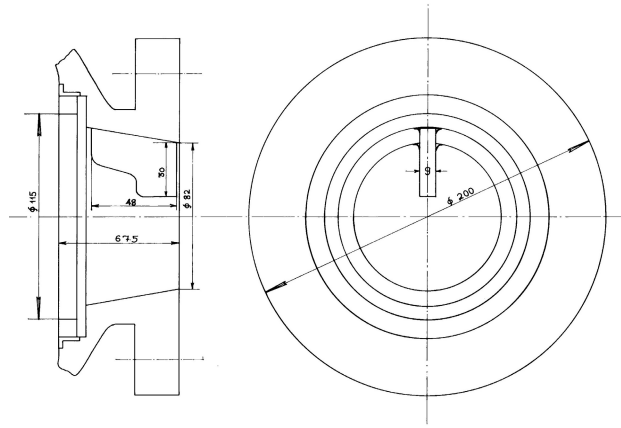

Figure A5.30, Geometry of the casing eye rib for the 46.4 rpm PAT

The overall dimensionless characteristics of the two stages are compared in Figure A5.31 where it is seen that the head number curve for the CRA stage falls below the CRP curve beginning from the part-load region. The curves seem to join each other in the overload region and deep in to overload region the head number curve falls back again. In the range from no-load to part-load line there is an increase in the CRA head requirement. The power curve for the CRA stage falls consistently beginning from the part-load region till the overload region. The drop of power is quite substantial. The efficiency curve in the BEP region has dropped by 0.3 % to 0.5% due to greater impact from decreased power consumption. The BEP is summarized for the two stages in Table A5.22.
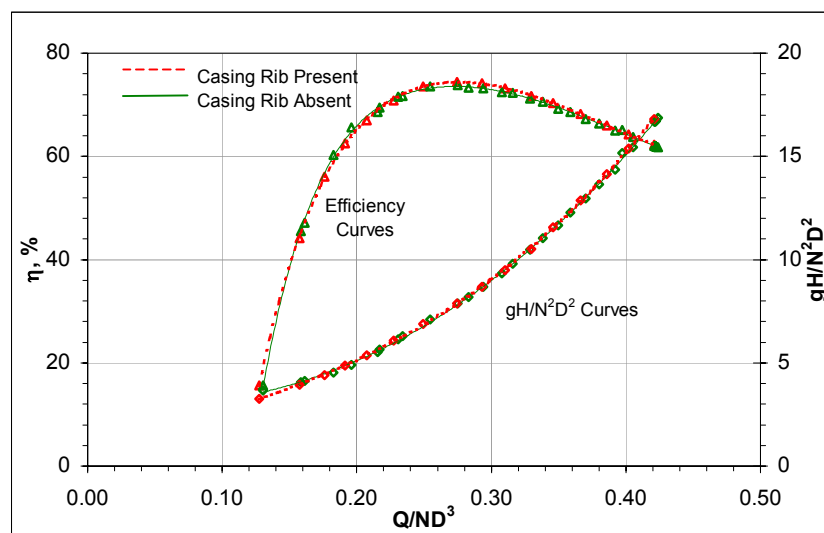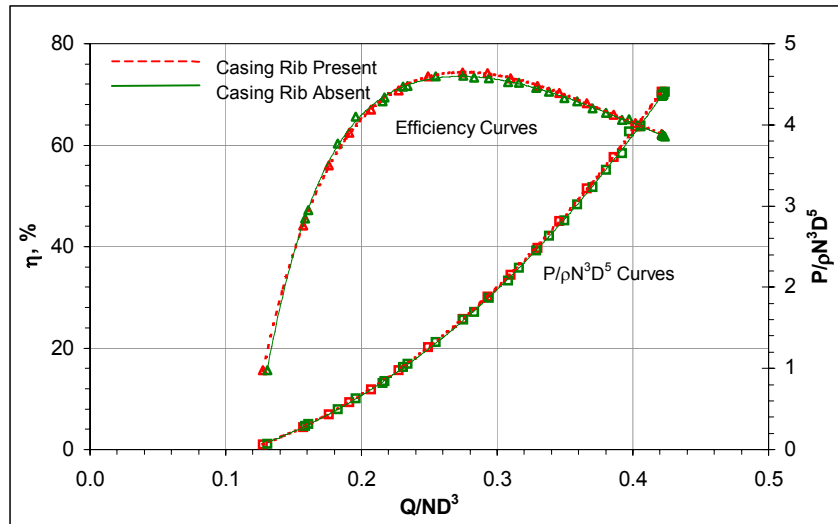
Figure A5.31, Comparisons of dimensionless characteristics for Optimization Stage IV on the 46.4 rpm PAT

Table A5.22, BEP summary for two stages of Optimization Stage IV on the 46.4 rpm PAT

Stage	ϕ	ψ	p	η
Casing Rib Present	0.275	7.888	1.612	74.3%
Casing Rib Absent	0.275	7.819	1.592	74.0%

The percentage analysis diagram in Figure A5.32 shows a consistent drop in the power improvement line at –1% to –1.3% throughout the operating range beginning from part-load line. On the other hand the head reduction line is positive throughout the operating range with maximum gains of +1.2% in the part-load region and +1.5% to +2% in the overload region. At the BEP region the head reductions falls in the range of 0.8% to 0.4%. The efficiency rise curve runs below the abscissa in the main operating region due to excessive power drop. The relative influences at the part-load, overload and the BEP regions are summarized in Table A5.23.

Table A5.23, Relative study at part-load, BEP and overload lines for Optimization Stage IV on the 46.4 rpm PAT

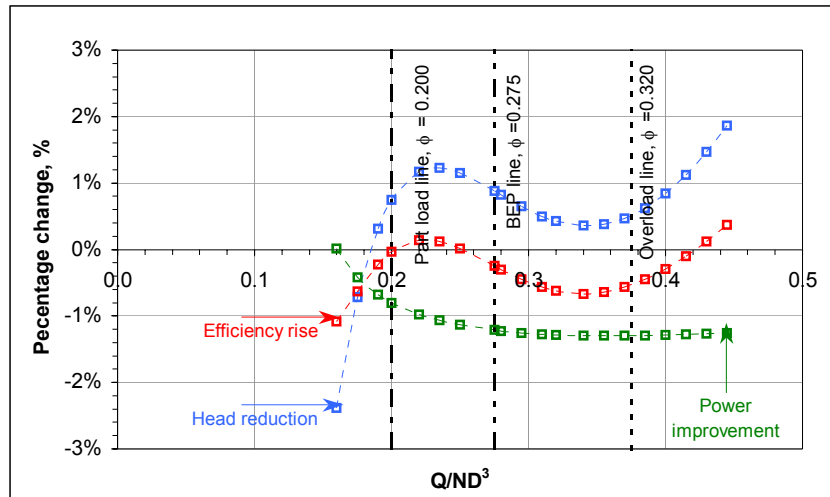| | Part-load line | BEP line | Overload line |
	ϕ = 0.200	ϕ = 0.275	ϕ = 0.375
Head reduction	+0.7%	+0.9%	+0.4%
Power improvement	-0.8%	-1.2%	-1.3%
Efficiency rise	+0.0%	-0.2%	-0.6%

Figure A5.32, Percentage Analysis Plot for Optimization Stage IV on the 46.4 rpm PAT

Discussion of Results of 46.4 rpm PAT

The consistent decrease of power generation in the CRA stage can be owed to either increased exit rotational momentum or increased losses in the impeller zone *v* and *iv* or a combination of both. However the behaviour of the head reduction curve between the part-load line and the BEP line (Figure A5.32), where the reduction peaks reveals greater influences of exit rotational momentum. Some positive hydraulics in zone *vi* due absence of rib are also included in the head reduction curve. Within this operating range the losses within the impeller does not seem to been affected.

The decrease of head reduction in the main operating region (between BEP and overload line) may be due to the probable absence of the influence of the rotational momentum effects (exit swirls of the two stages are nearly identical) and increased losses in the PAT control volume. However the power improvement line is constant and stable (negative zone in Figure A5.32) suggesting that there is still a presence of the net rotational momentum effects. The internal swirl comparison of the BEP load (in section A5.4.2.2, Appendix A) can add more light to this behaviour.

However, in the overload region the head reduction curve rises exponentially indicating strong influence of the enhanced swirls. The increased exit rotational momentum also contributes to drop of power.

The swirl component of losses (ζ component in Equation (2.20), Chapter 2) associated with zone *vi* should also increase in the part-load and overload regions. However on the 46.4 rpm PAT, this component does not seem to have such a dominating effect as much as the decreased frictional component (λ component in Equation (2.20), Chapter 2) associated with the absence of rib.

A5.4.2.2   Internal Performance Comparison
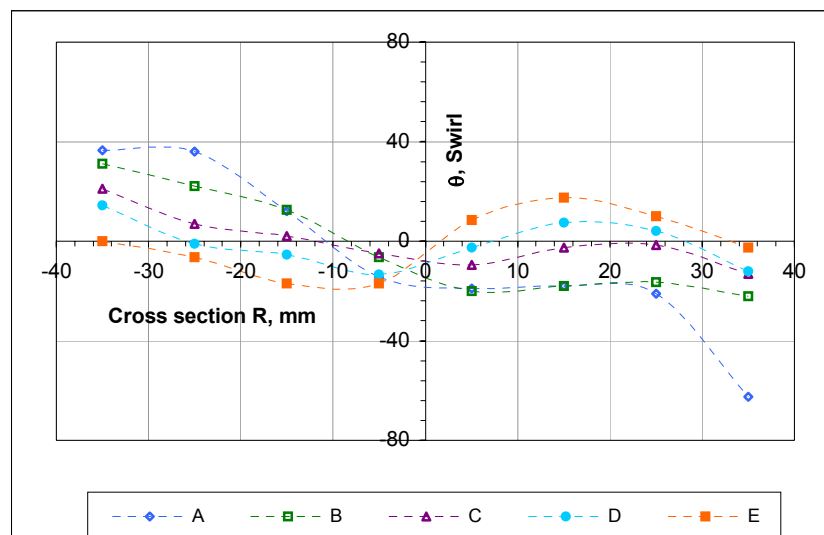
The swirl profiles for the CRP and the CRA stages of the 46.4 rpm PAT are plotted in Figure A5.33 and A5.34 at 5 load points summarized below in Table A5.24.

Table A5.24, Definition of load points for swirl flow comparisons on the 46.4 rpm PAT

Load Point	Condition	$Q/ND^3_{(CRP)}$	$Q/ND^3_{(CRA)}$
A	No Load	0.185	0.188
B	Part-load	0.219	0.224
C	BEP	0.284	0.284
D	Overload	0.345	0.352
E	Overload	0.445	0.452

The profiles of the CRP stage in Figure A5.33 show only a mediocre level of symmetry for loads A, B, C and D. Only load E shows a reasonable symmetry, which also a displays a complete negative swirl. The BEP load C has a positive wall swirl of 15^0 to 20^0 and transforms itself to a negative swirl profile within the cross section.

The profiles for the CRA stage in Figure A5.34 display a much better symmetry. The magnitude of the swirl angles at various loads have been magnified compared to the CRP stage.

Figure A5.33, Swirl profiles for the CRP stage on the 46.4 rpm PAT
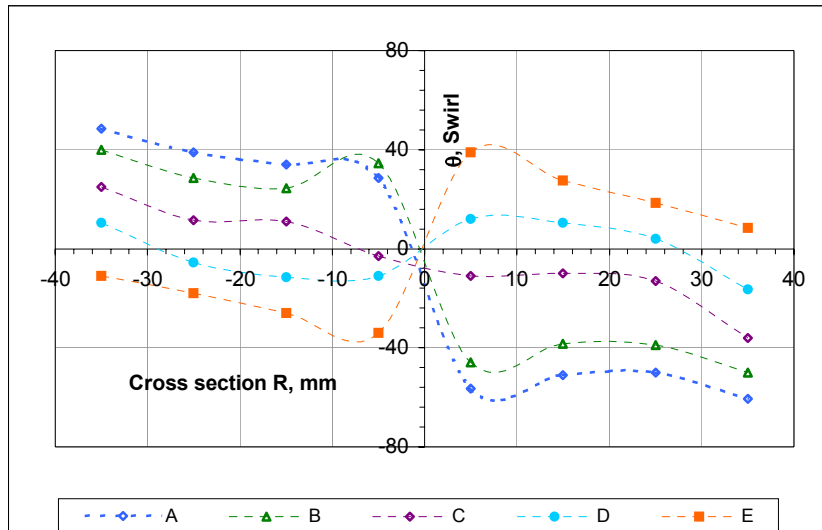
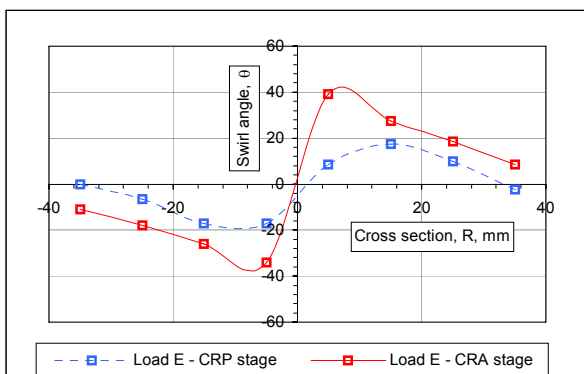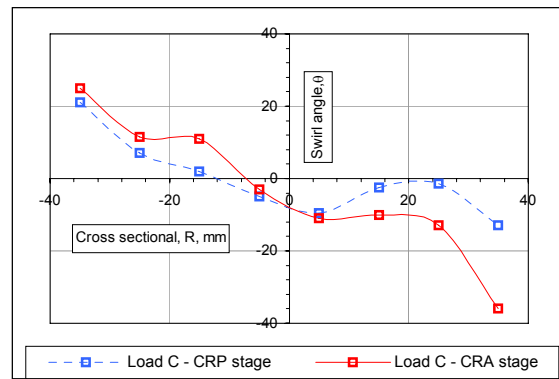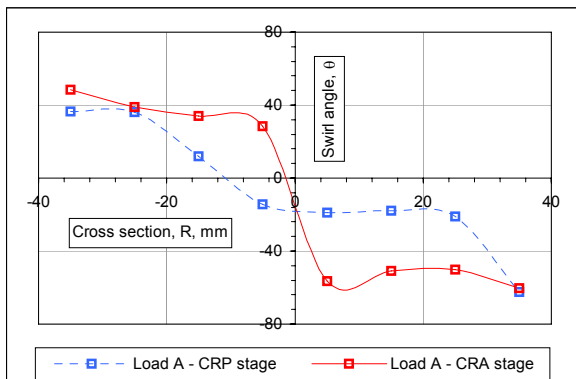Figure A5.34, Swirl profiles for the CRA stage on the 46.4 rpm PAT

Figure A5.35, Comparisons of the swirl profiles for the CRP and CRA stage of the 46.4 rpm PAT at load A, C and E

The comparison of the swirl profiles of loads A, C and E are carried out in Figure A5.35. It is seen at load A, that the CRA swirl magnitudes have increased 2 to 3 folds compared to the

CRP values at corresponding locations of the cross section. Even at the BEP load 'C' the CRA stage has enhanced swirl magnitudes. At the overload point the CRA stage naturally displays much greater swirls compared to the CRP stage. Therefore the comparisons of swirl profiles reveal that there is greater rotational momentum at the PAT exit for the CRA stage at all load points, even at the BEP.

Therefore with increased swirls still persisting in the BEP region, the head reduction can be minimized (drops toward the abscissa as seen in Figure A5.32) only by an increase of any of the loss components in the PAT control volume. However for the power trend line to be very stable in the negative quadrant, the decreased net rotational momentum and an increased impeller loss component should combine very well with each other. In all probability the impeller loss component is dominating over the rotational momentum component. This increased impeller loss component is therefore the main cause for the head reduction curve to fall in the BEP region despite presence of a slightly higher exit rotational momentum. This impeller loss component however diminishes after the overload line (behaviour of the head reduction in Figure A5.32) with excessive rotational momentum effects.

A5.4.3   79.1 rpm PAT

A5.4.3.1   Overall Performance Comparison

The conditions of zone *vi* for the 79.1 rpm PAT shown in Figure A5.36 is very different from other PAT designs studied, in that instead of the conventional converging type of design, it has a gradually expansion moving from plane '2' to plane 's'. Also instead of a single rib plate, there are two diametrically opposite ribs.
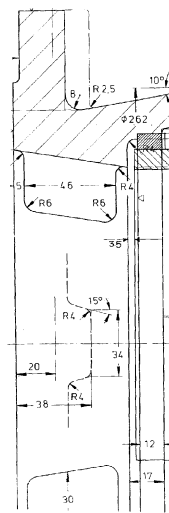

Figure A5.36, Geometry of the casing eye rib for the 79.1 rpm PAT

The influence of casing ribs on the characteristics is studied in Figure A5.37. The CRA stage of the 79.1 rpm PAT shows decreased head consumption only in the no-load region followed by an increased consumption in the part-load region. In the BEP and overload region the

head number characteristics are essentially identical. The power characteristics do not display any difference in the part-load region. But after the BEP there is a drop in the magnitude of CRA power generation. The efficiency has dropped only in the overload region. The BEP point is summarized in Table A5.25, where it is seen that the efficiency for the CRA stage has dropped from 76.1% to 75.7% due to a marginal increase of head number and simultaneously to marginal drop of power.
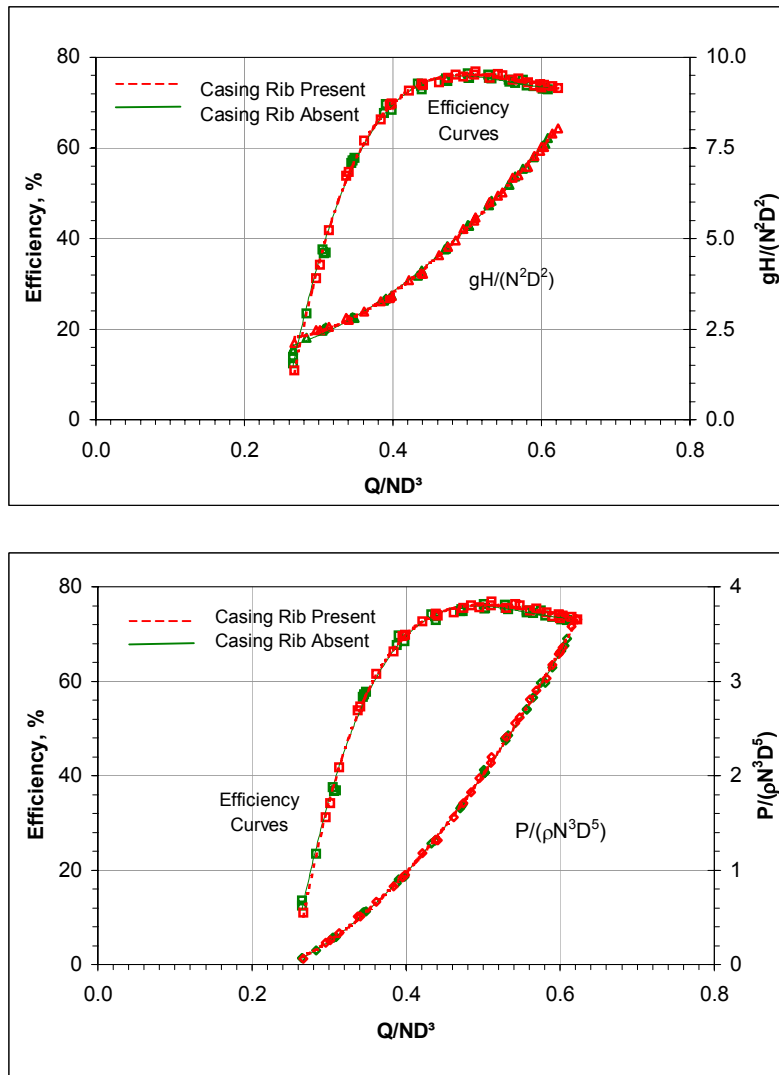
Figure A5.37, Comparisons of dimensionless characteristics for Optimization Stage IV on the 79.1 rpm PAT

Table A5.25, BEP summary for two stages of Optimization Stage IV on the 79.1 rpm PAT

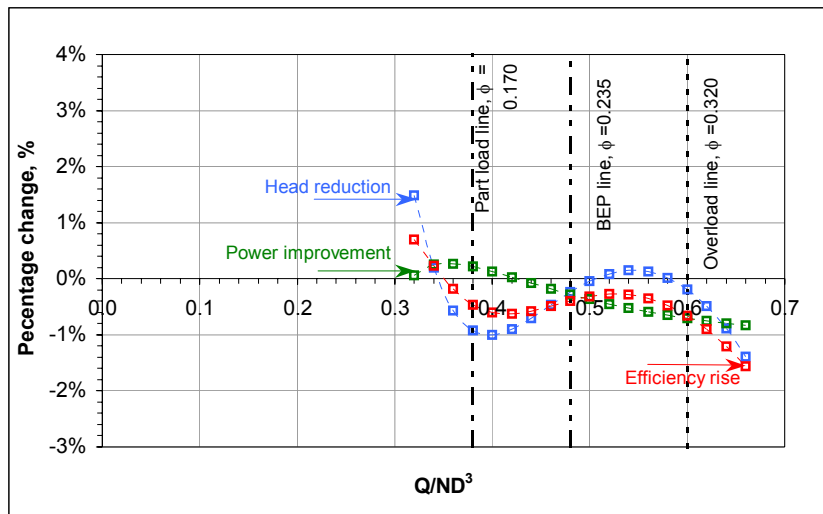| Stage	ϕ	ψ	p	η
Casing Rib Present	0.480	4.881	1.783	76.1%
Casing Rib Absent	0.480	4.893	1.778	75.7%

Figure A5.38, Percentage Analysis Plot for Optimization Stage IV on the 79.1 rpm PAT

The percentage analysis of Figure A5.38 shows a slight improvement of power in the part-load region, but soon the trend becomes negative and there is a continuous drop from 0% to 0.8% towards the overload line. As seen the head reduction curve represents seesaw behaviour across the abscissa, but is primarily in the negative quadrant. The efficiency rise line is essentially below the abscissa showing degradation of performance in the CRA stage. The relative gains within the part-load, BEP and overload region summarized in Table A5.26.

Table A5.26, Relative study at part-load, BEP and overload lines for Optimization Stage IV on 79.1 rpm PAT

	Part-load line ϕ = 0.380	BEP line ϕ = 0.480	Overload line ϕ = 0.600
Head reduction	-0.9%	-0.2%	-0.2%
Power improvement	+0.2%	-0.3%	-0.7%
Efficiency rise	-0.5%	-0.4%	-0.7%

Discussion of Results

The behaviour of the head reduction curve in the part-load region signifies increased losses within the PAT control volume. As seen in the other PATs that the part-load conditions are associated with higher swirl. But there is no evidence of increased exit rotational momentum on the head curve. With power improvement curve continuously dropping suggests either a condition of increased exit swirls or degradation conditions within the impeller.

Though towards the BEP the influence of rotational momentum is reflected both on the head reductions (climb towards the positive quadrant in Figure A5.38) and power improvement (continuous drop into negative quadrant in Figure A5.38).

In the overload region the power number shows signs of increased exit swirls, but head reduction curve moves drastically into the negative zone indicating no signs of increase in exit rotational momentum. For the head reduction curve to behave in this way, there should be a tremendous increase of losses in the PAT control volume (zone *iv*, *v* and *vi*). The mechanisms leading to the behaviour of the head reduction curve cannot be easily explained in physical terms.

A6   Results of CSHN Analysis on PATs

A6.1   24.5 rpm PAT

The CSHN curve for the 24.5 rpm PAT under laboratory conditions is plotted in Figure A6.1 at constant speeds of 500 rpm, 600 rpm, 700 rpm, 800 rpm, 900 rpm and 1000 rpm respectively. The data points for all the test speeds have virtually collapsed together giving a single CSHN curve. Table A6.1 summarizes the cavitation conditions at the minimum CSHN point and the BEP respectively. The minimum CSHN occurs at ϕ = 0.137, which is essentially in the overload region of the PAT characteristics.
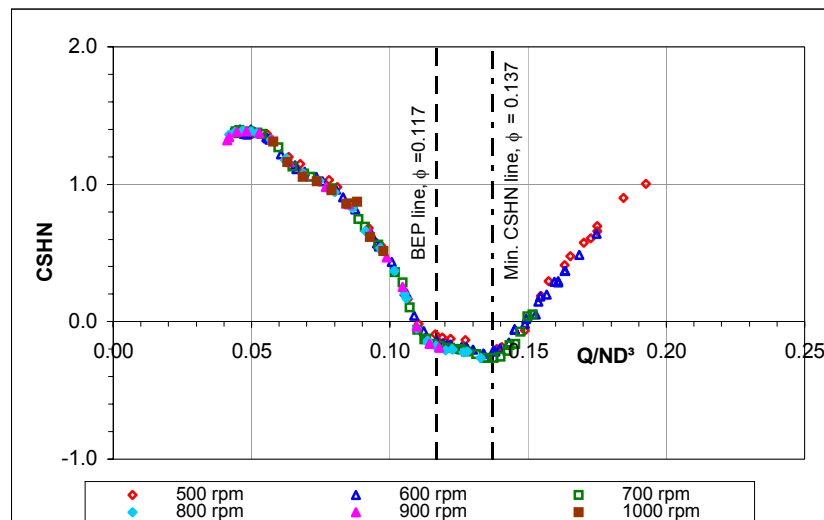
Figure A6.1, CSHN curve for the 24.5 rpm PAT

Table A6.1, Cavitation summary at the BEP and minimum CSHN conditions for the 24.5 rpm PAT

Condition	ϕ	CSHN	N_{ss} (From Dixon)	N_{cr} (rpm)	$NPSH_{cr}$ (m)
BEP	0.117	-0.170	0.63	2730	6.28
Min. CSHN	0.137	-0.270	0.63	2450	5.61

The Table A6.1 also states the necessary speed and NPSH for the PAT to reach the critical suction specific speed of 0.63. At BEP conditions the PAT would require a speed of 2730 rpm and NSPH of 6.28 m while at the minimum CSHN condition the PAT would require a speed of 2450 rpm and NPSH of 5.61 m. The given PAT therefore should be operated below the critical speeds and above the limiting NPSH at respective conditions specified in Table A6.1.

A6.2 36.4 rpm PAT

Figure A6.2 summarizes the CSHN characteristics for the 36.4 rpm PAT at two speeds 1000 rpm and 1200 rpm respectively. The curves for the two speeds collapse well into each other. It is also found that minimum CSHN conditions occurs far into the overload region at ϕ = 0.280, while the 'ϕ' at BEP is 0.185. The Table A6.2 shows that the this PAT would require a speed of 2540 rpm and NPSH of 4.35 m when operating at the minimum CSHN point, while at BEP conditions the machine would require a speed of 3120 rpm and NPSH of 5.01 m for entering the critical cavitation zone.
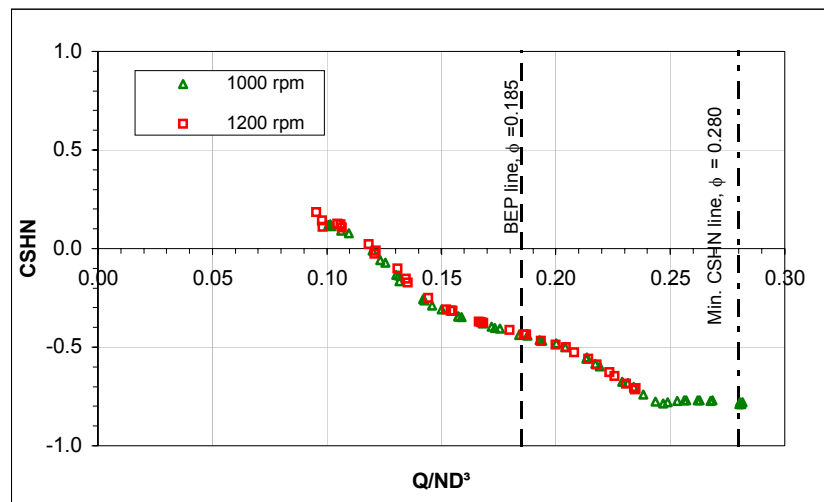

Figure A6.2, CSHN curve for the 36.4 rpm PAT

Table A6.2, Cavitation summary at the BEP and minimum CSHN conditions for the 36.4 rpm PAT

Condition	ϕ	CSHN	N_{ss} (From Dixon)	N_{cr} (rpm)	$NPSH_{cr}$ (m)
BEP	0.185	-0.438	0.63	3120	5.01
Min. CSHN	0.280	-0.780	0.63	2540	4.35

A6.3 39.7 rpm PAT

The CSHN curves for the 39.7 rpm PAT plotted together in Figure A6.3 at speeds corresponding to 800 rpm, 900 rpm and 1000 rpm show a good collapsing property. The minimum CSHN occurs at ϕ = 0.240, while the BEP at ϕ = 0.200. Table A6.3 describes the cavitation conditions where it is seen that a BEP the machine would require a speed of 2350 rpm with NPSH of 6.88 m, while at minimum CSHN conditions at speed of 2170 rpm and NPSH of 6.71 m for it operate in the critical cavitation zone.
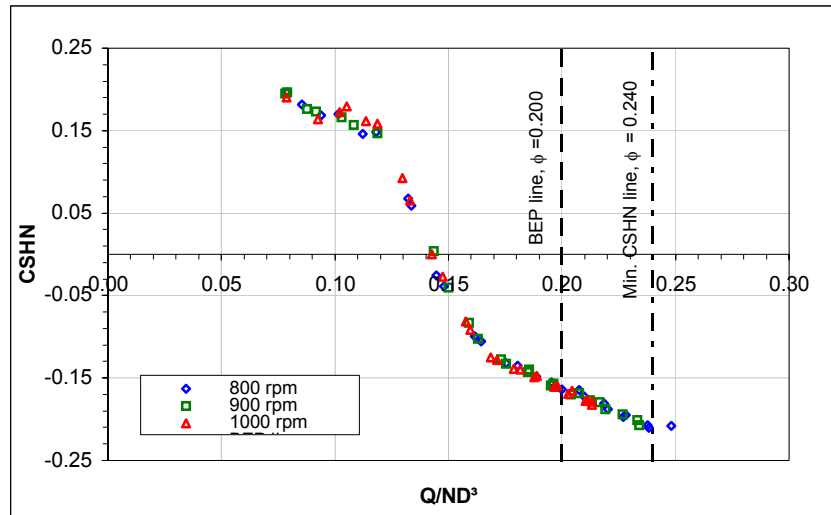
Figure A6.3, CSHN curve for the 39.7 rpm PAT

Table A6.3, Cavitation summary at the BEP and minimum CSHN conditions for the 39.7 rpm PAT

Condition	ϕ	CSHN	N_{ss} (From Dixon)	N_{cr} (rpm)	$NPSH_{cr}$ (m)
BEP	0.200	-0.164	0.63	2350	6.88
Min. CSHN	0.240	-0.210	0.63	2170	6.71

A6.4   45.2 rpm PAT

The CSHN characteristics plotted in Figure A6.4 shows a reasonable collapsibility at 800 rpm, 1000 rpm, 1200 rpm and 1400 rpm. The minimum CSHN is found to occur deep into the overload region at ϕ = 0.340 while the BEP at ϕ = 0.235. For the machine to enter the critical cavitation zone it would require a speed of 2960 rpm and a NPSH of 6.99 m when operating at BEP and a lower speed of 2520 rpm and NPSH of 6.51 m at minimum CSHN conditions as seen in Table A6.4.

Table A6.4, Cavitation summary at the BEP and minimum CSHN conditions for the 45.2 rpm PAT

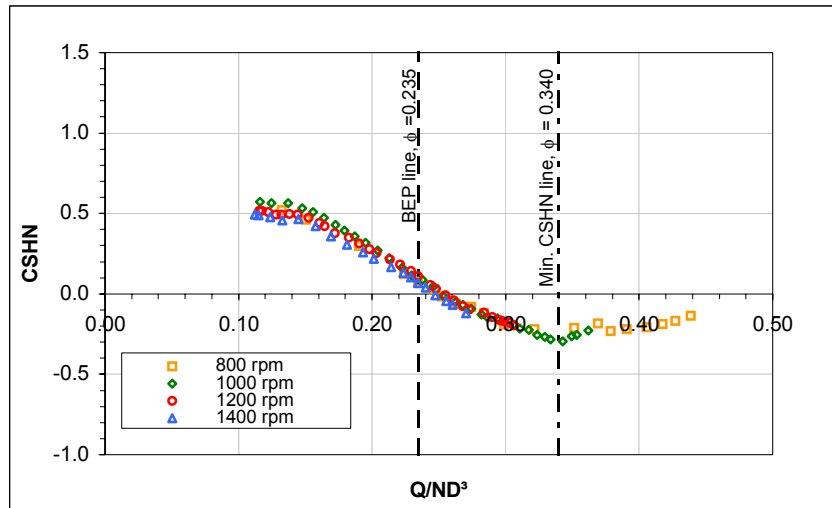| Condition	ϕ	CSHN	N_{ss} (From Dixon)	N_{cr} (rpm)	$NPSH_{cr}$ (m)
BEP	0.235	-0.170	0.63	2960	6.98
Min. CSHN	0.340	-0.300	0.63	2520	6.51

Figure A6.4, CSHN curve for the 45.2 rpm PAT

A6.5   46.4 rpm PAT

The CSHN curves plotted at 600 rpm, 800 rpm, 1000 rpm and 1300 rpm show a wonderful collapsibility in Figure A6.5. But it should be pointed out that the minimum CSHN conditions could not be achieved even after penetrating deep into the overload region. Table A6.5 describes the cavitation at BEP, which reveals that the PAT would be need to be operated at 3650 rpm and a NPSH of 5.75 m for critical cavitation to occur.
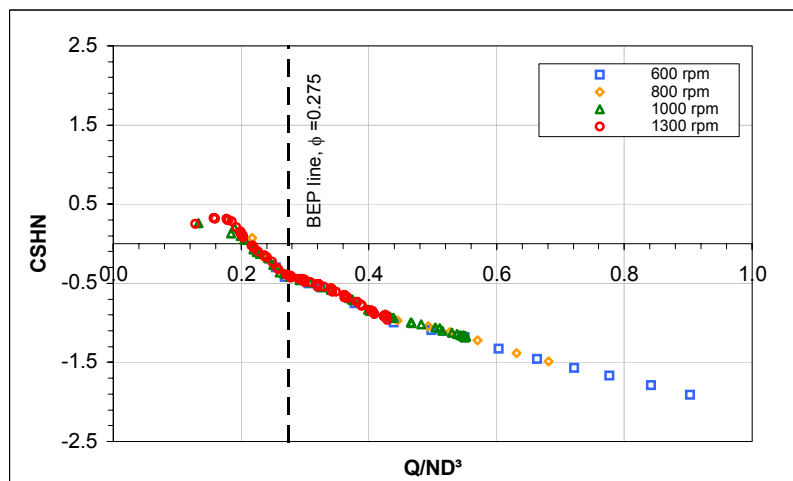

Figure A6.5, CSHN curve for the 46.4 rpm PAT

Table A6.5, Cavitation summary at the BEP and minimum CSHN conditions for the 46.4 rpm PAT

Condition	ϕ	CSHN	N_{ss} (From Dixon)	N_{cr} (rpm)	$NPSH_{cr}$ (m)
BEP	0.275	-0.400	0.63	3650	5.75
Min. CSHN	-	-	-	-	-

A6.6 79.1 rpm PAT

Figure A6.6 shows that the CSHN plot at various speeds of the PAT namely, 800 rpm, 1000 rpm, 1100 rpm and 1200 rpm to have excellent collapsibility property. Once again the minimum CSHN is found to occur after the BEP condition. From Table A6.6 it is found that the when operated at BEP the machine would start to cavitate in the critical zone when operated above a speed of 2240 rpm and NPSH as high as 8.17 m. At the minimum CSHN conditions a lower speed of 2010 rpm and NPSH of 7.72 m would be needed.
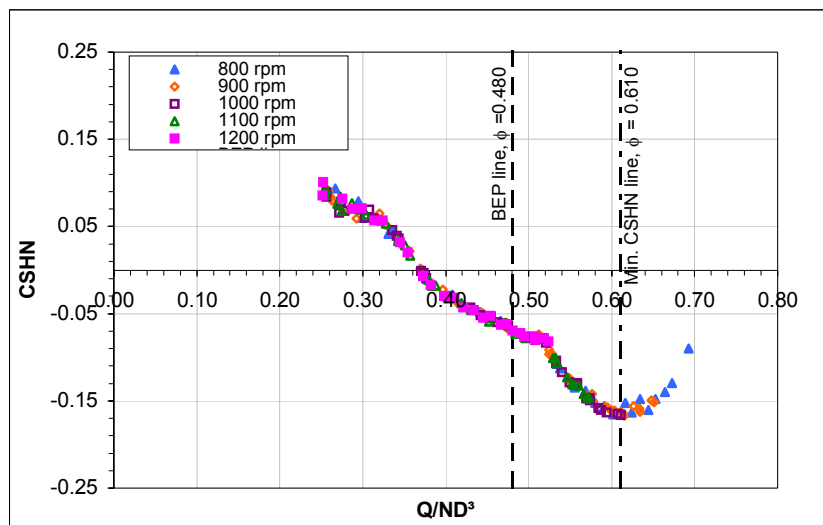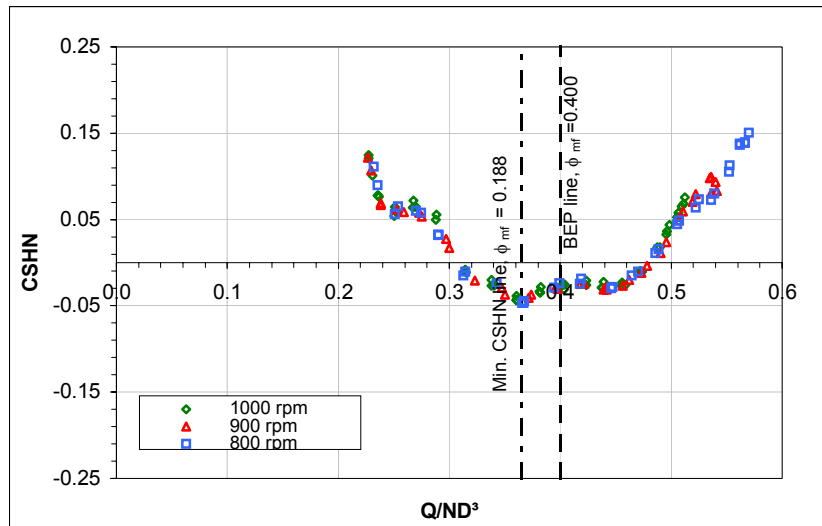

Figure A6.6, CSHN curve for the 79.1 rpm PAT

Table A6.6, Cavitation summary at the BEP and minimum CSHN conditions for the 79.1 rpm PAT

Condition	ϕ	CSHN	N_{ss} (From Dixon)	N_{cr} (rpm)	$NPSH_{cr}$ (m)
BEP	0.480	-0.070	0.63	2240	8.17
Min. CSHN	0.610	-0.165	0.63	2010	7.72

A6.7 94.4 rpm PAT

The CSHN characteristics for the mixed flow PAT are plotted at 800 rpm, 900 rpm and 1000 rpm in Figure A6.7, which again shows all the curves coming together to given a single line characteristics. But the most interesting feature is that the minimum CSHN point occurs at a discharge number of 0.365 before the BEP at ϕ = 0.400.

Figure A6.7, CSHN curve for the 94.4 rpm PAT

In Table A6.7 the mixed flow PAT would begin to cavitate when operated above the 2350 rpm with a NPSH of 8.26 m at minimum CSHN conditions. However at BEP, it would cavitate at much lower speed of 2300 rpm with a NSPH of 8.42 m.

Table A6.7, Cavitation summary at the BEP and minimum CSHN conditions for the 94.4 rpm PAT

Condition	ϕ_{mf}	CSHN	N_{ss} (From Dixon)	N_{cr} (rpm)	$NPSH_{cr}$ (m)
BEP	0.400	-0.030	0.63	2300	8.42
Min. CSHN	0.365	-0.047	0.63	2350	8.26

A7   Experimental-CFD Correlation

As mentioned in section 4.2, Chapter 4, this section deals with the detailed comparisons of the experimental and CFD results for the remaining PAT specimens. The absolute CFD characteristics for the 3 PATs that are used for comparison in this section, namely the 24.5 rpm PAT, 35.3 rpm PAT and the 39.7 rpm (CRP stage) PAT are available in <u>Figure B3.2</u>, <u>Figure B3.4</u> and <u>Figure B3.6</u> (section B3.2 in Appendix B) respectively.

A7.1   24.5 rpm PAT

<u>Figure A7.1</u> compares the dimensionless characteristics obtained separately from experimental and CFD approaches. It is seen that the head number curve for the CFD falls below the experimental curve throughout the operating range considered. The margin of head reduction for the CFD is very substantial. The power characteristics from the CFD on the other hand describe two kinds of behaviours. In the no-load region the CFD power lies above the experimental curve, while in the part-load, BEP and overload region it runs blow it. The margin of power decrease is increasing towards the BEP and overload region. Owing to the independent behaviour of the power and head characteristics the CFD efficiency displays a rise in the part-load region. However before the BEP region and the overload region the CFD efficiency curve falls below the experimental curve.

There is also a displacement of the BEP obtained from the two methods, while the experimental BEP occurs at ϕ = 0.112, the CFD predicts BEP to occur at ϕ = 0.108 representing at deviation of over 3.5%. <u>Table A7.1</u> summarizes the head numbers and power numbers (which display large variations) at individual BEPs.

<p align="center"><u>Table A7.1</u>, BEP from CFD and Experiment for the 24.5 rpm PAT</p>

	CFD	Experiment
Q/ND^3	0.108	0.112
gH/N^2D^2	9.601	11.774
$P_{hyd}/\rho N^3D^5$	0.806	1.058
η_{hyd}	77.7%	80.2%

To find the exactness of the results, the comparisons are carried out at the ϕ = 0.112 in <u>Table A7.2</u>. Though the final efficiencies are comparable (with 3% deviation), it makes less sense since the head number and power number deviations are quite substantial.
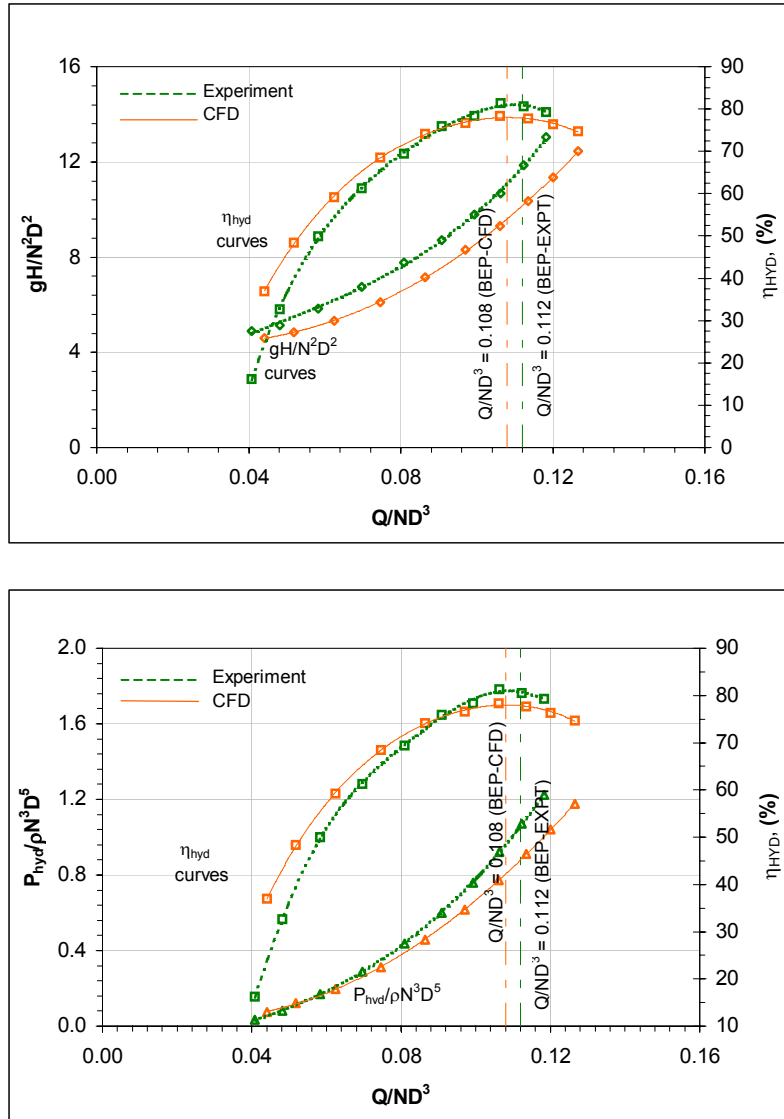
Figure A7.1, Comparisons of dimensionless characteristics for Experiment-CFD correlation on the 24.5 rpm PAT

Table A7.2, Comparison of the experimental and CFD results at the experimental BEP for the 24.5 rpm PAT

Stage	ϕ	ψ	p	η
Experiment	0.112	11.774	1.058	80.2%
CFD	0.112	10.152	0.880	77.4%

The percentage analysis chart plotted in Figure A7.2 shows the head reduction curve for the CFD remains positive throughout the operating range. The head reductions are about +12% to +13.5% in the part-load region and +13.5% to +21% in the BEP and overload regions. Except for a couple of points in the no-load region, the power improvement line remains excessively negative beginning from the part-load region (-5% to –15%) to the BEP and

overload region with a steadily rising trend (-15% to –25%). The net efficiency rise curve lies above the abscissa till the part-load line (+12% to +0.5%) and then gets into the negative quadrant (0% to –4%).

The relative influences of the various parameters of comparison are summarized at the part-load, BEP and overload lines in Table A7.3.
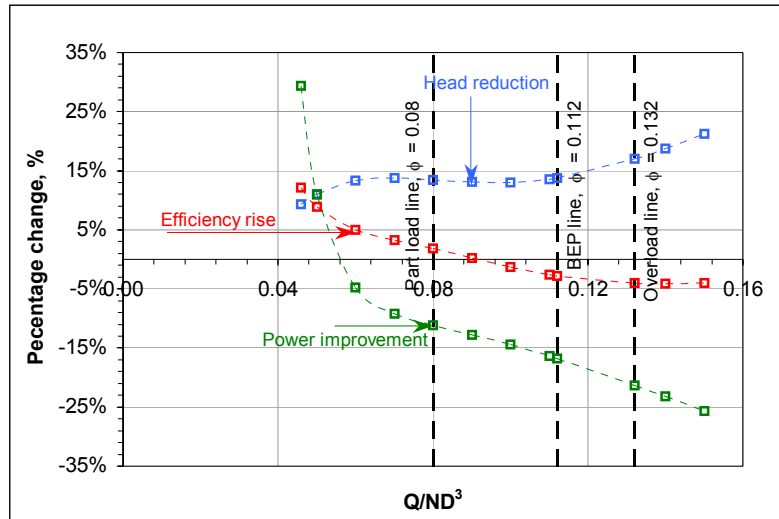
Figure A7.2, Percentage Analysis Plot for Experiment-CFD correlation on the 24.5 rpm PAT

Table A7.3, Relative study at part-load, BEP and overload lines for Experiment-CFD correlation on 24.5 rpm PAT

	Part-load line ϕ = 0.080	BEP line ϕ = 0.112	Overload line ϕ = 0.132
Head reduction	+13.5%	+13.8%	+17.0%
Power improvement	-11.2%	-16.8%	-21.3%
Efficiency rise	+1.9%	-2.8%	-4.1%

Discussion of Results on the 24.5 rpm PAT

Focusing on the region from the part-load region (Q/ND^3 =0.056 onwards) through to the overload region the power improvement line is increasingly negative, signifying that the CFD is predicting either higher losses within impeller or lowered rotational momentum (From procedure in section 3.1.3.1, Chapter 3). In the same region positive head reduction mean that either the CFD is predicting a lower rotational momentum or an overall decrease of losses. These two physical conditions point towards the lower estimation of rotational momentum by the CFD as compared to the miscalculation of losses. However the miscalculation of losses cannot be ruled out.

A7.2   35.3 rpm PAT

The overall dimensionless characteristics for the two methods are compared in Figure A7.3, where it can be observed that CFD head number is consistently below the experimental curve. The difference between the two curves gets magnified towards the overload region. The power number curve as obtained from CFD is also lower compared to the experimental power curve throughout the operating range. The resulting efficiency curve from the CFD is much degraded and totally displaced compared to the experimental curve with deviations of the order of 15%.
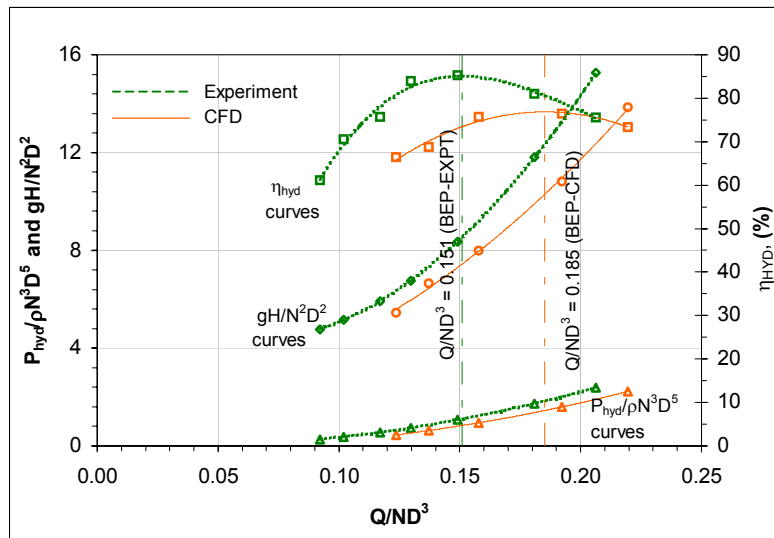
Figure A7.3, Comparisons of dimensionless characteristics for Experiment-CFD correlation on the 35.3 rpm PAT

In fact the locations of the BEPs for the two methods have been badly misplaced, with the experimental BEP occurring at ϕ = 0.151 and the CFD BEP at ϕ = 0.181. The respective BEPs are summarized in Table A7.4.

Table A7.4, BEP from CFD and Experiment for the 39.7 rpm PAT

	CFD	Experiment
Q/ND^3	0.185	0.151
gH/N^2D^2	10.278	8.539
$P_{hyd}/\rho N^3D^5$	1.445	1.099
η_{hyd}	76.0%	85.2%

Comparing the conditions at the same discharge number of ϕ = 0.151, large deviations in the power, head numbers and efficiencies as seen in Table A7.5.

Table A7.5, Comparison of the experimental and CFD results at the experimental BEP for the 35.3 rpm PAT

Stage	ϕ	ψ	**p**	η
Experiment	0.151	8.539	1.099	85.2%
CFD	0.151	7.438	0.838	74.6%

The comparative percentage analysis in Figure A7.4 reveal that the head number reductions for the CFD are positive in the entire range with over 12% reductions at the BEP and 18% to 21% in the overload region. The power improvement curve remains entirely negative with over 32% decrease in the part-load region to 23% decrease at the BEP and over 18% power decrease within the overload region. The efficiency curve remains entirely negative except in the overload region where it becomes marginally positive.
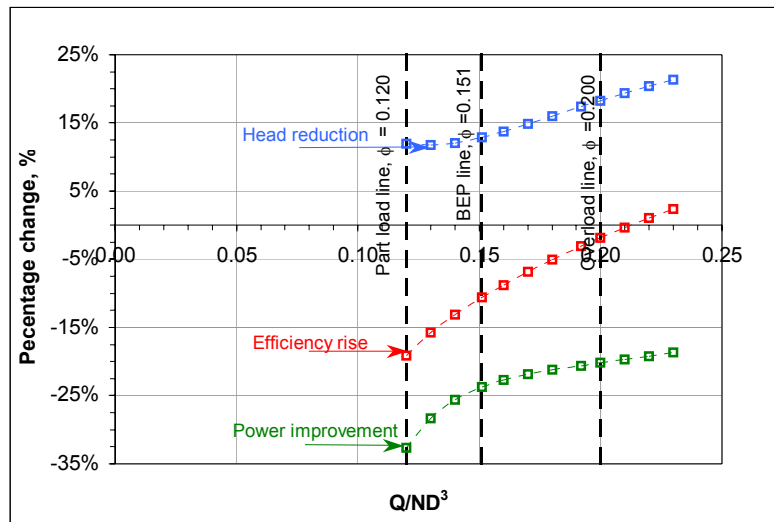

Figure A7.4, Percentage Analysis Plot for Experiment-CFD correlation on the 35.3 rpm PAT

The relative differences of the various parameters at the part-load, BEP, overload regions are summarized in Table A7.6.

Table A7.6, Relative study at part-load, BEP and overload lines for Experiment-CFD correlation on the 35.3 rpm PAT

	Part-load line ϕ = 0.120	BEP line ϕ = 0.151	Overload line ϕ = 0.200
Head reduction	11.9%	12.9%	21.3%
Power improvement	-32.6%	-23.8%	-18.7%
Efficiency rise	-19.1%	-10.6%	2.4%

Discussion of Results for the 35.3 rpm PAT

The negative behaviour of the power improvement characteristics (based on section 3.1.3.1, Chapter 3) indicate that the CFD model is predicting either worsened hydraulic conditions within the impeller or decreased net rotational momentum compared to the experiment. The positive head reductions for the CFD also indicate a lowered net rotational momentum or improved hydraulics within the entire control volume.

Therefore there is a stronger possibility for CFD model to be predicting lowered net rotational momentum. Though there is a small chance of the model making wrong predictions of the losses within the impeller and other stationary zones of the PAT control volume.

A7.3 39.7 rpm PAT - Casing Rib Present Stage

The comparison of the dimensionless characteristics in Figure A7.5 reveals that the CFD power number curve remains entirely below the experimental curve with increased margins of power drop towards the BEP and overload regions. While the head number curves show very good resemblance, however the CFD curve marginally below the experimental curve. The efficiency curve for the CFD model is lower compared to the experimental efficiency curve. However there is still a small displacement with respect to positioning the BEP, while the CFD predicts the BEP to happen at ϕ = 0.1825, the experimental BEP occurs at ϕ = 0.200. The respective BEPs are compared in Table A7.7.

Table A7.7, BEP from CFD and Experiment for the 39.7 rpm PAT (CRP stage)

	CFD	Experiment
Q/ND^3	0.1825	0.200
gH/N^2D^2	6.203	7.088
$P_{hyd}/\rho N^3D^5$	0.928	1.200
η_{hyd}	82.0%	84.7%

Comparing the conditions at the same discharge number (ϕ = 0.200) in Table A7.8 it is found that the CFD is predicting a considerably lower power number and a marginally lower head number compared to that of the experiment with efficiency drop of 3%.

Table A7.8, Comparison of the experimental and CFD results at the experimental BEP for the 39.7 rpm PAT (CRP stage)

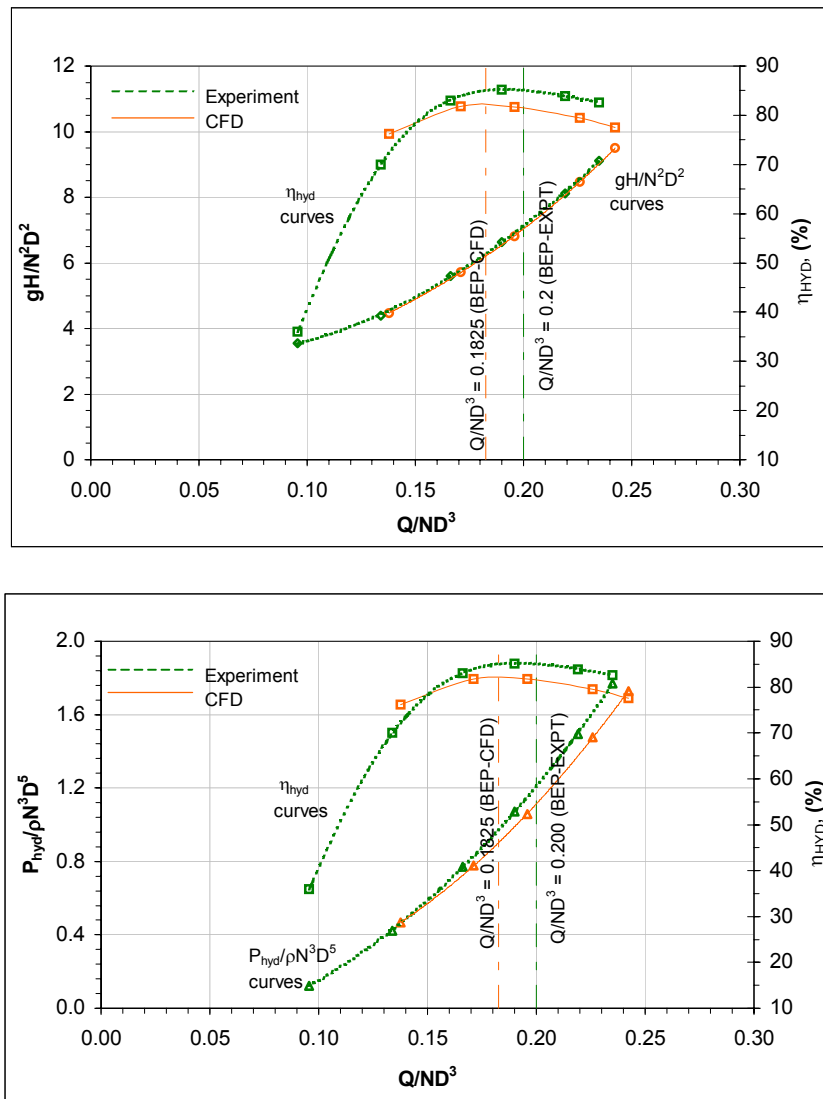| Stage	ϕ	ψ	**P**	η
Experiment	0.200	7.088	1.200	84.7%
CFD	0.200	7.035	1.147	81.6%

Figure A7.5, Comparisons of dimensionless characteristics for Experiment-CFD correlation on 39.7 rpm PAT (CRP stage)

The comparative percentage analysis in Figure A7.6 essentially shows that the CFD power improvement curve is mainly negative in the entire BEP and overload regions (the decrease of power in the range of 0% to –5%). The head reduction curve on the other hand is essentially positive throughout the operating range however the reductions are marginal (in the range of +0.5% to +0.7% only). The efficiency rise curve is positive for a couple of points in the part-load region, however it becomes negative within the part-load region itself and continuously drops towards the BEP and overload region (with efficiency drop in the range of -3% to -4%). The relative deviations of CFD and experiment at the part-load, BEP and overload lines are summarized in Table A7.9.
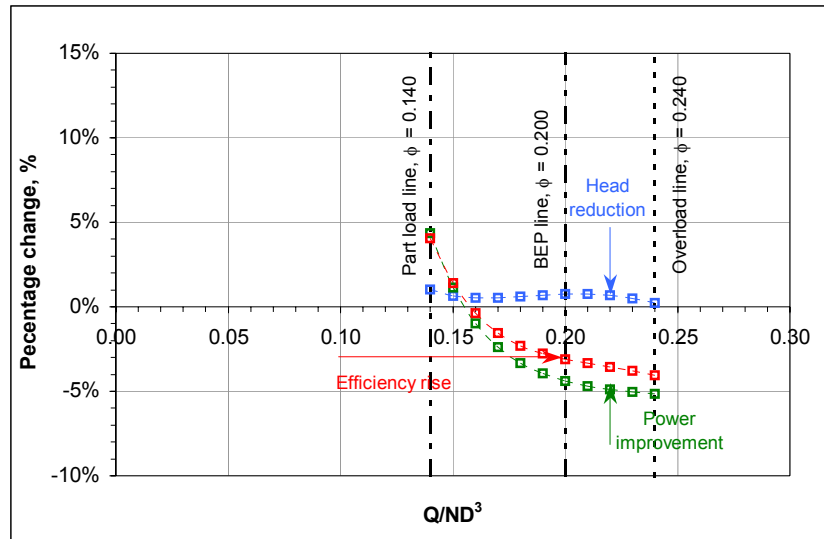
<u>Figure A7.6</u>, Percentage Analysis Plot for Experiment-CFD correlation on the 39.7 rpm PAT (CRP stage)

<u>Table A7.9</u>, Relative study at part-load, BEP and overload lines for Experiment-CFD correlation on the 39.7 rpm PAT (CRP stage)

	Part-load line $\phi = 0.140$	BEP line $\phi = 0.200$	Overload line $\phi = 0.240$
Head reduction	+1.0%	+0.7%	+0.2%
Power improvement	+4.4%	-4.4%	-5.2%
Efficiency rise	+4.1%	-3.1%	-4.1%

Discussion of Results on the 39.7 rpm PAT (CRP stage)

The similitude between the CFD and experiment results are reasonable good, however in physical terms the CFD predictions need to be discussed. The behaviour of the power curve in a very small zone of the part-load region (from Q/ND^3 = 0.140 to 0.155) indicate that the CFD could be either predicting greater net rotational momentum or decreased losses within the impeller zone (from analogy developed in section 3.1.3.1, Chapter 3). In the same range the head reduction curve for the CFD is positive, which either implies that the CFD predicts lower losses within the entire PAT control volume or lower net rotational momentum across the impeller control volume. From the above two behaviours the possibility of the CFD model predicting decreased losses within the impeller and other zones is greater.

However, in the remaining operating region (from Q/ND^3 = 0.155 onwards) covering the BEP and overload region, it is seen that the power predictions from CFD are much lower compared to that of the experiment. This behaviour of the power improvement line suggests that there could be either a condition of CFD model predicting lower net rotational

momentum or greater losses in the impeller zone. On the other hand the head reductions remain marginally positive, indicating either a lower rotational momentum or decrease of losses within the PAT control volume. From the behaviour of the power improvement and the head reduction curves, there is a greater possibility of the CFD predicting lower rotational momentum. Nevertheless the possibility of miscalculation of losses in the PAT control volume cannot be ruled out.

A8   Application Theory in PATs

A8.1   Four Quadrant Analysis in Pumps

The special operating conditions of pumps received considerable interest from early researchers namely Thoma [54], Engel [12] and Kittredge [27]. These conditions essentially consist of 4 quadrants of head – discharge capacity (H-Q) curves for the positive pump rotation and the remaining 4 quadrants for the negative pump rotation. Knapp [29] also carried out investigations on a radial flow pump and published its complete operating characteristics. Stepanoff [52] gave a detailed treatment to the special operating conditions assimilating results from all the above early researchers and some contemporary researchers like Swanson [53]. He also brought about charts for radial flow, mixed flow and axial flow pumps.

In general some of the special operating conditions are unavoidable, others accidental and further some of them can be achieved only in an elaborate laboratory setup. For example, operation of a pump as a hydraulic turbine (which happens to be the focal point of the dissertation), behaviour of pump in event of a power failure and starting a pump running in reverse, are some of the few conditions.

It is a common practice to represent the pump and turbine characteristics taking head and discharge as co-ordinates while speed and power as the parameters. Figure A8.1 displays the total characteristics of a typical radial flow PAT with all the relevant quadrants. The characteristics of mixed and axial flow pumps are slightly different with respect to the quadrant distribution.

A8.1.1   Sign Convention

The sign convention and basic features of 8 quadrants (4 for pump mode and other 4 for turbine mode) are summarized below.

Sign Convention

+Q   -   Discharge direction in pump mode

+H   -   Head at volute plane is greater than the head at suction plane

+N   -   Direction of pump rotation

-Q   -   Discharge direction in turbine mode

-H   -   Head at suction plane is greater than head at volute casing plane

-N   -   Reverse direction of pump or direction of turbine rotation

+P   -   Power supplied to the pump

-P   -   Power taken from the pump

+T   - $\dfrac{+P}{+N}$ or $\dfrac{-P}{-N}$

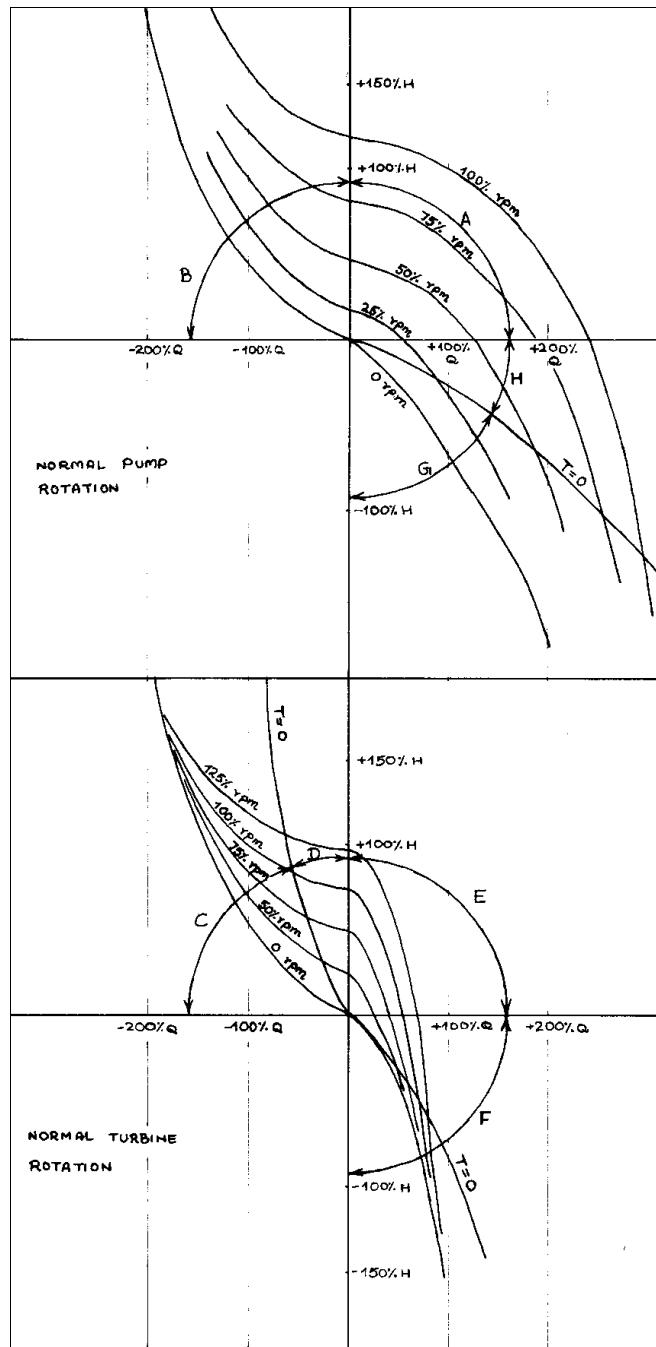-T   - $\dfrac{+P}{-N}$ or $\dfrac{-P}{+N}$

Figure A8.1, Complete operating characteristics of the typical radial flow pump in both pump and turbine modes on H-Q coordinates

A8.1.2   Pump mode quadrants

Quadrant A: represents the normal pump characteristics at different operating speeds (between the +H ordinate and the +Q abscissa).

Quadrant B: A higher head compared to the pump shut off for a given speed causes the flow to get reversed (lies between the +H ordinate and the –Q abscissa)

Quadrant H: The flow being forced into the pump with the suction head greater than the delivery head (represented by +Q abscissa and the T = 0 no-load line). This quadrant is referred to as 'reverse flow turbine'

Quadrant G: Similar condition as in quadrant H, but bound by the T = 0 line and the –H ordinate and is called the energy dissipation zone.

A8.1.3 Turbine mode quadrants

Quadrant C: This is the main energy generation zone bound by –Q abscissa and the T = 0 line. However effective energy output is limited by the N = 0 line.

Quadrant D: It is bound by the no-load line and the nearest +H ordinate or –Q abscissa moving in opposite direction to the quadrant C called the energy dissipation zone.

Quadrant E: Is called the reverse speed pump, with flow direction and head corresponding to pump mode operation, but the direction of speed in reversed.

Quadrant F: Is essentially between the +Q abscissa and the –H ordinate, and is also energy dissipation zone.

The above representation of the complete characteristics with co-ordinates of head and discharge are not very well readable, hence a new co-ordinate system with speed and discharge as the co-ordinates while torque and head are taken as the parameters is given consideration. This new system has advantages of combining all the pump and turbine mode quadrants in one diagram. The ultimate goal of studying the 4-quadrant analysis of pumps is two fold.

1. To get the exact representation of the quadrant D, which is the only possible quadrant in which the PAT can enter within a micro hydro system with radial flow machines.

2. To get the behaviour of the critical no-load line with respect to the zero speed line (locked rotor) not only to evaluate the runaway condition but also to study the movement of the characteristics in quadrant D.

Therefore for a micro hydro PAT application with radial flow machines only two quadrants are realistically possible, namely quadrant D and C.

A8.2 Mechanical Design in Synchronized PAT systems

A8.2.1 Design and Selection of Drive System

A single driven shaft with many driven units necessarily entails the incorporation belt drive systems between the respective PAT units and the generator. The mechanical design

consideration involves appropriate selection of the type of drive system. Though single wedge belts are most popular, new forms like poly-wedge belts can be considered. A conventional design procedure of the belts should be followed, which would eventually yield the number of belt strips needed to handle the load conditions safely for given pulley diameters and belt length. The belt length is often imposed based on the center-to-center distance between shafts needed. The pulley diameters are selected based on the speed ratio needed, however it is recommended to use larger and heavier pulleys for having advantages of flywheel action. The design should eventually give the exact magnitude of the net belt thrust (perpendicular to the shaft axis) and also its location on the shaft axis of the respective driver and driven units.

A8.2.2   Shaft and Bearing Design or Verification

Though the design of shaft and bearings are well established, they should not be overlooked as small errors can lead to major problems. The consideration for driven shaft and driver shaft are treated separately below.

A8.2.2.1   Driven Shaft

The driven shaft for the synchronized PAT system will obviously form the most crucial design study. Because of the complex kinds of loads acting on it, extreme care should be enforced while designing the shaft. The driven shaft comprises of coupling units, transmission pulleys and bearing units.

The first stage consists of fixing the shaft diameter for given material, which is evaluated from the combined theory bending and torsional loads along with the fatigue theory of alternate loading from the bending forces. To evaluate the bending moment on the different locations of the shaft, the appropriate positions of the bearings should be fixed. A conventional procedure of analyzing the force and bending moment diagrams will need to be followed.

The next stage of design is with respect to the bearing system. The choices include deep groove ball bearings, spherical roller bearings, which are of self-aligning type or even cylindrical roller bearings. The type of operation, the magnitudes of forces acting on bearing centerlines along with estimated life helps in making appropriate bearings selection. The crucial aspect of the bearing design is that of the housing and type of lubrication. The bearing housing should have excellent heat transfer properties for being able to dissipate the heat arising from the bearing quickly. The type of lubrication also needs to be given considerable thought for aiding heat transfer. Two types of lubrication namely, grease or oil lubrication, is generally foreseen.

A8.2.2.2   Driver Shafts

The driver shafts and mounted bearings are standard parts that accompany the selected pump for turbine operation. But they are already designed from the pump mode operational criterion. Therefore instead of design procedure, a verification procedure needs to be carried out to check if the shaft and bearings can withstand the complex loading. If the shaft or bearings are found to be unsafe, either shaft material may have to be reconsidered or the bearings reselected.

A8.2.3   Critical Speed analysis

Similar to any rotary system subjected to both lateral and torsional loading, it is necessary to evaluate critical resonance frequencies. The design criterion should be to isolate the natural frequency from the operating frequency. If the resonance conditions are reached under operation dangerous vibrations are set in, which may eventually lead to the premature failure of the shaft or associated components. It is enough if the critical speeds based on the first natural frequency from both perspectives, namely lateral and torsional loading are to found out. Though the lateral critical speed determination is quite straight forward, the torsional critical speeds determination needs the solution of a poly order matrix equation corresponding to the number rotating masses on the shaft. However numerical techniques are available to deal with such problems.

A9   Case Study-Supplements

A9.1   Background

The envisaged project for the Case Study is decentralized in nature and designed to cater to the complete electric load of the tea factory only during the rainy season extending over a period of 4 months a year. The garden is known as Ambootia Tea Estate, which is producing tea since the year 1869 and acclaimed to be the first organic tea manufacturers in the entire region of Darjeeling. The tea garden has a historic micro hydro power plant built in the 1900s with a classical pelton turbine, which has been non-operational for many years.

The tea management decided to install another new micro hydro system using some of the original civil works like forebay tank and channels. The contract for the project was awarded to Sahyadri Energy Systems Pvt. Ltd, a renewable energy company in India. The author also being a co-founder of the above company, along with his supervisor received an enquiry to design the system and also participate its execution and evaluation. The initial feasibility study looked promising for a multiple PAT system. Subsequently the Institute for Water Resources Management, Hydraulics and Rural Engineering (IWK), University of Karlsruhe got officially involved with Sahyadri beginning from the design phase until the end of the commissioning phase. Though the boundary conditions were very challenging for a PAT system, it was taken up as the project would be the first occasion when a multiple synchronized PAT system would be put into use and there was no better point to prove the worthiness of PATs especially after the successful and encouraging laboratory tests.

The first enquiry for project came in January 2004, after which a feasibility report with basic selection and synthesis of the performance characteristics was submitted. The project got its approval and immediately a rigorous design phase was initiated pertaining mainly to the hydro-mechanical system. Sahyadri had initiated the civil works independently in March 2004 itself. The pumps selected for the project were ordered in March 2004 from the reputed company, Kirloskar Brothers Limited, who have also been the industrial partners in the PAT research programme carried out by IWK. The mechanical assembly of the PATs, fabrication of base plate, shaft assembly of bearings/accessories and the manufacture of the hydraulic manifold lines were finished in June 2004 in workshop owned by Sumuki Associates in Mysore, a south Indian city.

The successful commissioning of the multiple synchronized PAT system was done during the last week of the August 2004. There were however shortcomings in some of the sub-components like the penstock and drive mechanisms, which were subsequently rectified.

A9.2 Design of the Turbine System – PAT3

The boundary conditions for the design and selection of the PAT for unit 3 are listed in Table A9.1.

Table A9.1, Boundary condition for the selection and design of PAT3

Design Net Head	H	74 m
Design Discharge	Q	50 l/s
Operating Speed	N	1500 rpm
Specific speed (SI)	$N_{q\,t}$	13.3 rpm
Specific speed (cordier)	σ	0.084

The intersection of the $\sigma = 0.084$ line with the mean and other tolerance curves for radial PATs in Figure 5.1, Chapter 5 yields 3 specific diameters that are summarized along with the absolute diameters in Table A9.2.

Table A9.2, Specific and reference diameter range for the selection of PAT3

Δ_{mean}	7.987		D_{mean}	326 mm
Δ_{lower}	7.476		D_{lower}	306 mm
Δ_{upper}	8.489		D_{upper}	347 mm

Step 1: Diameter Selection

A low specific speed pump of diameter ϕ329 mm is found from the manufacturers catalogue, Kirloskars [23] that suits the range of diameters proposed by the Cordier analysis. The pump has a duty point defined at 1450 rpm with a discharge of 27.8 l/s and net head of 33 m with an operating efficiency of 74.0%. The pump specific speed is found to be, $N_{q\,p}$ = 17.6 rpm. On the dimensionless scale the BEP point is represented with the ψ_{BEP} = 5.121 and ϕ_{BEP} = 0.0323.

Step 2: Range of Specific Speeds (operating speeds)

With the given diameter of ϕ329 mm, the specific diameter line, i.e. $\Delta = 8.049$ is determined. Subsequently the range of dimensionless specific speeds is obtained from Figure A9.1 and summarized along with absolute operating speeds in Table A9.3.
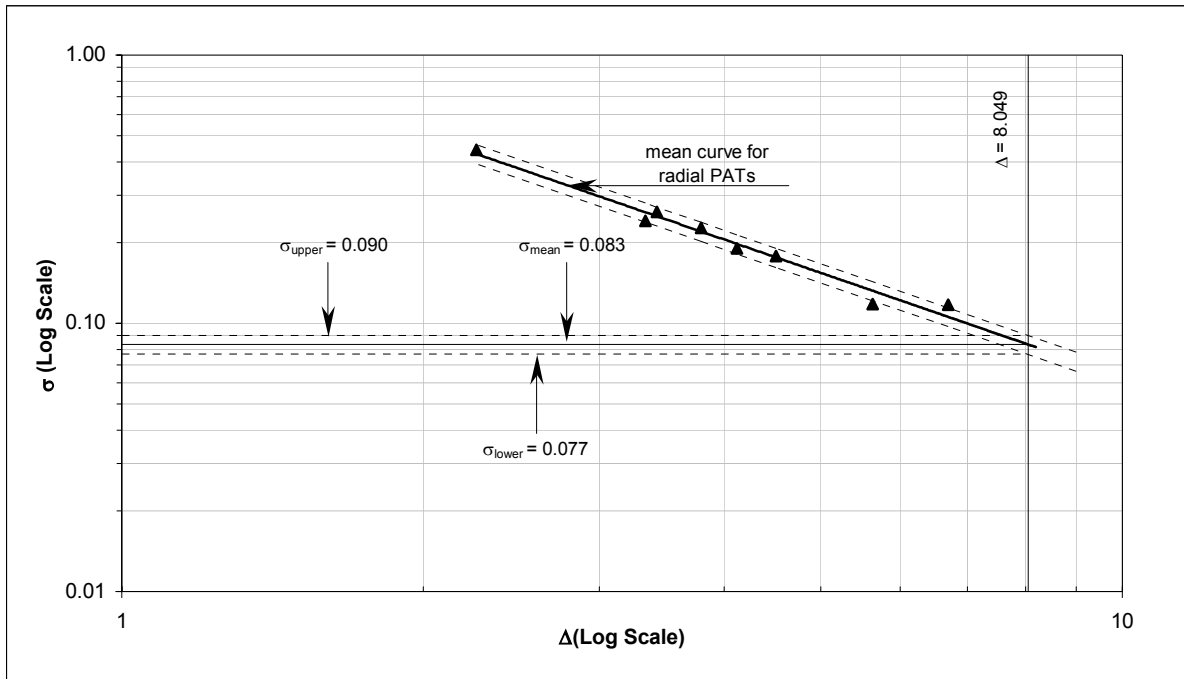
Figure A9.1, Interaction of the constant specific diameter line with Cordier lines for design of PAT3

Table A9.3, Specific and operating speed range for the selected PAT3

σ_{mean}	0.083		N_{mean}	1485 rpm
σ_{lower}	0.077		N_{lower}	1364 rpm
σ_{upper}	0.090		N_{upper}	1606 rpm

Step 3: Range of Head numbers and Discharge numbers

The range of operating head and discharge numbers based on the boundary conditions and selected diameter of ϕ329 is listed in Table A9.4.

Table A9.4, Range of 'boundary' head number and discharge number ratios for PAT3

$(gH/N^2D^2)_{mean}$	10.946		$(Q/ND^3)_{mean}$	0.0567
$(gH/N^2D^2)_{lower}$	12.978		$(Q/ND^3)_{lower}$	0.0618
$(gH/N^2D^2)_{upper}$	9.356		$(Q/ND^3)_{upper}$	0.0524

It is also found that the $\psi_{mean} = 10.946$ line intersects the mean $(\psi - \phi)_{BEP}$ trend line of Figure 5.3 at $\phi_{mean} = 0.051$ ('required' discharge number)

Step 4: Suitability of the selected PAT

1. Boundary discharge to be fully utilized

The boundary discharge number from mean cordier considerations $\phi_{mean} = 0.0567$ seems to be greater than the obtained from the experimental trend line $\phi_{mean} = 0.0510$. This is only a preliminary verification and further considerations would need to undertaken to check its suitability.

2. Verification of head and discharge ratios between turbine and pump modes

Table A9.6 compares the BEP points of turbine mode with that of the pump mode (Table A9.5), from the mean, lower tolerance and upper tolerance considerations (from 'boundary' numbers in Table A9.4).

Table A9.5, Pump mode ψ, ϕ and N_{qp} at the BEP for PAT1

ψ_p	5.12
ϕ_p	0.0323
N_{qp}	17.6 rpm

Table A9.6, Range of head number and discharge number ratios for PAT3

Cordier limits	ψ_t/ψ_p	ϕ_t/ϕ_p
Mean conditions	2.14	1.76
Lower tolerance limit	2.53	1.91
Upper tolerance limit	1.83	1.62

The closest experimentally tested PAT characteristics available are that of the 21 rpm as seen in Figure 5.2 and 5.3 (Chapter 5). The BEP point at non-dimensional scale of the selected pump is compared with that of the 21 rpm (from section B1, Appendix B) on pump mode basis in Table A9.7.

Table A9.7, Comparison of the pump mode duty points for the 17.6 rpm and 21 rpm PATs

Parameters	17.6 rpm pump (ϕ329 mm)	21 rpm pump (ϕ258 mm)
ϕ_p	0.0323	0.0379
ψ_p	5.12	4.50

It is seen that the 17.6 rpm pump has a lower discharge number and a higher head number compared to the 21 rpm, which rendering a lower specific speed. Similar expectation can also be placed with the turbine mode operations as well.

Step 5:   Selection of the final operating point, ψ_t and ϕ_t

The final selection of the BEP point for the turbine mode operation based on the cordier and other considerations (namely the ratios for 21 rpm PAT in Table B1.2, Appendix B) are illustrated in Table A9.8. It can be seen that BEP points selected are very close to that obtained from the mean Cordier line in Figure A9.1. The position of this point is plotted on the selection and performance chart for radial PATs in Figure A9.2.

Table A9.8, Final selection of the ψ_t and ϕ_t at BEP for PAT3

ϕ_t	ψ_t	ϕ_t/ϕ_p	ψ_t/ψ_p
0.0562	10.730	1.74	2.10
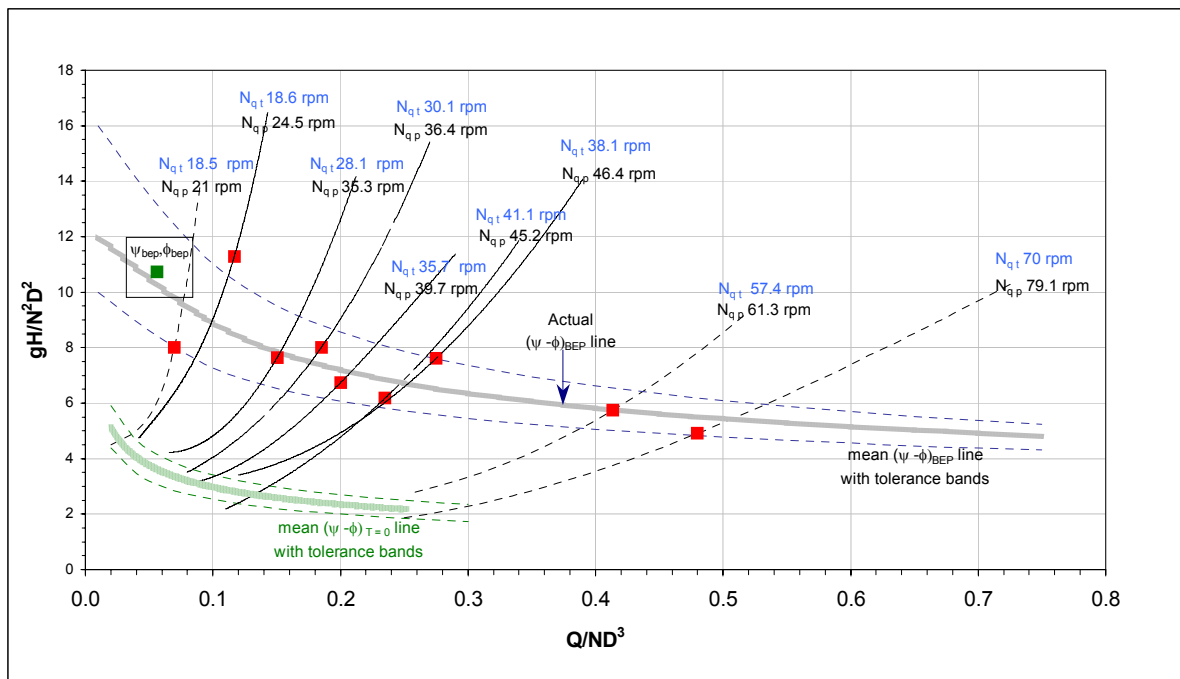
Figure A9.2, Locating the selected ψ_t and ϕ_t on the overall ψ-ϕ characteristics for radial PATs

Step 6:   Synthesis of the complete operating characteristics

Similar procedure is employed in the synthesis of the (ψ - ϕ) and the (η - ϕ) characteristics of the 17.6 rpm PAT (PAT3). With the established BEP points in the Table A9.7, and the no-

load point identified at $\phi_{no-load} = 0.0018, \psi_{no-load} = 6.500$, the characteristics are drawn as shown in the exaggerated chart of <u>Figure A9.3</u>. This figure also shows the (ψ - ϕ) and the (η - ϕ) characteristics for the 21 rpm and 24.5 rpm PATs, which aids the process of synthesis. The value of maximum efficiency chosen for the PAT3 is 72%, mainly from size and geometric considerations.
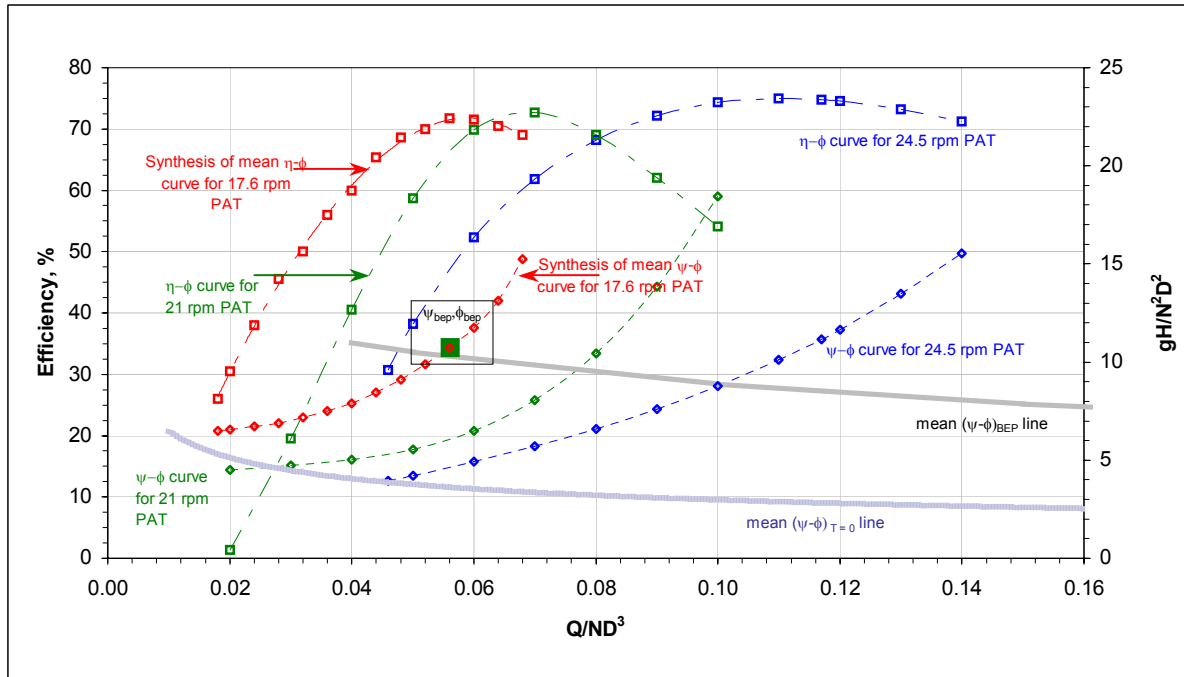

<u>Figure A9.3</u>, Synthesis of the ψ-ϕ and η-ϕ characteristics for the PAT3

Step 7: Uncertainty Bands

The upper and lower tolerance bands for the mean synthesized characteristics with a maximum displacement of discharge number, $\pm\Delta\phi$ = 0.006 ($\pm$11% deviation) are constructed in <u>Figure A9.4</u>.

Step 8: Muschel characteristics

The muschel characteristics are developed based on the mean characteristics in <u>Figure A9.5</u> and comprises of the following curves.

1. Constant speed curves: at 1100 rpm, 1200 rpm, 1300 rpm, 1400 rpm and 1500 rpm.

2. Constant power curves: of 5 KW, 10 KW, 15 KW, 20 KW, 25 KW, and 30 KW.

3. Constant efficiency curves: at 40%, 50%, 60%, 70%, and BEP (72%).

4. No-load or Runaway line

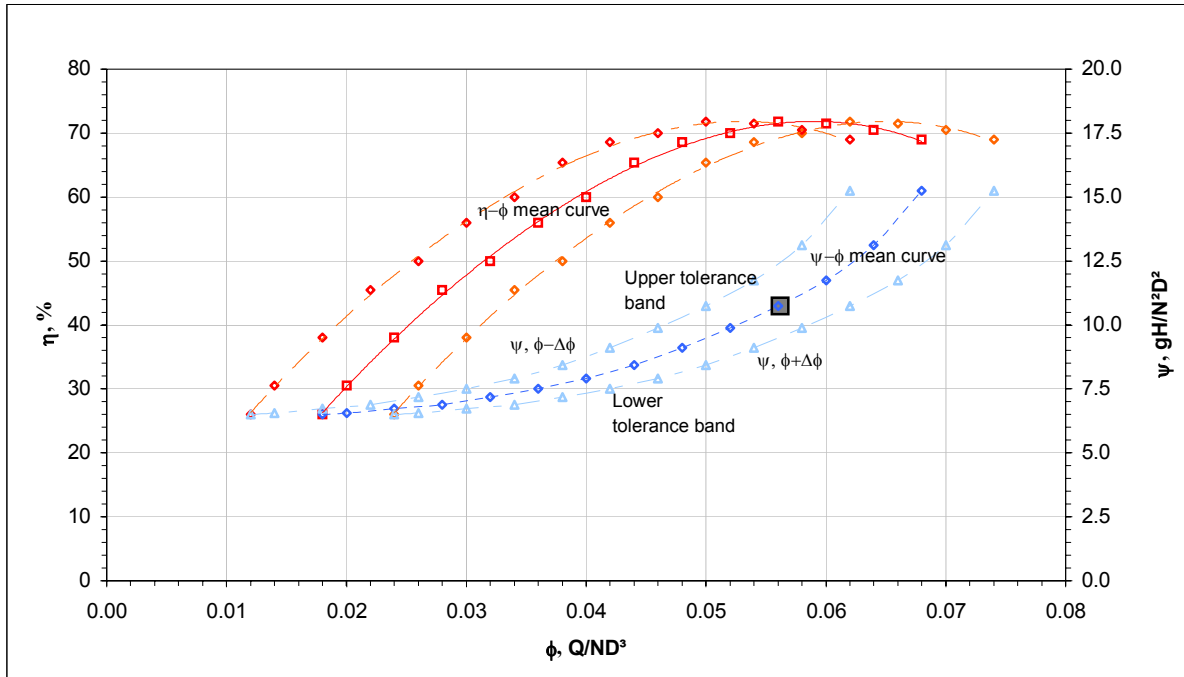5.   System resistance line given by Equation (6.4), Chapter 6.

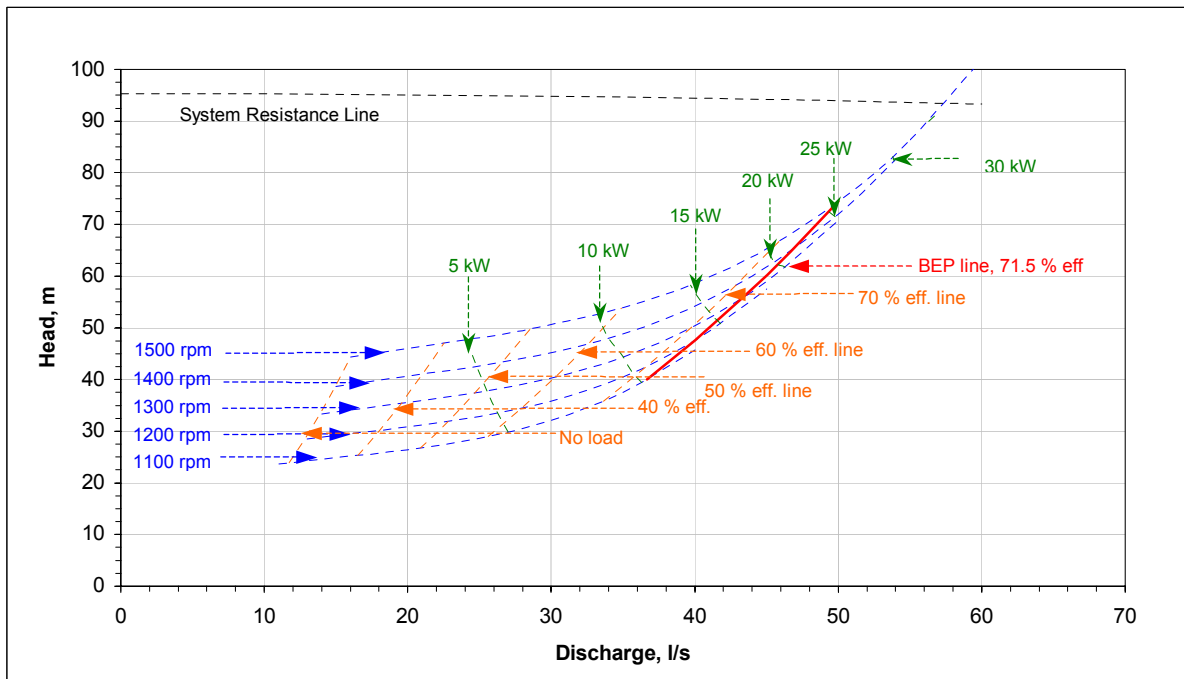Figure A9.4, Uncertainty bands for the ψ-φ and η-φ characteristics of the PAT3

Figure A9.5, Muschel characteristics for PAT3 with system resistance line

Step 9:   Final selection of operating speed

Based on the analysis of intersection of the system resistance curve with the muschel curve, it is found that 1500 rpm is ideal design speed for the operation of PAT3 because this speed satisfies the constraints of the lean power generation and also matches with the synchronous speed of the generator.

Step 10:   Uncertainty analysis at design speed

Figure A9.6 displays the mean characteristics of PAT 3 on absolute scale at 1500 rpm with upper and lower tolerance bands. The system resistance curve (based on Equation (6.4)) is also plotted. It is seen that the system resistance curve intersects the set of machine curves essentially in the overload region. The maximum variations of the performance parameters are summarized in Table A9.9.
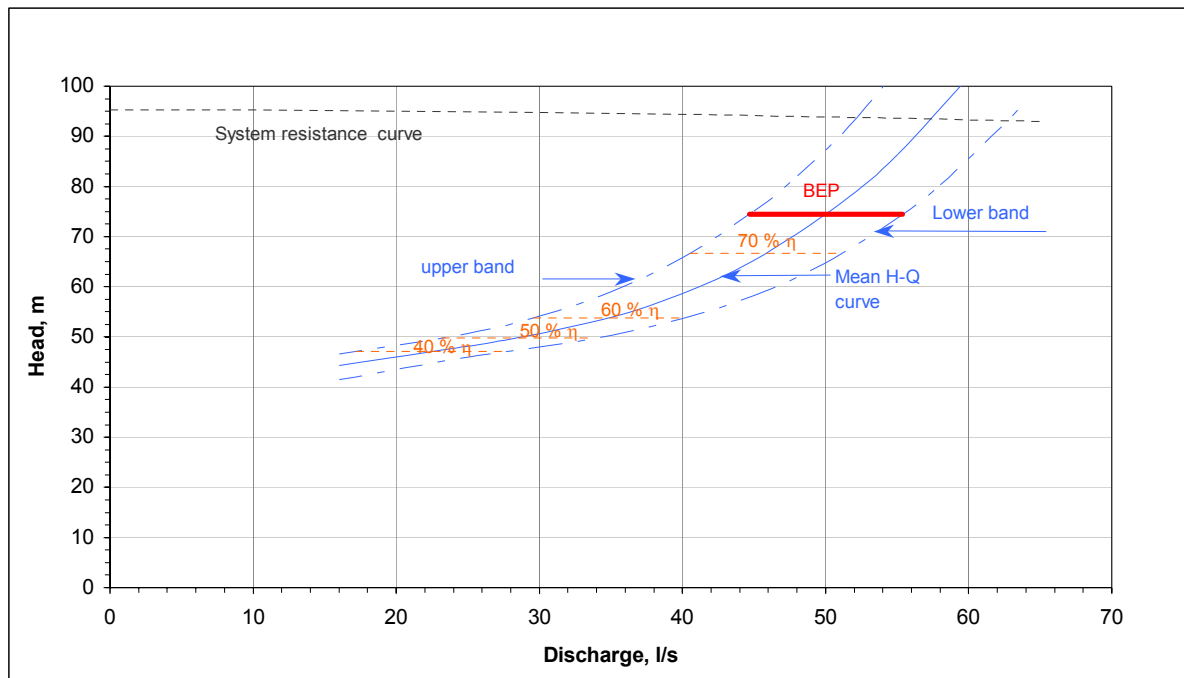

Figure A9.6, Uncertainty bands for the constant speed (design) H-Q curve of PAT3

Table A9.9, Maximum operating range of PAT3 considering uncertainties

	H	Q	P_{mech}
Upper Band	93.8 m	52.2 l/s	33.5 KW
Mean	93.5 m	57.5 l/s	36.9 KW
Lower Band	92.9 m	62.6 l/s	40.2 KW

A9.3   Salient Features of the Mechanical System

A9.3.1   Drive System

As mentioned in section 6.5.2.3, Chapter 6, the tensioning for the drive system for all PAT units could be accomplished only by idler or jockey rollers. With poor performance of single wedge belts under load from idler rollers, poly-rib wedge belts were chosen for the drive. The drive conditions and the configuration selected for drive units 1, 2 and 3 are summarized in <u>Table A9.10</u>.

<u>Table A9.10</u>, Drive conditions and configuration for PAT units 1, 2 and 3

Drive Conditions		
	PAT1 and 2	PAT3
Driver speed	1260 rpm	1500 rpm
Driven speed	1500 rpm	1500 rpm
Maximum Transmission power	90 KW	30 KW
Center to center distance	650 ±10mm	650 ±10mm
Drive Configuration		
	PAT1 and 2	PAT3
Total belt thrust	7782 N	2748 N
Number of ribs	12	5
Belt length	2388 mm	2286 mm
Diameter of driver pulley	ϕ367 mm	ϕ307 mm
Diameter of driven pulley	ϕ307 mm	ϕ307 mm
Actual center to center distance	664.2 mm	661 mm
Weight of driver pulley	35.0 Kgs	10.0 Kgs
Weight of driven pulley	25.5 Kgs	10.0 Kgs
Idler pulley diameter	ϕ 300 mm	ϕ 300 mm

A9.3.2   Shaft System

A9.3.2.1   Design and Analysis of Main Shaft Unit

A9.3.2.1.1   Boundary Conditions

The line diagram of the main shaft system along with the position of the driven pulleys is shown in Figure A9.7. The material selected for the shaft is EN – 24 having a yield stress, σ_{yield} = 275 N/mm^2 and ultimate strength, σ_{ul} = 500 N/mm^2. Table A9.11 summarizes the boundary conditions for the shaft design and analysis.
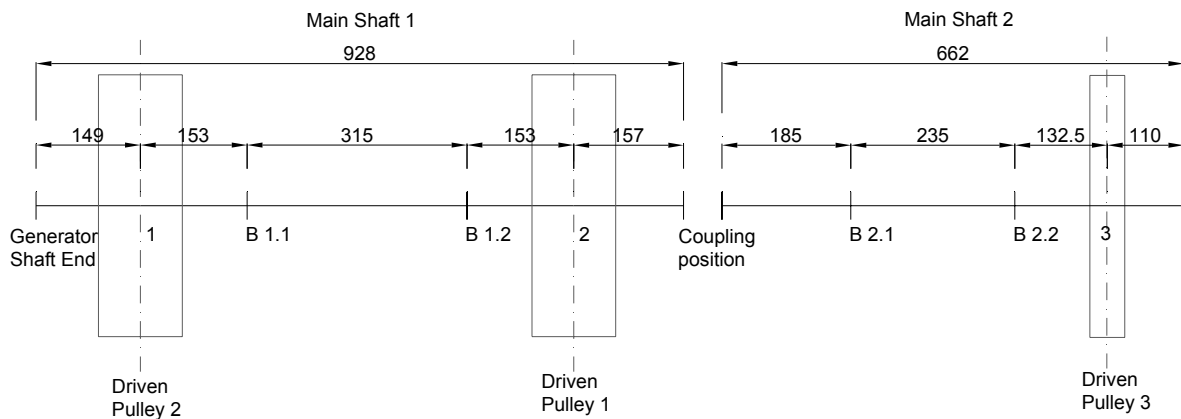

Figure A9.7, Line diagram of main shaft

Table A9.11, Drive conditions for main shaft 1 and 2

Main Shaft 1	
Weight of driven pulley 1	25.5 Kgs
Weight of driven pulley 2	25.5 Kgs
Drive speed	1500 rpm
Total Transmission power	180 KW
Factory of safety	3.5
Bending thrust at centerline of pulley 1	7782 N
Bending thrust at centerline of pulley 2	7782 N

Main Shaft 2	
Weight of driven pulley 3	10 Kgs
Drive speed	1500 rpm
Total Transmission power	30 KW
Factory of safety	3.5
Bending thrust at centerline of pulley 3	2748 N

A9.3.2.1.2 Stress Analysis

Table A9.11 illustrates the forces, bending moments, torques, bearing loads along with design diameters from the combined load theory and fatigue theory.

Table A9.12, Summary of the complete design of main shaft 1 and 2

	Main shaft 1	Main shaft 2
Bearing Load	$F_{1.1}$ = 15368 N	$F_{2.1}$ = 1554 N
Bearing Load	$F_{1.1}$ = 15368 N	$F_{2.1}$ = 4308 N
Combined bending moment, M	1191.6 Nm (at B1.1, B1.2)	365 Nm (at B2.2)
Torque, T	1146 Nm	191 Nm
Design diameter (combined bending and torsion)	ϕ 58.5 mm	ϕ 37.3 mm
Design diameter (fatigue)	ϕ 63.3 mm	ϕ 42.7 mm

As seen from Table A9.12, the diameter requirement for the main shaft 1 is more than that for the main shaft 2. From fatigue consideration the minimum diameter for the main shaft 1 is ϕ 63.3 mm. Therefore ϕ 70 mm is selected for the bearing surfaces and ϕ 64 mm as the minimum step diameter. Though the shaft requirement for the main shaft 2 is about ϕ 43 mm, for reasons of duplicity of manufacture ϕ 70 mm is retained. Figure A9.8 displays the complete shaft drawing for main shaft 1 and 2.
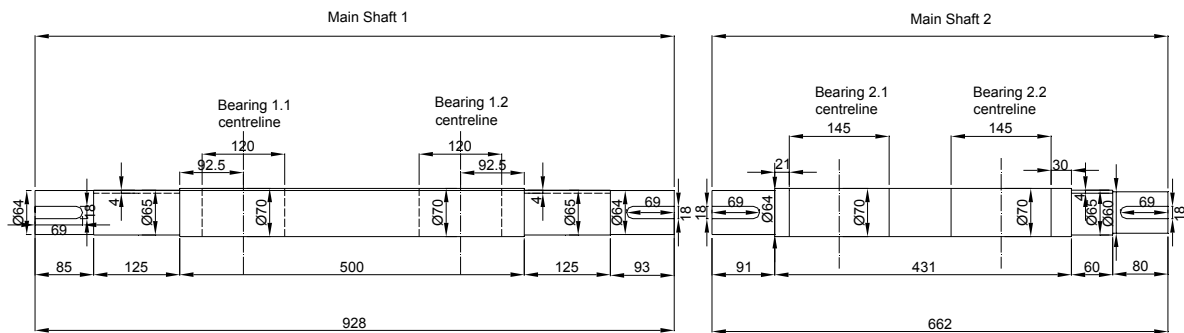
Figure A9.8, Final design drawing of main shaft 1 and 2

A9.3.2.1.3 Bearing Selection

Table A9.13 describes the complete summary of the loads, required load capacities from the bearing units and selected bearings and housings. Spherical roller bearings are selected for the bearings on the main shaft 1 while deep grove ball bearings that for the main shaft 2. It is seen that the dynamic capacities of the spherical roller bearings are slightly smaller than the 10-year lifetime capacity requirements, however this is not a critical situation.

Table A9.13, Summary of the complete bearing requirement on main shaft

	Bearing unit	Load, P	Bearing requirements		Selected bearing		Housing
			(factor)	C_{reqd}	Spec.	C_{dyn}	Spec.
Main Shaft 1	1.1	15368 N	15	230520 N	22216 EK	210000 N	SN 516
	1.2	15368 N	15	230520 N	22216 EK	210000 N	SN 516
Main Shaft 2	2.1	1554 N	20	31080 N	1316 K	88400 N	SN 616
	2.2	4308 N	20	86160 N	1316 K	88400 N	SN 616

All the bearing units were of taper-lock bush type and grease lubrication was selected as cooling mechanism.

A9.3.2.1.4 Critical Speed Analysis

Lateral Critical Speeds

The lateral resonance is determined based on the static deflection at the various load point along the main shaft 1 and 2. Karassik [21] showed that the first lateral resonance is related to the static deflection 'm' by the equation,

$$N_{C1.lateral} = \frac{946}{\sqrt{m}} \text{ in rpm} \qquad (A9.1)$$

Table 6.28 summarizes the static deflection and first resonance speeds at points 1, 2 and 3 on the main shaft system. All the critical speeds are greater than individual operating and runaway speeds (Table A9.14).

Table A9.14, Summary of the lateral resonance speeds on the main shaft

	Load points	Static deflection	First lateral resonance speed
Main shaft 1	1	0.132 mm	2604 rpm
	2	0.132 mm	2604 rpm
Main shaft 2	3	0.026 mm	5867 rpm

Torsional Critical Speeds

The torsional mass system under investigation comprising of the generator rotor, the couplings and pulley masses on the main shaft system is shown in Figure A9.9. The Figure also gives the moment of inertias of the masses and torsional stiffness of the intermediate shaft lengths.
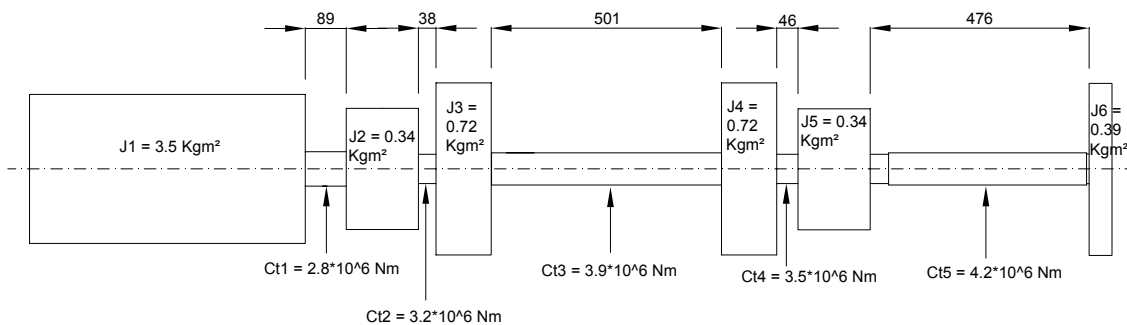

Figure A9.9, Torsional mass system on the main shaft and generator rotor

The 6 resonance frequencies of the 6 mass rotary system can be determined by equating the determinant of the given 6 degree matrix to zero (from Dresig and Holzweizig [19]).

$$
\begin{vmatrix}
C_{t1}-\omega^{2}*J_{1} & -C_{t1} & 0 & 0 & 0 & 0 \\
-C_{t1} & C_{t1}+C_{t2}-\omega^{2}*J_{2} & -C_{t2} & 0 & 0 & 0 \\
0 & -C_{t2} & C_{t2}+C_{t3}-\omega^{2}*J_{3} & -C_{t3} & 0 & 0 \\
0 & 0 & -C_{t3} & C_{t3}+C_{t4}-\omega^{2}*J_{4} & -C_{t4} & 0 \\
0 & 0 & 0 & -C_{t4} & C_{t4}+C_{t5}-\omega^{2}*J_{5} & -C_{t5} \\
0 & 0 & 0 & 0 & -C_{t5} & C_{t5}-\omega^{2}*J_{6}
\end{vmatrix}
$$

The first four resonance speeds obtained are, 0 rpm, 2820 rpm, 15000 rpm and 33000 rpm. The fifth and the sixth resonance speeds are extremely high with no relevance. It is seen that the second resonance speed of 2820 rpm is much higher compared to the operating speed of 1500 rpm and also the runaway speed of 2200 rpm (Table 6.13, Chapter 6).

A9.3.2.2   Verification Analysis of Shaft of PAT1, PAT2 and PAT3

A9.3.2.2.1   Verification of PAT Shaft 1 and 2

A9.3.2.2.1.1   Boundary Conditions

The line diagram for the shaft system for PAT1 and PAT2 is shown in Figure A9.10. The material selected for the shaft is AISI 4140 having a yield stress range, σ_{yield} = 500 – 720 N/mm^2 and ultimate strength range, σ_{ul} = 500 – 1450 N/mm^2. The boundary conditions for the shaft verification are listed in Table A9.15.
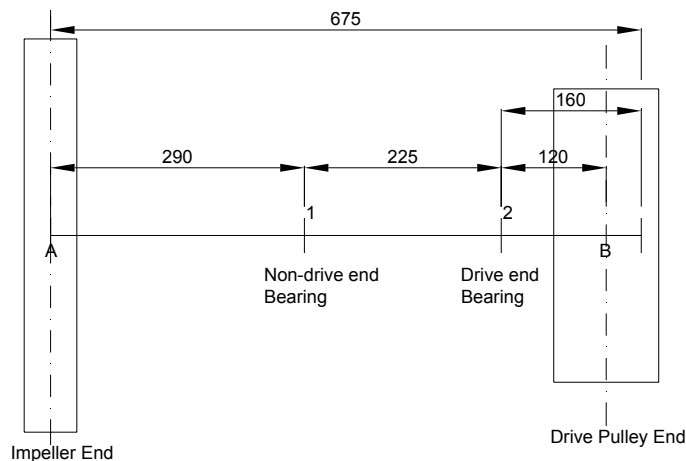

Figure A9.10, Line diagram for shaft of PAT1 and PAT2

Table A9.15, Drive conditions for shafts of PAT1 and PAT2

PAT Shaft 1 and 2	
Weight of driver pulley 1	35 Kgs
Weight of Impeller	16 Kgs
Drive speed	1260 rpm
Total Transmission power	90 KW
Factory of safety	3.5
Bending thrust at centerline of pulley 1	7782 N
Minimum shaft diameter	ϕ48 mm

A9.3.2.2.1.2   Stress Analysis

The required stresses are calculated based on reference diameter of the shaft (ϕ48 mm in Table 6.29) and the various parameters are summarized in Table A9.16.

Table A9.16, Stress analysis for shafts of PAT1 and PAT2

	PAT shaft 1
Bearing Load	F_1 = 4154 N
Bearing Load	F_2 = 11952 N
Combined bending moment, M	936 Nm (at B1, B2)
Torque, T	682 Nm
Yield stress reqd., σ (combined bending and torsion)	356.8 N/mm^2
Fatigue stress reqd., σ_f	301.8 N/mm^2
Ultimate strength reqd., σ_{ul}= 3*σ_f	905 N/mm^2

It is seen that the required yield stress and the ultimate strength for the shaft material are far below that of the material (AISI 4140) specifications.

A9.3.2.2.1.3   Bearing Verification

The dynamic load capacities of the bearings on the PAT shaft 1 and 2, along with required capacities are compared in Table A9.17, which shows that the bearing 1 is completely safe but the bearing 2 is marginally overloaded with required capacity of 167328 N as to the available dynamic capacity of 158600 N.

Table A9.17, Summary of the complete bearing requirement on PAT1 shaft

Bearing Unit	Bearing Details			Load, P	Bearing Requirements	
	Code	Nos.	C_{dyn}		(factor)	C_{reqd}
1	NU 311	1	102000 N	4154 N	19	78926 N
2	7311	2	158600 N	11952 N	14	167328 N

A9.3.2.2.1.4   Critical Speed Analysis

Lateral Critical Speed

The first lateral critical speeds at load point A and B (i.e. the impeller and the pulley end respectively) in Figure A9.11 are summarized in Table A9.18. The first critical speed at A is much higher than the operating and runaway speed, but the lateral resonance conditions at B (1935 rpm) is closer to runaway speed of PAT 1 (1815 rpm from section 6.5.3 and Table 6.14).

Table A9.18, Summary of the lateral resonance speeds on the PAT1 shaft

Load point	Static deflection	First lateral critical speed
A	0.043 mm	4562 rpm
B	0.132 mm	1935 rpm

Torsional Critical Speed

The second torsional resonance speed for a two mass system is determined using a simple formula, (from Mahadevan [35]), as the first critical speed is always 0.

$$\omega_2 = \sqrt{C_t \times \frac{(J_1 + J_2)}{J_1 \times J_2}} \qquad (A9.2)$$

The rotational moment of inertia of the impeller, J_1, is approximately determined to be 0.65 Kgm^2, while that of the pulley, J_2, to be 0.94 Kgm^2. With the torsional stiffness C_t for the given shaft system equal to 0.712×10^5 Nm, the second torsional resonance speed is found to be 4117 rpm. Therefore even from torsional considerations, the critical resonance is not affecting the shafts of PAT 1 and 2.

A9.3.2.2.2   Verification of PAT Shaft 3

The line diagram for the PAT shaft 3 is shown in Figure A9.11 with impeller at one end and driver pulley 3 at the other along with two intermediate bearings. The material of the shaft is AISI 4140 similar to that of shaft 1 and 2.
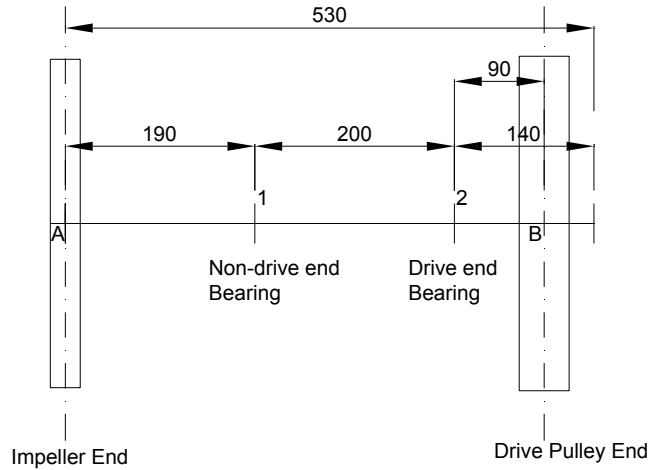

Figure A9.11, Line diagram for shaft of PAT3

A9.3.2.2.2.1   Boundary Conditions

Table A9.19 summarizes the boundary conditions needed for verifying the shaft design.

Table A9.19, Drive conditions for the shaft of PAT2

PAT Shaft 3	
Weight of driver pulley 3	10 Kgs
Weight of Impeller	8 Kgs
Drive speed	1500 rpm
Total Transmission power	30 KW
Factory of safety	3.5
Bending thrust at centerline of pulley 3	2748 N
Minimum shaft diameter	ϕ42 mm

A9.3.2.2.2.2   Stress Analysis

The required stress conditions under the given load is summarized in Table A9.20, where is it found that yield stress and ultimate strength are within the permissible limits of AISI 4140 shaft material.

Table A9.20, Stress analysis for the shaft of PAT3

	PAT shaft 3
Bearing Load	F_1 = 1237 N
Bearing Load	F_2 = 3985 N
Combined bending moment, M	248.4Nm (at B1, B2)
Torque, T	191 Nm
Yield stress reqd., σ (combined bending and torsion)	143.6 N/mm^2
Fatigue stress reqd., σ_f	119.5 N/mm^2
Ultimate strength reqd., σ_{ul}= 3*σ_f	358.5 N/mm^2

A9.3.2.2.2.3   Bearing Verification

The Table A9.21 illustrates the conditions on the bearings along with the specifications, which shows that all the load capacities are in permissible limits.

Table A9.21, Summary of the complete bearing requirement on the shaft PAT3

Bearing Unit	Bearing Details			Load, P	Bearing Requirements	
	Code	Nos.	C_{dyn}		(factor)	C_{reqd}
1	NU 309	1	72100 N	1237 N	20	24740 N
2	7309	2	117000 N	3985 N	15	59775 N

A9.3.2.2.2.4   Critical Speed Analysis

Lateral Critical Speed

The static deflections at load points A and B on the PAT 3 shaft along with the first critical frequencies are summarized in Table A9.22. It is observed that the deflections are marginal and the critical speeds nowhere near the operating speed or the runaway speed (Table 6.13, section 6.5.3, Chapter 6).

Table A9.22, Summary of the lateral resonance speeds on the shaft of PAT3

Load point	Static deflection	First lateral critical speed
A	0.012 mm	8636 rpm
B	0.099 mm	3007 rpm

Torsional Critical Speed

The torsional critical speed is determined based on Equation (A9.2) with given moment of inertia of impeller, J_1 = 0.17 Kgm^2, that of the pulley, J_2 = 0.19 Kgm^2 and torsional stiffness, C_t = 0.176×10^5 Nm, the critical speed determined is 4230 rpm, which is over operational and runaway criteria.

A9.3.3   Couplings

Flexible tyre couplings are selected due to the advantages of shock absorption, easy installation, and greater degree of handling misalignments. Each coupling 1 and 2 can transmit 180 KW at a speed of 1500 rpm.

A9.4   Uncertainty Analysis of Field Measurements

The measurement methodology for the field trials has been restricted to simplicity and hence the degree of errors could be considerable. This section reviews the maximum possible uncertainty in these measurements. The uncertainty analysis will be carried out on the full load test of the PAT2 (as in Table 6.17, Chapter 6), for which all the parameters have been measured. The uncertainties associated with the three variables, net head, discharge and electrical power are shortly discussed, before the overall uncertainty.

1. Net head:

    The basic, static head component of net head is determined using standard pressure gauges, which can be assumed to have fixed error. Although it is not possible to exactly quantify the uncertainty for the velocity head component, a maximum random error for the net head, ΔH = ±1 m is assumed throughout the scale of the gauge.

2. Discharge:

    Discharge is determined from the Rehbock weir formula (International Electromechanical Commission [20]), whose prime requisite is the height of water

over the weir. No calibrated pointer scale was installed to determine this height. The height was more crudely determined by holding a scale at the weir edge. Therefore a maximum uncertainty for this weir height is fixed at higher value of, $\Delta h_w = \pm 1$ cm. Using this Δh_w the maximum error in discharge is calculated using the formula given below.

$$\delta Q = \pm \frac{\partial Q}{\partial h_w} \delta h_w \qquad (6.6)$$

$$Q = 2/3 \; \varsigma b_w \sqrt{2g} \; (h_w)^{3/2} \qquad (A9.3)$$

3. Electrical Power:

   The electrical power is determined based on the simple formula,

$$P_{Elec} = \frac{3V_B^2}{R} \qquad (A9.4)$$

Both the ballast voltage and resistance have individual uncertainties that are assumed to be, $\Delta V_B = \pm 5V$ and $\Delta R = \pm 0.1$ ohm. The overall uncertainty in the electric power is given by,

$$\partial P_{Elec} = \frac{\partial P_{Elec}}{\partial V_B} \delta V_B + \frac{\partial P_{Elec}}{\partial R} \delta R$$

$$\delta P_{Elec} = \pm \left[\left(\frac{\partial P_{Elec}}{\partial V_B} \delta V_B \right)^2 + \left(\frac{\partial P_{Elec}}{\partial R} \delta R \right)^2 \right]^{1/2} \qquad (A9.5)$$

The overall uncertainty table for the full load test on PAT2 is illustrated in Table A9.23. It is observed that the uncertainties associated with discharge are range of $\pm 15\%$ to $\pm 20\%$, while that with power are in the range of $\pm 7.5\%$ to $\pm 11\%$. The errors in head measurements are however marginal. The net uncertainty in efficiency at the load point 7 is $\pm 9.3\%$ as to $\pm 12.3\%$ load point 2.

Table A9.23, Absolute uncertainty table for field measurements on PAT2

Load	Head			Discharge			Power			Efficiency
Point	H	δH	$\delta H/H$	Q	δQ	$\delta Q/Q$	P	δP	$\delta P/P$	$\delta \eta$
	(m)	(m)		(l/s)	(l/s)		(KW)	(KW)		(%)
2	52.5	±1	±1.9%	63.3	±14.3	±22.5%	15.8	±1.8	±11.3%	±12.3%
3	48.4	±1	±2.1%	63.3	±14.3	±22.5%	16.4	±1.8	±11.1%	±13.8%
4	65.2	±1	±1.5%	86.2	±15.8	±18.4%	33.2	±2.9	±8.7%	±12.3%
5	75.8	±1	±1.3%	102.8	±16.8	±16.4%	45.6	±3.6	±7.9%	±10.9%
6	81.2	±1	±1.2%	111.5	±17.3	±15.5%	51.2	±3.9	±7.7%	±10.0%
7	85.6	±1	±1.2%	120.4	±17.8	±14.7%	57.0	±4.2	±7.4%	±9.3%

The uncertainty analysis for the PAT3 test results can be determined only with respect to the power measurement as illustrated in Table A9.24. In the BEP and overload region the uncertainties are in the range of $\pm10\%$ to $\pm12\%$.

Table A9.24, Absolute uncertainty table for the field measurement on PAT3 (for the power variable only)

Power		
P_{elec} (KW)	δP (KW)	$\delta P/P$
1.9	±0.6	$\pm29.1\%$
5.7	±1.0	$\pm17.5\%$
11.4	±1.5	$\pm12.9\%$
12.8	±1.6	$\pm12.3\%$
14.3	±1.7	$\pm11.8\%$
15.8	±1.8	$\pm11.3\%$
19.1	±2.0	$\pm10.5\%$
20.9	±2.1	$\pm10.2\%$

The uncertainties (Table A9.23 and A9.24) are very high and reflect the mediocre quality of measurements carried out. However, this study gives a fair enough idea regarding the extent of deviation existing in the field results.

Appendix-B

B1 Turbine Mode and Pump Mode Comparisons

B1.1 Pump Mode Performance at BEP

The pump mode performances for both the radial flow and the mixed flow pumps are summarized in Table B1.1 at the best efficiency point. The data presented in Table B1.1 are obtained from manufacturer's test catalogue. The diameters (D_1) provided below are also listed in Table A4.1 and A4.3 (section A4, Appendix A) respectively for the radial and mixed flow pumps respectively.

Table B1.1, Summary of the pump mode BEPs and reference diameters for the radial and mixed flow PATs

Sl. No.	$N_{q\,p}$ (rpm)	Head H_p (m)	Discharge Q_p (l/s)	Speed N_p (rpm)	Efficiency η_p (%)	Diameter D_1 (mm)
Radial Flow Pumps						
1	21.0	14.5	10.8	1500	77%	225
2	24.5	21.5	26.5	1500	78%	258
3	35.3	12.8	25.4	1500	78.5%	206
4	36.4	8.38	15.27	1450	74.4%	174
5	39.7	19.8	65.9	1450	85%	264
6	45.2	10.5	33	1450	80%	200
7	46.4	5.6	13.5	1450	76%	139
8	61.3	6.4	28.9	1450	72%	165
9	79.1	10.6	103.0	1450	84%	224
Mixed Flow pumps						
Sl. No.	$N_{S\,p}$	H_p	Q_p	N_p	η_p	D_{1f}
1	72.8	21.5	251.4	1450	84%	338
2	94.4	8.3	101.4	1450	83%	236

B1.2 Experimental Comparison of Turbine and Pump Mode BEP

Table B1.2 compares the dimensionless results of the pump mode and the turbine mode BEPs for all the experimentally tested machines and evaluates the head number and

discharge number ratios respectively. It is seen that the lower specific speed radial flow pumps (21 rpm and 24.5 rpm) have extremely higher values of both head number and discharge number ratios, which are in the range of 1.8 and 2.2. For other pumps the head number ratios are in the range of 1.3 to 1.7 and the discharge number ratios in the range of 1.3 to 1.5.

The two mixed flow pumps that are analyzed show an interesting result, in which the discharge number ratios are marginal (1.25 – 1.3), while the head number ratios are considerably higher, in the range of 1.53 to 1.75. This result only suggests that the turbine mode characteristics (ψ-ϕ) for mixed flow pumps are very steep, in that the turbine mode BEP occurs at greater heads but with a limited rise of discharges.

<u>Table B1.2</u>, Experimental comparison table of the turbine and pump mode performance

Sl. No.	Pump Mode				Turbine Mode				Comparisons	
	$N_{q\,p}$ (rpm)	ϕ_p	ψ_p	η_p	$N_{q\,t}$ (rpm)	ϕ_t	ψ_t	η_t	ϕ_t/ϕ_p	ψ_t/ψ_p
Radial Flow PATs										
1	21.0	0.038	4.496	77.0%	18.5	0.070	8.000	72.5%	1.85	1.78
2	24.5	0.062	5.070	78.0%	18.6	0.117	11.170	76.5%	1.90	2.20
3	35.3	0.116	4.734	78.5%	28.1	0.151	7.640	81.0%	1.30	1.61
4	36.4	0.120	4.650	74.4%	30.1	0.185	8.000	71.5%	1.54	1.72
5	39.7	0.148	4.772	85.0%	35.7	0.200	6.700	83.5%	1.35	1.40
6	45.2	0.171	4.409	80.0%	41.1	0.235	6.180	79.5%	1.38	1.40
7	46.4	0.208	4.850	76.0%	38.1	0.275	7.600	76.0%	1.32	1.57
8	61.3	0.266	3.949	72.0%	57.6	0.414	5.748	74.3%	1.56	1.46
9	79.1	0.379	3.555	84.0%	70.0	0.480	4.900	75.5%	1.27	1.38
Mixed Flow PATs										
Sl. No.	$N_{q\,p}$ (rpm)	$\phi_{p\,(mf)}$	$\psi_{p\,(mf)}$	η_p	$N_{q\,t}$ (rpm)	$\phi_{t\,(mf)}$	$\psi_{t\,(mf)}$	η_t	ϕ_t/ϕ_p	ψ_t/ψ_p
1	72.8	0.269	3.161	84.0%	54.9	0.353	5.520	80.0%	1.31	1.75
2	94.4	0.319	2.503	83.0%	76.9	0.400	3.823	83.0%	1.25	1.53

B1.3   Review of the Prediction Methods

There are many prediction methods that have been developed for predicting the turbine mode BEP points of a pump (as briefly mentioned in section 1.1.2 of chapter 1 and section

5.1.1 of chapter 5). These methods are essentially based on the combination of pump mode parameters at BEP, the absolute efficiency and specific speed. Some of these methods also use the expected turbine mode efficiency and also turbine mode specific speed. Williams [57] has made a very intense study of the origin and categorization of these prediction methods.

Table B1.3 summarizes the 9 methods used for the comparisons with experimentally obtained ratios. It is seen that the prediction equations given by Cohrs [7] requires the determination of the Pfleiderer's slip factor 'p' (discussed in section 2.3.3 of Chapter 2) and hence renders the method more complicated over the others.

Table B1.3, Summary of the available BEP prediction methods for turbine mode performance

Sl. No.	Method	ϕ_t/ϕ_p	ψ_t/ψ_p
1.	Stepanoff [52]	$\dfrac{1}{\eta_p}$	$\dfrac{1}{\eta_t \times \eta_p}$
2.	Childs [5]	$\dfrac{1}{\eta_p^2}$	$\dfrac{1}{\eta_p^2}$
3.	Sharma [44]	$\dfrac{1}{\eta_p^{0.8}}$	$\dfrac{1}{\eta_p^{1.2}}$
4.	Alatorre-Frenk [2]	$\dfrac{0.85 \cdot \eta_p^5 + 0.385}{2 \cdot \eta_p^{9.5} + 0.205}$	$\dfrac{1}{0.85 \cdot \eta_p^5 + 0.385}$
5.	Schmiedl [42]	$1.4 - \dfrac{2.5}{\left(\eta_p^{0.5} \cdot \eta_t^{0.5}\right)^{0.5}}$	$1.5 - \dfrac{2.4}{\eta_p^{0.5} \cdot \eta_t^{0.5}}$
6.	Grover [16]	$2.379 - 0.0264 \cdot N_{qt}$	$2.693 - 0.0229 \cdot N_{qt}$
7.	Hergt [18]	$1.3 - \dfrac{1.6}{N_{qt} - 5}$	$1.3 - \dfrac{6}{N_{qt} - 3}$
8.	Gopalakrishnan [15]	$\dfrac{1}{\eta_p}$	$\dfrac{1}{\eta_p^2}$
9.	Cohrs [7]	$1 + \dfrac{1}{\left(\eta_p \cdot u_1^2 \middle/ H_p \cdot \mathbf{p} \cdot g\right) - 1}$	$\dfrac{1 + \dfrac{1}{\left(\eta_p \cdot u_1^2 \middle/ H_p \cdot \mathbf{p} \cdot g\right) - 1}}{\eta_p \cdot \eta_t}$

B1.4   Results of Comparisons

The discharge and head number ratios from the various methods listed in Table B1.3 are determined from the input data from Table B1.1 and B1.2. For the determination of slip 'p' for the Cohrs' method of prediction, a simplified Pleiderer's slip equation presented by Cooper [8] is used.

B1.4.1   Discharge Number Ratios - ϕ_t/ϕ_p

Table B1.4 compares the predicted discharge number ratios with the experimental ratios for both the radial and mixed flow PATs, while Figure B1.1 and B1.2 compares these ratios graphically against the pump specific speeds for radial flow and mixed flow pumps respectively.

Table B1.4, Summary of discharge number ratios from experimental and prediction methods

Pump	Expt. (Tab. B1.2)	Stepanoff [53]	Childs [5]	Sharma [45]	Alatorre [2]	Schmiedl [43]	Grover [16]	Hergt [18]	Gopalakrishnan [15]	Cohrs [7]
$N_{q\,p}$	ϕ_t/ϕ_p	ϕ_t/ϕ_p	ϕ_t/ϕ_p	ϕ_t/ϕ_p	ϕ_t/ϕ_p	ϕ_t/ϕ_p	ϕ_t/ϕ_p	ϕ_t/ϕ_p	ϕ_t/ϕ_p	ϕ_t/ϕ_p
Radial Flow Machines										
21.0	**1.85**	1.30	1.69	1.23	1.65	1.49	1.89	1.18	1.30	1.38
24.5	**1.90**	1.28	1.64	1.22	1.60	1.44	1.89	1.18	1.28	1.40
35.3	**1.30**	1.27	1.62	1.21	1.57	1.40	1.64	1.23	1.27	1.34
36.4	**1.54**	1.34	1.81	1.27	1.78	1.53	1.59	1.24	1.34	1.27
39.7	**1.35**	1.18	1.38	1.14	1.21	1.32	1.44	1.25	1.18	1.33
45.2	**1.38**	1.25	1.56	1.20	1.49	1.40	1.29	1.26	1.25	1.34
46.4	**1.32**	1.32	1.73	1.25	1.70	1.47	1.37	1.25	1.32	1.45
61.3	**1.56**	1.39	1.93	1.30	1.87	1.52	0.86	1.27	1.39	1.24
79.1	**1.27**	1.19	1.42	1.15	1.26	1.40	-	1.28	1.19	1.38
Mixed Flow Machines										
72.8	**1.31**	1.19	1.42	1.15	1.26	1.36	-	1.27	1.19	-
94.4	**1.25**	1.20	1.45	1.16	1.32	1.34	-	1.28	1.20	1.23

It is seen from the patterns in Figure B1.1 that no single method closely resembles the experimental pattern for the complete range of the pump specific speeds. In low specific speed range Grover's [16] ratios fits well with that of the experimental ones. However in the

middle range ($N_{q\,p}$ of 35 to 45 rpm), Schiemdl's [42] method seems to be the closest. In the specific speed range from 50 to 70 rpm, it again seems that the Schiemdl's [42] method is the only method that is compatible. At the final specific speed (79.1 rpm) Gopalakrishnan's [15] and Hergt's [18] ratio patterns tend to match with the experimental patterns.
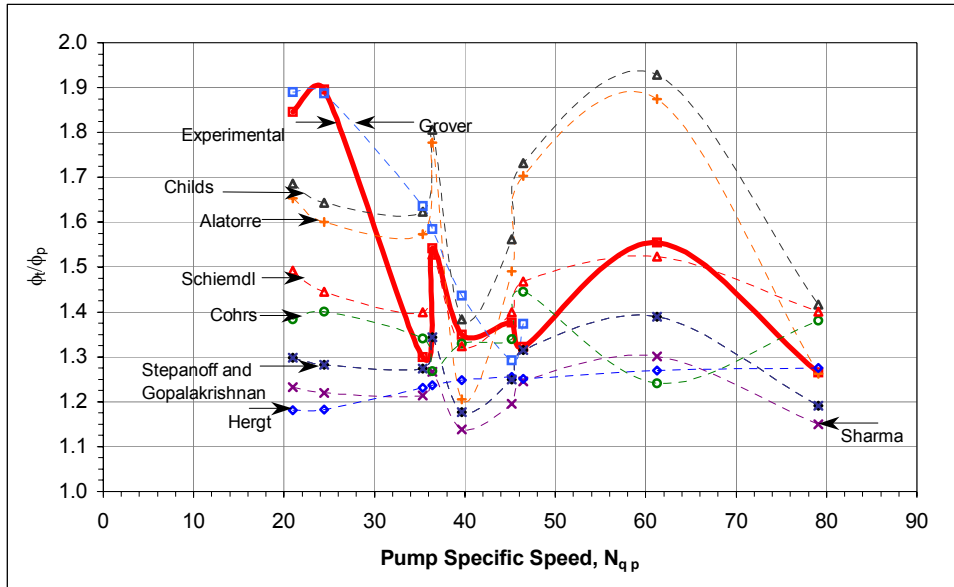

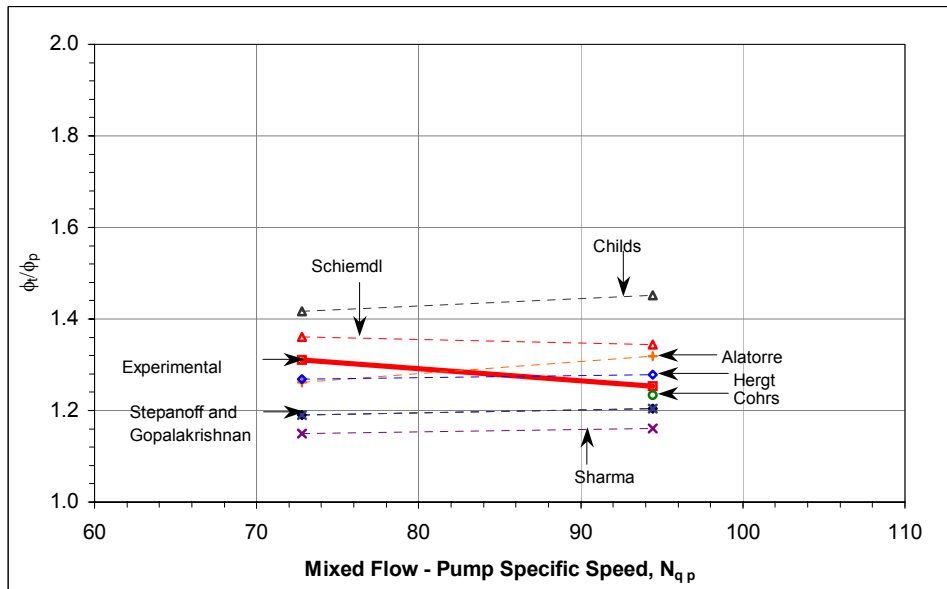Figure B1.1, Overall discharge number ratio chart for radial flow pumps

Figure B1.2, Overall discharge number chart for mixed flow pumps

For the mixed flow pumps it is seen from Figure B1.2 that both the Hergt [18] and the Alatorre [2] methods give good coincidence of the discharge number ratios with the experimental patterns. The Cohrs [7] method that predicts only the 94.4 rpm PAT shows

very good similarity. Schmiedl's [43] and Childs [5] method are predicting higher discharge number ratios.

B1.4.1   Head Number Ratios - ψ_t/ψ_p

The head number ratios for radial flow and mixed flow pumps are illustrated in Table B1.4 and plotted in <u>Figure B1.3</u> and <u>B1.4</u>.

Table B1.4, Summary of head number ratios from experimental and prediction methods

Pump	Expt. (Tab. B1.2)	Stepanoff [53]	Childs [5]	Sharma [45]	Alatorre [2]	Schmiedl [43]	Grover [16]	Hergt [18]	Gopalakrishnan [15]	Cohrs [7]
$N_{q\,p}$	ψ_t/ψ_p	ψ_t/ψ_p	ψ_t/ψ_p	ψ_t/ψ_p	ψ_t/ψ_p	ψ_t/ψ_p	ψ_t/ψ_p	ψ_t/ψ_p	ψ_t/ψ_p	ψ_t/ψ_p
Radial Flow Machines										
21.0	**1.78**	1.79	1.69	1.37	1.63	1.71	2.27	0.91	1.69	1.69
24.5	**2.20**	1.68	1.64	1.35	1.59	1.61	2.27	0.92	1.64	1.67
35.3	**1.61**	1.57	1.62	1.34	1.57	1.51	2.05	1.06	1.62	1.54
36.4	**1.72**	1.88	1.81	1.43	1.73	1.79	2.00	1.08	1.81	1.50
39.7	**1.40**	1.41	1.38	1.22	1.31	1.35	1.88	1.12	1.38	1.46
45.2	**1.40**	1.57	1.56	1.31	1.51	1.51	1.75	1.14	1.56	1.53
46.4	**1.57**	1.73	1.73	1.39	1.67	1.66	1.82	1.13	1.73	1.77
61.3	**1.46**	1.87	1.93	1.48	1.82	1.78	1.37	1.19	1.93	1.45
79.1	**1.38**	1.58	1.42	1.23	1.35	1.51	-	1.21	1.42	1.60
Mixed Flow Machines										
72.8	**1.75**	1.49	1.42	1.15	1.35	1.43	-	1.27	1.42	-
94.4	**1.53**	1.45	1.45	1.16	1.39	1.39	-	1.28	1.45	1.34

It can be observed from <u>Figure B1.3</u> that Grover's method predicts higher head ratios even in the low specific speed range, but still are compatible with the experimental ratios. However it is very interesting to find that in the mid specific range ($N_{q\,p}$ of 35 to 45 rpm) that the Schiemdl's [42], Alatorre's [2], Stepanoff's [52] Child's [5] and Gopalakrishnan's [15] ratio patterns show extremely good resemblance with the experimental curve.

For the next specific speed range ($N_{q\,p}$ of 55 to 70 rpm) none of the above methods give the right ratios, rather Sharma's [44] and Cohrs' [7] technique seems to agree with the experimental patterns. In the higher specific speed ($N_{q\,p}$ over 79 rpm) region only the head

ratios from Alattore's [2], Childs' [5] and Gopalakrishnan's [15] methods are somewhat agreeable. Hergt's [18] is totally displaced from the experimental and other predicted patterns.

As seen from the mixed flow prediction diagram in Figure B1.4, all the methods predict a lower head number compared to the experimental evaluated ones. Amongst the methods, Stepanoff's [52] and Gopalakrishnan's [15] methods display the least deviation.
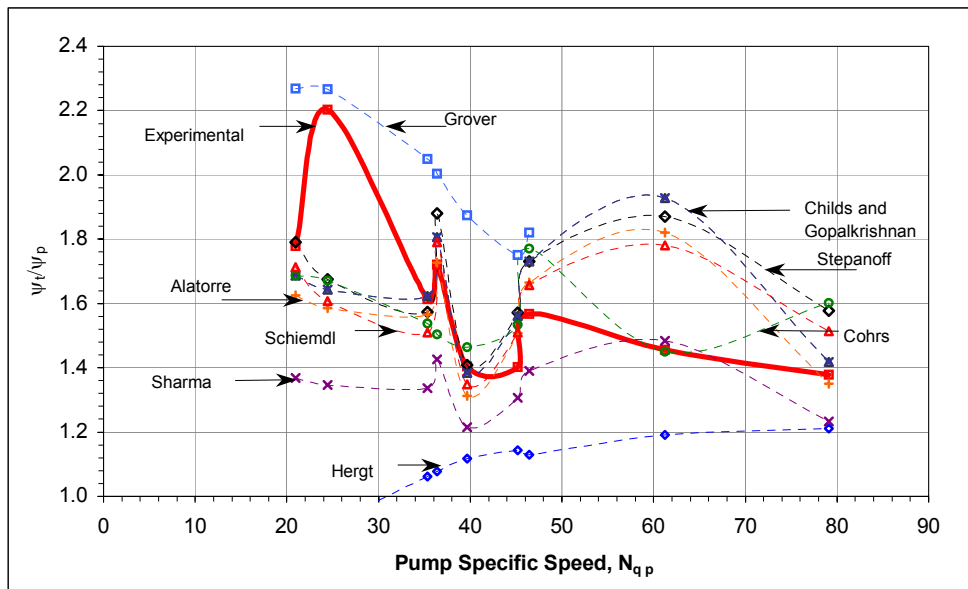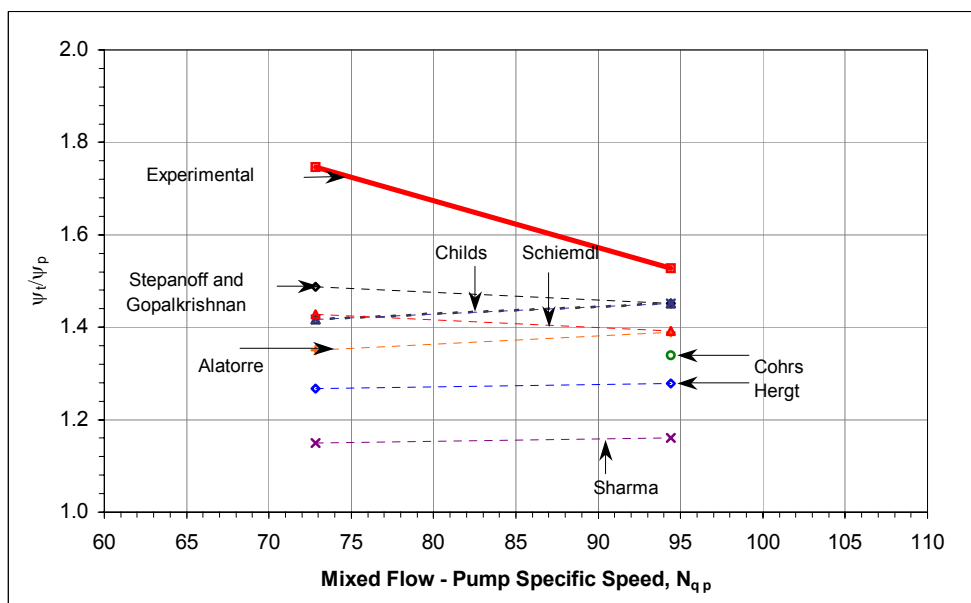

Figure B1.3, Overall head number ratio chart for radial flow pumps

Figure B1.4, Overall head number chart for mixed flow pumps

B1.5 Discussion

The validity of any prediction method is based on accurate predictions of both the head ratios and the discharge ratios accurately for a given range of specific speed. It is not enough if the method predicts either of the head or discharge ratios accurately. The predictions for the radial flow and mixed flow PATs needs to be separately analyzed since there are fundamental differences in geometry of both these machines.

1. Radial Flow PATs

For the low specific speed radial flow pumps ($N_{q\,p}$ - 20 rpm to 25 rpm), it is seen that the Grover's [16] approach is reasonably well predicting both the head and discharge ratios. However in the mid specific speed range ($N_{q\,p}$ - 35 rpm to 45 rpm), there appears to be some controversies. There are many methods that are satisfying the experimental head ratio patterns, but for the discharge ratios most these have very poor conformance. Only the Schiemdl's [42] method that is predicting both the head and discharge ratios reasonably accurately in this mid specific speed range.

In the range of specific speed between 50 rpm and 70 rpm, there is not a single method that is satisfying both the head number and discharge number ratios consistently. For higher specific speed radial pumps ($N_{q\,p}$ over 79 rpm), it is found that only the prediction technique from Gopalakrishnan [15] is satisfying the experimental head and discharge ratios patterns.

Therefore Grover's [16], Schiemdl's [42] and Gopalakrishnan's [15] techniques are making good predictions in respective ranges of specific speeds for radial pumps, however by no means it can be concluded that these methods will necessarily hold good for all pumps.

2. Mixed Flow PATs

The prediction analysis for the mixed flow pumps have been very interesting, in that no single method is together making accurate predictions of both the head and discharge ratios. While Alatorre's [2] and Hergt's [18] methods are predicting the discharge ratios accurately, their predictions of the head ratios are seen to be totally out of the range. Though Stepanoff [52] and Gopalakrishnan [15] are the closer to the experimental head ratio line, they are very bad as far as the discharge ratios are concerned. Therefore for the mixed flow pumps, it is very difficult make any conclusion. No method is able to convincingly or accurately evaluate the hydraulic in a mixed flow PAT.

3. Summary

The experience concerning the validity of these prediction methods of other researchers have been extremely mixed. While Williams [57] after analyzing more than 34 pumps,

concluded that the Sharma's [44] was the only method that made more accurate predictions compared to all other methods. It has to be pointed out from the comparisons in Table B1.1 and Table B1.2 along with Figures B1.1, B1.2, B1.3 and B1.4, Sharma's method is making underestimated predictions consistently and the corresponding deviations are too large to even recommend it for further applications.

Hirschberger [19] also made comparisons of both single suction and double suction pumps and found the approaches from Stepanoff [42], Gopalakrishnan [15] and Cohrs [7] to be making predictions with a tolerance band of ±10%.

In general the predictions methods should be considered only as precursor to the PAT study and should not be taken as reference or benchmark during the critical design and application considerations.

B2 Application of Cavitation Study

B2.1 Draft Tube and Cavitation Summary of Tested PATs

It is seen for the application of the CSHN analysis (in section 2.5.2.2, Chapter 2) it is required to know the details of the general boundary condition governing the draft tubes used for the various tested PATs. The requirements for the evaluation of CSHN as seen from Equation (2.36) other than the speed (N) and discharge (Q) are the impeller reference diameter D, exit reference diameter D_e, exit draft tube diameter D_a, the draft tube coefficient, λ_d. Equations (2.36) and (2.37) from Chapter 2 are recalled once again.

$$CSHN = \frac{1}{N^2 D^2}\left[\left(\frac{1}{D_a^4} - \frac{1}{D_e^4}\right) \cdot \frac{8 \cdot Q^2}{\pi^2 \cdot g} + \lambda_d \frac{8 \cdot Q^2}{\pi^2 \cdot g \cdot D_e^4}\right] \qquad (2.36)$$

$$CSHN = \frac{Q^2}{N^2 D^2}\left[-\lambda_{VG} + \lambda_d^1\right] \qquad (2.37)$$

Table B2.1 summarizes the various coefficients that determine the CSHN as defined by Equations (2.36) and (2.37). Along with the boundary conditions, the experimentally determined conditions at minimum CSHN and BEP are defined (for results in section 4.1.2, Chapter 4 and section A6, Appendix A) are also summarized in Table B2.1.

Table B2.1, Summary of the boundary conditions and important coefficients for CSHN analysis

Sl. No.	PAT	D	D_e	D_a	λ_d^1	λ_{VG}	z_s	Min. CSHN		BEP Conditions	
		(mm)	(mm)	(mm)			(m)	Q/ND^3	CSHN	Q/ND^3	CSHN
1	24.5 rpm	$\phi258$	$\phi100$	$\phi280$	467	813	1.31	0.137	-0.270	0.117	-0.170
2	35.3 rpm	$\phi206$	$\phi100$	$\phi280$	467	813	1.31	0.181	-0.188	0.15	-0.120
3	36.4 rpm	$\phi174$	$\phi80$	$\phi280$	940.8	2003.2	1.31	0.280	-0.780	0.185	-0.438
4	39.7 rpm	$\phi264$	$\phi150$	$\phi280$	45.3	149.7	1.31	0.240	-0.210	0.2	-0.164
5	45.2 rpm	$\phi200$	$\phi126$	$\phi280$	185.7	314	1.31	0.340	-0.900	0.235	0.110
6	46.4 rpm	$\phi139$	$\phi80$	$\phi280$	940.8	2003.2	1.31	-	-	0.275	-0.400
7	79.1 rpm	$\phi224$	$\phi190$	$\phi280$	26.8	49.9	1.31	0.611	-0.165	0.48	-0.070
8	94.r rpm	$\phi236$	$\phi190$	$\phi280$	26.9	74.6	1.31	0.365 $_{mf}$	-0.047	0.400 $_{mf}$	-0.030

B2.2 Application Problems

There are two levels of application of the cavitation analysis. The first one is with respect to the identical model PAT, but with a different draft tube design. The other application problem is for a new PAT with its own draft tube design. Some of the equations defined in Chapter 2 need to be re-organized appropriately to solve the various problems.

B2.2.1 Model PAT with new Draft Tube Design

The extensive procedure of evaluating the CSHN of a model PAT with a new draft tube design has been presented in section 2.5.2.2.2 of Chapter 2. Equation (2.35) is re-incorporated and modified to Equation (B2.1) as shown below.

$$CSHN_1 = CSHN + \frac{v_e^2(\lambda_{d1} - \lambda_d) + (v_{a1}^2 - v_a^2)}{2g \times (N^2 D^2)} \quad (2.35)$$

$$CSHN_1 = CSHN + \cdot \frac{Q^2}{N^2 D^2}\left[\left(\lambda^1_{d1} - \lambda^1_d\right) + \frac{8}{\pi^2 \cdot g}\left(\frac{1}{D_{a1}^4} - \frac{1}{D_a^4}\right)\right]$$

$$CSHN_1 = CSHN + D^4 \cdot \left[\frac{Q}{ND^3}\right]^2 \cdot \left[\left(\lambda^1_{d1} - \lambda^1_d\right) + \frac{8}{\pi^2 \cdot g}\left(\frac{1}{D_{a1}^4} - \frac{1}{D_a^4}\right)\right] \quad (B2.1)$$

Problem B2.1

The 39.7 rpm PAT is considered for this application problem. The Table B2.2 compares the boundary conditions of the old and new draft tube designs on the considered PAT.

Table B2.2, Summary of the boundary conditions of old and new draft tube designs for the 39.7 rpm PAT

Original Draft Tube		New Draft Tube	
D	ϕ 264 mm	D	ϕ 264 mm
D_e	ϕ150 mm	D_e	ϕ150 mm
D_a	ϕ280 mm	D_{a1}	ϕ360 mm
λ^1_d	45.3	λ^1_{d1}	200.0
λ_{VG}	149.7	λ_{VG1}	168.1
z_s	1.31 m	z_{s1}	4.00 m
Q/ND^3_{BEP}	0.240	Q/ND^3_{BEP}	0.240
$Q/ND^3_{min.\ CSHN}$	0.200	$Q/ND^3_{min.\ CSHN}$	0.200

The next step is to determine the altered values of the CSHN at the two important conditions namely the BEP and minimum CSHN. The new CSHN values are determined from Equation (B2.1) using all the coefficients from Table B2.2 and summarized in Table B2.3.

Table B2.3, CSHN values at BEP and minimum CSHN conditions for problem B2.1

Original Draft Tube (From Sl. No. 4, Table B2.1)		New Draft Tube (From Equation (B2.1))	
CSHN $_{BEP}$	-0.164	CSHN $_{BEP}$	-0.133
Min. CSHN	-0.210	Min. CSHN	-0.165

From the CSHN values at the above to conditions, the critical cavitation behaviour corresponding Dixon's criterion (N_{ss} = 0.63) is summarized in Table B2.4. It is seen that in general (under both conditions) the PAT with the new draft tube design would cavitate at much lower speed compared to that with the original draft tube design. At minimum CSHN condition, the new configuration would have cavitation inception at a speed of 1850 rpm compared to the 2350 rpm for the original configuration.

Table B2.4, Summary of the cavitation behaviours of old and new draft tube design for problem B2.1

Parameters	Original Draft Tube		New Draft Tube	
	BEP	Min. CSHN	BEP	Min. CSHN
$p_e/\rho g$	-3.10 m	-3.26 m	-5.05 m	-5.14 m
N_{cr}	2350 rpm	2170 rpm	1980 rpm	1850 rpm
NPSH $_{cr}$	6.88 m	6.71 m	4.93 m	4.83 m

B2.2.2   New PATs

As mentioned in section 2.4.4.3 of chapter 2, a new PAT is compared with the given series of model PATs (Table B1.1 and B1.2) to essentially find the discharge number at BEP and minimum CSHN conditions. The elaborate procedure followed in section 5.2, Chapter 5 to selection and synthesis the characteristics of a new PAT essentially leads to the determination of the discharge number at the BEP. However the determination of the same discharge number at minimum CSHN conditions may not be straightforward. Nevertheless

useful comparisons between the new PAT and the model PAT machines can be useful in getting an approximate location of the minimum CSHN conditions.

Once these values of discharge numbers are obtained, Equation (2.38), Chapter 2 is reincorporated and with the draft tube boundary conditions of the new PAT, the constants λ^1_d and λ_{VG}, the CSHN can be evaluated by,

$$ \text{CSHN} = \left[\frac{Q}{N \cdot D^3}\right]^2 \left[\lambda^1_d - \lambda_{VG}\right] \times D^4 \qquad (2.38) $$

Problem B2.2

To apply the cavitation analysis on a new PAT, the PAT1 (that is used in the Case Study – Ambootia micro hydro project, Chapter 6) is selected. The characteristics for the PAT1 have already been synthesized in section 6.4.1, Chapter 6. Hence the BEP conditions (Q/ND^3) are also known. It is now necessary to determine the Q/ND^3 at minimum CSHN condition.

It also seen that the PAT1 (from Table 6.6) has a pump specific speed on 20 rpm. The nearest model pump available as seen from Table B2.1 is the 24.5 rpm PAT. It is also observed that the minimum CSHN condition for the 24.5 rpm PAT (Figure A6.1 and Table A6.2, Section A6.1, Appendix A) is found to occur in the overload region.

The 20 rpm PAT has its BEP fixed at a Q/ND^3 of 0.072 (Table 6.10, section 6.4.1, Chapter 6) and the Q/ND^3 for the minimum CSHN condition can be conveniently assumed to be in the range of 0.075 to 0.08.

Table B2.5 summarizes the various boundary conditions for the PAT1's draft tube system. Inputs of these conditions are taken from the analysis of the draft tube 1 in section 6.3.3.1 of Chapter 6.

Table B2.5, Boundary conditions for draft tube in problem B2.2

D	D_e	D_a	λ^1_d	λ_{VG}	z_s	Q/ND^3_{BEP}	$Q/ND^3_{min.\ CSHN}$
ϕ449 mm	ϕ200 mm	ϕ300 mm	21.6	41.4	1.5 m	0.072	0.08

The coefficients from Table B2.5 are substituted in Equation (2.38) to obtain the CSHN both at the BEP and minimum CSHN conditions respectively, which are summarized in Table B2.6.

Table B2.6, CSHN values at BEP and minimum CSHN conditions for problem B2.2

Condition	Value of CSHN
CSHN $_{BEP}$	-0.004
Min. CSHN	-0.005

With CSHN values for the above conditions the critical cavitation conditions from the availability criterion can be evaluated. The Table B2.7 summarizes the cavitation parameters at minimum CSHN and BEP conditions respectively. It is seen that PAT1 would reach critical conditions (From Dixon's criterion, i.e. N_{ss}=0.63, section 2.5.1, Chapter 2) of cavitation at speed of 2070 rpm with a NPSH of 8.35 m, when operated at the minimum CSHN conditions (i.e. at Q/ND^3 = 0.080). The normal operating speed of PAT1 is 1260 rpm (step 9, section 6.4.1, Chapter 6), which is no way near the critical cavitation conditions.

Table B2.7, Summary of the cavitation behaviours for PAT1 in problem B2.1

Condition	ϕ Q/ND^3	CSHN	N_{ss} (From Dixon)	N_{cr} (rpm)	NPSH$_{cr}$ (m)
BEP	0.072	-0.004	0.63	2130	8.37
Min. CSHN	0.080	-0.005	0.63	2070	8.35

B3   CFD Model and Analysis

B3.1   Numerical Means of Solution – CFD

It has been mentioned in the introductory section of Chapter 3 that Computational Fluid Dynamics, CFD, is another possible means of solutions to the identified problem regarding the optimization of the internal hydraulics within a PAT control volume (section 1.3.1, Chapter 1). In addition to this another important workout is to compare the results from the CFD and experimental methods at identical geometrical conditions of the given PATs. The objective of these comparisons is to calibrate the CFD model to make accurate predictions of hydraulic conditions in PATs under different optimization stages. This eventually helps in making recommendation for the different geometric modifications on the PAT to get required performance alleviation.

An accurate CFD model has many advantages over the experimental means. The model not only evaluates the global variables (as described in section 3.1.2, Chapter 3), but also determines the pressure losses in various flow zones of the PAT control volume. As seen (from considerations in Chapter 2) the internal zone losses have a great significance in understanding the hydraulic phenomenon and also more importantly give direction to the performance optimization.

It is also observed in the experimental optimization study (section 3.1.3.1, Chapter 3), which has been based on the theoretical considerations (section 2.2.2, Chapter 2), is only helpful is giving the trend regarding the change in the magnitude of hydraulic losses but fails determine its absolute value.

B3.1.1   Introduction

There have been only 3 PATs that have been tested through the CFD approach (as mentioned in the introductory section of Chapter 3), that are summarized in Table B3.1 along with details of the corresponding test stages, implementing agencies and the references.

Table B3.1, Reference details of the PATs analyzed through the CFD model

Sl. No.	PAT	Stage No.	Test Stage	Implementing Agency	Reference
1	24.5 rpm PAT	1	Non-modified	Nottingham Trent University	Rodrigues et al[41]
2	35.3 rpm PAT	1	Non-modified	Kirloskar Brothers Limited	Singh et al[49] and Kirloskar [25]
3	39.7 rpm PAT	1	Casing rib present	Kirloskar Brothers Limited]	Singh et al[46]
		2	Casing rib absent		

It is seen from Table B3.1 that the 24.5 rpm and the 35.3 rpm PATs have been analyzed only at the non-modified stage, while the 39.7 rpm PAT has been essentially analyzed for the optimization stage IV, i.e. absence of casing eye rib (section 2.4.4, Chapter 2).

Table B3.2 summarizes the complete the modeling, the geometry and boundary conditions employed for different PATs.

B3.1.2   Mathematical Model

The flow through all the 3 PATs has been simulated through the commercial code CFX 5.0, which incorporates the 3-D incompressible Reynolds-averaged Navier-Stokes equations. The standard K-ε turbulence model along with log-law distribution for wall is commonly used for all test specimens. However there are few differences with respect to the schemes incorporated for convergence of computational results.

B3.1.3   Geometric Model and Grid

The entire geometry comprising of all the seven zones (only hydraulic passages), beginning from the inlet measurement plane till the draft tube exit (explained in section 2.1, Chapter 2) has been modeled for all the PATs. The axial clearances, X_A (shown in Figure A4.3, section A4.1, Appendix A) existing in radial flow PATs are not considered in the geometric construction. This effectively means that the hydraulics between the outer shroud surface (both front and back shrouds) and the casing surfaces along with the leakage flow through the wear ring and the seal is essentially neglected.

The total size of the grid for the tested PATs has been summarized in Table B3.2. Due to the periodicity characteristics of the impeller only a single blade passage has been modeled.

B3.1.4   Boundary Conditions

The boundary conditions used for the 3 PATs have a slight variance that has been pointed on in Table B3.2. For the 35.3 rpm and the 39.7 rpm, the boundary conditions comprise of the total pressure at the inlet measurement plane (Figure 2.1, Chapter 2) and the mass flow rate at the exit of the draft tube. The application of boundary conditions for the 24.5 rpm PAT has been reversed with mass flow rate specified at the inlet measurement plane and atmospheric pressure at the draft tube exit. (zone *vii* of Figure 2.3, Chapter 2).

The simulations are carried out at the identical load point from the experimental study. The variables that are transferred from experimental measurements are the discharge (or mass flow rate) and operating speed (N). The discharge used here is the net discharge across the PAT control volume without any considerations for leakage flow. The CFD model then

essentially evaluates the net head (H) across the inlet and exit measurement planes and the hydraulic output torque (T).

Table B3.2, Summary of the CFD modeling parameters for the PATs

Sl. No.	PAT	Turbulence model	Grid size	Boundary conditions
1	24.5 rpm PAT	K-ε model	400000 nodes	Mass flow rate at PAT inlet and atmospheric pressure at draft tube exit
2	35.3 rpm PAT	K-ε model	500000 nodes	Total pressure at PAT inlet and mass flow rate at the draft tube exit
3	39.7 rpm PAT	K-ε model	910000 nodes	Total pressure at PAT inlet and mass flow rate at the draft tube exit

B3.1.5　　Methodology of Analysis

The methodology of the CFD analysis comprises of,

i. Analyzing the performance characteristics of a given PAT based on global variables for the 24.5 rpm, 35.3 rpm and 39.7 rpm PAT.

ii. Analyzing the optimization stage IV on the 39.7 rpm PAT

iii. Evaluating the internal variables (as in section 3.1.3.2, Chapter 3) for 39.7 rpm PAT.

B3.1.5.1　　Performance of Characteristics of given PAT

The methodology of the CFD analysis at any stage consists of essentially two sections namely,

i. The zonal loss distribution

This section studies the losses within three regions of the PAT control volume, i.e. the zone *i-ii*, zone *iii-iv-v* and zone *vi* in the entire operating range.

ii. Overall performance characteristics

The global variables that are simulated from the CFD model, namely the net head (H) and the hydraulic output torque (T) along with the given variables of discharge (Q) and speed (N) are used to evaluate the various dimensionless numbers (in section 2.2, Equations (2.1), (2.2) and (2.3), Chapter 2) and plotted to obtain the overall dimensionless characteristics.

It is to be noted that the CFD evaluates the hydraulic torque, hence the efficiency defined by Equation (3.1) (Chapter 3) needs to be altered.

$$\eta_{hyd} = \frac{2\pi N T_{hyd}/60}{\rho g Q H} \qquad (B3.1)$$

B3.1.5.2 Optimization Study

This study is essentially based on the procedure detailed out in section 3.1.3.1, Chapter 3. The optimization study, as always, includes the comparison of the overall dimensionless characteristics between the two test stages and also the analysis through the 'percentage analysis plot'.

B3.1.5.3 Internal Performance Study

The methodology of the internal performance study from CFD is essentially identical to the methodology listed in section 3.1.3.2 of Chapter 3. In addition to the swirl (θ) profiles it also looks into the evidence of the presence of a radial flow (δ) component at the PAT exit. The radial component had been categorically neglected for simplifying the experimental analysis in section A1, Appendix A.

B3.2 CFD Results

B3.2.1 24.5 rpm PAT

B3.2.1.1 Zonal Loss Distribution

The internal loss distribution is plotted in <u>Figure B3.1</u> and summarized in <u>Table B3.3</u> for a constant speed of 800 rpm of the PAT. It is seen that the losses in zone *i* (volute casing) show a steady increase with discharge except for a discontinuity beginning from 26.1 l/s and higher flows. The contribution of this loss component is quite considerable throughout the operating range, 30% to 40% of the total control volume losses in the BEP and overload regions. The losses in zone *ii* (radial clearance) follow a parabolic trend with lowest value in the part-load region. This loss component increases towards the BEP-overload points and are in the range of 10% to 20% of the total control volume losses.

The losses of the impeller zone (*iii*, *iv* and *v*) form a major portion of the losses and also follow a parabolic trend. It is to be pointed out that the minimum impeller losses occur in the beginning of the part-load region only. Within the BEP and overload region the impeller control volume losses represents 40% to 45% of the total losses. However the most

significant loss pattern is that of zone *vi*. While these losses form over 50% to 60% of the total losses in the part-load region, it becomes barely negligible in the BEP region. The zone *vi* losses could be associated to the swirl flow, which is found to be predominant in the part-load region and less dominating in the BEP and overload region (as seen in section 4.1.1.4, Chapter 4).
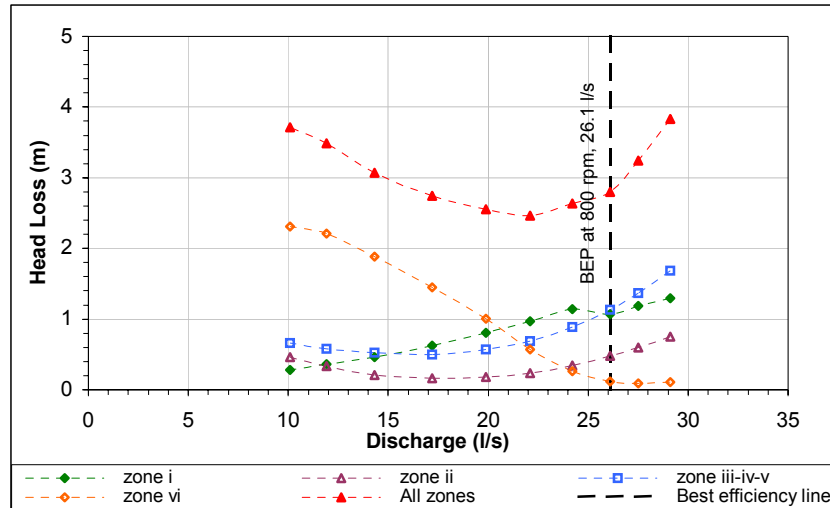
Figure B3.1, Distribution of losses (absolute) in the control volume of the 24.5 rpm PAT

Table B3.3, Distribution of losses (percentage) in the control volume of the 24.5 rpm PAT

Discharge (l/s)	zone *i*	zone *ii*	zone *iii-iv-v*	zone *vi*
29.1	34%	20%	44%	3%
27.5	36%	19%	42%	3%
26.1	38%	17%	40%	4%
24.2	43%	13%	34%	10%
22.1	39%	10%	28%	23%
19.9	32%	7%	22%	39%
17.2	23%	6%	18%	53%
14.3	15%	7%	17%	61%
11.9	10%	10%	17%	63%
10.1	8%	12%	18%	62%

B3.2.1.2   Overall Performance Characteristics

Figure B3.2 summarized the head number, power number (hydraulic output) and efficiency characteristics at 10 load points at constant operating speed of 800 rpm. The fitting and continuity of various data points are relatively good. The BEP obtained from the CFD model occurs at a discharge number, ϕ = 0.108, is defined in Table B3.4.

Table B3.4, The BEP point for the 24.5 rpm PAT as defined by CFD

Parameter	Value
Q/ND^3	0.108
gH/N^2D^2	9.601
$P_{hyd}/\rho N^3D^5$	0.806
η_{hyd}	77.7%
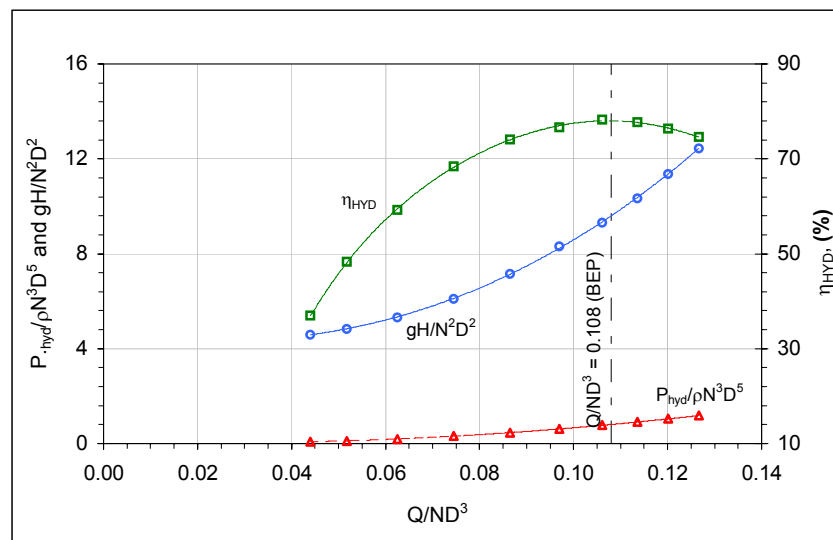
Figure B3.2, Complete dimensionless characteristics for the 24.5 rpm PAT using CFD

B3.2.2   35.3 rpm PAT

B3.2.2.1   Zonal Loss Distribution

For the 35.3 rpm PAT, only 5 load points have been analyzed covering the main operating region at constant operating speed at 1000 rpm. The loss patterns of various zones along with the BEP line (at a discharge of 27 l/s) are plotted in Figure B3.3. The distribution of the

losses is summarized in Table B3.5. In the CFD model the loss components in zone *i* and *ii* have not been separated out. It is seen that losses in zone *i-ii* continuously increases with discharge and forms around 30% of the total control volume losses in the BEP region. The impeller losses (zone *iii*, *iv* and *v*) on the other hand forms a considerable portion of the total loss, which is in the range of 55% to 65% at all tested loads. The impeller losses have a minimum value for part-load flows (between 18 l/s and 20 l/s) and subsequently these losses increase exponentially with higher discharges.

The zone *vi* losses are greater only in the part-load and overload regions forming a trough in the vicinity of the BEP region (which is also attributed to swirl flow behaviour). This component forms a relatively small component of the total loss, 15% to 25% in the part-load region and 8% to15% in the BEP and overload region.
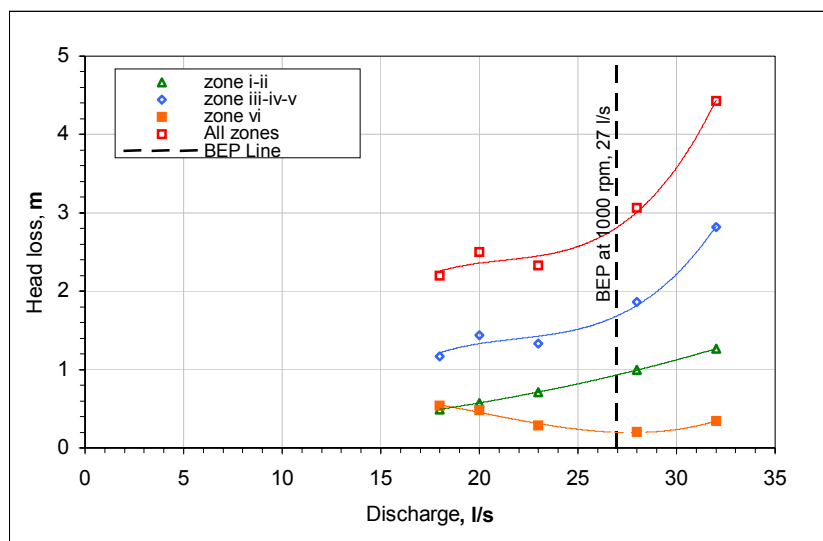
Figure B3.3, Distribution of losses (absolute) in the control volume of the 35.3 rpm PAT

Table B3.5, Distribution of losses (percentage) in the control volume of the 35.3 rpm PAT

Discharge (l/s)	zone *i-ii*	zone *iii-iv-v*	zone *vi*
18	22%	53%	24%
20	26%	65%	22%
23	32%	61%	13%
28	45%	85%	9%
32	58%	128%	15%

B3.2.2.2   Overall Performance Characteristics

The overall dimensionless characteristics are plotted in <u>Figure B3.4</u>, where the data points show a reasonable fitting. The BEP is found to occur at ϕ = 0.185 and the other parameters are summarized in <u>Table B3.6</u>.

<u>Table B3.6</u>, The BEP point for the 35.3 rpm PAT as defined by CFD

Parameter	Value
Q/ND^3	0.185
gH/N^2D^2	10.278
$P_{hyd}/\rho N^3 D^5$	1.445
η_{hyd}	76.0%
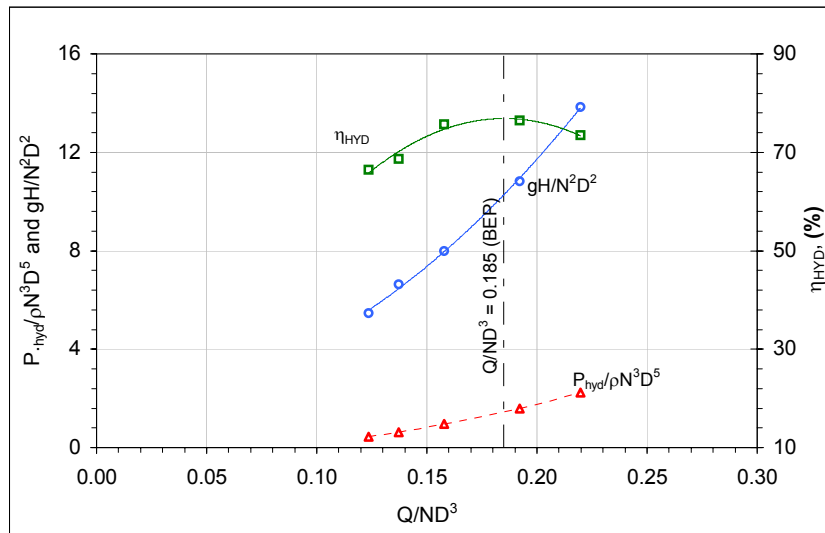
<u>Figure B3.4</u>, Complete dimensionless characteristics for the 35.3 rpm PAT using CFD

B3.2.3 39.7 rpm PAT

B3.2.3.1 Casing Rib Present Stage

B3.2.3.1.1 Zonal Loss Distribution

The distribution of losses within the various zones of the PAT control volume are plotted in <u>Figure B3.5</u> and summarized in <u>Table B3.7</u>. Five load points within the main load region are analyzed using the CFD model at constant operating speed of 800 rpm. The losses in zone *i* and *ii* increases continuously with flow and forms 40% to 45% of the total losses at the BEP and overload region.

The impeller (zone *iii*, *iv* and *v*) losses are found to be constant for discharges of 34 l/s and 42.3 l/s but then steeply rise in the BEP–overload region. This loss components forms nearly 50% of the control volume losses at all load points. The losses in zone *vi* forms the smallest component of all the losses, which is in the range of 10% to 15% of total losses in part-load and reduces to 7% in the BEP/overload regions. It also displays a characteristic increasing trend in the part-load and overload regions only.
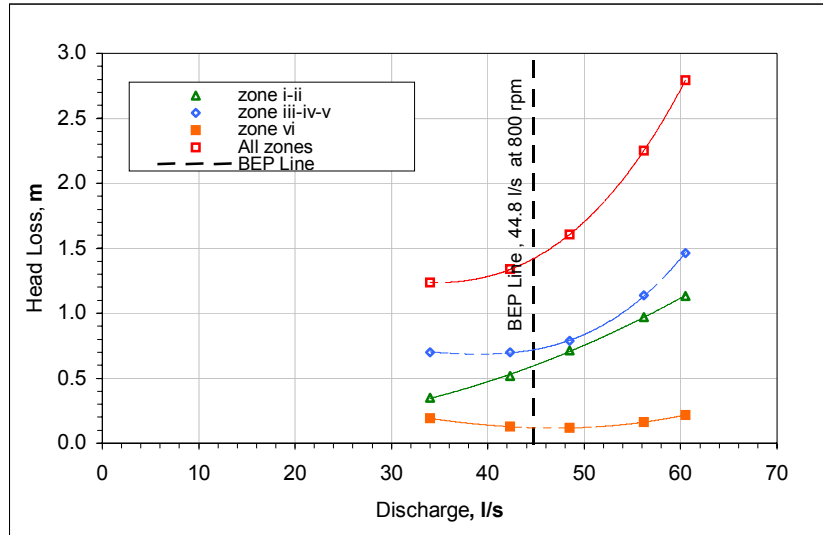
Figure B3.5, Distribution of losses (absolute) in the control volume of the 39.7 rpm PAT (CRP stage)

Table B3.7, Distribution of losses (percentage) in the control volume of the 39.7 rpm PAT (CRP stage)

Discharge (l/s)	Zone *i-ii*	zone *iii-iv-v*	zone *vi*
34	28%	57%	15%
42.3	39%	52%	10%
48.5	45%	49%	7%
56.2	43%	50%	7%
60.5	41%	52%	8%

B3.2.3.1.2   Overall Performance Characteristics

The dimensionless characteristics obtained from the CFD model is plotted in Figure B3.6. The BEP is found occur at ϕ = 0.1825 and the other parameters listed in Table B3.8.

Table B3.8, The BEP point for the 39.7 rpm PAT (CRP stage) as defined by CFD

Parameter	Value
Q/ND^3	0.1825
gH/N^2D^2	6.203
$P_{hyd}/\rho N^3D^5$	0.928
η_{hyd}	82.0%
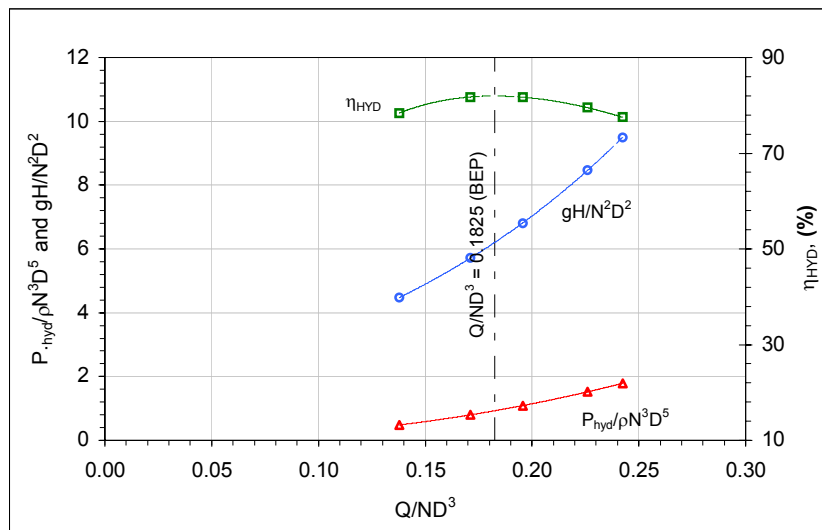
Figure B3.6, Complete dimensionless characteristics for the 39.7 rpm PAT (CRP stage) using CFD

B3.2.3.2   Casing Rib Absent Stage

B3.2.3.1.1   Zonal Loss Distribution

As seen from the loss distribution plot in Figure B3.7 and Table B3.9 the casing and the impeller loss component for this stage follows the similar trend as that of the CRP stage (Figure B3.6). However the losses in zone *vi* of the CRA stage show a substantial reduction. In the CRA stage this forms only 3.5% to 4% in the BEP/overload region as to 7% to 8% in the CRP stage.
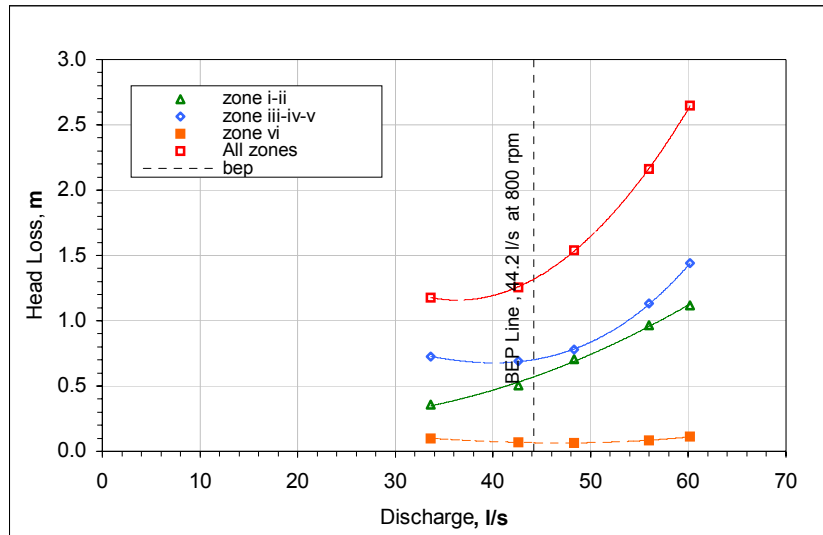
Figure B3.7, Distribution of losses (absolute) in the control volume of the 39.7 rpm PAT (CRA stage)

Table B3.9, Distribution of losses (percentage) in the control volume of the 39.7 rpm PAT (CRA stage)

Discharge (l/s)	zone *i-ii*	zone *iii-iv-v*	zone *vi*
33.6	30%	62%	9%
42.6	40%	55%	5%
48.3	46%	51%	4%
56.0	45%	52%	4%
60.2	42%	54%	4%

B3.2.3.1.2   Overall Performance Characteristics

The dimensionless characteristics are plotted in Figure B3.8 with BEP found to occur at a discharge number, ϕ = 0.180. Table B3.10 summarizes the other parameters at BEP.
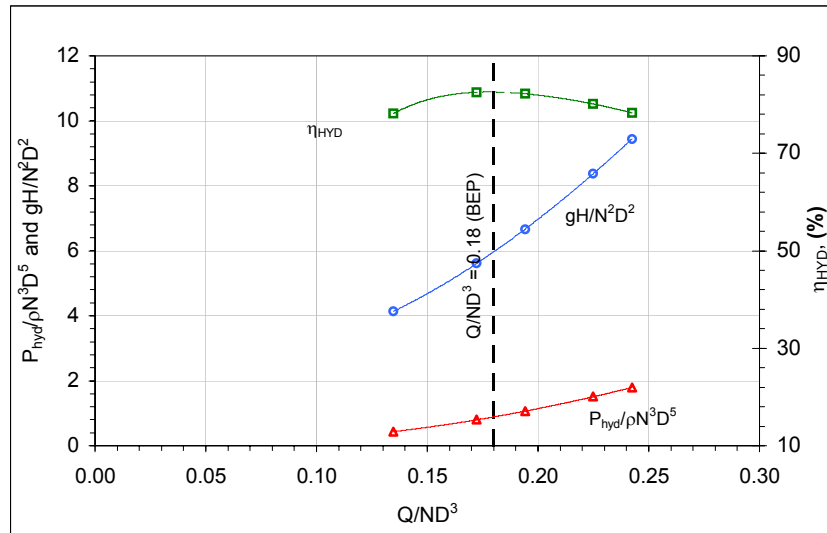
<u>Figure B3.8</u>, Complete dimensionless characteristics for the 39.7 rpm PAT (CRA stage) using CFD

<u>Table B3.10</u>, The BEP point for the 39.7 rpm PAT (CRA stage) as defined by CFD

Parameter	Value
Q/ND^3	0.180
gH/N^2D^2	5.965
$P_{hyd}/\rho N^3D^5$	0.887
η_{hyd}	82.6%

B3.2.3.3   Internal Performance of CRP and CRA stages

The internal performance or swirl flow analysis for the CRP and CRA stage is carried out at identical points defined in section 4.1.1.4.1.2, Chapter 4. The CFD studies revealed radial components of velocity within the cross-section, which has been categorically neglected throughout the experimental study. <u>Figure B3.9</u> and <u>B3.10</u> describe the plot of radial flow angle for the CRP and CRA stages. It is found that within the core of the cross-section there are large values of radial angles. However in the main flow region, the radial flow angle is very marginal, which stays essentially less than 5^0.
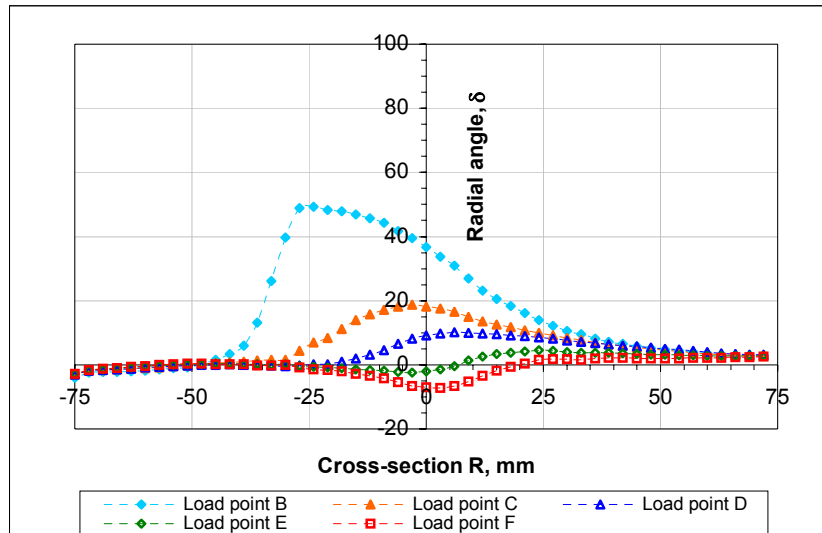
Figure B3.9, Radial angle profiles for the CRP stage on the 39.7 rpm PAT
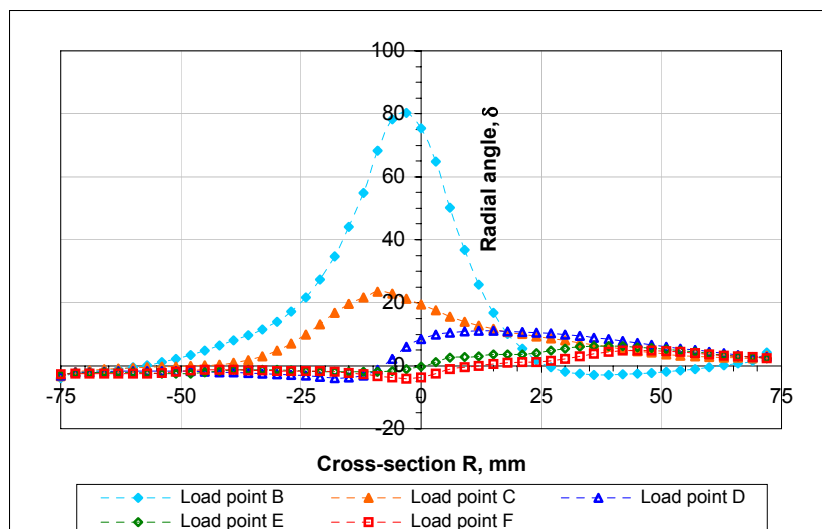
Figure B3.10, Radial angle profiles for the CRA stage on the 39.7 rpm PAT

The swirl profiles of the CRP stage in Figure B3.11 show a marginal symmetry across the mean axis. The BEP swirl profile displays a characteristic swirl reversal within the core of the cross-section, but is still not symmetric across the central axis. All the other overload profiles (load E and F) exhibit positive wall swirl, but within the main flow region the swirl direction gets reversed.
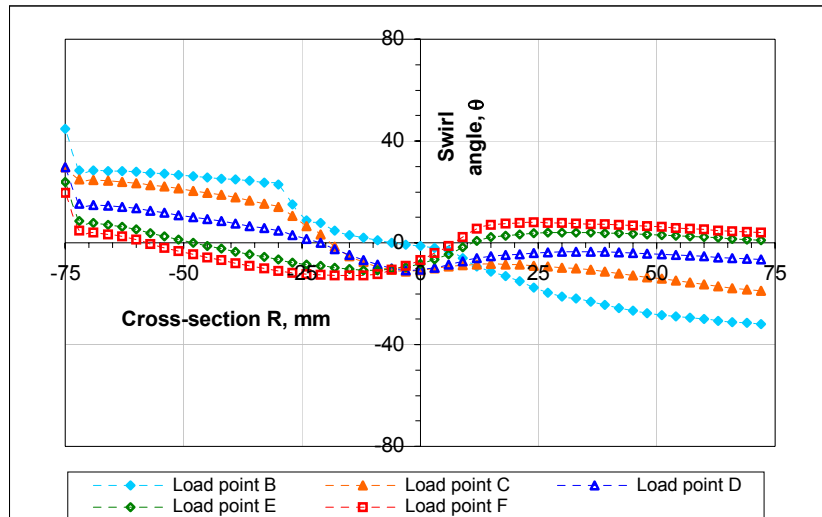
Figure B3.11, Swirl profiles for the CRP stage on the 39.7 rpm PAT

The swirl angle profiles for the CRA stage in Figure B3.12 on the other hand exhibits magnified swirls a corresponding points throughout the cross-section compared to the CRA stage. The symmetry of the profiles for load C and D are not very good. However there is an improvement of the symmetry for profiles B, E and F.
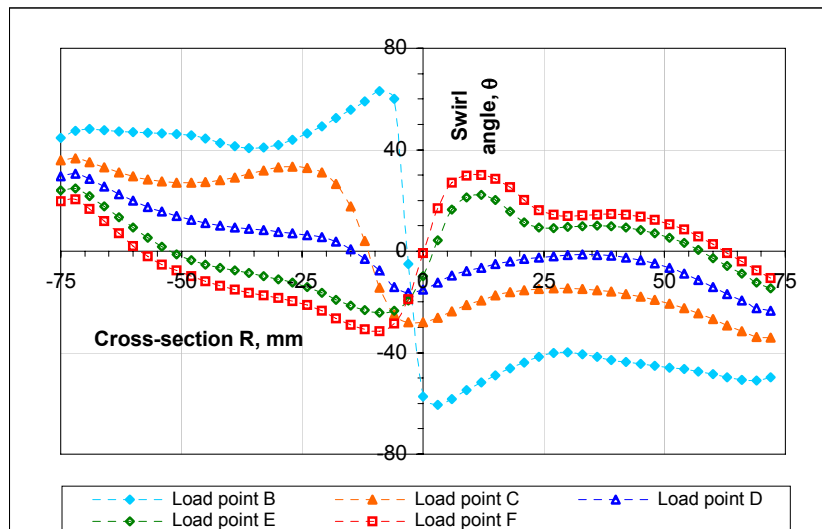
Figure B3.12, Swirl profiles for the CRA stage on the 39.7 rpm PAT

B3.2.3.4   Optimization Stage IV – CFD Perspective

The dimensionless characteristics for the two stages are plotted in Figure B3.13, where it is seen that the head number for the CRA stage have fallen below that of the CRP stage throughout the operating range with magnified effects of the head reduction restricted only to

the part-load and BEP range. In the overload region only a marginal head reduction is recorded. The power characteristics for the CRA stage on the other hand show decreased generation in the part-load and BEP regions. In the overload region there is evidence of a very slight rise in the power number values for CRA stage.
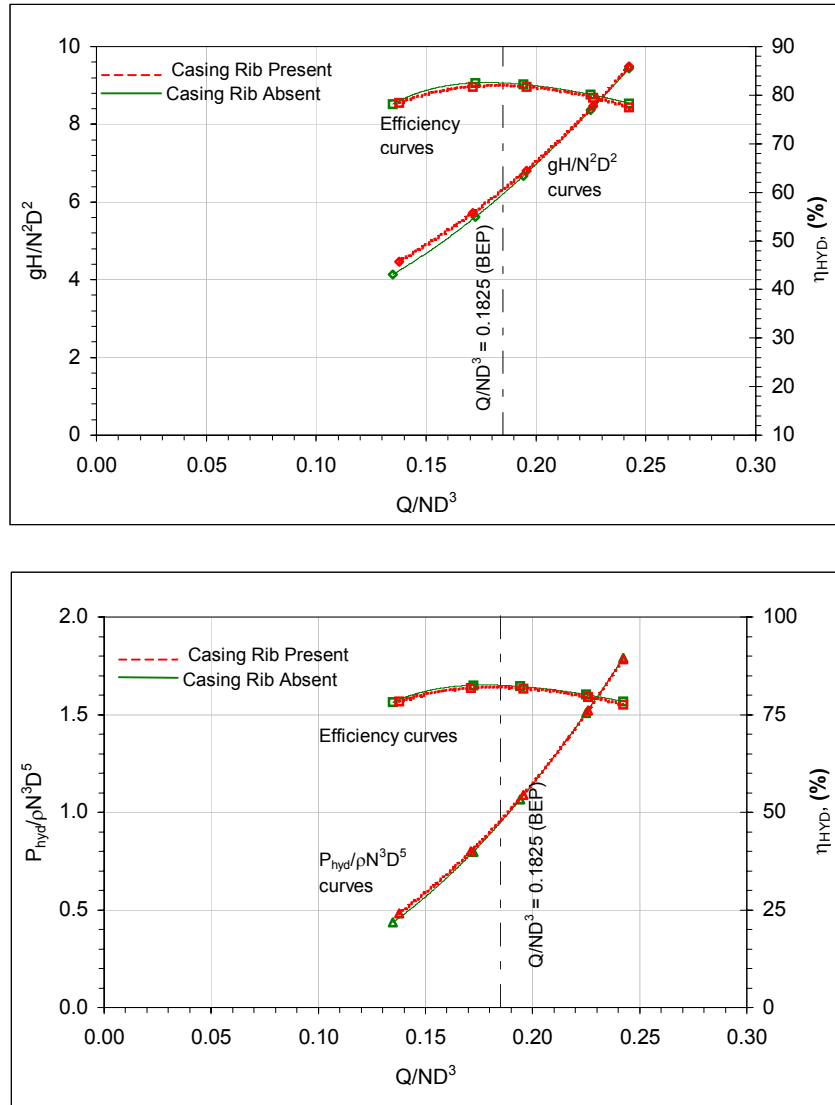
Figure B3.13, Comparisons of dimensionless characteristics for Optimization Stage IV on the 39.7 rpm PAT using CFD

The net efficiency resulting from the behaviour of the head number and power number is slightly improved for the CRA stage. The BEP analysis for the two stages is carried out in Table B3.11 at ϕ = 0.1825, where it is seen that the CRA head number drops from 6.203 units to 6.085 units, while power number increases from 0.928 to 0.917 units resulting in an efficiency rise from 82.0% to 82.6%.

Table B3.11, BEP summary for two stages of Optimization Stage IV on the 39.7 rpm PAT using CFD

Stage	ϕ	ψ	**p**	η
Casing Rib Present	0.1825	6.203	0.928	82.0%
Casing Rib Absent	0.1825	6.085	0.917	82.6%

The percentage analysis chart of Figure B3.14 shows that within the CRA stage there is decreased power generation in the part-load region (-5% to -0.5%). However improvement line becomes positive in the overload region with a marginal power rise of +0% to +0.4%. The head reduction line on the other hand is positive throughout the operating range considered with gains of 5% at the part-load line, while the reduction drops to 2% to 1.5% in the BEP region. The head reduction falls to a minimum of +0.3% in the overload region before it starts to rise again in the range of +1% to +1.5%. Owing to the stronger influence of the head reduction the efficiency rise curve is positive throughout with a consistent rise of 0.5% to 0.8%.

The relative influence of head and power parameters at the part-load, BEP and overload lines are summarized in Table B3.10.
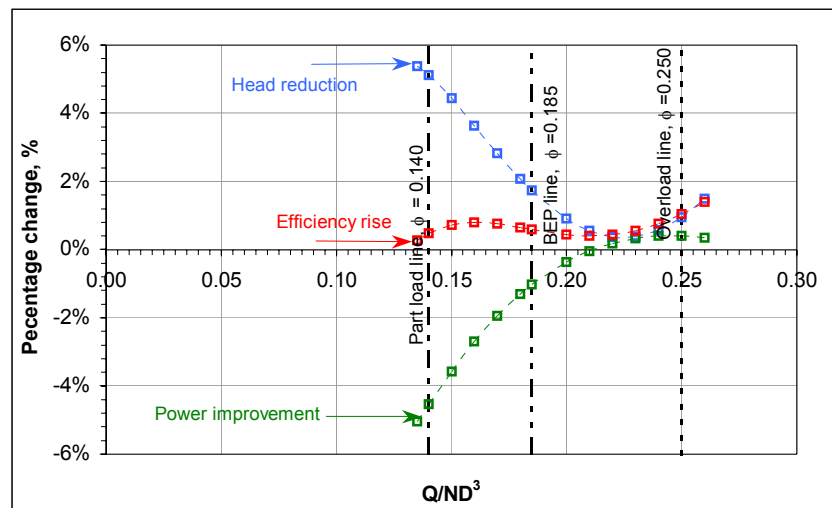
Figure B3.14, Percentage Analysis Plot for Optimization Stage IV on 46.4 rpm PAT using CFD

Table B3.12, Relative study at part-load, BEP and overload lines for Optimization Stage IV on the 39.7 rpm PAT using CFD

	Part-load line $\phi = 0.140$	BEP line $\phi = 0.200$	Overload line $\phi = 0.250$
Head reduction	+5.1%	+0.9%	+0.9%
Power improvement	-4.5%	-0.4%	+0.4%
Efficiency rise	+0.5%	+0.4%	+1.0%

Discussion of Results on the 39.7 rpm PAT

The decrease of the CRA power in the part-load and BEP region can imply either a decrease of the net rotational momentum across the impeller or increase of losses in the impeller control volume. Corresponding to this range there is a decrease of the head number for the CRA stage, which signifies drop of control volume losses or drop of rotational momentum. Though it is certain that zone *vi* losses have slightly decreased, the behaviour of the two parameters only suggest that the net rotational momentum across the PAT should be lowered for the CRA stage. The momentum effects associated with swirl are found to be highest in the part-load and overload regions.

However within the BEP and overload region, there is an increase of power, which could be resulting from the combination of the decreased net rotational momentum and increased drop of losses within the impeller zone. Also it is seen that the head reduction curve falls to a minimum, which suggests that the influence of rotational momentum have become negligible in this region. Therefore only positive effects from the impeller zone are present, which get added to the head reduction curve. Its not very clear about the behaviour of the losses in zone *vi* in this identical operating range, however the head reduction patterns suggest no changes to the distribution of losses in this zone.

Deep in the overload region, the head reduction rises continuously, which can imply a combination of positive impeller effects, decrease of losses in zone *vi* and also a decrease of net rotational momentum.

Internal Performance Comparison

The swirl profiles predicted from the CFD model for the CRP and CRA stages are compared at loads B, D and F in Figure B3.15. As expected the swirl profiles for the CRA stage are excessive in comparison to the CRP stage at part-load point B in the range of 15^0 within the main flow region of the cross-section and to about 60^0 in the core. The BEP load profiles (point D) for the two stages are more or less similar but there are regions where CRA stage exhibits slightly greater swirl. The swirl comparisons at the overload point F, also clearly

show that the CRA stage has excessive swirls in the range of 5^0 to 25^0 throughout the cross-section.

The overall performance comparison in Figure B3.13 and B3.14 revealed that the rotational momentum effects are highest only within the part-load regions and BEP region, with reduced power and reduced net head patterns. But within the BEP and overload line the overall performance comparisons revealed little influence of rotational momentum effects. The internal comparison showed higher swirl (Figure B3.15) or rotational momentum at overload point F (ϕ =0.242), which has not been categorically reflected in the overall performance results at the identical load point (in Figure B3.14). Therefore in the overload region there is a discrepancy between the two approaches.
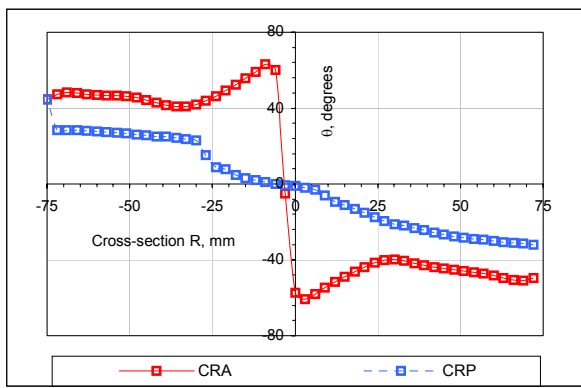
Load B
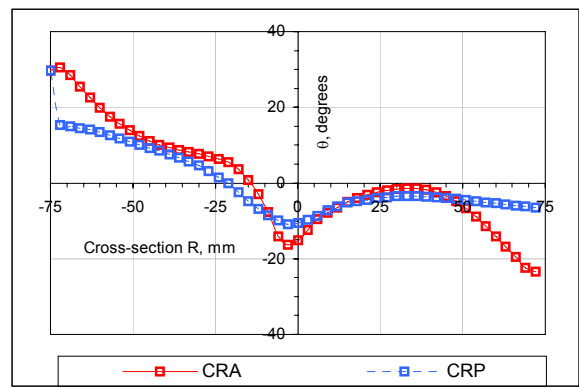
Load D
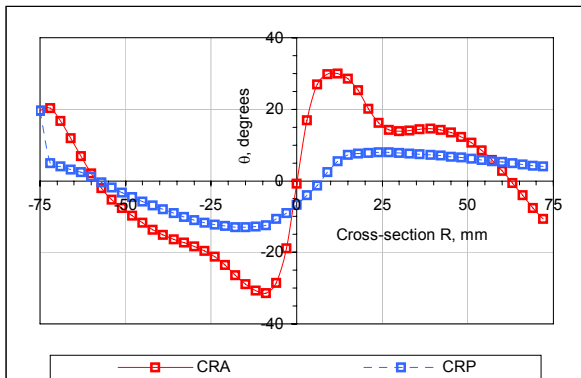
Load F

Figure B3.15, Comparisons of the swirl profiles for the CRP and CRA stage of the 39.7 rpm PAT at load B, D and F using CFD

B4   Muschel Curves for Tested PATs
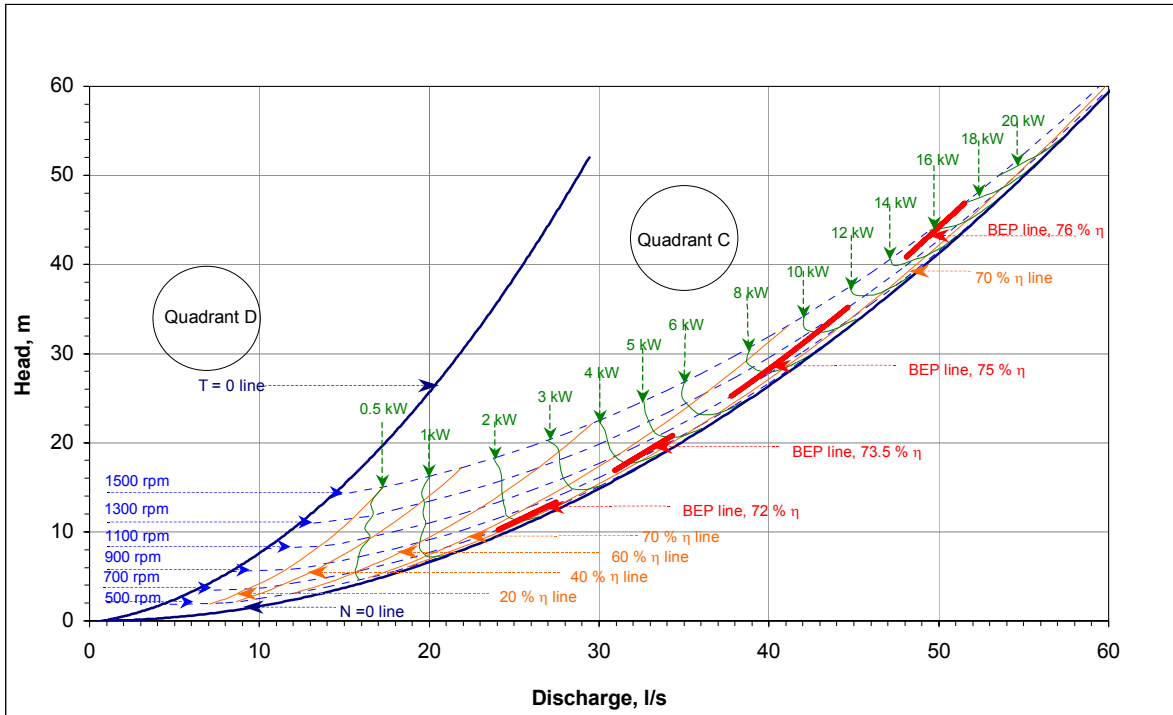
Figure B4.1, Muschel Curves for Inlet Rounded 24.5 rpm PAT
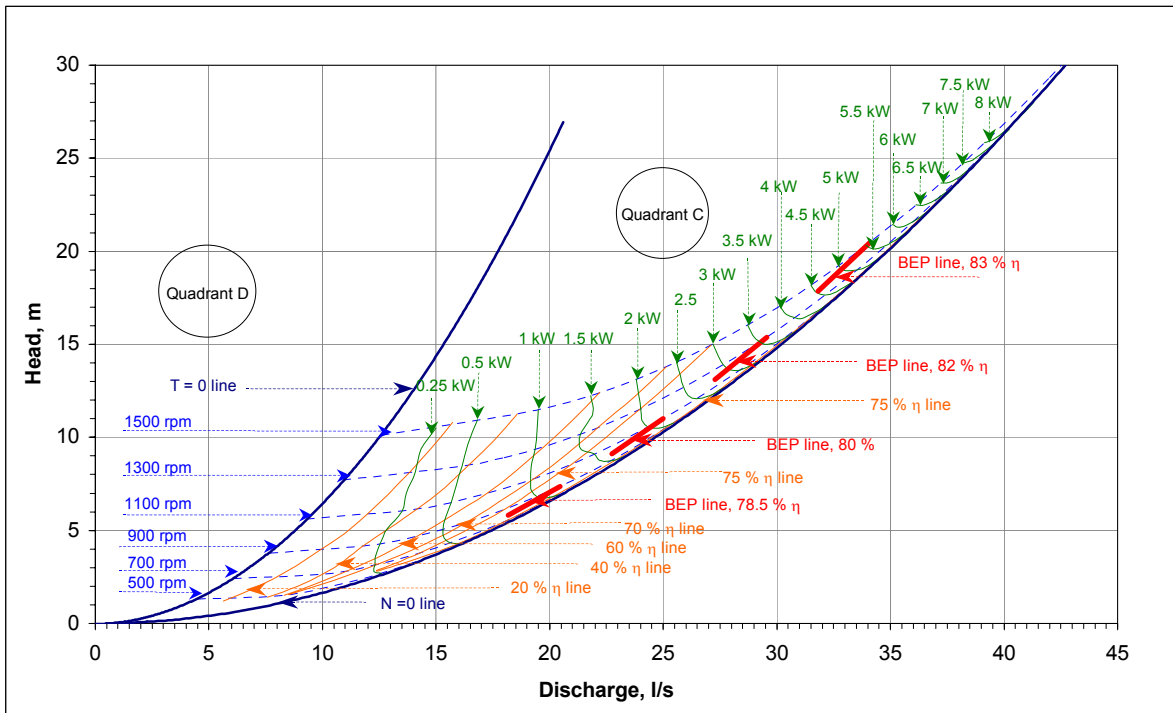
Figure B4.2, Muschel Curves for Inlet Rounded 35.3 rpm PAT
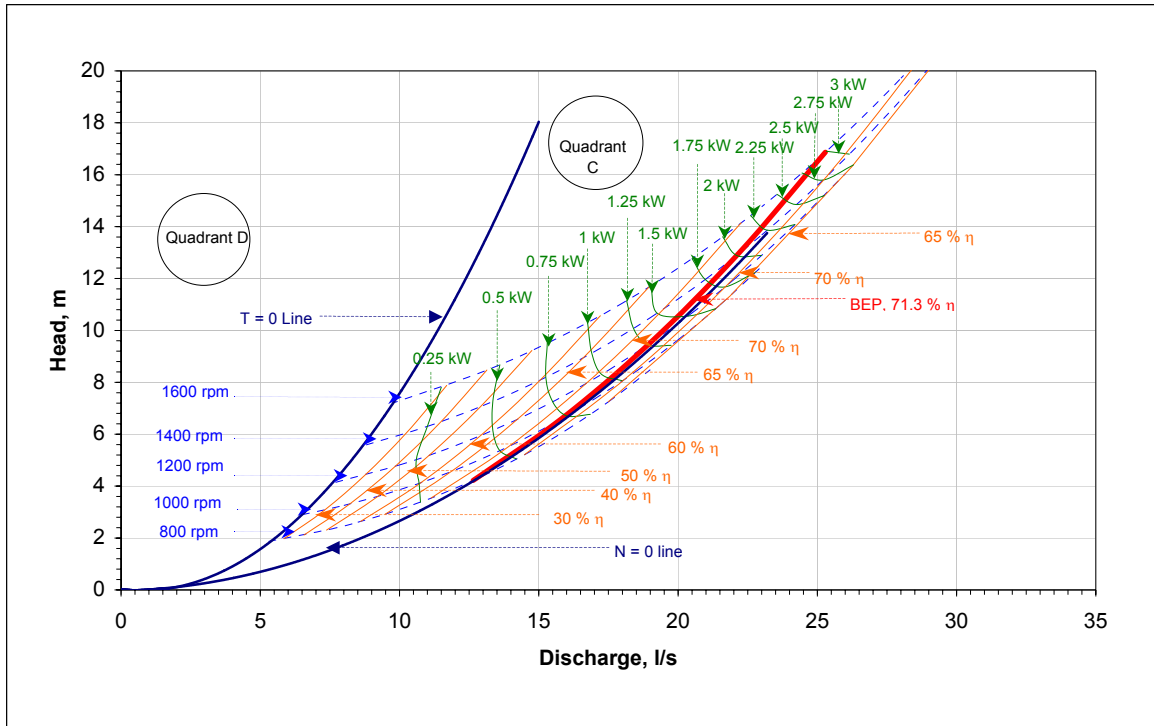
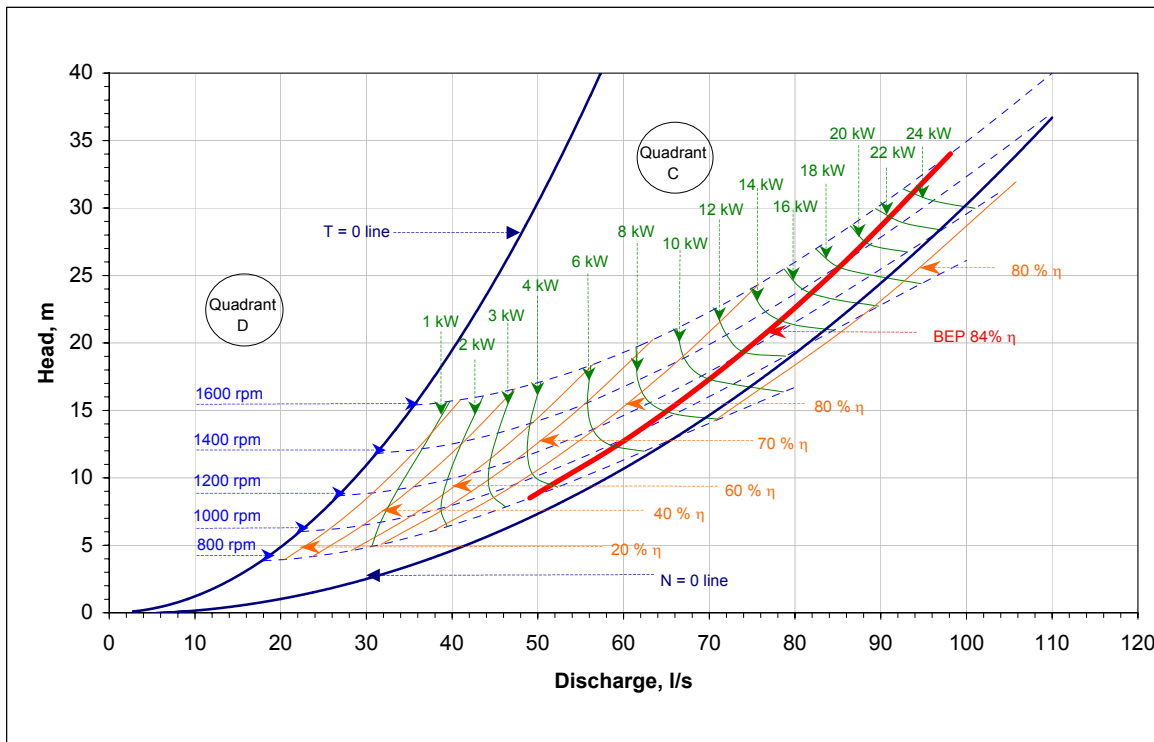Figure B4.3, Muschel Curves for Inlet Rounded 36.4 rpm PAT

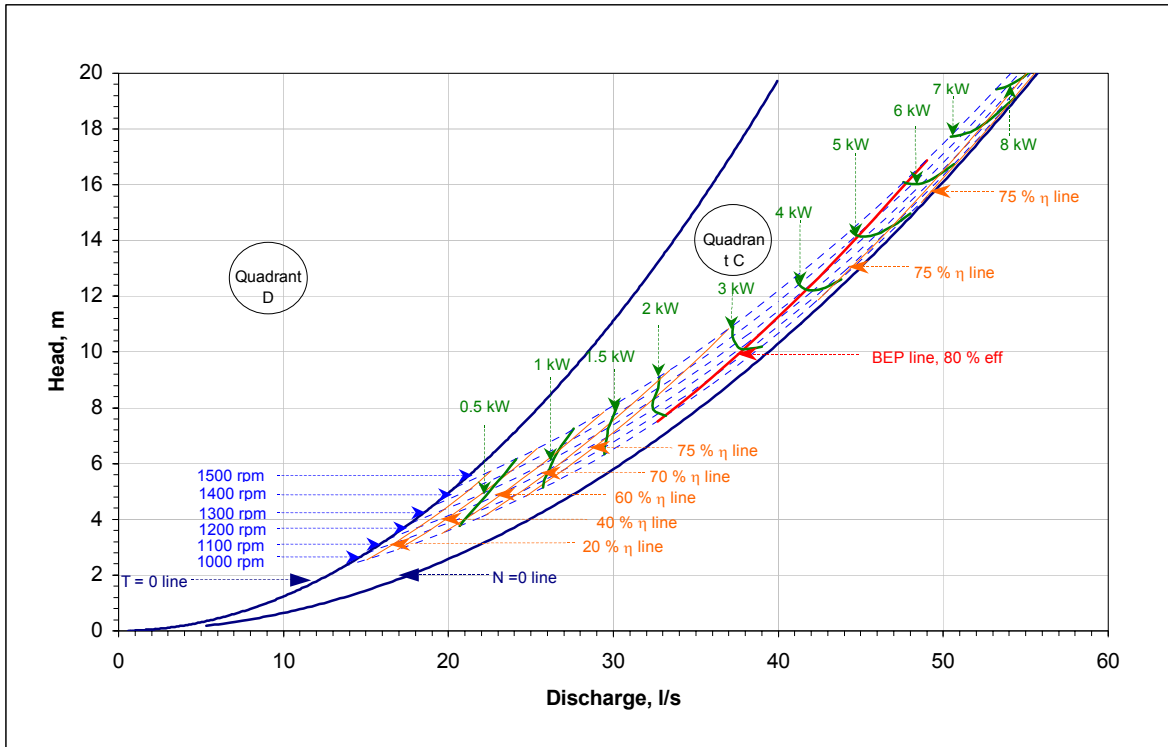Figure B4.4, Muschel Curves for Inlet Rounded 39.7 rpm PAT

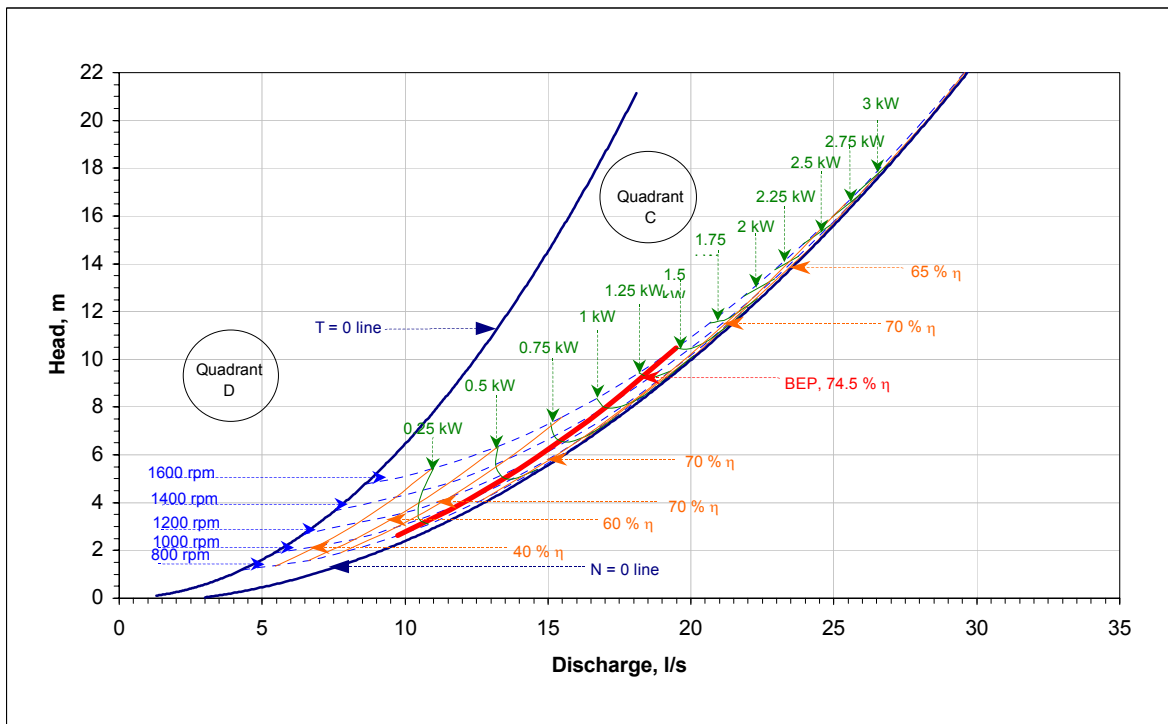Figure B4.5, Muschel Curves for Inlet Rounded 45.2 rpm PAT

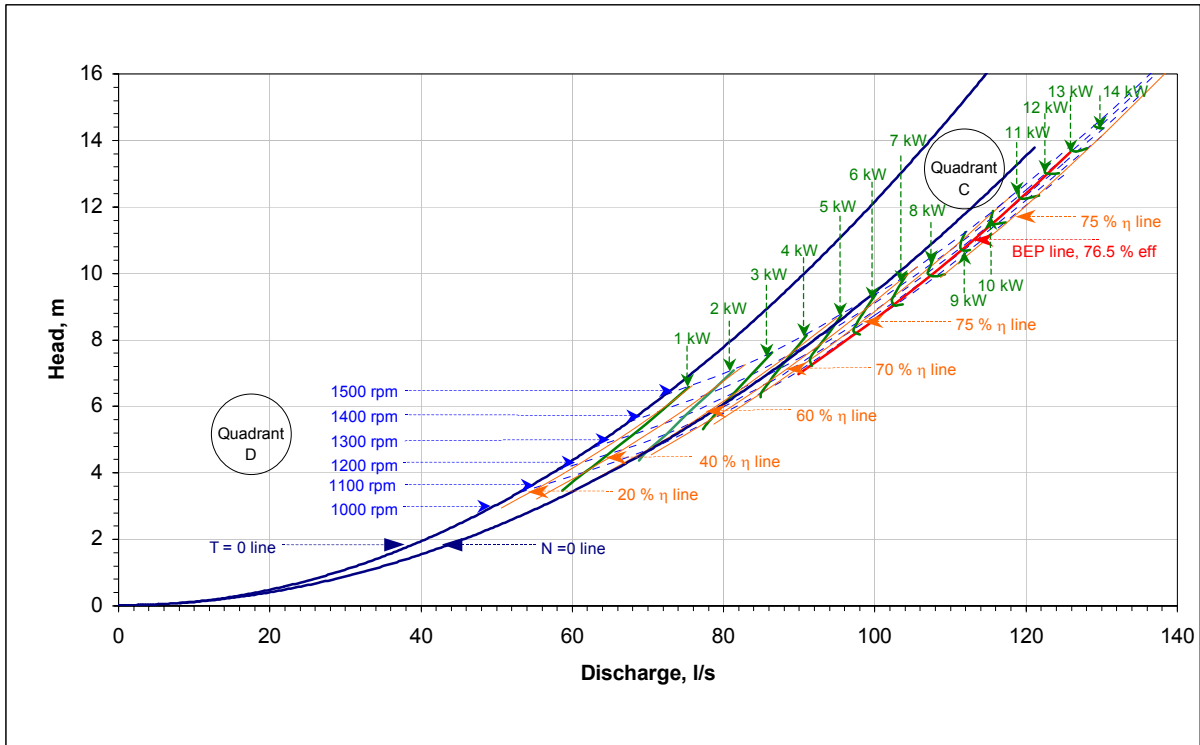Figure B4.6, Muschel Curves for Inlet Rounded 46.4 rpm PAT

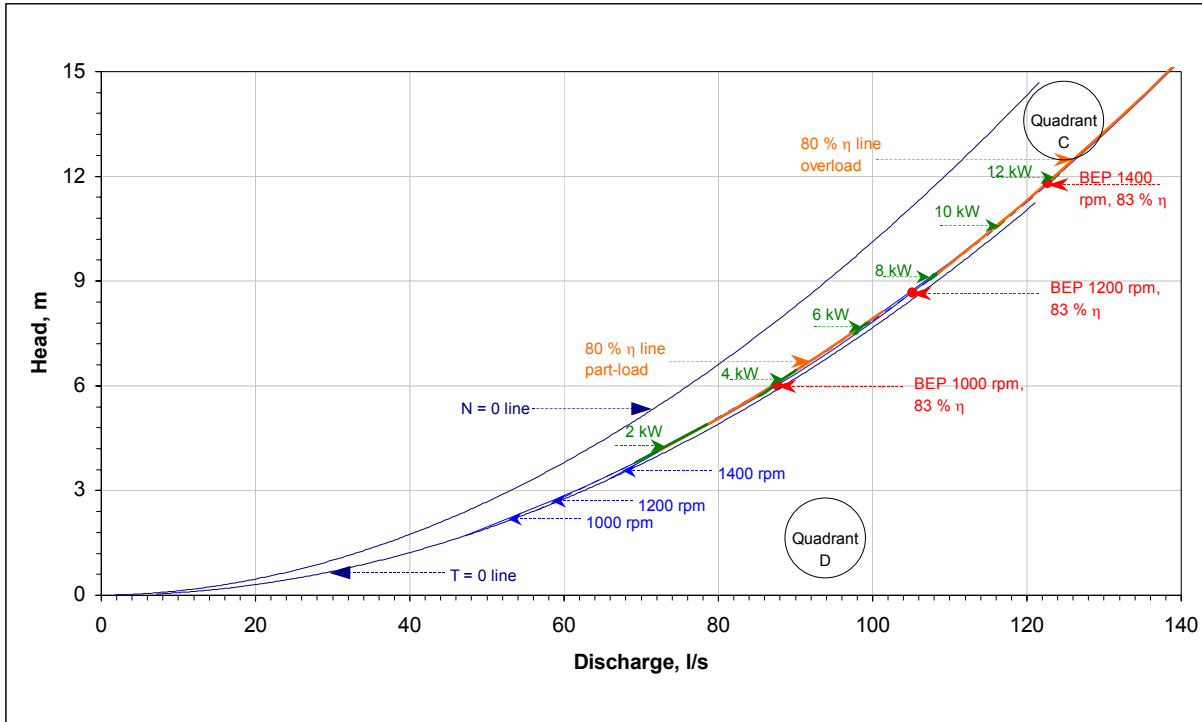Figure B4.7, Muschel Curves for 79.1 rpm PAT with Inlet Casing Rings

Figure B4.8, Muschel Curves for Inlet Rounded 94.4 rpm PAT

B5   Uncertainty Analysis

B5.1   Uncertainty Analysis at BEP

The uncertainty analysis is implemented on the global variables that are contributing to the overall performance of the PATs. It restricted only to the determination of the maximum uncertainty at the BEP for the respective machines under the non-modified stage.

The overall efficiency as represented by Equation (3.1) in Chapter 3 is reincorporated.

$$\eta = \frac{2\pi NT/60}{\rho gQH} \qquad (3.1)$$

The uncertainty equation for efficiency (η) is expressed as a partial differential based on the 4 global variables, head (H), torque (T), speed (N) and discharge (Q) as follows.

$$\partial\eta = \frac{\partial\eta}{\partial T}\cdot\delta T + \frac{\partial\eta}{\partial N}\cdot\delta N + \frac{\partial\eta}{\partial H}\cdot\delta H + \frac{\partial\eta}{\partial Q}\cdot\delta Q \qquad (B5.1)$$

$$\delta\eta = \pm\left[\left(\frac{\partial\eta}{\partial T}\cdot\delta T\right)^2 + \left(\frac{\partial\eta}{\partial N}\cdot\delta N\right)^2 + \left(\frac{\partial\eta}{\partial H}\cdot\delta H\right)^2 + \left(\frac{\partial\eta}{\partial Q}\cdot\delta Q\right)^2\right]^{\frac{1}{2}} \qquad \text{(B5.2)}$$

$$\frac{\delta\eta}{\eta} = \pm\left[\left(\frac{\delta T}{T}\right)^2 + \left(\frac{\delta N}{N}\right)^2 + \left(-\frac{\delta H}{H}\right)^2 + \left(-\frac{\delta Q}{Q}\right)^2\right]^{\frac{1}{2}} \qquad \text{(B5.3)}$$

The individual uncertainties within the global variables are determined based on inputs from the Table A3.3 (section A3, Appendix A) and summarized in Table B5.1. The uncertainties summarized below are a combination of random and systematic errors. The manufacturers guarantees and recommendation on the maximum possible errors of respective instruments (Table A3.3, section A3, Appendix A) are used as the starting tool for the determination of overall uncertainty.

Table B5.1, Summary of the fundamental uncertainties associated with global variables

Variable	Maximum Uncertainty	Comments
δH	$\delta H = 1\%\cdot 0.8\cdot 20 + 2\%\cdot 0.2\cdot 2 = \pm 0.168\,\text{m}$	80% weight to Inlet head (0-20 m) and 20% weight to Exit head (0-2m)
δQ	$\delta Q = 1\%\cdot Q_{max\cdot range}$	$Q_{max\cdot range}$ is electronically altered for various PATs (summarized in Table B5.2)
δN	$\delta Q = \pm 1\,\text{rpm}$	Constant throughout
δT	$\delta T = 0.1\%\cdot 100\,\text{Nm} = \pm 0.1\,\text{Nm}$	Constant throughout

The overall uncertainties for the respective BEPs are summarized in Table B5.2 for all the PATs at experimentally tested speeds. The maximum uncertainty for the efficiency ($\delta\eta$) is determined based on Equation (B5.2) and individual uncertainties listed in Table B5.1.

Table B5.2, Absolute uncertainty table for the tested PATs at the respective BEPs

PAT	BEP Details					Maximum (Absolute) Uncertainty in Variables						
	N	Q	H	T	η	δH	δQ		δN	δT	$\delta\eta$	$\eta\pm\delta\eta$
							$Q_{max.range}$	δQ				
	(rpm)	(l/s)	(m)	(Nm)	(%)	(m)	l/s	(l/s)	(rpm)	(Nm)	(%)	(%)
24.5 rpm	900	30.1	17.1	40.9	76.5%	± 0.168	200.0	± 2.0	± 1	± 0.10	$\pm 5.1\%$	76.5% $\pm$ 5.1%

35.3 rpm	1300	28.6	15.5	25.9	81.0%	± 0.168	200.0	± 2 .0	± 1	± 0.10	± 5.7%	81.0% ± 5.7%
36.4 rpm	1400	22.7	13.4	14.6	71.5%	± 0.168	50.0	± 0.5	± 1	± 0.10	± 1.9%	71.5% ± 1.9%
39.7 rpm	1100	67.5	16.0	76.8	83.5%	± 0.168	100.0	± 1.0	± 1	± 0.10	± 1.5%	83.5% ± 1.5%
45.2 rpm	1400	43.9	13.7	32.0	79.5%	± 0.168	200.0	± 2.0	± 1	± 0.10	± 3.8%	79.5% ± 3.8%
46.4 rpm	1600	19.7	10.6	9.3	76.0%	± 0.168	50.0	± 0.5	± 1	± 0.10	± 2.4%	76.0% ± 2.4%
79.1 rpm	1200	107.9	10.0	63.8	75.5%	± 0.168	150.0	± 1.5	± 1	± 0.10	± 1.6%	75.5% ± 1.6%
94.4 rpm	1100	96.4	7.3	49.7	83.0%	± 0.168	150.0	± 1.5	± 1	± 0.10	± 2.3%	83.0% ± 2.3%

The Table B5.2 summarizes only the absolute values of uncertainties. However it would be useful to analyze the relative influences (from the different variables, H, Q, T, N), which are carried out in Table B5.3 for the identical points of Table B5.2. This table helps in analyzing the dominating and non-dominating uncertainties.

Table B5.3, Relative uncertainty table for the tested PATs at respective BEPs

PAT	δ H/H (%)	δ Q/Q (%)	δ T/T (%)	δ N/N (%)	δ η/η (%)
24.5 rpm	± 1.0%	± 6.6%	± 0.2%	± 0.1%	± 6.7%
35.3 rpm	± 1.1%	± 7.0%	± 0.4%	± 0.1%	± 7.1%
36.4 rpm	± 1.2%	± 2.2%	± 0.7%	± 0.1%	± 2.6%
39.7 rpm	± 1.1%	± 1.5%	± 0.1%	± 0.1%	± 1.8%
45.2 rpm	± 1.2%	± 4.6%	± 0.3%	± 0.1%	± 4.7%
46.4 rpm	± 1.6%	± 2.5%	± 1.1%	± 0.1%	± 3.2%
79.1 rpm	± 1.7%	± 1.4%	± 0.2%	± 0.1%	± 2.2%
94.4 rpm	± 2.3%	± 1.6%	± 0.2%	± 0.1%	± 2.8%

The observations from Table B5.2 and B5.3 are summarized below.

i. It is seen from <u>Table B5.2</u> that the maximum uncertainty for efficiency ($\delta\eta$) with the 24.5 rpm and 35.3 rpm PAT is over $\delta\eta = \pm$ 5%, which is quite considerable. Correspondingly from <u>Table B5.3</u>, the relative efficiency uncertainty, ($\delta\eta/\eta$) and relative discharge uncertainty ($\delta Q/Q$) are in the range of ±6.5% to ±7%. It is therefore clearly evident that the major source of error is coming from the discharge uncertainty, which is firstly due the range of the flow meter scale selected (0-200 l/s causing a higher $\delta Q = \pm 2$ l/s) and secondly due to the fact that maximum discharge measured is in the range of only 30 l/s. The relative contribution of head uncertainty ($\delta H/H$) is over ±1%, which also plays a secondary role to discharge. The contributions from the torque and speed uncertainties are however negligible.

ii. The 45.2 rpm PAT has a absolute uncertainty in efficiency ($\delta\eta$) of about ±3.8% and relative uncertainty ($\delta\eta/\eta$) of ±4.7%. This level of uncertainty is arising firstly from discharge uncertainties ($\delta Q/Q = \pm 4.6\%$) as seen in <u>Table B5.3</u> and secondly from head uncertainties ($\delta H/H = \pm 1.2\%$).

iii. In the 46.4 rpm PAT the overall uncertainty ($\delta\eta = \pm 2.4\%$) and the relative uncertainty ($\delta\eta/\eta = \pm 3.2\%$) is caused mainly due a relative discharge uncertainty of ($\delta Q/Q = \pm 2.5\%$) and a relative head uncertainty of ($\delta H/H = \pm 1.6\%$). The influences of discharge uncertainties have reduced slightly after the range of the flow meter scale (0 – 50 l/s) was made more compatible with the magnitude of measurements made.

iv. The absolute uncertainty in efficiency for the 36.4 rpm PAT has reduced to ($\delta\eta = \pm 1.9\%$), mainly due to the improvement in discharge uncertainties.

v. The 94.4 rpm mixed flow PAT has an absolute uncertainty in efficiency of ($\delta\eta = \pm 2.3\%$) and relative uncertainty of ($\delta\eta/\eta = \pm 2.8\%$), with a dominating contribution coming from relative head uncertainty ($\delta H/H = \pm 2.3\%$). A higher value of relative head uncertainty persists due to a lower magnitude of net head (H) recorded (H = 7.3 m). The relative discharge uncertainty is only ($\delta Q/Q = \pm 1.6\%$) due to a better range for the flow meter and higher magnitude of discharge measured.

vi. The overall uncertainty in efficiency for the 39.7 rpm and 79.1 rpm PAT is in the range of ±1.5%. However there are differences regarding the causes of the same. In the 39.7 rpm PAT the relative discharge uncertainty ($\delta Q/Q$) has a greater influence on the overall uncertainty in efficiency, while for the 79.1 rpm PAT the relative head uncertainty ($\delta H/H$) plays a dominating role.

B5.2   Uncertainty Analysis for Experimental-CFD Correlation

In this section an estimate of the uncertainties present experimental and CFD approach for comparison will be carried out separately. The focus will be on the experimental approach developed in section 3.1.3.4, Chapter 3.

B5.2.1   Experimental Uncertainty

It is seen in section 3.1.3.4.1 (Chapter 3) that leakage and mechanical loss corrections were incorporated for the experimental results. These corrections are necessarily subjected to uncertainties, which needs to be determined separately along with the uncertainties for random/systematic errors discussed in section B5.1.

B5.2.1.1   Leakage and Mechanical Loss

It is shown in section 3.1.3.4.1, Chapter 3 that the leakage discharge (Equation (3.13)) is given by,

$$Q_{Le} = \mu \cdot A_{Le} \cdot \sqrt{\frac{2\Delta p_{Le}}{\rho}} \qquad (3.13)$$

The leakage uncertainty can be determined from the following differentially equation assuming the individual uncertainties associated with only the t_{Le} thickness of leakage cross-section and Δp_{Le}, the pressure difference.

$$\delta Q_{Le} = \pm \left[\left(\frac{\partial Q_{Le}}{\partial t_{Le}} \cdot \delta t_{Le} \right)^2 + \left(\frac{\partial Q_{Le}}{\partial (\Delta p_{Le})} \cdot \delta (\Delta p_{Le}) \right)^2 \right]^{\frac{1}{2}} \qquad (B5.4)$$

The uncertainty associated with the dependent variables of Equation (B5.4) is summarized in Table B5.4.

Table B5.4, Summary of the fundamental uncertainties associated with variables for leakage discharge calculation

Variable	Maximum Uncertainty	Comments
(Δp_{Le})	$\delta(\Delta p_{Le}) = \pm 0.168$ m or 1648 N/m^2	Similar to δH in Table B5.1
t_{Le}	$\delta t_{Le} = \pm 0.2$ mm	50% of existing clearance (0.4 mm)

The experimental power output is determined from Equation (3.12), Chapter 3. The efficiency assumed for the mechanical system (bearings, disc friction and seals), is subjected to uncertainties. It is seen that the other parameters of the power Equation (3.12) namely torque and speed also have uncertainties as illustrated in Table B5.1. The overall uncertainty in power can be determined from Equation (B5.5) assuming $\delta\eta_{mech} = \pm 2\%$, $\delta T = \pm 0.1$ Nm and $\delta N = \pm 1$ rpm.

$$\delta P_{hyd} = \pm\left[\left(\frac{\partial P_{Lhyd}}{\partial \eta_{mech}} \cdot \delta\eta_{mech}\right)^2 + \left(\frac{\partial P_{Lhyd}}{\partial T} \cdot \delta T\right)^2 + \left(\frac{\partial P_{Lhyd}}{\partial N} \cdot \delta N\right)^2\right]^{\frac{1}{2}} \qquad (B5.5)$$

The overall uncertainties in leakage discharge and output powers are summarized in Table B5.5 at the BEP for the various PATs on which experimental-CFD comparisons are carried out in section 4.2, Chapter 4.

Table B5.5, Absolute uncertainty table for the Q_{Le} and P_{hyd} of the tested PATs (experiment-CFD) at respective BEPs

PAT		Q**	Q_{Le}	δQ_{Le}	δQ_{Le}/Q**	P_{hyd}	δP_{hyd}	δP_{hyd}/P_{hyd}
		(l/s)	(l/s)	(l/s)	(%)	(watts)	(watts)	(%)
24.5 rpm		24.4	1.66	±0.83	±3.4%	2527	±52.1	±2.1%
35.3 rpm		21.7	1.29	±0.65	±3.0%	1824	±38.6	±2.1%
39.7 rpm	CRP	47.1	1.44	±0.72	±1.5%	3360	±68.9	±2.1%
39.7 rpm	CRA	46.9	1.43	±0.72	±1.5%	3385	±69.8	±2.1%

It is seen from Table B5.5, the uncertainties in the overall discharge through the impeller due the possible leakage errors is ±3% to ±3.5% for the 35.3 rpm PAT and the 24.5 rpm PAT to ±1.5% for the 39.7 rpm PAT. The power uncertainty remains constant at 2.1% for all the PATs.

B5.2.1.2   Overall Uncertainty

The overall uncertainty (relative) combining all the random/systematic errors with the leakage and mechanical loss errors are summarized in Table B5.6 for the same PATs at the respective BEPs.

Table B5.6, Relative uncertainty table for the tested PATs (experiment-CFD) at the respective BEPs

PAT		N	Q**	H	T	P_{hyd}	η_{hyd}	δ H/H	δ Q**/Q**	δP_{hyd}/P_{hyd}	$\delta\eta_{hyd}$/η_{hyd}
		(rpm)	(l/s)	(m)	(Nm)	(watts)	(%)	(m)	(%)	(%)	(%)
24.5 rpm		803	24.4	13.0	29.6	2527.0	81.3%	±1.3%	±9.6%	±2.1%	±9.9%
35.3 rpm		1002	21.7	10.0	17.1	1823.7	85.3%	±1.7%	±10.2%	±2.1%	±10.5%
39.7 rpm	CRP	808	47.1	8.5	39.1	3359.6	85.2%	±2.0%	±1.6%	±2.1%	±3.3%
39.7 rpm	CRA	811	46.9	8.5	39.3	3384.8	86.3%	±2.0%	±1.6%	±2.1%	±3.3%

It is clearly seen that the overall relative uncertainty of discharge is maximum for the 24.5 rpm and 35.3 rpm PATs with over ±10% maximum deviations. The discharge uncertainties for the 39.7 rpm PAT is comparatively negligible. The power and head uncertainties are relatively constant for all the PATs within a maximum deviation of ±2%.

B5.2.2   CFD Uncertainty

The determination of the uncertainty for the CFD results is not so straightforward. An attempt is made to determine the quality of the model using the internal flow measurements (swirl angle and axial velocities) at the reference plane 'e' (Figure 2.3, Chapter 2). The Table B5.7 summarizes the discharges calculated from the area integration of the axial velocity profiles and boundary discharge.

As seen the discharges obtained from velocity integration method are not matching with the given boundary discharges at all loads except load B and are consistently higher. At load D an error of 14% is recorded, which is very high, while for loads E and F the errors are more sympathetic within the range of 3% to 5%. These deviations give an indication of the level of uncertainty that may occur in the CFD predictions, though it cannot be used accurately to determine the overall uncertainty of power number, head number and efficiency.

Table B5.7, Uncertainties associated with the discharge variable using CFD

Load	Boundary Discharge	Calculated Discharge $\int v_x \, dA$	Error
	(l/s)	(l/s)	(%)
B	33.6	33.4	0.6%
C	42.6	45.8	-7.5%
D	48.4	55.2	-14.0%
E	56.0	59.2	-5.7%
F	60.2	62.1	-3.2%

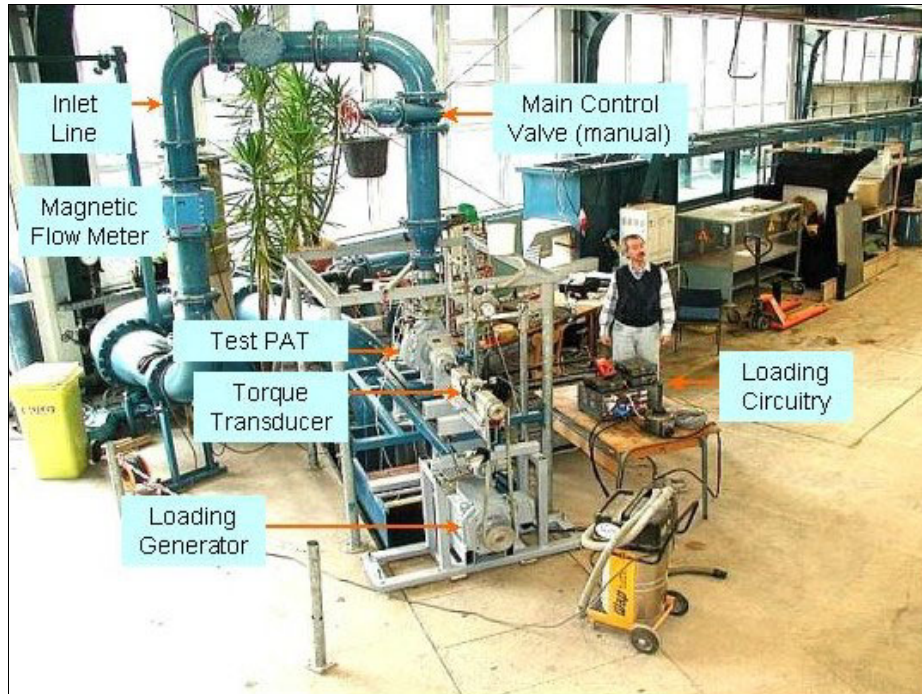# B6 Journey in Pictures

B6.1 Test-Rig
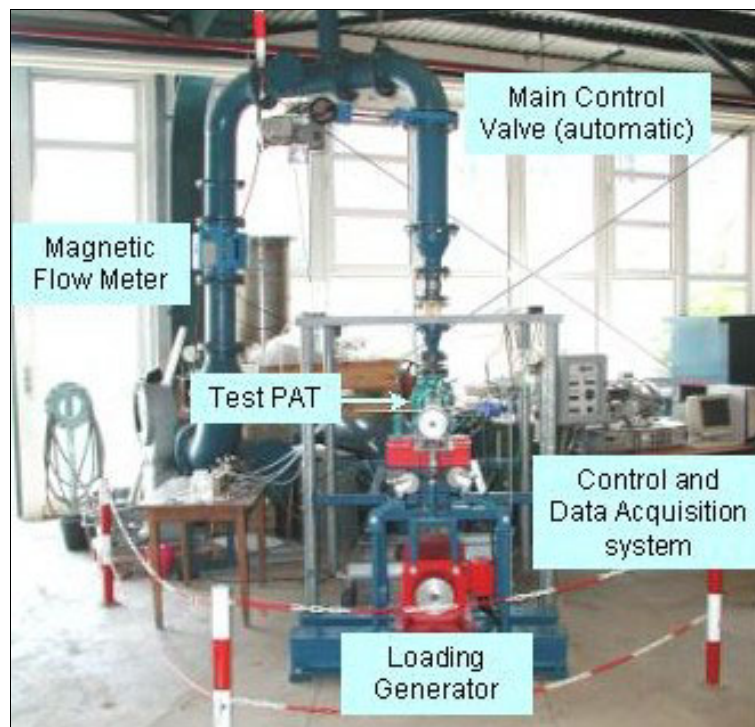

Figure B6.1, Test-Rig Layout 1
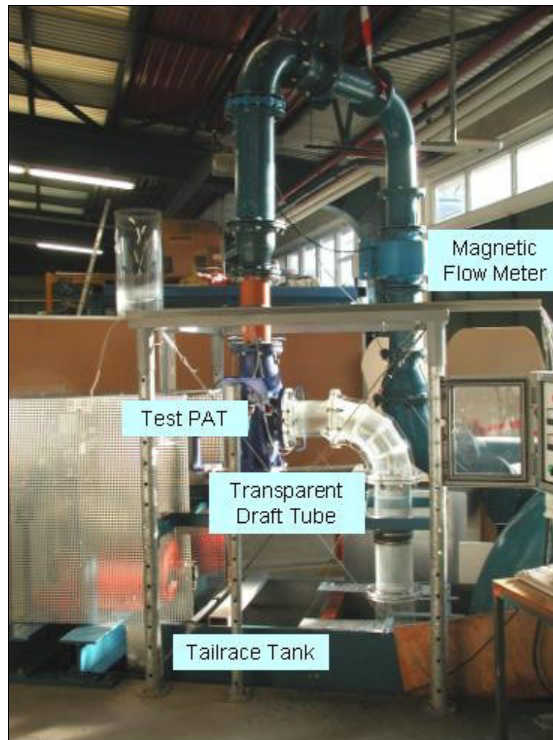

Figure B6.2, Test-Rig Layout 2
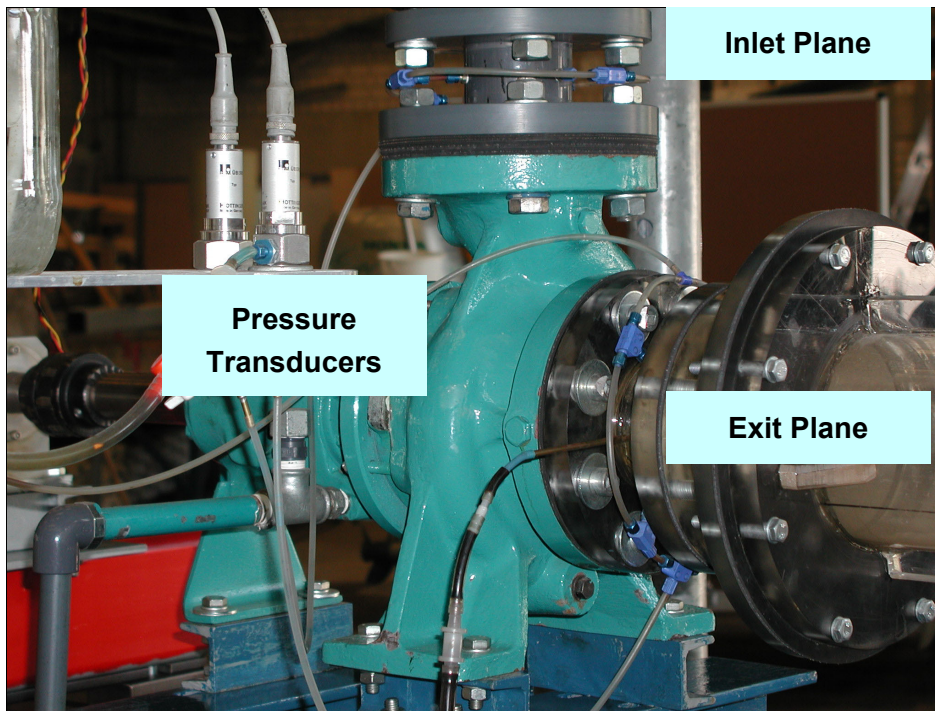
Figure B6.3, Test-Rig Layout 3

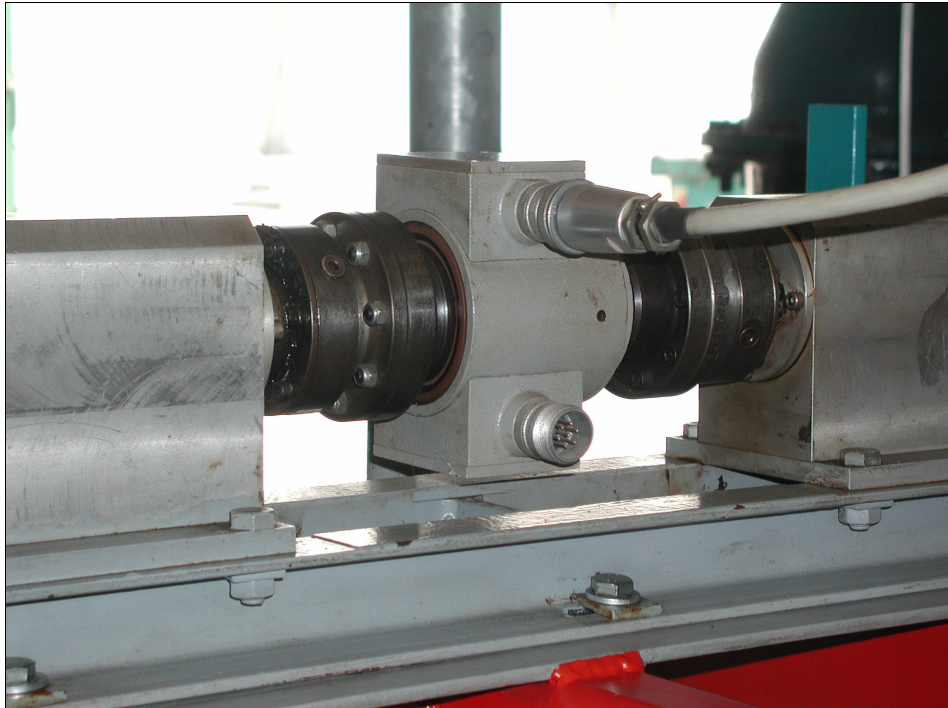Figure B6.4, The Pressure Transducers

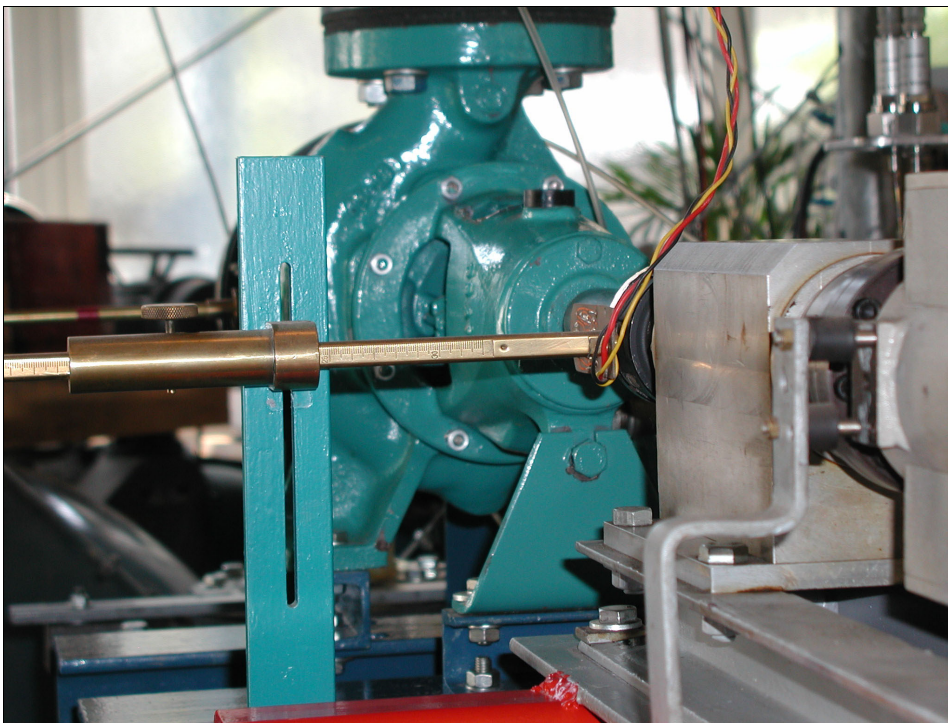Figure B6.5, The Torque Transducer

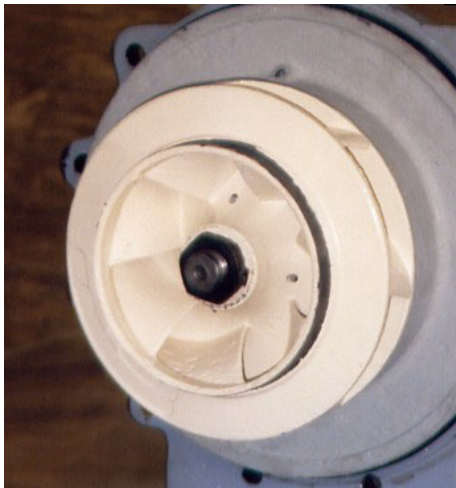Figure B6.6, The Speed Sensor

B6.2   PATs Tested

Figure B6.7, 24.5 rpm Impeller

Figure B6.8, 24.5 rpm PAT

Figure B6.9, 35.3 rpm Impeller

Figure B6.10, 35.3 rpm PAT

Figure B6.11, 36.4 rpm Impeller

Figure B6.12, 36.4 rpm PAT

Figure B6.13, 39.7 rpm Impeller

Figure B6.14, 39.7 rpm PAT
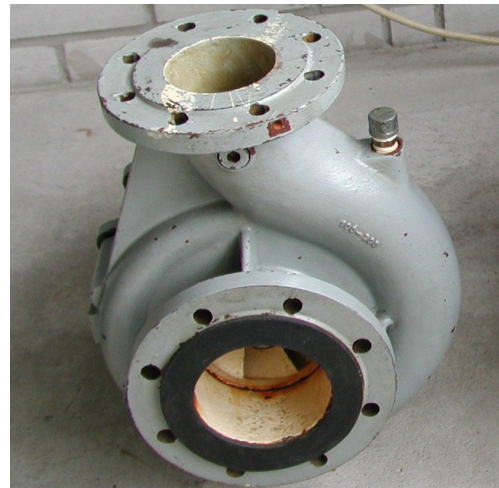

Figure B6.15, 45.2 rpm Impeller

Figure B6.16, 45.2 rpm PAT

Figure B6.17, 46.4 rpm Impeller

Figure B6.18, 46.4 rpm PAT

Figure B6.19, 79.1 rpm Impeller

Figure B6.20, 79.1 rpm PAT

Figure B6.21, 94.4 rpm Impeller

Figure B6.22, 94.4 rpm PAT

B6.3 PAT Installation

Figure B6.23, The Assembled PAT System with Main Shaft (Ex-Workshop)

Figure B6.24, Installation of the Manifold Lines and Draft Tubes

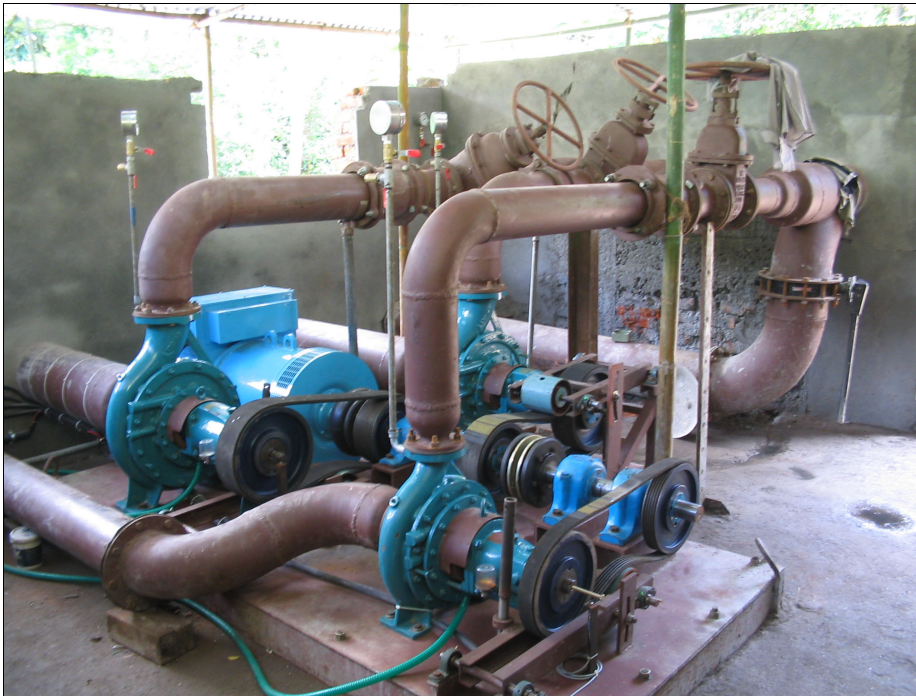Figure B6.25, The Hydro-Mechanical System with Bypass Line
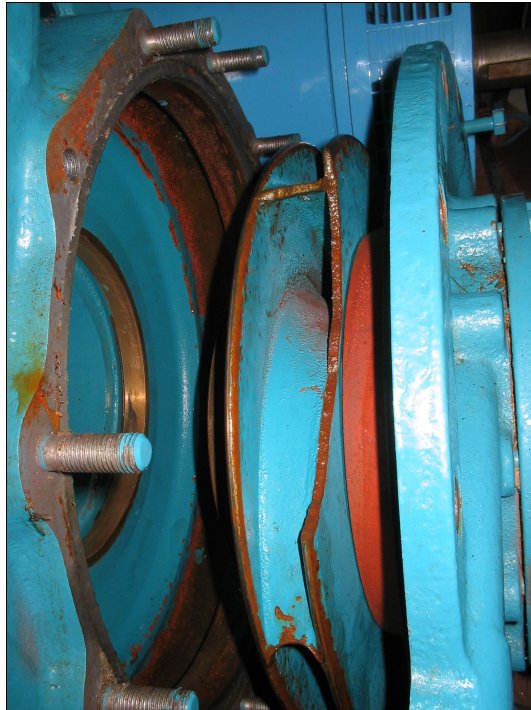

Figure B6.26, The Powerhouse

Figure B6.27, The damaged impeller

Curriculum Vitae

Name		Punit Singh
Birth	15.09.1976	New Delhi
Schooling	1982 – 1987	Primary School, Bangalore
	1987 – 1992	Middle and High School, Bangalore
	1992 – 1994	Pre – University School, Bangalore
Professional Education	1994 – 1998	Bachelors in Mechanical Engineering, University of Mysore
Work Experience	1998 – 1999	Field work in Micro Hydro at Samvada (an NGO - Non Governmental Organization), Bangalore
Higher Education	1999 – 2001	Masters in Energy Studies, Indian Institute of Technology Delhi
	2001 – 2005	Doctoral Research on 'Pumps as Turbines' at the Faculty of Civil, Geology and Environmental Science, University of Karlsruhe